The evolution of massive stars in the Small Magellanic Cloud

Dissertation
zur
Erlangung des Doktorgrades (Dr. rer. nat.)
der
Mathematisch-Naturwissenschaftlichen Fakultät
der
Rheinischen Friedrich-Wilhelms-Universität Bonn

von
Abel Schootemeijer
aus
Amsterdam, Niederlande

Bonn, 15.11.2018

Dieser Forschungsbericht wurde als Dissertation von der Mathematisch-Naturwissenschaftlichen Fakultät der Universität Bonn angenommen und ist auf dem Hochschulschriftenserver der ULB Bonn http://hss.ulb.uni-bonn.de/diss_online elektronisch publiziert.

1. Gutachter:	Prof. Dr. Norbert Langer
2. Gutachter:	Prof. Dr. Peter Schneider
Tag der Promotion:	15.02.2019
Erscheinungsjahr:	2019

‘LIFE WITHOUT KNOWLEDGE IS DEATH IN DISGUISE’
— Scooter

Abstract

In this work we study stars that are born massive enough to explode as supernovae at the end of their lives: massive stars. With their high luminosities, especially during their their final moments, these massive stars can be studied individually in galaxies other than our own Milky Way – supernovae can even be observed from so far away that we can use them to probe the early universe. The same is true for the coalescence of their neutron star or black hole remnants in close binary systems. The recently detected gravitational waves emitted during this process have opened a new window to study massive stars.

To comprehend the deaths of massive stars and that what remains of them afterwards, it is crucial to have a deep understanding of massive stars themselves – but at the moment many processes that strongly affect massive stars are uncertain. These regard, e.g., stellar wind mass loss, internal mixing and the effects of binarity. Studying the pre-supernova evolution of massive stars in the distant, early universe is practically impossible because they appear so dim. Fortunately, the Small Magellanic Cloud (SMC) satellite galaxy is a unique, nearby, laboratory to study stars in the same conditions. The early universe alike, it is deficient in elements heavier than helium – by 80%. The goal in this thesis is to improve our understanding of massive star evolution in the SMC, with a focus on internal mixing. For this, we compute large grids of stellar evolution models using the detailed stellar evolution code MESA.

First, we attempt to understand the formation of Wolf-Rayet (WR) stars in the SMC. These are the stripped cores of evolved massive stars. In principle, the absence of a massive hydrogen-rich envelope can be explained by aforementioned wind mass loss, internal (rotational) mixing and binary interaction. We find a subgroup of hot, hydrogen-rich, apparently single WR stars that do not match chemically homogeneous evolution induced by rotational mixing. We find that the remaining parts of the hydrogen envelopes contain a steep H/He gradient, likely caused by other internal mixing. We cannot exclude wind mass loss, but we argue that the most likely way to form these WR stars is through binary interaction late in their evolution. A dedicated observational campaign could provide a definitive answer.

Given that we inferred that internal mixing has taken place in these WR stars, we attempt to constrain internal mixing processes for the majority of massive stars in the SMC. We compute evolutionary models, simultaneously varying the efficiency of convective core overshooting, semiconvection and rotational mixing. We find that significant internal mixing occurs only for combinations where semiconvective mixing is efficient and overshooting is not too strong. We then compare our models to observations of blue and red supergiants. Again, efficient semiconvection and intermediate overshooting match best – with the data that is available. This strengthens our earlier conclusion about these processes.

Sadly, we can not do a complete comparison with observations because no full spectroscopic analysis of the massive stars in the SMC has (yet) been performed. Therefore, we create synthetic color-magnitude diagrams to compare with existing complete photometric data. We tentatively identify a population of blue supergiants with the same color as predicted for stars that experienced efficient semiconvection.

In this thesis we have, via two different methods, found indications for internal mixing in massive stars. Observational follow-up on our work could anwser two important questions about the evolution of massive stars at low metallicity: First, can they lose their hydrogen-rich envelopes in isolation? Second, can we get further constraints on internal mixing – and what process drives it?

Contents

CHAPTER 1

Introduction

1.1 The study of space throughout time – a brief history of astronomy

The visual spectacle offered by the night sky has intrigued mankind since day one. Especially in the bygone days where all humans lived in areas without light pollution, it is easy to imagine that the structures in the sky (and their motions) played a big role in their lives. Thus, in ancient cultures they started studying the motions of the Sun, the Moon and the countless smaller sources. Examples of these ancient cultures are the Babylonians, the Egyptians, the Scottish and the ancient Greeks. Apart from the hard-to-miss motions in the sky of the Sun and the Moon (with respect to the light sources in the background), they noticed that also some of the smaller sources cross a large part of the sky on the timescale of a year. These were dubbed the 'wanderers', a word that translates from English into ancient Greek as 'planets'. The others, which do not change their positions enough for their motion to be noticeable by eye, are the ones we call the stars.[1]

Aristotle thought that the cosmos had no beginning an no end – it was eternal and also unchanging. However, throughout history, humankind has noticed several changes in the night sky. For example, there are historical recordings of apparently new stars, which rapidly grew in brightness and then faded in the timescale of about a year. The brightest of these events, so-called supernovae, occurred in the year 1006 (Stephenson, Clark and Crawford, 1977). This supernova was more than a thousand times brighter than the brightest star at night and only ten times less bright than the full Moon, making it visible even during day time. We know know that the appearance of these 'new' stars does not mark the birth of a new star, but a violent stellar death.

More of the ancient world (or universe) views have changed compared to the present day. The belief that the Earth was in the center of the universe (i.e., the geocentric model) made place for a model in which the Earth orbited the Sun: this is the heliocentric model, as proposed by Copernicus in the sixteenth century. Finally, the belief that our universe has no beginning is no longer popular. The discovery of Edwin Hubble that the universe is expanding (Hubble, 1929)[2] ultimately lead to the now commonly accepted picture where the universe started as an extremely hot and dense point – somewhere 13.8 billion years ago (Planck col. 2015) – and that it has been expanding ever since. This starting point is referred to as the 'Big Bang'.

Since the ancient days, much has also been unveiled about the nature of stars. Let us take the example

[1] Many observers thought that there is information about the future hidden in the positions of stars and planets. This, however, has not (yet) been scientifically proven (Zarko 2011).

[2] He observed that the further away a galaxy is, the faster it moves away from us.

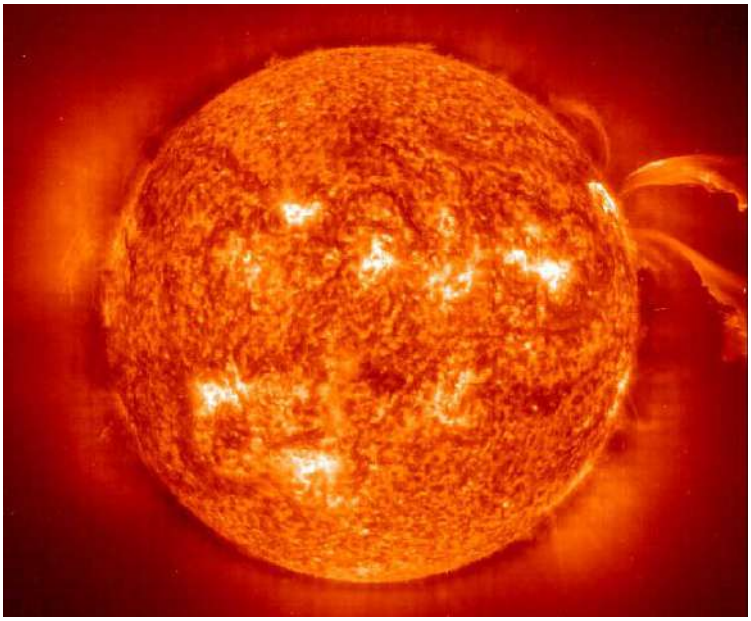

Figure 1.1: Image of the most famous star at Earth: the Sun. Image was taken with the Extreme ultraviolet Imaging Telescope (EIT) on board of the Solar and Heliospheric Observatory (SOHO), which is a space telescope.

of the Sun. Given that it appears to be a colossal ball of fire (Fig. 1.1), a reasonable guess would be that it is powered by chemical reactions. Then, one can calculate what would be the lifetime of the Sun if it consisted of, for example, methane and oxygen[3]. The result is that, given its observed mass and luminosity, the Sun would be able to burn for around fifty thousand years. A similar result would be obtained for other chemical reactions. This number was orders of magnitudes off compared to estimates of the minimum age of the Earth that were available in the eighteenth and nineteenth century, which indicated an age in excess of a hundred million years.

A new idea was provided by Hermann von Helmholtz in 1850, who proposed that the energy released by gravitational contraction would be the source of power for the Sun. Assuming that it started as a much larger sphere of gas, he calculated that this source of energy could power the Sun for around 20 million years. This was a step in the right direction, but it still did not match age estimates that were becoming available, indicating an age of the solar system of around 4.5 billion years. Finally, the solution was provided by nuclear fusion reactions. It was found that the fusion of hydrogen atoms into helium in the center of the Sun[4] could provide enough energy for the Sun to burn for around ten billion years. This was proposed by Sir Arthur Eddington even before nuclear fusion reactions were discovered (Eddington, 1920). In that paper, he wrote the following prophecy that we quote for its wisdom and poetic value:

> *"If, indeed, the sub-atomic energy in the stars is being freely used to maintain their great furnaces, it seems to bring a little nearer to fulfillment our dream of controlling this latent power for the well-being of the human race — or its suicide."*

At the same time, our knowledge of other stars also started to grow. With the advent of systematic observational astronomy, early 20$^{\text{th}}$ century astronomers Hertzsprung and Russell mapped the absolute

[3] Burned via $CH_4 + 2\,O_2 \longrightarrow CO_2 + 2\,H_2O$

[4] Netto reaction: $4\,{}^1\text{H} + 2\,\text{e} \longrightarrow {}^4\text{He}$.

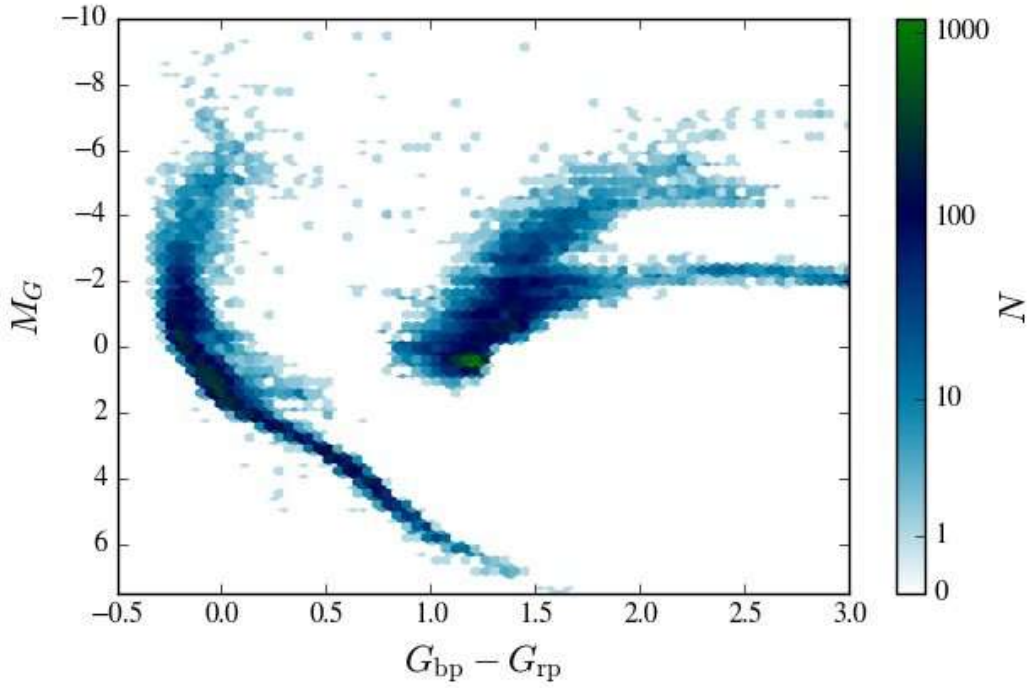

Figure 1.2: Color-magnitude diagram of the brightest 63278 sources in the sky (in the GAIA G band: all have an apparent magnitude $G < 8$). The shade of blue indicates the number of stars in each pixel. The absolute magnitudes M_G are calculated using the distances and extinction A_G as provided in the GAIA database. The color $G_{\rm bp} - G_{\rm bp}$ is corrected for the reddening $E(G_{\rm bp} - G_{\rm bp})$. This figure was made using data from the GAIA DR2 catalog (Gaia Collaboration, Brown, Vallenari et al., 2018). This catalog is publicly available at `https://gea.esac.esa.int/archive`.

magnitude and color of many stars in the sky[5]. We first give a bit of historical background to familiarize the reader with the concept of magnitudes and colors.

Magnitudes were introduced by the Greek astronomers, who divided them into six classes: the brightest stars belonged to the first magnitude and those that are only barely visible by eye to the sixth magnitude. Thus, the lower the magnitude the brighter the star. Hertzsprung and Russell used filters through which they measured the flux (energy per time) of the light that was transmitted. Then, they converted these fluxes into magnitudes. Different filters are transparent to light of different wavelengths: e.g., only blue light passes through the B filter and the V filter only transmits light in the middle of the visible part of the spectrum. The 'color' of a star is defined as the bluer magnitude minus the redder magnitude, e.g., $B - V$. The higher the value, the redder the star is. In Fig. 1.2 we show the color $G_{\rm bp} - G_{\rm rp}$ on the x-axis. On the y-axis of a color-magnitude diagram, the absolute magnitude is shown (in Fig. 1.2, M_G). This is the magnitude that a star would have if it would be at a distance of 10 parsec[6] (pc) - i.e., it is a measure for the luminosity. The $G_{\rm bp} - G_{\rm rp}$ color and M_G magnitude are obtained with filters on board of the recently launched GAIA satellite (Gaia Collaboration, Prusti, de Bruijne et al., 2016). This GAIA satellite carries out a revolutionary mission in which it precisely measures the positions and motions of unprecedented amount of sources – we will use observational data from this GAIA satellite in Chapter 4.

When Hertzsprung and Russell compiled their color-magnitude diagrams, they saw a picture similar to

[5] The diagram in which they plotted these quantities is called the color-magnitude diagram or the Hertzsprung-Russell diagram.
[6] This corresponds to $3.1 \cdot 10^{16}$ meter or 3.3 light year.

what is shown in Fig. 1.2 (except that this figure is created using data obtained with the GAIA satellite). At the left (blue, higher temperature) side, there is a narrow band of stars that is called the main sequence. At the right (red, lower temperature) side, there is the horizontal branch at $M_G \approx -2$ and the red giant branch, which extends to lower magnitudes (i.e., it contains more luminous stars). This finding raised a number of questions: why do stars 'prefer' to stay in these locations in the color-magnitude diagram? Which stars occupy which locations?

Similarly, with the important question about the energy source of stars answered, an innumerable and ever-increasing amount of questions concerning stars still remained. For example, where do the supernovae, that we mentioned earlier, originate from? Could stars collapse into black holes (which were thought to be an anomaly from the theory of general relativity by Einstein himself)? What is the origin of the heavy elements[7] in the universe? If gravitational waves, which are predicted by general relativity, exist: what are their progenitors? We elaborate on the progress in answering these questions in the next section.

1.2 Massive stars as spiders in the cosmic web

Massive stars are intimately connected to many marvelous objects, processes and phenomena that we observe in the sky. Below, we highlight some of these to illustrate the central role that massive stars play in astrophysics.

1.2.1 Supernovae

In relation to the question about the origin of supernovae that was posed earlier, we start with what defines a star as 'massive'. Early calculations of stars with various masses showed that lower-mass stars, such as the Sun, in their centers never reach temperatures high enough to continue nuclear burning after helium is synthesized into carbon and oxygen. After that, the core of such a star contracts and can become a white dwarf[8] after losing the outer layers. If a star is born with a certain mass that is higher than the mass of the Sun, it can also fuse carbon in the center and ends up as an oxygen-neon-magnesium white dwarf.

For even higher initial masses, nuclear fusion can continue until the mass of the iron core, which has become degenerate at that point, exceeds the Chandrasekhar mass (the maximum mass where electron degeneracy can provide pressure support). Then, the core collapses while the the outer layers are ejected. Stars that are massive enough to go through this path of evolution are the ones we refer to as 'massive stars'. The initial mass required for a core collapse supernova is not well known, but it is has been estimated to be around seven to nine times the mass of the Sun (Woosley and Heger, 2015).

Supernovae come in different types that show different behaviour. Traditionally, supernovae are divided into two groups: those that are hydrogen free (type I) and those that are hydrogen-rich (type II). These are again divided into subtypes (see e.g. Langer, 2012), such as Ia[9] (strong silicon lines), Ib (no silicon lines, helium lines), and Ic (no silicon lines, no helium lines). Type II supernovae can show distinct subtypes such as IIP, where the light curve (luminosity or magnitude as a function of time) shows a plateau phase, IIL, where the light curve shows more linear decay, IIn, which show narrow emission lines attributed to interaction with material ejected shortly before the supernova, or IIb, which show hydrogen lines only

[7] All elements that are heavier than hydrogen and helium. These light elements are thought to be the only elements created in a significant amount during the Big Bang.

[8] This is very dense object that has no nuclear fusion in its core. Approximately, it contains the mass of the Sun in a volume equal to that of the Earth.

[9] These are not thought to originate from massive strars, but from accreting or colliding white dwarfs (see e.g. Neunteufel, Yoon and Langer, 2016).

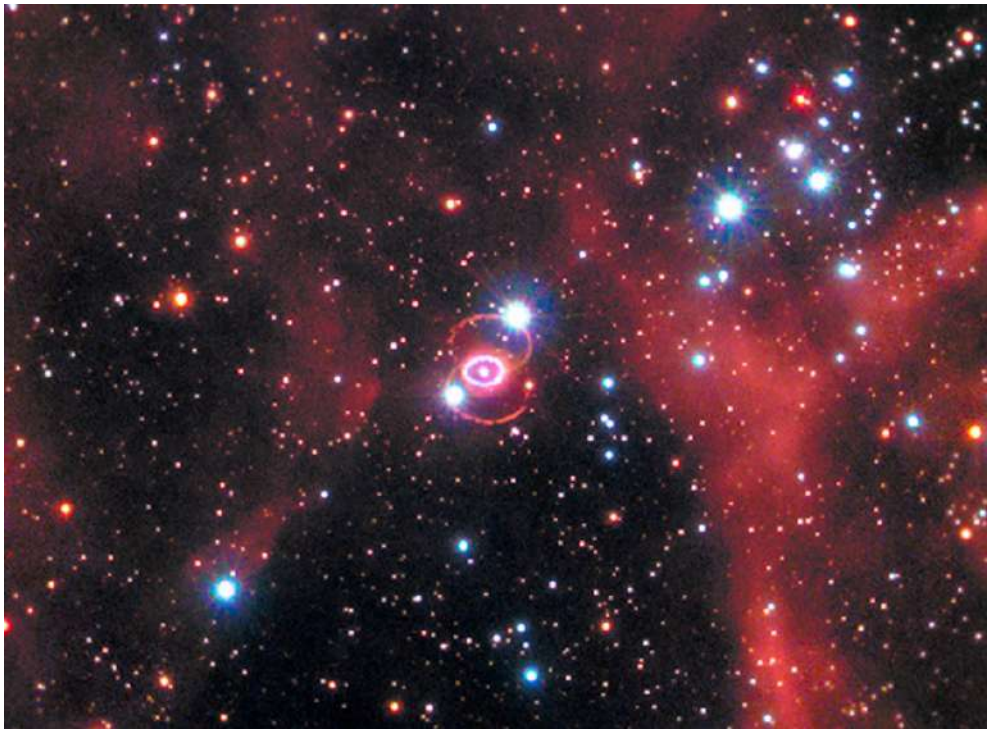

Figure 1.3: Image of the remnant of supernova 1987A. The supernova remnant is the center of the image, in the middle of the narrowest of the three rings. This image was taken by the Hubble Space Telescope in 2017 for the celebration of the 30$^{\text{th}}$ 'birthday' of the supernova (or, alternatively, one can say: to commemorate the 30$^{\text{th}}$ death day of its progenitor star Sanduleak $-69^{\circ}202$a). Image credit: NASA / ESA / R. Kirshner, Harvard-Smithsonian Center for Astrophysics and Gordon and Betty Moore Foundation / P. Challis, Harvard-Smithsonian Center for Astrophysics.

early on. Recently, the class of superluminous supernovae (around a hundred times more luminous than a typical supernova) has been identified (Gal-Yam, 2012).

To understand this large variety of supernova, it is essential that we understand the evolution of their massive star progenitors. This can be illustrated by the example of the famous supernova 1987A (for a recent review see McCray and Fransson, 2016), which is the closest supernova that took place in the era of modern astronomy. This type II supernova occurred in the Large Magellanic Cloud, a satellite galaxy of the Milky Way. Contrary to what was expected from stellar evolution predictions, the progenitor star was a blue supergiant with an effective temperature T_{eff} of 15 to 18 kK (Woosley, 1988) instead of a red supergiant with $T_{\text{eff}} < 4$ kK. An additional unexpected feature are the three ring structures around it (Fig. 1.3), which in combination with its blue color raised the question if it could be a merger product (Podsiadlowski and Joss, 1989). In Chapter 3 and 4 we will at length discuss blue and red supergiants.

1.2.2 Neutron stars and black holes

After a supernova, a number of different remnants can be left behind. An option is that the stellar core contracts until it reaches a radius of around 10 kilometers (as proposed by Baade and Zwicky, 1934). Then, neutron degeneracy pressure impedes further contraction and a neutron star is formed – an otherworldly object with an average density over 10^{14} times the density of liquid water on Earth[10]. Although uncertain, the general picture is that neutron star progenitors are born as massive stars with

[10] If your fingernail had the same density, it would be about as heavy as the whole human population on Earth.

masses between eight and twenty-something solar masses (O'Connor and Ott, 2011; Sukhbold, Ertl, Woosley et al., 2016). Cores of stars born even more massive might completely collapse under their own gravity upon the end. As a result, they form an object so dense that not even light can escape from it: a black hole. Unlike for the formation of a neutron star, this process is not necessarily accompanied by a supernova (Heger, Fryer, Woosley et al., 2003) – the star might just discreetly vanish from sight as its entirety morphs into a black hole. Finally, it is also possible that the massive star does not leave behind any remnant. For a pair instability supernova – where in very hot cores the pressure support is reduced by the formation of electron-positron pairs, leading to a runaway effect (Fowler and Hoyle, 1964) – this is predicted to happen.

In the Crab Nebula, the first of these compact objects was observed (Hewish, Bell, Pilkington et al., 1968) – a neutron star. Only a few years later, indications of the presence of a black hole in the X-ray source Cygnus X-1 were reported (Bolton, 1972; Webster and Murdin, 1972). Due to the difficulties with observing black holes, this claim remained contested for decades. Now, of the order of twenty black holes (or candidates) are observed in a binary system with a stellar companion (Casares, 2007; Casares and Jonker, 2014). The individual masses are uncertain, but have in general masses between four and fifteen times the mass of the Sun.

1.2.3 Gravitational waves

On the historical day of the 14th of September, 2015, gravitational waves were directly detected for the first time by the LIGO observatory (B. P. Abbott, Abbott, Abbott et al., 2016a). The signal taught us that two black holes, of masses of around 36 and 29 $M_\odot$, coalesced into one 62 $M_\odot$ black hole[11]. Many aspects of this discovery were revolutionary. First of all, the detection of the first gravitational waves meant that the theory of general relativity passed yet another test, as the waveform (Fig. 1.4) of the signal followed its predictions. Second, it taught us that double black hole binaries do exist – no such system had ever been discovered before. Third, it was the discovery of the two most massive black holes ever detected, since the masses of the black holes far exceeded those of all known stellar mass black holes (see Sect. 1.2).

Of course, this event sparked a discussion about how these objects are formed. The three major channels that have been proposed are: i) via a stable mass transfer (see Sect. 1.3.6) event in a binary system followed by unstable mass transfer, which should bring both objects close enough together for them to merge on a timescale shorter than the age of the universe (Belczynski, Holz, Bulik et al., 2016); ii) two stars are in a (near-) contact binary – their rapid rotation (induced by tidal forces) causes homogeneous evolution, allowing them to remain compact and collapse into a black hole without mass transfer taking place (de Mink, Cantiello, Langer et al., 2009; Marchant, Langer, Podsiadlowski et al., 2016; de Mink and Mandel, 2016; Mandel and de Mink, 2016). Finally, there is iii) the dynamical channel, where the black holes form in isolation and are bound in a binary via three-body interactions in dense clusters (Banerjee, Baumgardt and Kroupa, 2010; Rodriguez, Chatterjee and Rasio, 2016).

In the two years that followed, another gravitational wave detection stood out as truly spectacular. This time, two neutron stars coalesced (B. P. Abbott, Abbott, Abbott et al., 2017a). In contrast to the earlier binary black hole mergers, electromagnetic radiation was detected as well (B. P. Abbott, Abbott, Abbott et al., 2017b). The gravitational waves were accompanied by a long-duration gamma ray burst, while an afterglow of photons in radio to X-ray wavelength ranges was also observed. In this afterglow, the signatures of heavy elements (such as gold) were found (Pian, D'Avanzo, Benetti et al., 2017), proving

[11] The energy radiated away in this process amounted to $E \approx 3M_\odot c^2 \approx 7 \cdot 10^{54}$ erg in the form of gravitational waves, most of which was emitted in the timescale of tenths of a second. During a brief period, the event was more luminous than all of the stars in the visible universe combined.

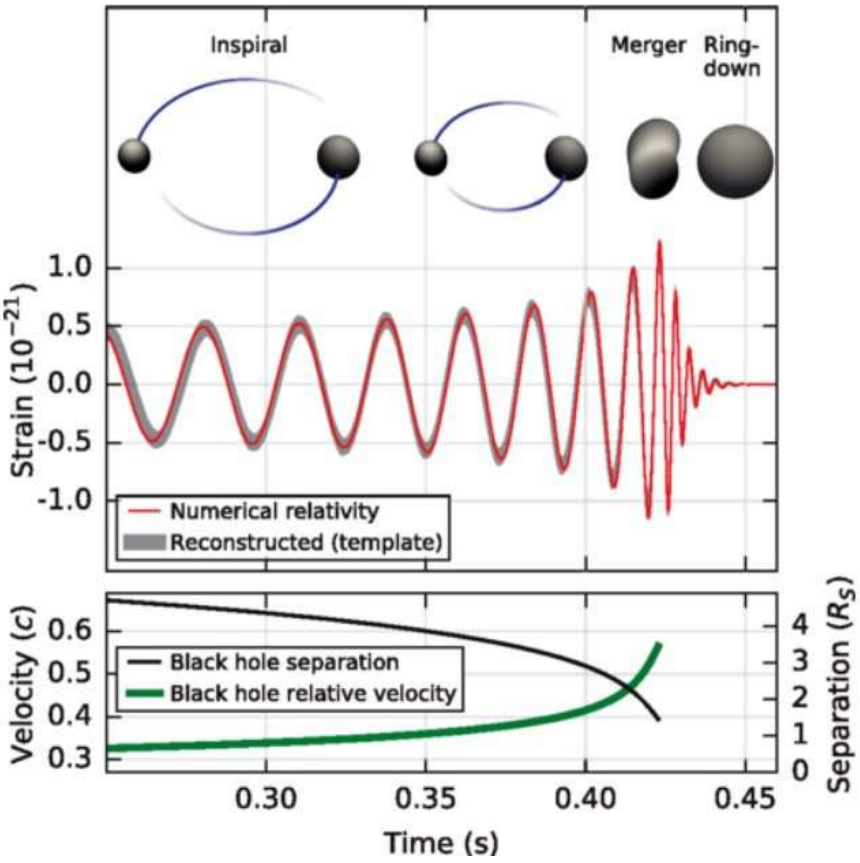

Figure 1.4: The signal and waveform from the first-ever detected gravitational wave, GW150914. The top panel shows the fractional stretching of space, referred to as the 'strain', as a function of time. The bottom panel shows the time evolution of the relative black hole velocities in units of the speed of light c. and their separation in Schwarzschild radii (R_s). This figure is taken from B. P. Abbott, Abbott, Abbott et al. (2016a).

for the first time that such elements can be synthesized upon the merger of two neutron stars (as proposed by Lattimer, Mackie, Ravenhall et al., 1977; Eichler, Livio, Piran et al., 1989).

1.2.4 Massive stars and their environments

When a supernova explosion occurs, layers of the star that are enriched in heavy elements are blown into the surroundings. Thereby, they enrich gas clouds from which new stars can form. This can explain to some extent that we observe that the Sun consists for nearly two per cent of heavy elements (Grevesse and Sauval, 1998; Asplund, Grevesse, Sauval et al., 2009), but also other mechanisms are at play. Another such mechanism that includes massive stars are stellar winds, which become stronger for stars that are born more massive (Vink, de Koter and Lamers, 2001). If born sufficiently massive, stellar winds can blow away layers with heavy elements such as carbon and oxygen during late evolutionary stages (Conti and McCray, 1980) – see also Gamow (1943). In that case, a Wolf-Rayet star is formed. This is a very hot and luminous star that is characterized by strong emission lines originating from a dense stellar wind. In addition, very recently it has been proven that elements even heavier than iron are created upon the coalescence of two neutron stars (Pian, D'Avanzo, Benetti et al., 2017, see above). Finally, another source of heavy elements is the winds of asymptotic giant branch stars, which are stars that end their lives

Figure 1.5: An image of the star cluster R136 taken with the Hubble Space Telescope. This cluster consists of the emsemble of blue sources concentrated slightly to the top-right of the image. Feedback from the stars has created a bubble around the star cluster. Image credit: NASA/ESA.

as white dwarfs but release products of nuclear fusion during late burning phases (e.g. Karakas, 2010).

In addition to chemical enrichment, the material that massive stars blow into their environments provides mechanical feedback. Combined with the ionizing radiation emitted by massive stars, this regulates the formation of new stars in galactic environments (Hopkins, Kereš, Oñorbe et al., 2014). An example of how massive stars affect their surroundings is shown Fig. 1.5. This is an image of the young massive cluster R136 in the Large Magellanic Cloud, where the massive stars have created a hot, high-pressure bubble around the cluster (Chu and Kennicutt, 1994; Pellegrini, Baldwin and Ferland, 2011).

1.3 Physical processes in massive stars

Through a combined effort over many decades, computational methods have been developed that form the backbone of the theoretical study of stellar evolution. These allow for the tuning and testing of a large variety of input physics. Examples are wind mass loss, initial chemical composition, and a variety of mixing processes. We first discuss some of the most important input physics in massive stars, putting extra emphasis on internal mixing processes because these are a major topic in this thesis. Then, we show the evolution of a $32\,M_{\odot}$ star as an example.

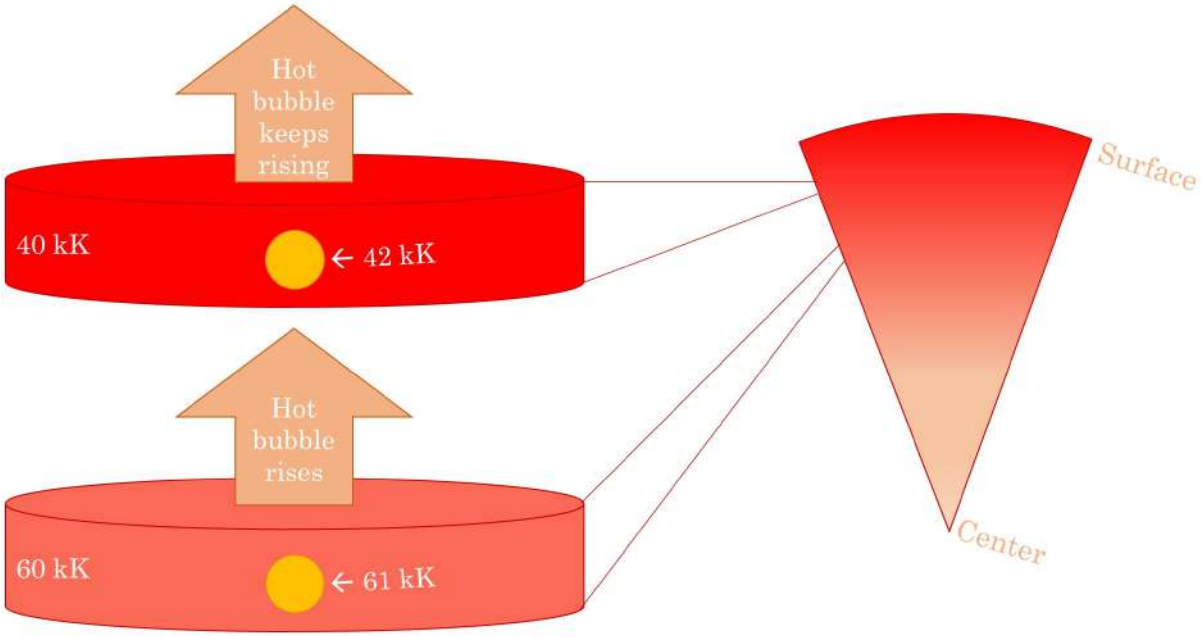

Figure 1.6: Schematic illustration of how convection works in stars. The numbers that show the temperature in thousands of Kelvin (kK) have been chosen for didactic purposes. On the right side, we show a 'pizza slice' of a star. On the left side, we zoom in on two of its layers.

1.3.1 Convection and convective overshooting

Convection is a well-known mixing process that occurs not only in stars, but also at Earth. For convection to take place, a temperature gradient is necessary. This temperature gradient needs to increase/decrease in the same direction as the pressure gradient. To explain this, we consider a blob of material in a convective envelope of a star (Fig. 1.6). This blob is slightly hotter than its environment – therefore, it is less dense (according to ideal gas law). This is illustrated in the bottom left of Fig. 1.6. Because of its lower density, it rises to a layer closer to the surface as a result of buoyancy (top left of Fig. 1.6). Then, if the adiabatically[12] expanding blob of material cools down more slowly than its environment, the difference in temperature, and therefore density, will be amplified. This is then a runaway process – hence, the situation is convectively unstable. Similarly, blobs that are colder than their environments will keep sinking.

There are several examples of environments at our planet where convective mixing takes place. One example is the Labrador Sea near Greenland (Talley and McCartney, 1982). Surface water cooled by melting ice creates a temperature gradient between the surface and the bottom of the sea, resulting in convective motions. Another example of convection taking place is in the mantle of the Earth (Gurnis, 1988), where a temperature gradient is present between the hotter edge near the core and the cooler edge near the crust.

We will discuss the criterion for convection in a bit more detail. As hinted above, a fluid is convectively unstable if the adiabatic temperature gradient is smaller than the radiative temperature gradient of its surroundings. This can be expressed as the Schwarzschild criterion for convection:

$$\nabla_{\mathrm{rad}} > \nabla_{\mathrm{ad}}. \tag{1.1}$$

[12] This means that no heat exchange with the environment takes place.

Here, $\nabla_x = (d \log T / d \log P)_x$ with T being the temperature and P the pressure. The adiabatic temperature gradient ∇_{ad} has a value that can vary between $\nabla_{ad} = 0.4$ for a gas pressure dominated gas to $\nabla_{ad} = 0.25$ for a radiation pressure dominated gas (see e.g. Kippenhahn and Weigert, 1990). The radiative temperature gradient ∇_{rad} can have a larger range of values and is defined by the following formula:

$$\nabla_{rad} = \frac{3}{16\pi acG} \frac{\kappa l P}{m T^4}. \tag{1.2}$$

Here, κ is the opacity, l is the luminosity, P is the pressure, and m is the mass coordinate. For the constants: a is the radiation constant, c is the speed of light and G is the gravitational constant. To quantify ∇_{rad}, one needs to do detailed modeling. Qualitatively, however, one can understand from Eq. 1.1 and Eq. 1.2 that convection occurs in i) the centers of massive stars, where l/m is large, and ii) the outer layers of red giant stars, which are cold and where κ can become large.

If gradients of the mean molecular weight are taken into account, one considers the Ledoux criterion for convection, which is

$$\nabla_{rad} > \nabla_{ad} + \nabla_{\mu} \tag{1.3}$$

for an ideal gas[13]. The mean molecular weight gradient is defined as $\nabla_{\mu} = d \log \mu / d \log P$.

So far we have implied that mixing as a result of convection only takes places in zones that fulfill Eq. 1.1 (or Eq. 1.3). However, this is not entirely accurate. Consider, e.g., a hydrogen burning star with a convective core. The border of the convective core as defined by Eq. 1.1 (or Eq. 1.3) defines the point where the convective *acceleration* becomes zero, but the velocity of the convective blobs is still nonzero. Thus, in this case material can be expected to mix further outward than the convective boundary. How far, however, is poorly understood from theory (e.g. Canuto, 1999a) and observational studies have notoriously different outcomes (Maeder and Mermilliod, 1981; Bressan, Chiosi and Bertelli, 1981; Brott, de Mink, Cantiello et al., 2011, and see Grin et al., in prep.).

1.3.2 Semiconvection

In the last section, we stated that according to Ledoux criterion for convection, no convective mixing is expected to take place in layers that are Schwarzschild unstable to convection but have a stabilizing mean molecular weight gradient. However, in these layers a less efficient mixing process is expected to operate – semiconvection. This process has been described by Kato (1966). Similar to convective overshooting, the efficiency of semiconvection in stars is not well constrained either theoretically (Merryfield, 1995; Grossman and Taam, 1996; Canuto, 1999b; Zaussinger and Spruit, 2013) or observationally. Typically, its efficiency is parametrized by an efficiency factor called α_{sc} (Langer, El Eid and Fricke, 1985).

As was the case for convection, semiconvection has been shown to occur at Earth. Here, we consider the example of Lake Kivu (Fig. 1.7, left). This lake lies in Africa between Rwanda and Congo, in a region with geothermal activity. Because it is heated from below, the bottom of the lake is the warmest part, as is shown in the right panel of Fig. 1.7 (Schmid, Busbridge and Wüest, 2010). Thus, when going up from the bottom of the lake, both the temperature and the pressure decrease. As a result, $d \log T / d \log P$ is positive – enough to exceed ∇_{ad}, so the Schwarzschild criterion for convection if fulfilled. However, the salinity and concentration of CO_2 are also the highest at the bottom (Fig. 1.7, right – presumably originating from geothermal springs). As a result, a stabilizing mean molecular weight gradient is present.

Still, some mixing can occur in the form of semiconvection. The driving mechanism for semiconvection is heat loss from an upwards moving blob of material that is slightly hotter than its surroundings. Because

[13] In case radiation pressure starts to play a role, ∇_{μ} has to be multiplied by a positive factor that is smaller than 1.

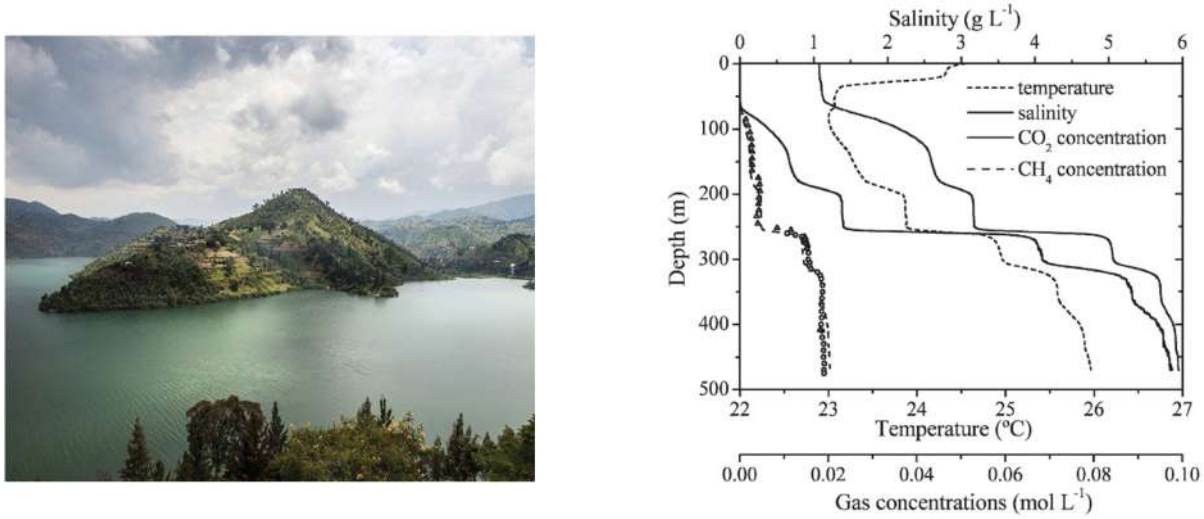

Figure 1.7: **Left:** Image of Lake Kivu, Rwanda. Image credit: New Planet Agency. **Right:** diagram showing how the water temperature, salinity (dissolved solids) and gas concentrations in Lake Kivu depend on depth. This diagram was taken from Schmid, Busbridge and Wüest (2010).

of the heat loss, this blob will sink more quickly than it rises. This instability causes mixing on a timescale that is larger than for convection. In Lake Kivu, it forms isothermal 'staircases' that are about half a meter high (Newman, 1976).

1.3.3 Rotational mixing

A number of rotational mixing processes can be important for massive stars. The most important ones can be subdivided into two classes that operate via a different mechanism – meridional circulations and shear mixing. We describe both below. The effectiveness of these rotational mixing processes in evolutionary models depends on input physics such as wind mass loss (because it can spin down the star - we discuss wind mass loss in Sect. 1.3.4) and angular momentum transport by magnetic fields. The latter process is known as the Tayler-Spruit dynamo (Tayler, 1973; Spruit, 1999), where magnetic fields arise as a result of differential rotation. These magnetic fields inhibit differential rotation and if they do that efficiently enough, they can cause close-to-rigid rotation in stars.

Meridional circulations In the rotating evolutionary models that we present in this thesis, meridional circulations are the dominant rotational mixing process. The reason is that we include the physics of the Tayler-Spruit dynamo, which quenches the differential rotation that drives shear mixing.

Meriodional circulations arise because of a thermal imbalance that occurs over equipotential surfaces. Below, we attempt to give an intuitive description. We consider equipotential surfaces of an oblate star at the polar region and at the equator. At the equator, the equipotential surfaces where Ψ = constant (Ψ consists of a gravitational and a rotational term) will be further apart because the radius at the equator is larger than the radius at the pole. This is caused by the centrifugal forces. Now we consider the effective gravity:

$$g_{\rm eff} = -\nabla\Psi. \tag{1.4}$$

We can see from this equation that $g_{\rm eff}$ will be smaller at the equator because the gradient of the potential

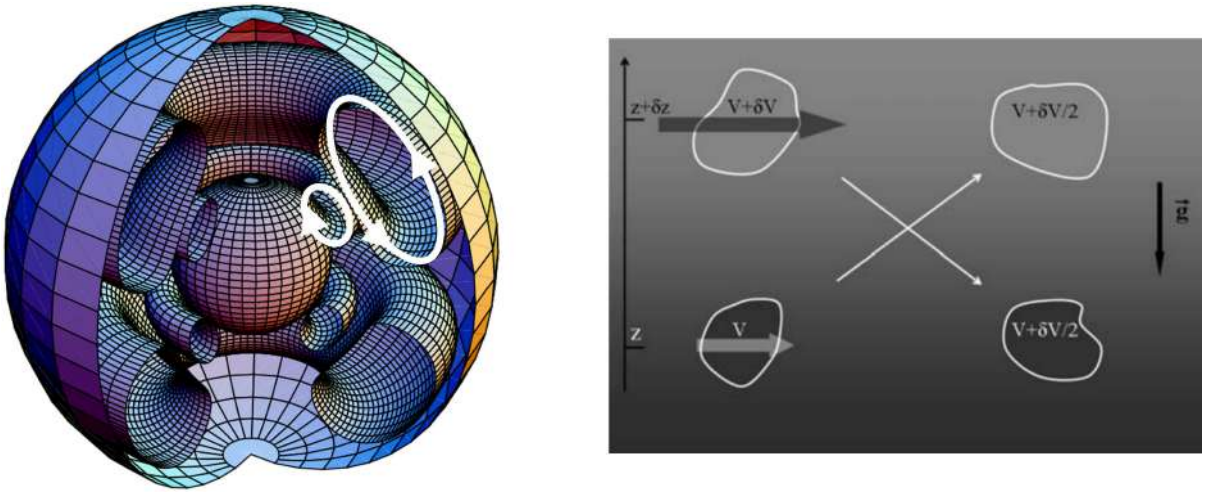

Figure 1.8: **Left:** Illustration of the stream lines of the meriodional circulations in a 20 $M_\odot$ star. Its initial rotation velocity is 300 $km\,s^{-1}$. Image was taken from Meynet and Maeder (2002). We added white arrows to indicate the direction of the currents. **Right:** Schemaric representation of two blobs initially moving with a differential velocity, shown before (left) and after (right) homogenization. Image was taken from Maeder (2009).

is smaller (since the equipotential surfaces are further apart, as described below). Now, it is known from the von Zeipel theorem (von Zeipel, 1924) that the radiative flux is proportional to the effective gravity. Thus, the radiative flux at an equipotential surface is smaller at the equator than at the poles. This thermal imbalance drives the meridional current that is also referred to as the Eddington-Sweet circulation (Eddington, 1925; Sweet, 1950). Such currents are illustrated in Fig. 1.8.

Shear mixing Another means by which rotation can trigger internal mixing is via shear. We consider a simple situation where a less dense layer resides on top of a denser layer, and they are rotating with a different velocity. This situation is illustrated in Fig. 1.8 (right). Without a velocity difference, the two left blobs would be stable against mixing because homogenizing them would require the following amount of work δW:

$$\delta W = g\,\delta\rho\,\delta z. \tag{1.5}$$

Here, g is the gravitational acceleration, $\delta\rho$ is the density difference and δz is the vertical displacement. However, given that there *is* a velocity difference δV, kinetic energy can be released if the blobs are homogenized. This energy δK is equal to:

$$\delta K = \frac{1}{2}\rho\left((V^2 + (V+\delta V)^2) - 2(V + \frac{1}{2}\delta V)^2\right) = \frac{1}{4}\rho\delta V^2 \tag{1.6}$$

Thus, if $\delta K > \delta W$, mixing is energetically favoured. This situation is referred to as the dynamical shear instability (Heger, Langer and Woosley, 2000; Maeder, 2009). This type of mixing can be included in our stellar evolution code MESA, as well as a slower mixing process that can occur when $\delta K < \delta W$ called the secular shear instability (Heger, Langer and Woosley, 2000).

1.3.4 Wind mass loss and initial chemical composition

Wind mass loss can dramatically affect the evolution of stars. For example, wind mass loss predictions for stars in our galaxy imply that stars with a birth weight of ~20 $M_\odot$ lose roughly half of this mass

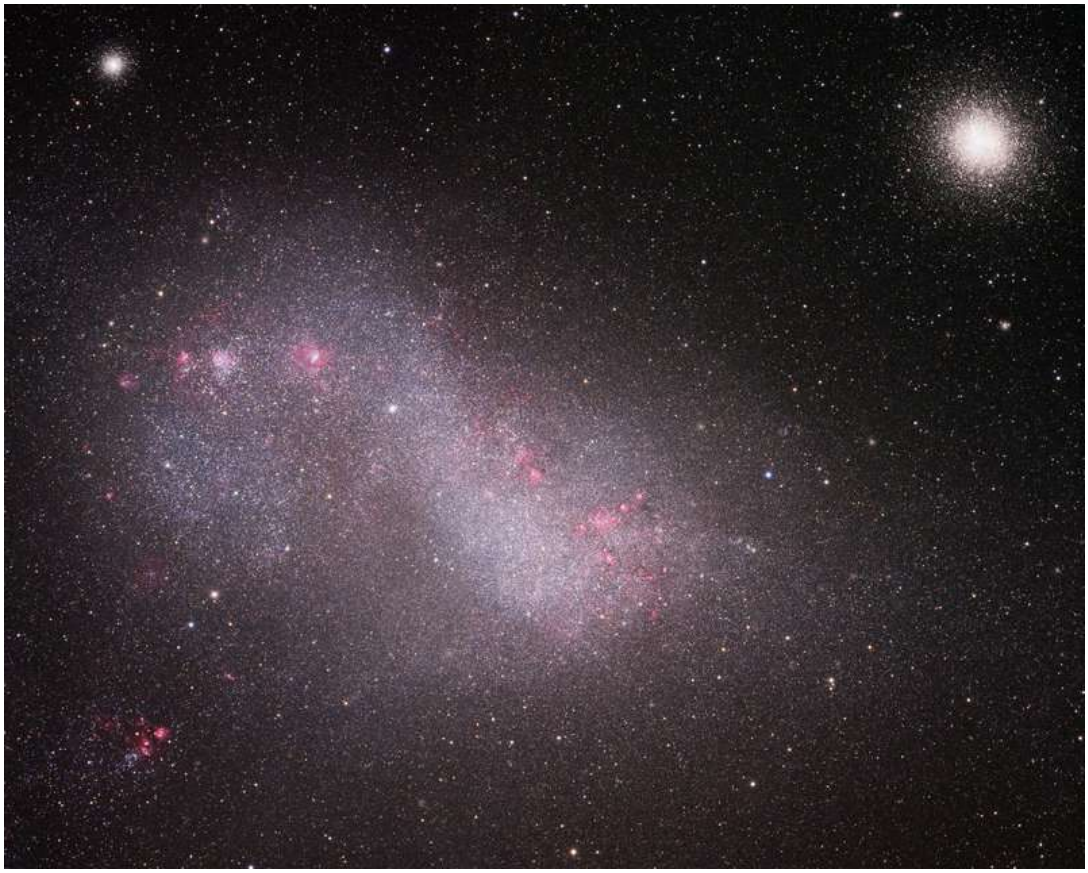

Figure 1.9: An image of the Small Magellanic Cloud. This dwarf galaxy is a satellite of the Milky way. The bright concentration of stars in the top right is the star cluster 47 Tuc, which is in the Milky Way. Image credit: Jason Jennings.

during their lives (e.g. Renzo, Ott, Shore et al., 2017). This fractional mass loss increases with initial mass, allowing stars of around ~35 $M_\odot$ to lose their hydrogen-rich layers and manifest themselves as Wolf-Rayet stars at the end of their lives. Note, however, that this number is only valid for stars in our galaxy – and even then its uncertainty is considerable.

The driving mechanism for at least the winds of hot stars is thought to be radiation pressure (Castor, D. C. Abbott and Klein, 1975). In the outer layers of massive stars, the absorption of photons transfers momentum to the matter that is present there. Thus, a higher opacity leads to stronger wind mass loss. An important contribution to the opacity comes from heavy elements (which have a high number of absorption lines), in particular iron. As a result, one naively expects wind mass loss to be stronger in environments with a high metallicity. Indeed, this is confirmed by e.g., Vink, de Koter and Lamers (2001) and and Hainich, Shenar, Sander et al. (2017), who find that hot star mass loss is nearly proportional to metallicity. However, hot star mass loss rates are uncertain (a factor 2-3: Smith, 2014), and at the cold side, the situation is even more precarious.

For these cold stars, not only are the uncertainties even larger, but also their driving mechanism is unknown (Bennett, 2010; Smith, 2014). Possibilities are, for example, pulsations and radiation pressure on dust grains. The consequence of not knowing the mechanism of cold star mass loss is that also the

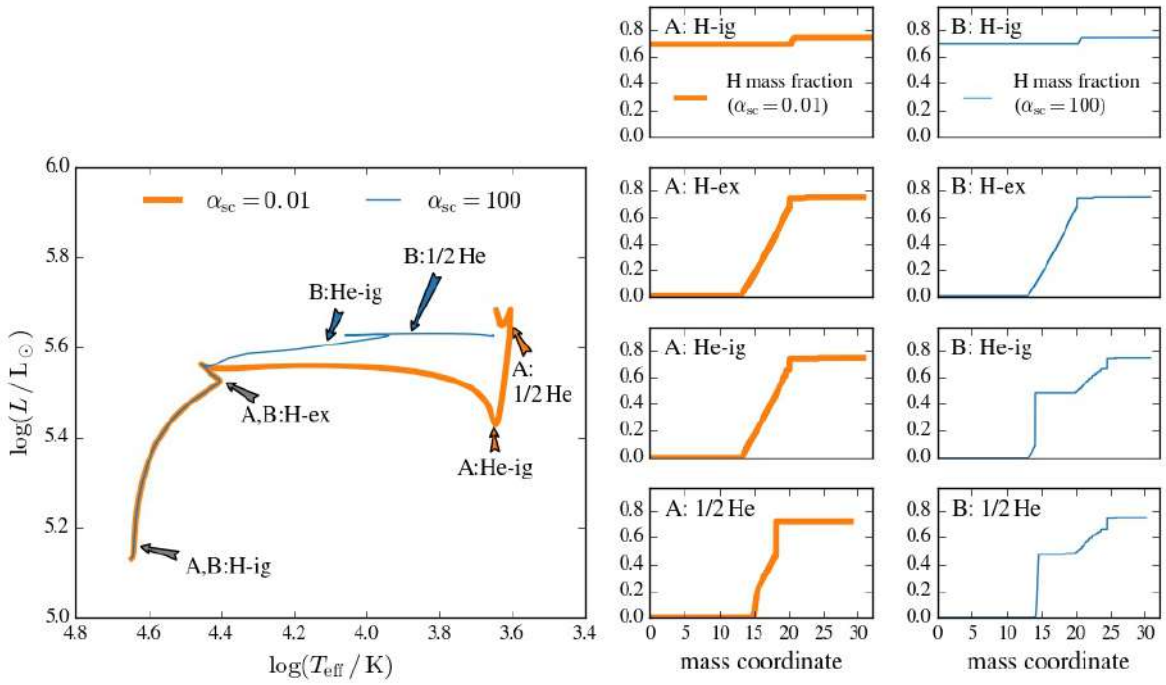

Figure 1.10: **Left:** Hertzsprung-Russell diagram with evolutionary sequences of 32 $M_\odot$. In all cases, the size of the overshooting region is 0.33 pressure scale heights. We show a case where the semiconvection efficiency parameter $\alpha_{sc} = 0.01$ (sequence A) and where $\alpha_{sc} = 100$ (sequence B). **Right:** Hydrogen profile during four phases of hydrogen/helium burning. These phases are: shortly after hydrogen ignition, where the mass fraction of hydrogen in the core has a value of $X_c = 0.7$ (H-ig); right before hydrogen exhaustion in the core ($X_c = 0.01$, H-ex); right after helium ignition in the core, when the helium mass fraction $Y_c = 0.99$ while $X_c = 0$ (He-ig); halfway helium core burning ($Y_c = 0.5$, 1/2 He). The presented models are obtained with the stellar evolution code MESA (Paxton, Bildsten, Dotter et al., 2011; Paxton, Cantiello, Arras et al., 2013; Paxton, Marchant, Schwab et al., 2015; Paxton, Schwab, Bauer et al., 2018).

metallicity dependence remains unclear[14]. Because of these uncertainties, for what range of initial masses isolated stars can remove their own envelopes and become Wolf-Rayet stars is poorly understood at lower metallicity (Georgy, Ekström, Eggenberger et al., 2013; Hainich, Pasemann, Todt et al., 2015).

Observational studies of these low-metallicity stars are in most cases not possible. The infant universe was virtually free of heavy elements, which then built up over time. Thus, to study metal-poor environments, one would need to observe galaxies that are so far away that the light that we see is light emitted when they were still young. However, stars that far away are too dim to be studied individually. Fortunately, the Milky way has a satellite galaxy that is also deficient in metals – its metal content is about one fifth of that of the Sun (Venn, 1999; Korn, Becker, Gummersbach et al., 2000). This is the Small Magellanic Cloud (Fig. 1.9). At a distance of around 200 thousand light years (Hilditch, Howarth and Harries, 2005) it is close enough to observe massive stars individually. Thus, it provides a unique opportunity to study stars in the early universe.

[14] Dust grains are built with heavy elements, so a dust-driven wind can be expected to depend on metallicity. For a pulsationally driven wind, this is not necessarily the case.

1.3.5 Example: evolution of a 32 $M_\odot$ star

To familiarize the reader with how massive single stars typically evolve, we now show as an example a 32 $M_\odot$ evolutionary sequence with SMC composition. To demonstrate the effect that internal mixing processes can have, we consider two cases: with inefficient semiconvection, where its efficiency parameter (see Langer, El Eid and Fricke, 1985) has a value of $\alpha_{sc} = 0.01$ (sequence A) and with efficient semiconvection ($\alpha_{sc} = 100$; sequence B).

The left panel in Fig. 1.10 shows how the surface temperature and luminosity of the models evolve. In the SMC, when a star is born its mass consists of around 75% hydrogen and 25% helium (inferred from the results of M. Peimbert, Luridiana and A. Peimbert, 2007). Heavy elements make up only a few tenths of a per cent of its mass. The star starts burning hydrogen at a relatively high surface temperature and a low luminosity. This hydrogen burning takes place in the very center of the star – but because the core is convective, convection and convective overshooting homogenize the star's inner layers from the center all the way to mass coordinate $m = 20\,M_\odot$[15]. This is visible in the plot with the label 'A: H-ig', where we show the hydrogen mass fraction throughout the star of a stellar model that has just started burning hydrogen. As central hydrogen burning progresses, the convective core shrinks[16]. This leaves a H/He gradient between $m = 13\,M_\odot$ and $m = 20\,M_\odot$ that is not very steep at the moment that hydrogen is exhausted in the core (i.e., the end of the main sequence – referred to as H-ex). This core hydrogen burning phase is the longest phase in the life of a star, typically making up for 90% of its lifetime. This long main sequence lifetime explains that so many stars are observed in the main sequence band (the feature on the left in Fig. 1.2).

Fig. 1.10 shows that evolution of the shown model sequences during the main sequence does not depend on the efficiency of semiconvection. The reason is that no significant semiconvective regions develop in this phase. This changes, however, after hydrogen is exhausted in the core. Then, the core contracts and hydrogen is ignited in the shell. This provokes semiconvecive mixing in the deep hydrogen envelope (where the H/He gradient is present). In the case where $\alpha_{sc} = 0.01$, this mixing is not efficient enough to lead to significant changes in the chemical structure: the second (H-ex) and third (He-ig = helium ignition) hydrogen profile of sequence A thus look the same (Fig. 1.10). The opposite is true for sequence B, where $\alpha_{sc} = 100$. Here, the semiconvective mixing after hydrogen core exhaustion pushes hydrogen-rich layers deeper into the star. This significantly changes the hydrogen profile of the star (compare in Fig. 1.10 the 'B: H-ex' panel with the 'B: He-ig' panel, where the H/He gradient is much steeper) and, as a result, the evolution of the star. Sequence B burns helium at a surface temperature that is between 15 kK and 7 kK for most of the time, making it appear blue. In contrast, sequence A burns helium at a surface temperature of 4 kK or lower, making it look red to the human eye. During helium core burning, hydrogen shell burning proceeds to some extent. This slightly changes the H/He gradient of the models but not dramatically (Fig. 1.10). We will discuss this H/He gradient extensively in Chapters 2 and 3).

These red, post main sequence stars give rise to the second feature in the observed population that we showed previously in Fig. 1.2 – the 'cloud' of objects to the right, with a red color[17]. This figure's final feature that we promised to explain at the end of Sect. 1.1 is the horizontal branch around $M_G = -2$. The reason that stars accumulate there follows from the requirement that a helium core needs to grow to about 0.5 $M_\odot$ before helium can be ignited. As a result, there is a population of stars with initial masses

[15] The mass coordinate is the mass enclosed by a spherical shell at a certain radius.

[16] As hydrogen is converted into helium, the electron scattering opacity is diminished, which reduces the radiative temperature gradient (Eq. 1.2). The result of this is that the criterion for convection is only fulfilled in a smaller fraction of the star.

[17] In this figure, mainly low and intermediate mass stars are present. These tend to burn helium at low temperatures, even if semiconvection is efficient – see e.g. Ekström, Georgy, Eggenberger et al. (2012).

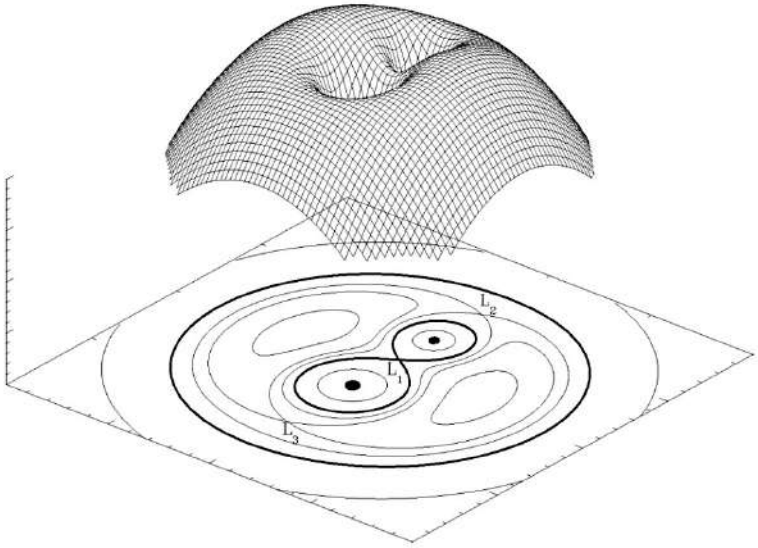

Figure 1.11: **Top:** graphical representation of the Roche potential of a binary system with a mass ratio of $M_2/M_1 = 0.5$ in the corotating frame. **Bottom:** same, but now the lines show equipotentials. Also, three of the five Lagrangian points are indicated (L_1, L_2 and L_3).

between 0.8 and 2.5 $M_\odot$ that ends the main sequence with a lower core mass, burning hydrogen in a shell until the helium core reaches a mass of 0.5 $M_\odot$. Thus, there is a surplus of stars with a helium core mass of 0.5 $M_\odot$, which have a very similar luminosity (or M_G) but not the same temperature (or color) because they have different hydrogen envelope masses. These are the stars that form the horizontal branch.

1.3.6 Binary interaction

The evolution of a star can be greatly affected by the presence of a binary companion. If this companion is close enough, a star can expand beyond the radius where material is gravitationally bound to it (see the illustration in Fig. 1.11)[18]. This radius is called the 'Roche radius'. Then, a phase of Roche lobe overflow (RLOF) commences, during which material is transferred to the binary companion.

RLOF can occur during different evolutionary phases in the mass donor's life. Typically, a distinction is made between the following three scenarios (see e.g. Kippenhahn and Weigert, 1967; Lauterborn, 1970): case A mass transfer, where the donor star is still on the main sequence; case B mass transfer, where the donor is hydrogen shell burning; and finally case C mass transfer, where it is helium shell burning. For these various cases, very different timescales apply: the burning timescale ratio for hydrogen core: hydrogen shell: helium core is about 1000: 1: 50 for the 32 $M_\odot$ evolutionary models that we have shown in Sect. 1.3.5. This can be expected to affect for example the mass transfer efficiency (see e.g. Wellstein, Langer and Braun, 2001; Langer, Wellstein and Petrovic, 2003), while the separation at the onset of mass transfer is also important (Lubow and Shu, 1975).

The products of binary interaction are expected to be ubiquitous. According to Sana, de Mink, de Koter et al. (2012), seven out of ten stars born as O-type stars (i.e., born more massive than 15 $M_\odot$) will interact with a binary companion during their lifetime. What seems to be less clear is what happens during binary

[18] To envision where a mass element described by this potential will move, imagine that it is a marble lying on the surface shown in the top of this figure. It will be accelerated in the direction where the marble would roll to, because the acceleration is determined by the gradient of the potential (cf. Eq. 1.4).

interaction – we describe possible outcomes below. We discriminate between unstable and stable mass transfer:

Unstable mass transfer In some cases, the onset of RLOF leads to a situation where the transfer of material can not be stable. This happens when during mass transfer, the Roche lobe of the donor star shrinks faster than the star itself (or in general, when $\dot{R}_L < \dot{R}$, where the dot indicates a time derivative). This can happen, e.g., when the envelope of the donor star is convective: in that case, its size will increase instead of decrease when mass is removed from it (Paczyński, 1965).

Another cause of unstable mass transfer can be an extreme mass ratio. In general, mass transfer from a massive component to a lighter component will shrink the orbit (Benacquista, 2013). This is likely to bring such systems into contact when the difference in mass is large.

When the two stars in a binary come into contact, the accretor star is pulled into the envelope of the donor star due to drag forces. This scenario is referred to as common envelope evolution (CEE – for a review see Ivanova, Justham, Chen et al., 2013). Then, two things can happen: either the stars merge, or the energy budget of the system (most importantly, the orbital energy) is sufficiently high to gravitationally unbind the envelope of the donor star. This is a process that happens quickly and will bring the binary components close together. Unfortunately, CEE is a notoriously difficult problem of which the outcome is very uncertain.

The products of a successful common envelope ejection event are thought to be a strongly stripped donor star and a barely affected companion: the timescale of CEE is thought to be too small for significant mass accretion or spin up. In case of a stellar merger, it is possible that the evolution of the merger product mimics the evolution of a single star (e.g., when its progenitors are early main sequence stars). However, it is also possible that a star is formed with an exotic chemical structure (see e.g. Podsiadlowski and Joss, 1989). It can have a relatively small core mass, which makes it more likely to be a blue supergiant. This is a possible explanation for the fact that the progenitor star of supernova 1987A was observed to be a blue supergiant (see also Menon and Heger, 2017, Sect. 1.2.1 and Fig. 1.3). Because of the high angular momentum of the pre-merger stars, the product is expected to be a rapid rotator.

Stable mass transfer In case the stars can stay inside their Roche lobes during mass transfer, it is referred to as a stable mass transfer event. During this event, most of the hydrogen-rich envelope of the donor star tends to be stripped, until it fits in its Roche lobe again (e.g. Gotberg, de Mink and Groh, 2017). If mass transfer is efficient, most of the stripped material ends up on the donor star. However, the efficiency of mass transfer is poorly known (de Mink, Pols and Hilditch, 2007) and most likely depends on initial conditions, as mentioned above. If efficient, the accretion of material could have similar effects to those we described above for a stellar merger (see also Braun and Langer, 1995).

It is puzzling that, despite the large number of pre-interaction binaries that we see (Zinnecker and Yorke, 2007; Mason, Hartkopf, Gies et al., 2009; Sana, de Mink, de Koter et al., 2012), only few post-interaction binaries (i.e., stripped star + accretor systems) are known – especially in the low to intermediate mass range. A possible explanation is given by Schootemeijer, Götberg, Mink et al. (2018), who claim that most of the stripped-envelope stars that we observe are in a rare, luminous phase. Their dimmer counterparts could have remained undetected due to observational biases (as discussed by de Mink, Sana, Langer et al., 2014).

1.4 This thesis

The internal mixing processes that are mentioned above strongly affect the chemical profile, and thus, the evolution of massive stars. As a result, to understand for example the genesis of exciting transient phenomena such as gravitational waves and supernovae it is imperative to understand these mixing processes[19]. Below, we describe how we attempt to better understand massive star evolution in the SMC in this thesis, with a focus on internal mixing processes.

1.4.1 Wolf-Rayet stars in the Small Magellanic Cloud as a testbed for massive star evolution

In Chapter 2 we focus on the formation of Wolf-Rayet stars in the SMC (which are very hot, very luminous and depleted in hydrogen). This satellite galaxy of our Milky way is deficient in heavy elements, which weakens the stellar winds and raises the question how these Wolf-Rayet stars could have lost their hydrogen-rich envelopes. We use two approaches to investigate their nature.

First, we model stars that rotate rapidly, which triggers internal mixing that incites chemically homogeneous evolution. This causes them to become hydrogen poor, as is observed. However, for the majority of the Wolf-Rayet stars we cannot simultaneously explain the high temperatures and the significant amount of hydrogen at surface this way.

Second, we use a grid of models with synthetic chemical profiles. Because these Wolf-Rayet stars are so hot that they must be helium burning, we consider helium-burning cores with a variety of hydrogen envelopes. We find that only thin hydrogen envelopes with a steep hydrogen/helium (H/He) gradient can explain the high temperatures. We suggest that these are formed by an internal mixing process, such as semiconvection.

In this project, my contribution was to run the simulations, to devise a strategy to model stars with a synthetic hydrogen profile, and to interpret the results.

1.4.2 Constraining internal mixing processes in massive stars of the Small Magellanic Cloud

We explore in Chapter 3 which internal mixing processes could create the steep H/He gradients that we inferred for the SMC Wolf-Rayet stars in Chapter 2. We do so by simulating a large grid of evolutionary sequences where we simultaneously vary the efficiency of semiconvection, convective core overshooting and rotational mixing. We find that the model sequences with efficient semiconvection and at most intermediate overshooting can develop these steep H/He gradients, while rotational mixing has a limited effect for the majority of stars.

Also, we consider the predictions of our grid with helium-burning blue and red supergiants. For our model sequences we find that there is a strong correlation between developing a steep H/He gradient and burning helium as a blue supergiant. We conclude that efficient semiconvection and intermediate overshooting are in best agreement with the observed stars in the SMC. This strengthens our conclusion about the efficiency of mixing required to produce the steep H/He gradients.

In this project, my contribution was to develop a strategy to explore these internal mixing processes, run the simulations, and to interpret the results.

[19] An example to illustrate this point: efficient semiconvective mixing can drastically delay the expansion of a star after the main sequence, as we have seen in Sect. 1.3.5. This, in turn, can affect the binary interaction that gravitational wave and supernova progenitors experience.

1.4.3 Synthetic color magnitude diagrams of massive stars in the Small Magellanic Cloud

While we armed ourselves with a set of theoretical predictions in Chapter 3, we were not able to do a full comparison with observations. The reason is that a full spectroscopic analysis of massive stars in the SMC has not (yet) been carried out. Therefore, we create a theoretical color-magnitude diagram of the SMC massive star population in Chapter 4. This allows us to compare our theoretical predictions with much more complete observational data sets: the *UBV* catalog of Massey (2002) and GAIA DR2 (Gaia Collaboration, Brown, Vallenari et al., 2018).

We find that the GAIA DR2 observational data set shows the best agreement with our theoretical predictions. In particular, we tentatively identify a distinct population of blue stars that have the same color as the helium-burning blue supergiants predicted in case of efficient internal mixing. To do a quantitative analysis, however, not only massive stars but also intermediate-mass stars would need to be included in the simulations.

In this project, my first duty was to devise a method to translate the temperatures and luminosities into colors and magnitudes and then use these to create theoretical color-magnitude diagrams. My second duty was to interpret the differences and similarities between the observed and theoretical color-magnitude diagrams.

CHAPTER 2

Wolf-Rayet stars in the Small Magellanic Cloud as testbed for massive star evolution

A. Schootemeijer & N. Langer
Argelander-Institüt für Astronomie, Universität Bonn, Auf dem Hügel 71, 53121 Bonn, Germany

Astronomy & Astrophysics, 2018, 611, A75

Abstract. *Context:* The majority of the Wolf-Rayet (WR) stars represent the stripped cores of evolved massive stars who lost most of their hydrogen envelope. Wind stripping in single stars is expected to be inefficient in producing WR stars in metal-poor environments such as the Small Magellanic Cloud (SMC). While binary interaction can also produce WR stars at low metallicity, it is puzzling that the fraction of WR binaries appears to be about 40%, independent of the metallicity.
Aims: We aim to use the recently determined physical properties of the twelve known SMC WR stars to explore their possible formation channels through comparisons with stellar models.
Method: We used the MESA stellar evolution code to construct two grids of stellar models with SMC metallicity. One of these consists of models of rapidly rotating single stars, which evolve in part or completely chemically homogeneously. In a second grid, we analyzed core helium burning stellar models assuming constant hydrogen and helium gradients in their envelopes.
Results: We find that chemically homogeneous evolution is not able to account for the majority of the WR stars in the SMC. However, in particular the apparently single WR star SMC AB12, and the double WR system SMC AB5 (HD 5980) appear consistent with this channel. We further find a dichotomy in the envelope hydrogen gradients required to explain the observed temperatures of the SMC WR stars. Shallow gradients are found for the WR stars with O star companions, while much steeper hydrogen gradients are required to understand the group of hot apparently single WR stars.
Conclusions: The derived shallow hydrogen gradients in the WR component of the WR+O star binaries are consistent with predictions from binary models where mass transfer occurs early, in agreement with their binary properties. Since the hydrogen profiles in evolutionary models of massive stars become steeper with time after the main sequence, we conclude that most of the hot ($T_{\rm eff} > 60$ kK) apparently single WR stars lost their envelope after a phase of strong expansion, e.g., as the result of common envelope evolution with a lower mass companion. The so far undetected companions, either main sequence stars or compact objects, are then expected to still be present. A corresponding search might identify the first immediate double black hole binary progenitor with masses as high as those detected in GW150914.

Key words. stars: rotation – stars: massive – stars: Wolf-Rayet

2.1 Introduction

Massive stars can become Wolf-Rayet (WR) stars late in their evolution. These objects are characterized by broad emission lines which originate from a fast, dense stellar wind. WR stars are luminous ($L > 10^{4.5}$ $L_\odot$) and typically very hot and hydrogen depleted, as a result of the removal of a significant part of their hydrogen envelopes. With strong stellar winds and dramatic deaths as supernovae they are thought to inject matter processed by nuclear burning into the interstellar medium. Thereby they play an essential role in the chemical evolution of galaxies as well as in providing mechanical and radiative feedback (see e.g., Hopkins, Kereš, Oñorbe et al., 2014).

Unfortunately, the late phases of massive star evolution are poorly understood, even for stars in our our own galaxy. This is even more so for massive stars in the early universe, which were more metal poor. The Small Magellanic Cloud (SMC) is a unique laboratory to study the evolution of low metallicity stars, since its stars are metal deficient and as a satellite galaxy of the Milky Way it is sufficiently close for detailed studies of its individual stars. Its metal content is around one fifth of the solar value (Venn, 1999; Korn, Becker, Gummersbach et al., 2000; Hunter, Dufton, Smartt et al., 2007), which corresponds to that of spiral galaxies at redshifts $z \approx 3.5$ (Kewley and Kobulnicky, 2007).

For lower metallicity, the stellar winds become weaker (D. C. Abbott, 1982; R. P. Kudritzki, Pauldrach and Puls, 1987; Mokiem, de Koter, Vink et al., 2007). Consequently, the winds are less likely to remove the hydrogen envelope, which raises the question if single stars can become WR stars at all. Indeed, it has been proposed that most of the SMC WR stars were formed via envelope stripping by a close binary companion (Maeder and Meynet, 1994; Bartzakos, Moffat and Niemela, 2001). Surprisingly, radial velocity studies (Foellmi, Moffat and Guerrero, 2003; Foellmi, 2004) indicate that the binary fraction of the SMC WR stars is only 40-50%, similar to that in the Milky Way, although this number is based on only twelve sources.

A possibility to form WR stars from single stars without invoking mass loss is offered by the scenario of rotationally induced chemically homogeneous evolution (CHE; see .e.g., Maeder, 1987; Langer, 1992; Yoon and Langer, 2005). This channel is indeed expected to work more efficiently for lower metallicity, since then mass loss induced spin-down, which stops the efficient rotational mixing, is reduced (Langer, 1998). CHE has been proposed to lead to long-duration gamma ray bursts (Yoon, Langer and Norman, 2006; Woosley and Heger, 2006), and, in close binaries, to very massive merging double black holes (Mandel and de Mink, 2016; Marchant, Langer, Podsiadlowski et al., 2016) like the gravitational wave source GW150914 (B. P. Abbott, Abbott, Abbott et al., 2016a).

Direct empirical evidence for CHE is scarce. Bouret, Lanz, Hillier et al. (2003), Walborn, Morrell, Howarth et al. (2004) and Mokiem, de Koter, Evans et al. (2006) find indications for CHE in several very massive O stars in the Magellanic Clouds. Martins, Hillier, Bouret et al. (2009) and and Martins, Depagne, Russeil et al. (2013) find CHE to be required to explain the properties of one SMC WR star as well as two WR stars in the Large Magellanic Cloud (LMC) and two WR stars in the Galaxy. Koenigsberger, Morrell, Hillier et al. (2014), Almeida, Sana, de Mink et al. (2015) and Shenar, Richardson, Sablowski et al. (2017) have interpreted observations of different massive close binaries as indications for CHE. However, Hainich, Pasemann, Todt et al. (2015) find that current evolutionary models cannot match all observed properties of the apparently single WR stars in the SMC.

To explain the origin of the SMC WR stars is of key importance for the understanding of massive star evolution at low metallicity. Here, we perform an in-depth theoretical analysis of these stars, singling out which of them could result from CHE, and deriving constraints on the envelope stripping process which

might have produced the majority of the remaining WR stars. This task is greatly facilitated by the recent determination of the stellar parameters of all the apparently single (Hainich, Pasemann, Todt et al., 2015) and binary (Shenar, Hainich, Todt et al., 2016) WR stars in the SMC.

After providing a brief overview of observational analyses that have been done on the WR stars in the SMC up to now in Sect. 2.2, we explain the computational method for our analysis in Sect. 2.3. In Sect. 3.3.2.4 we show and discuss our results for the rotationally mixed models, and in Sect. 2.5 we construct models for stars which have experienced envelope stripping. We present our conclusions in in Sect. 2.6.

2.2 Empirical properties of Wolf-Rayet stars in the Small Magellanic Cloud

The first observational overview of WR stars in the SMC, containing four objects, was provided by Breysacher and Westerlund (1978). This number was doubled by Azzopardi and Breysacher (1979), who introduced the nomenclature for the SMC sources with WR characteristics, which we adopt here. The number of known SMC WR stars grew from eight to nine after the work of Morgan, Vassiliadis and Dopita (1991). Interestingly, at that time all of the WR stars were thought to have an O-star binary companion due to the presence of hydrogen absorption lines in the spectra. Conti, Garmany and Massey (1989) argued however that the presence of these absorption lines could be the consequence of a weaker wind compared to Galactic and LMC WR stars. After more discoveries (Massey and Duffy, 2001; Massey, Olsen and Parker, 2003), radial velocity measurements were performed on all by then twelve SMC WR stars to establish their binary fraction (Foellmi, Moffat and Guerrero, 2003; Foellmi, 2004). These measurements indicate that only five of the twelve WR stars have a binary companion.

Recently, the stellar parameters of all seven single (Hainich, Pasemann, Todt et al., 2015) and all five binary sources (Shenar, Hainich, Todt et al., 2016) with a WR star in the SMC have been derived using model atmosphere calculations. The derived parameters are listed in Table 2.1 for the single WR stars and in Table 2.2 for those in binary systems. Due to the, for WR standards, rather weak winds of the SMC WR stars, signified by the presence of absorption lines in the spectra of most of them, the derived temperatures and radii are free of the ambiguity which is present in corresponding determinations in more metal-rich WR stars (Hamann, Gräfener and Liermann, 2006; Crowther, 2007).

Fig. 1 shows the location of the SMC WR stars in the HR diagram. Their luminosities range from $10^{5.5}\,L_\odot$ to $10^{6.3}\,L_\odot$, which implies WR star masses of about $15\ldots60\,M_\odot$ (Langer, 1989). While the initial mass range could be identical assuming CHE, their initial masses would have to be roughly in the range $40\ldots100\,M_\odot$ if they are stripped stars.

Four of the WR stars, that is, the two components of the double WR system SMC AB5 (HD 5980), and the apparently single WR sources SMC AB2 and 4 are located to the right of the zero age main sequence in the HR diagram, while the other nine objects are all considerably hotter. In the following, we will refer to both groups as to the cool and the hot SMC WR stars, respectively. Except for SMC AB8, which is a WO-type star in a close binary system with a massive O star, all SMC WR stars show significant amounts of hydrogen in their atmosphere.

In the analysis of the binaries, Shenar, Hainich, Todt et al. (2016) found odd properties for SMC AB6. In particular, its luminosity is found to greatly exceed its Eddington luminosity. The authors conclude that the observed parameters are probably erroneous due to light contamination by a third star. For this reason, we do not consider it later on in our analysis.

Table 2.1: Observed parameters of apparently single SMC Wolf-Rayet stars. All values are adopted from Hainich, Pasemann, Todt et al. (2015).

SMC AB	T_* [kK]	$\log \dot{M}$ [$M_\odot$ yr^{-1}]	$\log L$ [$L_\odot$]	X_H	v_{rot} [km s^{-1}]
1	79^{+6}_{-6}	$-5.58^{+0.2}_{-0.2}$	$6.07^{+0.2}_{-0.2}$	$0.5^{+0.05}_{-0.05}$	< 100
2	47^{+3}_{-3}	$-5.75^{+0.2}_{-0.2}$	$5.57^{+0.1}_{-0.2}$	$0.55^{+0.05}_{-0.05}$	< 50
4	45^{+3}_{-3}	$-5.18^{+0.2}_{-0.2}$	$5.78^{+0.1}_{-0.2}$	$0.25^{+0.05}_{-0.05}$	< 100
9	100^{+6}_{-6}	$-5.65^{+0.2}_{-0.2}$	$6.05^{+0.2}_{-0.2}$	$0.35^{+0.05}_{-0.05}$	< 200
10	100^{+6}_{-6}	$-5.64^{+0.2}_{-0.2}$	$5.65^{+0.2}_{-0.2}$	$0.35^{+0.05}_{-0.05}$	< 200
11	89^{+6}_{-6}	$-5.56^{+0.2}_{-0.2}$	$5.85^{+0.2}_{-0.2}$	$0.4^{+0.05}_{-0.05}$	< 200
12	112^{+6}_{-6}	$-5.79^{+0.2}_{-0.2}$	$5.90^{+0.2}_{-0.2}$	$0.2^{+0.05}_{-0.05}$	< 200

Table 2.2: Observed parameters of SMC Wolf-Rayet stars in binaries. The values are adopted from Shenar, Hainich, Todt et al. (2016). The orbital period P_{orb} and radial velocity amplitudes K_{WR} for the WR star and $K_{O\,star}$ for the O star (if known) are the values derived by Foellmi, Moffat and Guerrero (2003) and and Foellmi (2004). The exception are the WR stars 5_A and 5_B which reside in the same system; their orbital parameters are adopted from Koenigsberger, Morrell, Hillier et al. (2014).

SMC AB	T_* [kK]	$\log \dot{M}$ [$M_\odot$ yr^{-1}]	$\log L$ [$L_\odot$]	X_H	v_{rot} [km s^{-1}]	P_{orb} [d]	K_{WR} [km s^{-1}]	$K_{O\,star}$ [km s^{-1}]
3	78^{+5}_{-5}	$-5.3^{+0.1}_{-0.1}$	$5.93^{+0.05}_{-0.05}$	$0.25^{+0.05}_{-0.05}$	-	10.1	144	-
5_A	45^{+5}_{-5}	$-4.5^{+0.1}_{-0.1}$	$6.35^{+0.10}_{-0.10}$	$0.25^{+0.05}_{-0.05}$	< 300	19.3	214	-
5_B	45^{+10}_{-7}	$-4.5^{+0.3}_{-0.3}$	$6.25^{+0.15}_{-0.15}$	$0.25^{+0.20}_{-0.20}$	< 400		200	-
6	80^{+15}_{-10}	$-5.1^{+0.2}_{-0.2}$	$6.28^{+0.10}_{-0.10}$	$0.4^{+0.1}_{-0.1}$	-	6.5	290	66
7	105^{+20}_{-10}	$-5.0^{+0.2}_{-0.2}$	$6.10^{+0.10}_{-0.10}$	$0.15^{+0.05}_{-0.05}$	-	19.6	196	101
8	141^{+60}_{-20}	$-4.8^{+0.1}_{-0.1}$	$6.15^{+0.10}_{-0.10}$	$0.0^{+0.15}$	-	16.6	176	55

2.3 Method

We use the detailed one-dimensional stellar evolution code MESA (Paxton, Bildsten, Dotter et al., 2011; Paxton, Cantiello, Arras et al., 2013; Paxton, Marchant, Schwab et al., 2015) version 8845 to obtain our stellar models.

For the initial composition of our SMC models we adopt the one implemented by Brott, de Mink, Cantiello et al. (2011). Rather than being scaled down uniformly from solar abundances, initial abundances of the important elements C, N, O, Mg and Fe are based on different observations in the SMC. The helium mass fraction of $Y_{SMC} = 0.252$ is based on a linear interpolation between the primordial value of $Y = 0.2477$ (M. Peimbert, Luridiana and A. Peimbert, 2007) and the solar helium abundance $Y = 0.28$ (Grevesse, Noels and Sauval, 1996) as a function of metallicity. The opacity tables are obtained from the OPAL opacities (Iglesias and Rogers, 1996), using an 'effective' metallicity $Z = Z_\odot \cdot (X_{Fe,SMC}/X_{Fe,\odot})$.

Here, we take the solar values $Z_\odot = 0.017$ and $X_{\mathrm{Fe},\odot} = 0.00124$ from Grevesse, Noels and Sauval (1996) and the $X_{\mathrm{Fe,SMC}}$ value follows from $[\mathrm{Fe/H}]_{\mathrm{SMC}} = -0.6$ from Venn (1999).

The wind mass loss recipe we use also follows Brott, de Mink, Cantiello et al. (2011), where the choice of prescription depends on the properties of the stellar model. For stars hotter than ~25 kK that have a high surface hydrogen mass fraction of $X_\mathrm{s} > 0.7$, we use the wind recipe of Vink, de Koter and Lamers (2001). For hydrogen-poor hot stars with $X_\mathrm{s} < 0.4$, we use the WR mass loss recipe from Hamann, Koesterke and Wessolowski (1995), divided by ten to account for wind clumping and downward revisions of the mass loss rate in general (cf. Yoon and Langer (2005), Yoon, Langer and Norman (2006) and and Brott, de Mink, Cantiello et al. (2011)). For stars with in-between X_s values, $\log \dot{M}$ results from a linear interpolation between both. For all stars cooler than ~25 kK (i.e., the temperature of the bi-stability jump) we use the highest of the values given by the prescriptions from Vink, de Koter and Lamers (2001) and Nieuwenhuijzen and de Jager (1990). For all wind prescriptions, we assume a metallicity dependence of $\dot{M} \propto Z^{0.85}$ as in Vink, de Koter and Lamers (2001).

In convective zones, mixing is modeled according to the standard mixing-length theory (Böhm-Vitense, 1958). We use a mixing-length parameter $\alpha_{\mathrm{MLT}} = 1.5$. The convective boundaries are set by the Ledoux criterion for convection. Convective overshooting above the convective core is treated with a step overshoot parameter. We adopt $\alpha_{\mathrm{ov}} = 0.335$, as calibrated with the rotational velocities versus $\log g$ (Brott, de Mink, Cantiello et al., 2011) of a large sample of LMC stars observed with the VLT-FLAMES survey (Evans, Smartt, Lee et al., 2005). In the layers that are stable to convection according to the Ledoux criterion but not according to the Schwarzschild criterion, we assume that semiconvection takes place with an efficiency of $\alpha_{\mathrm{sc}} = 1$ (Langer, 1991).

Rotationally enhanced mass loss is implemented as a function of the ratio of the stellar rotation to the critical rotation velocity (Friend and D. C. Abbott, 1986): the $\dot{M}$ boost factor is set to $(1/(1-w))^{\xi}$, where $w = v/v_{\mathrm{crit}}$ and $\xi = 0.43$. For the efficiency of rotational mixing we use $f_\mathrm{c} = 1/30$, which is in agreement with calibrations of Brott, de Mink, Cantiello et al. (2011) to nitrogen enrichment in rotating stars analyzed by Hunter, Brott, Lennon et al. (2008).

In their analysis of SMC WR stars, Hainich, Pasemann, Todt et al. (2015) and Shenar, Hainich, Todt et al. (2016) provided a temperature T_* which is defined in a fashion similar to the effective temperature: at a radius R_*, defined as the radius where the Rosseland optical depth $\tau = 20$, T_* satisfies the equation $T_* = (L/(4\pi\sigma R_*^2))^{1/4}$. Here, L is the luminosity of the star and σ is Boltzmann's constant.

Therefore, in our models we also calculate T_* at $\tau = 20$, taking wind optical depth into account. The latter is calculated using Eq. (11) in Langer (1989). This formula assumes electron scattering opacity, but the effect on the resulting T_* is negligible for our WR stars with SMC metallicity. We note that the difference between this T_* and the effective temperature T_{eff} is typically smaller than a few percent in our models.

2.4 Rotationally mixed models

To demonstrate the effect that rapid rotation has on our massive star models, we show two distinct sets of tracks in Fig. 2.1. The evolutionary tracks are shown for models which have no rotation and models which have a high initial rotation velocity of 600 km s^{-1}. The fast-rotating models are able to avoid the significant expansion of the hydrogen envelope, as they are evolving chemically (quasi-)homogeneously. In this section, we compare the observed SMC WR stars to models that are in the core hydrogen burning phase (Sect. 2.4.1) and the core helium burning phase (Sect. 2.4.2). The reason we focus on these two phases is that the chance that a significant fraction of the SMC WR stars is in any other phase is small: both phases combined make up over 99% of the total stellar lifetime. In Appendix D we provide an

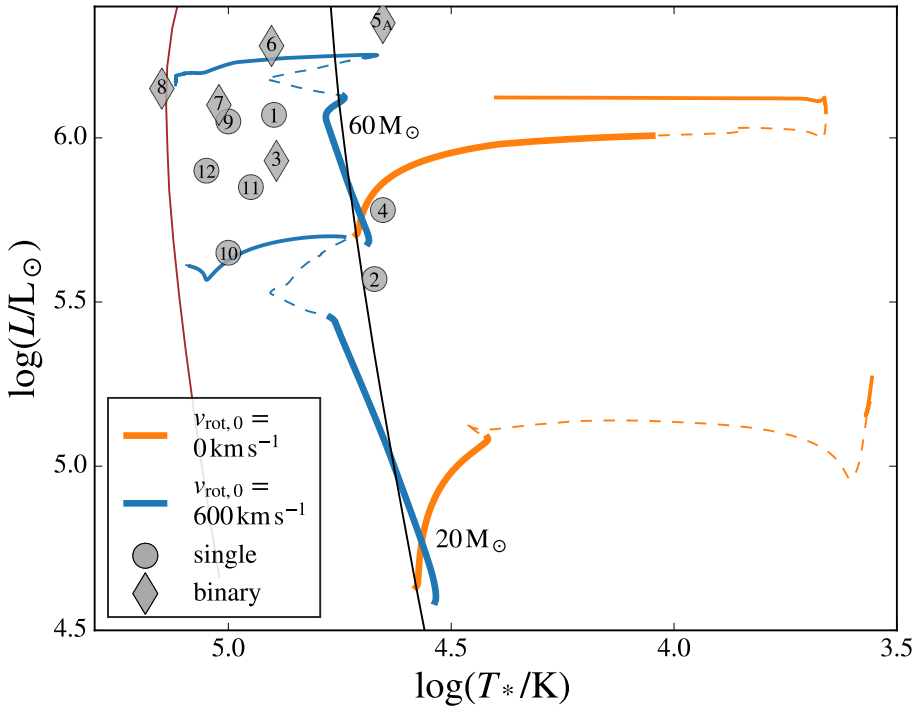

Figure 2.1: Hertzsprung-Russell diagram with tracks of MESA models with initial masses of 20 $M_\odot$ and 60 $M_\odot$ and different initial rotation velocities. The black line represents the zero-age main sequence for stars with the composition described in Sect. 2.3, while the brown line represents the zero-age main sequence for helium stars. Thick solid lines indicate that a model is core hydrogen burning with $X_c > 0.01$; thin solid lines indicate core helium burning; dashed lines indicate that a model is in an in-between, shorter-lived phase. The observed apparently single Wolf-Rayet stars (Table 2.1) are displayed as gray circles. Those in a binary system are displayed as gray diamonds (Table 2.2). The numbers indicate the identifier of the star, e.g., SMC AB1.

overview of the best fits to the observed stars for both families of models.

We explore the mass range $M_{\rm ini} = 20, \ldots, 100\,M_\odot$ with $5\,M_\odot$ intervals ($10\,M_\odot$ intervals above $70\,M_\odot$). The initial rotation velocities of the models cover the range $v_{\rm rot,ini} = 350, \ldots, 600\,{\rm km\,s^{-1}}$ with $10\,{\rm km\,s^{-1}}$ intervals.

2.4.1 Core hydrogen burning phase

As is shown in Fig. 2.1, the core hydrogen burning models do not reach the high temperatures that are observed for nine out of twelve SMC WR stars. The same tendency emerges in Fig. 2.2, where chemically homogeneous SMC models with different hydrogen mass fractions are displayed. This figure implies that even hydrogen-poor chemically homogeneous stars are cooler than these nine hot SMC WR stars.

Evolutionary models of rotationally mixed stars are not completely chemically homogeneous because the mixing is not infinitely fast. However, our models that experience blueward evolution always have a surface and central hydrogen abundance with a difference of $X_s - X_c < 0.1$. Therefore, the homogeneous models shown in Fig. 2.2 have a chemical profile comparable to these rotationally mixed models.

When comparing the observed stars to chemically homogeneous models with the same surface hydrogen mass fraction X_s, the observed stars can be as much as 0.3 dex hotter (i.e., 100 kK vs ~50 kK for SMC AB 10). The hydrogen-free models in Fig. 2.2 are considerably hotter than models which contain

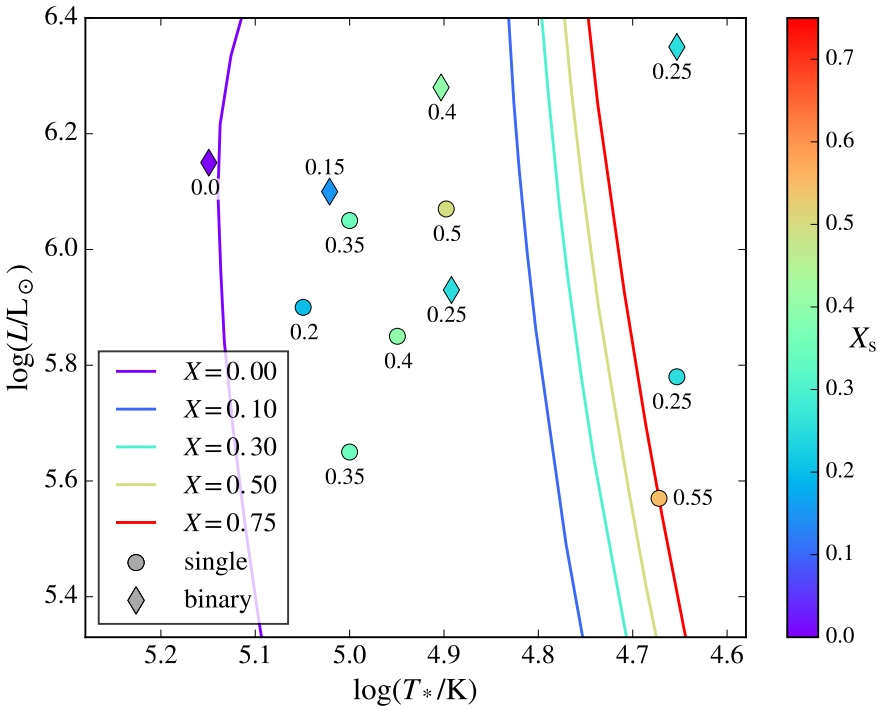

Figure 2.2: Hertzsprung-Russell diagram with lines indicating the positions of homogeneous stellar models with hydrogen mass fractions X of 0, 0.1, 0.3, 0.5, and 0.75. The metallicity Z is as described in Sect. 2.3, while the helium mass fraction Y is given by $Y = 1 - X - Z$. The models with $X = 0$ are helium burning, the others are hydrogen burning. The numbers near the scatter points indicate the surface hydrogen mass fractions X_s of the observed SMC WR stars. Both the lines and the scatter points are color coded for X_s. Circles indicate apparently single stars; diamonds indicate binaries.

hydrogen, as they have contracted until temperatures high enough for helium ignition were reached.

Apart from the temperatures, there is a modest conflict between the observed upper limits on the rotation velocities of the hot apparently single SMC WR stars and the rotational velocities of the models. Although depending on initial rotation velocity and angular momentum loss, the models typically retain $v_{\rm rot} > 250\,{\rm km\,s^{-1}}$; the upper limits on $v \sin i$ of these stars are 100-200 $\rm km\,s^{-1}$.

The terminal-age main sequence (TAMS), that is, the point where hydrogen is exhausted in the core, is followed by a short contraction phase in which the models do reach higher temperatures (Fig. 2.1). However, this phase is short lived ($\tau \approx \tau_{\rm MS}/1000$) and during the contraction the star spins up to even higher rotation velocities. As a result, the likelihood that the observed hot SMC WR stars are contracting stars that have just evolved past the main sequence is very small.

The objects that are not too hot to be core hydrogen burning are the apparently single stars SMC AB2 and 4 as well as both WR stars in the binary system SMC AB5. For the two single stars, the rotation velocities are with $v \sin i < 50\,{\rm km\,s^{-1}}$ (AB2) and $v \sin i < 100\,{\rm km\,s^{-1}}$ (AB4) relatively well constrained. Although the models spin down during their evolution, we find that it is unlikely that the low observed rotation velocities of the stars are an inclination effect. The models for which we achieve a best fit using the observed parameters T_*, L and X_s have rotation velocities of 302 and 183 $\rm km\,s^{-1}$ for SMC AB2 and 4, respectively. Then, following the formula provided by Grin, Ramirez-Agudelo, de Koter et al. (2017) we calculate that the chance that the observed $v \sin i$ limit is not exceeded is 1.4% for SMC AB2 and 16%

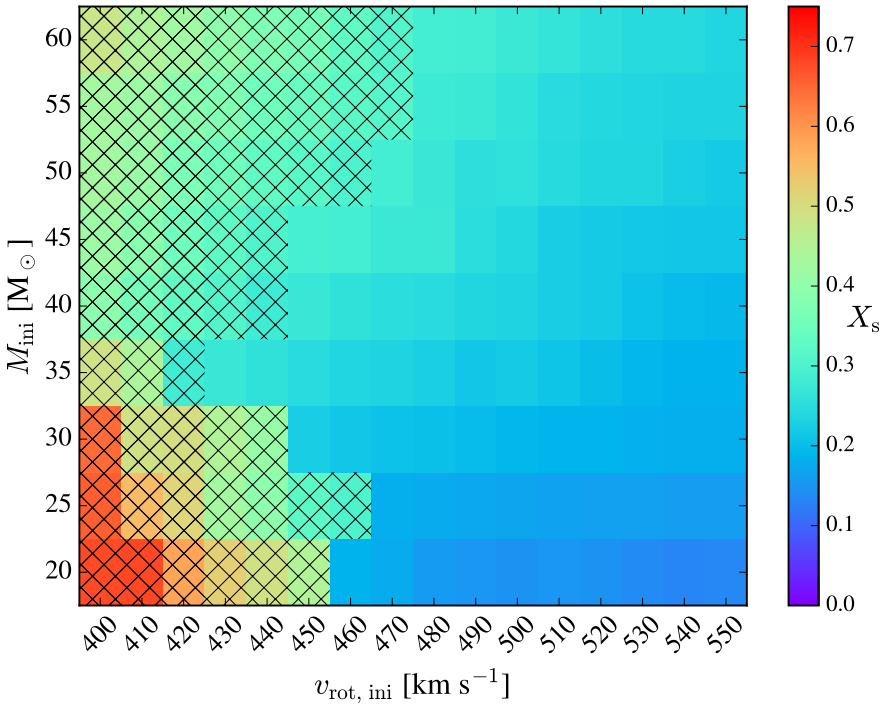

Figure 2.3: Diagram showing which models can become hot during helium burning. Each rectangle represents a model sequence with a certain initial rotation velocity and mass. The color indicates the surface hydrogen mass fraction $X_{\rm s}$ at the moment helium is ignited in the core. For the hatched systems, T_* does not overlap with the observed temperature range of the SMC WR stars during the entire core helium burning phase.

for SMC AB4. The probability to observe both stars pole-on enough at the same time therefore seems marginal.

Moreover, Vink and Harries (2017) have used spectropolarimetry to search for hints of rapid rotation in SMC WR stars. These were only found in the double WR system SMC AB5, which has high upper limits on $v \sin i$ (Table 2.2). Thus, their findings are in agreement with the upper limits from Shenar, Hainich, Todt et al. (2016).

Both WR stars in the source SMC AB5 are slightly on the cool side of the homogeneous models in Fig. 2.2. The observed parameters can be reproduced more accurately (i.e., all within 1σ, Table 4) by models with intermediately rapid rotation, in which rotational mixing becomes inefficient as they spin down during their evolution (e.g., the $v_{\rm rot,\,0} = 400\,{\rm km\,s^{-1}}$ track in Fig. 2.4). Alternatively, the temperatures can be lower than expected due to envelope inflation that can occur in very luminous stars (Sanyal, Langer, Szécsi et al., 2017). It is worth mentioning that the effective temperature of SMC AB5$_{\rm A}$ was unstable in the recent past: after a luminous blue variable type eruption in 1994, it has increased from ~25 kK to its current value of ~45 kK (Georgiev, Koenigsberger, Hillier et al., 2011). The high observed upper limits on $v \sin i$ are not in conflict with the rotational velocities of the models. Therefore, we conclude that these WR stars are in agreement with core hydrogen burning stars going through CHE, as was proposed by Koenigsberger, Morrell, Hillier et al. (2014).

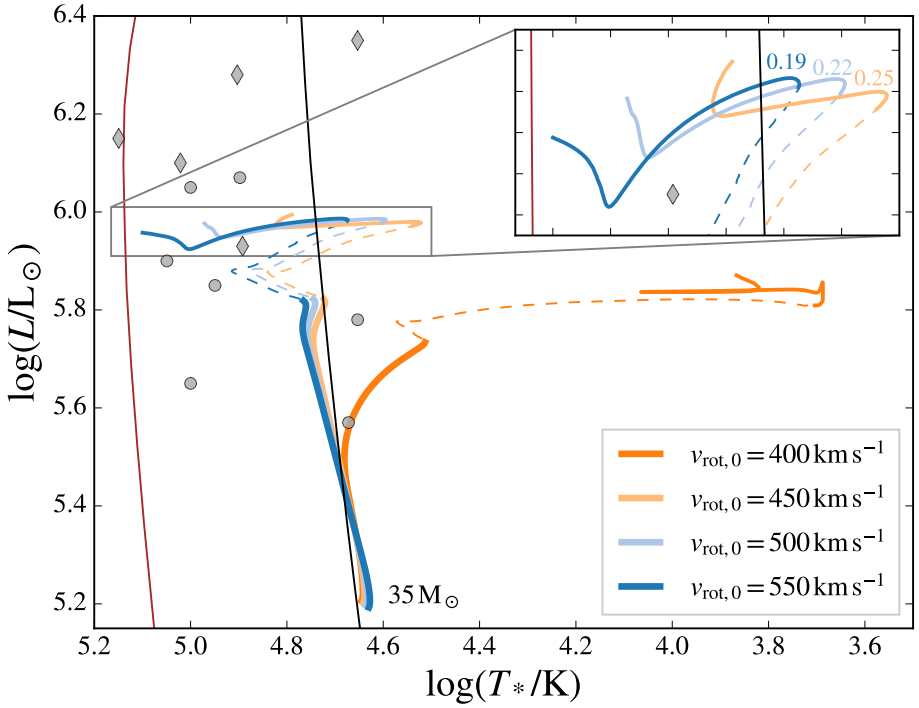

Figure 2.4: Same as Fig. 2.1, but now 35 $M_\odot$ models with various initial rotation velocities are displayed. The inset at the top right corner zooms in on the core helium burning phase. The numbers near the tracks in the inset indicate their surface hydrogen mass fraction X_s at the moment helium is ignited in the core.

2.4.2 Core helium burning phase

The surface hydrogen mass fraction X_s at the moment core helium burning commences, which we show in Fig. 2.3, depends on the initial mass and rotation velocity of the stellar model. As could be expected, it shows that initially more rapidly rotating models have lower X_s values.

Because rotational mixing is not infinitely efficient, the hydrogen envelope will have a shallow abundance gradient (Sect. 2.4.1) and therefore also a gradient in the mean molecular weight μ. In addition, due to stellar spin-down as a result of angular momentum loss via stellar winds, the mixing can become inefficient enough for the μ gradient to build up, which further inhibits mixing. This way, models which initially evolve almost homogeneously are able to retain intermediate surface hydrogen mass fractions through their core helium burning phase. For less massive stars, on the one hand a higher initial rotation velocity is required to mix the stellar interior to the surface. On the other hand, they have weaker stellar winds which result in less spin-down. As a result of these effects, the window for intermediate X_s values during core helium burning narrows down with lower masses.

When CHE is discontinued before the final stages of the main sequence evolution, a significant amount of hydrogen is retained and the star is unable to avoid the giant phase. This scenario is exemplified in Fig. 2.4 by the stellar model with $v_{\mathrm{rot},0} = 400\,\mathrm{km\,s^{-1}}$. We find that models which have $X_s \geq 0.3$ are cooler than the observed SMC WR star with the lowest T_* at all times during core helium burning. This means that the group of hydrogen-rich hot single WR stars (SMC AB 1, 9, 10, 11) and the binary WR star SMC AB6 do not match helium burning models which went through CHE, since all have $X_s \geq 0.35$.

The low temperature of these helium burning models with $X_s \geq 0.3$ is related to their hydrogen profile.

Because this hydrogen profile has a shallow gradient in the rotationally mixed models, the hydrogen envelope extends deep into the star - as a result, the star has a large radius. We discuss hydrogen profiles in more detail in Sect. 2.5.

In contrast to their hydrogen-rich counterparts, core helium burning models with $X_s \lesssim 0.25$ are able to reach the T_* that is observed for the cool WR stars. This is the case for the $v_{\mathrm{rot},0} = 450\,\mathrm{km\,s^{-1}}$ model in Fig. 2.4. However, it is not able to reach a value of T_* as high as observed for the hot stars. Models with higher initial rotation velocities are able to do so, but they have lower surface hydrogen mass fractions on the order of $X_s \approx 0.2$. Therefore, core helium burning quasi-CHE models are able to explain all observed properties of the relatively hydrogen-poor SMC WR stars. These include the hot single WR star SMC AB12 ($X_s = 0.2$) and those in WR+O binaries SMC AB3, 7 and 8 ($X_s = 0.25$, 0.15 and 0.0 respectively). For these objects, we are able to find solutions where the models meet the observed parameters T_*, L and X_s simultaneously within 1σ.

After their late core hydrogen burning phase, our models spin down enough for the upper limits on $v \sin i$ to agree with v_{rot} of the core helium burning models. A downside of this core helium burning quasi-CHE scenario however is that this phase is relatively short-lived: ~5% of the core hydrogen burning timescale. This would imply that for every core helium burning object, ~20 less evolved core hydrogen burning stars would be present in the population which are going through the same evolutionary scenario. Although these could be missed in observational campaigns due to a variety of biases (e.g., lower luminosity during core hydrogen burning, detectability of helium enrichment), this poses a potential problem. Previous observations of O-type and early B-type stars in the SMC (Mokiem, de Koter, Evans et al., 2006; Penny and Gies, 2009; Bouret, Lanz, Martins et al., 2013) indicate that their rotational velocity distribution is skewed to higher values than the rotational velocity distribution of their Galactic counterparts. However, the difference is modest. More extended surveys would be required to resolve this question in the future.

2.5 Stripped stars

As a next step we investigate whether helium burning stars that are partly stripped of their hydrogen envelopes can account for the observed properties of the SMC WR stars. The hydrogen envelope is defined as 'all layers that still contain hydrogen'. In principle, stripping of the envelope can be done by stellar winds, by short-lived outbursts of strong mass loss, or by a binary companion. We do not model the complete evolution of stars for these scenarios; instead we investigate a grid of stellar models with a helium core and a variety of hydrogen envelopes to compare with the observed parameters of SMC WR stars.

To characterize the hydrogen envelopes of these models we use two parameters: the hydrogen mass fraction at the stellar surface X_s and the slope of the hydrogen profile dX/dQ. To illustrate our method, we show an example of such a synthetic hydrogen profile in Fig. 2.5 (top). Here, Q is a normalized mass coordinate, with $Q = 0$ in the stellar center, and with $Q = 1$ defined as the mass coordinate where the linear slope of the hydrogen profile reaches $X(Q) = X_0$ (the hydrogen mass fraction at the zero-age main sequence; $X_{0,\mathrm{SMC}} = 0.746$). At the surface (blue dot) this model has a hydrogen fraction of $X_s = 0.4$. A model in which a layer with $X_s < X_0$ is exposed necessarily has a Q value at its surface of $Q_s < 1$. The value for Q_s is given by

$$Q_s = 1 - \frac{X_0 - X_s}{dX/dQ}. \tag{2.1}$$

Then, the hydrogen mass fraction $X(Q)$ throughout a star which is hydrogen-depleted at the surface in

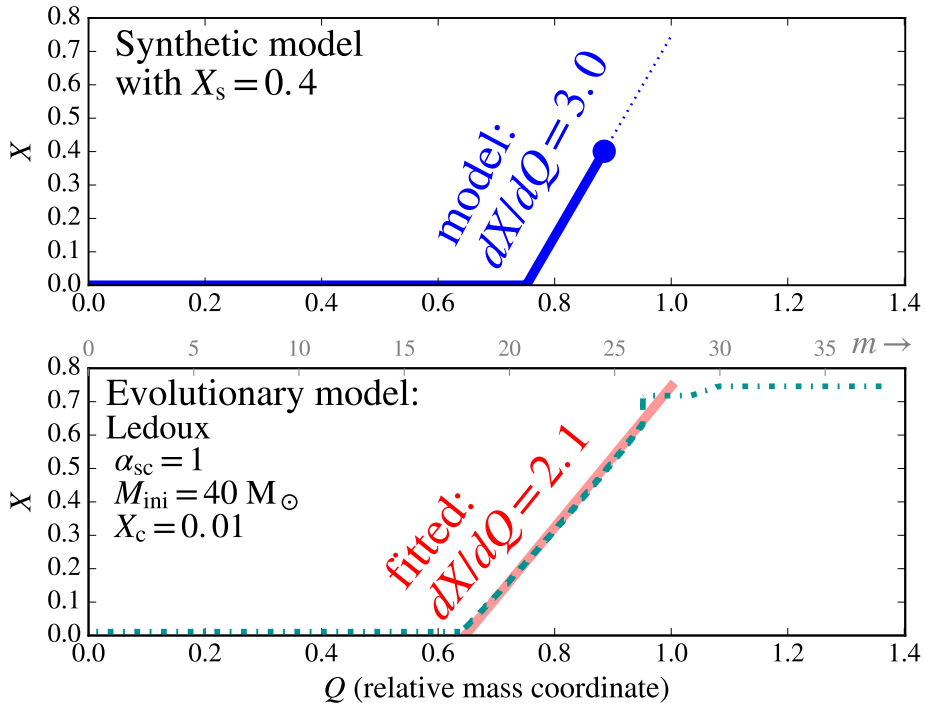

Figure 2.5: **Top:** Example of a synthetic hydrogen profile (solid line). The blue dot represents the surface. This model has a slope of $dX/dQ = 3.0$ and surface hydrogen fraction $X_s = 0.4$. **Bottom:** Hydrogen profile of a $40\,M_\odot$ star model near the end of core hydrogen burning. Plotted in red is the fitted slope of $dX/dQ = 2.1$. The part of the profile that was used for fitting is displayed with a dashed line, the rest is displayed with a dash-dotted line. For comparison, the mass coordinate m (in units of $M_\odot$) is also displayed at the top of this panel.

the range $0 \leq Q \leq Q_s$ is:

$$X(Q) = \max\left[0,\ X_s - (Q_s - Q)\,dX/dQ\right]. \tag{2.2}$$

At first glance the definition of the variable Q might seem overly complicated. However, it avoids that the value of the hydrogen profile slope becomes dependent on the stellar mass or on the surface hydrogen mass fraction X_s.

For comparison, we show a hydrogen profile of a $40\,M_\odot$ evolutionary model at the end of hydrogen core burning in the bottom of Fig. 2.5. As the mass of the convective core in massive main sequence stars is decreasing rather linearly as function of time, it leaves a hydrogen profile $X(Q)$ with a rather constant hydrogen gradient. Therefore, we are able to fit a slope with $dX/dQ = 2.1$ that closely represents the hydrogen profile in the model. We fit the slope of the hydrogen profile until a 'plateau' with a constant hydrogen fraction is encountered which contains more than 5% of the mass of the star. The part of the model that we use for the fit in the bottom of Fig. 2.5 thus has a hydrogen fraction $0.01 < X < 0.7$. $Q = 1$ is set by the point where the fitted slope $dX/dQ = 2.1$ reaches X_0. At core hydrogen exhaustion, $Q = 1$ typically coincides with the border of the convective core at the zero-age main sequence.

While hydrogen profiles in evolutionary models may be more complex than what we assume for our synthetic models, our approach is the first order approximation and contains the minimum number of parameters. Furthermore, it does not assume any evolutionary history and may thus cover scenarios that are not usually dealt with, like common envelope evolution or a stellar merger.

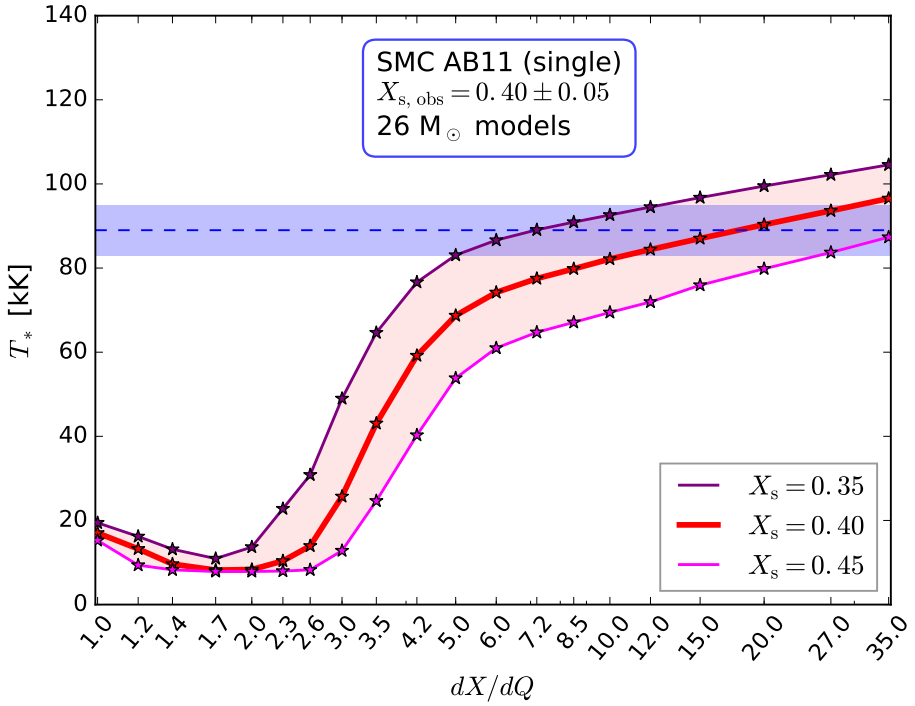

Figure 2.6: Diagram showing the best-fitting hydrogen slope dX/dQ for SMC AB11. The temperature T_* is plotted as a function of dX/dQ for models with surface hydrogen mass fractions $X_{\rm s}$ which correspond to $X_{\rm s,\,obs} \pm 1\sigma$. Each 'star' symbol represents a stellar model. The blue dashed line represents observed T_* of SMC AB 11 to which the models are compared, whereas the blue shaded area represents the error margin. We note that the x-axis is in log scale.

The stellar models computed for this section are simulated with the same physics assumptions as described in Sect. 3.2, but with different initial chemical profiles. The hydrogen mass fraction $X(Q)$ inside the star follows from the surface hydrogen fraction $X_{\rm s}$ and the adopted dX/dQ value as described by Eq.(2.2). The metallicity Z also corresponds to the value declared in Sect. 3.2, but since all material should have been processed by nuclear burning we assume CNO equilibrium. Finally, the helium mass fraction Y follows from $Y = 1 - X - Z$. The models are evolved until they have a central helium mass fraction of $Y_{\rm c} = 0.75$, while mixing and abundance changes due to nuclear burning in the hydrogen envelope are switched off. We note that in stellar envelopes as hot as those of the SMC WR stars, little mixing is expected to occur.

2.5.1 Inferred hydrogen profiles in SMC WR stars

In this section, we compare stellar models with various hydrogen profile slopes to the observed single and binary SMC WR stars. On average, the apparently single SMC WR stars are more hydrogen rich than their binary counterparts by $\Delta X_{\rm s} > 0.1$ (Tables 2.2 & 2.1). Naively one might expect that these more hydrogen-rich stars are also cooler, since hydrogen-free stars move toward the helium main sequence. Surprisingly, the observed temperatures show the opposite trend.

Our method is exemplified by Fig. 2.6, where we compare our models with the apparently single star SMC AB11. Each model in this figure has a helium core and a hydrogen profile which follows from the

adopted slope dX/dQ and the surface hydrogen abundance X_s, which is chosen close to the observed one, $X_{s,\,obs}$. The mass of the models is chosen such that their luminosity matches the observed luminosity. We consider hydrogen profile slopes in the range of $1 < dX/dQ < 35$.

Fig. 2.6 demonstrates that models with shallow slopes ($dX/dQ < 4$), which contain more hydrogen, are far cooler than the observed WR star. The dX/dQ range in which models with a surface hydrogen mass fraction of $X_{s,\,obs} \pm 1\sigma$ are able to reproduce the observed temperature $T_{*,\,obs} = 89\,kK$ covers $7 < dX/dQ < 35$ with a best-fitting value of $dX/dQ \simeq 20$. These values are much higher than in the example model we showed in Fig. 2.5, where we found $dX/dQ = 2.1$ for a star at the end of core hydrogen burning.

We repeat this exercise for the other SMC WR stars. For these objects, similar plots are provided in Appendix B, and the results of the fits are provided in Table 1. We display the dX/dQ range of models that match the observed surface temperatures of the WR stars in Fig. 2.7. They are divided into 'hot' objects (their T_* only matches helium burning models) and 'cool' objects (which can be both, helium and hydrogen burning). Below, we discuss the results for the apparently single WR stars (Fig. 2.7, top) and for the WR stars in binaries (Fig. 2.7, bottom).

- **Apparently single stars:** although for the five hot apparently single WR stars the scatter around the best-fitting dX/dQ value is rather large, we conclude that values on the order of $dX/dQ \approx 2$ can be ruled out according to our models (except for SMC AB12, which is marginally consistent with a shallow slope). However, all of them are in agreement with dX/dQ values of $10 - 15$ or even larger. SMC AB1 is most extreme, as it needs dX/dQ values of ~35 or more to approach $T_{*,obs}$. SMC AB12 could also be explained via CHE (cf., Sect. 4).

  The two remaining apparently single stars are the two cool single stars. These are SMC AB2 and 4, which are the two only apparently single SMC WR stars for which we find that they also have a temperature compatible with core hydrogen burning. The T_* of SMC AB2 matches the observed temperature only for a narrow interval around $dX/dQ \approx 6$; SMC AB4 matches to helium burning stripped star models.

- **Binaries:** here, it seems to be the other way around: all binary WR stars fit to models with shallow slopes, with the best fits occurring around $2 < dX/dQ < 3$. Therefore, unlike for the apparently single stars, this indicates that their hydrogen profile slopes are similar to those of the TAMS star model shown in Fig. 2.5. We again mention that for SMC AB5, the observed parameters could also be explained by both components going through CHE (cf., Sect. 4). Finally, the temperature of SMC AB8 is in agreement with that of a helium star. However, since no hydrogen has been detected at its surface we cannot consider the hydrogen profile of this star.

In summary, we find that the observed parameters of the SMC binary stars are similar to those of a $40\,M_\odot$ model stripped at the TAMS. On the other hand, we infer much steeper hydrogen profiles for the group of hot apparently single SMC WR stars. We also visualize this in Appendix A, where we provide HRDs showing models with the best-fitting dX/dQ values to the observed binary and hot apparently single SMC WR stars. In Table 1 we show the lifetimes of the inferred hydrogen envelopes, which we find to be in the same order as the core helium burning timescales.

2.5.2 Progenitor evolution and binary status of the SMC WR stars

To put the hydrogen slopes derived in the last section into perspective, we now investigate dX/dQ values of evolutionary models. To do this comprehensively is beyond the scope of this paper, since it relates

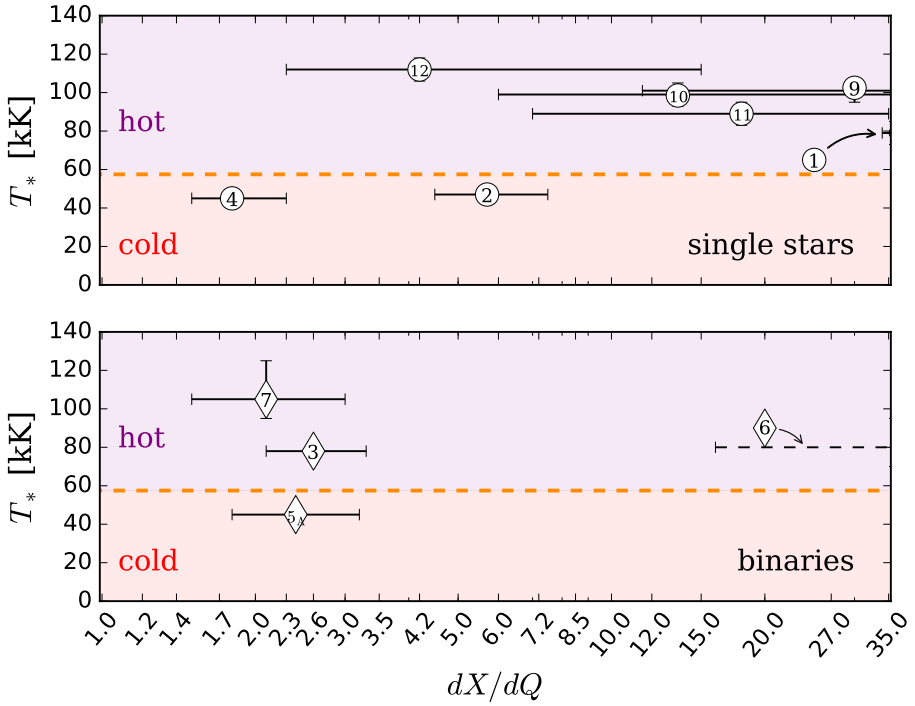

Figure 2.7: Best-fitting dX/dQ values for apparently single SMC WR stars (top) and those in binaries (bottom). SMC AB9 & 10 have the same $T_{*,\mathrm{obs}}$, but they are slightly offset for clarity. The numbers indicate the identifiers of the stars. The peculiar source SMC AB6 is displayed with a dashed line.

Table 2.3: Values for the fitted slope of the hydrogen profile dX/dQ for models with different initial masses and different values of the overshooting parameter α_{ov}. All models are at the end of core hydrogen burning.

M_0 [$M_\odot$]	15	25	40	60	85	110	avg.
$\alpha_{\mathrm{ov}} = 0.15$	1.5	1.8	1.8	1.8	1.7	1.7	1.7
$\alpha_{\mathrm{ov}} = 0.335$ (default)	1.8	2.0	2.1	2.0	2.1	2.1	2.0
$\alpha_{\mathrm{ov}} = 0.5$	2.1	2.3	2.4	2.4	2.4	2.4	2.3

to uncertain internal mixing process and their triggering, for example, by rotation or binary interaction (cf. Langer, 2012). For this purpose, we only consider single star models. That is, we do not model how these stars lose their hydrogen envelopes, but we discuss what the products of envelope stripping would look like.

2.5.2.1 Terminal-age main sequence

We compute nonrotating single star models in the initial mass range $15\,M_\odot \ldots 110\,M_\odot$ up to core hydrogen exhaustion, with the same assumptions as the models discussed in Sect. 4. These models cover the observed luminosity range of the SMC WR stars. Apart from models with our default value for the overshooting parameter α_{ov}, we also compute models for extreme cases, that is, with $\alpha_{\mathrm{ov}} = 0.15$ and $\alpha_{\mathrm{ov}} = 0.5$.

Until the end of hydrogen burning, the slope of the hydrogen profile in the models is relatively constant,

due to the constant recession speed of the convective core. Table 2.3 shows the values of dX/dQ derived for models with different initial parameters, at the time of core hydrogen exhaustion. Noticeably, the variation of dX/dQ with initial mass is very small. We find that the core overshooting parameter has a larger impact. However, overall the TAMS hydrogen profile slopes are restricted to the narrow range $1.5 \leq dX/dQ \leq 2.4$.

We consider this result to be robust. It is likely not sensitive to the adopted criterion for convection or to the efficiency of semiconvective mixing (Langer, El Eid and Fricke, 1985, see also Fig. 3.6).

Also the mass loss rates are so small that their uncertainty is not relevant here. However, in rapid rotators, the hydrogen gradient may be significantly different (cf., Sect. 4).

2.5.2.2 Post-main-sequence evolution

The post-main-sequence evolution of single stars involves more uncertainties than their main sequence evolution, many of which also affect the hydrogen profile. Here, we cannot systematically explore the whole parameter space, but restrict ourselves to elaborate on one emerging trend: namely that, in most considered cases, the hydrogen profile becomes steeper with time. We find this to be the case due to several effects.

After core hydrogen exhaustion the star contracts as a whole. As a consequence, a hydrogen burning shell source is ignited, which drives the expansion of the hydrogen-rich envelope. During this stage, convective and semiconvective regions form, at first above the hydrogen burning shell. Later on, when the star becomes a cool supergiant, envelope convection can occur and extend down into the region of varying hydrogen concentration, also known as dredge-up. Since all these mixing processes push hydrogen into deeper layers, that is, closer to hydrogen-depleted layers, the hydrogen profile becomes steeper as a consequence. The efficiency of this mixing, which is controlled by semiconvection, is poorly known, and as a consequence also the post-main-sequence radius evolution of massive stars is uncertain (e.g., Langer, El Eid and Fricke (1985)).

Yet, an increase of the steepness of the hydrogen profile after the ignition of the hydrogen burning shell is expected in any case. We illustrate this in Fig. 3.6, where we show the dX/dQ value as function of the stellar radius during the core helium burning evolution of a $40\,M_\odot$ stellar model, computed with the Schwarzschild criterion for convection. While the evolution starts with the TAMS value of $dX/dQ \simeq 2$, values of the order of 20 to 50 are achieved during the blue supergiant stage, while maximum values near 50 or even larger are obtained in the red supergiant stage.

A hydrogen profile of a model from this sequence where core helium burning has advanced to a core helium mass fraction of $Y_c = 0.75$ is shown in the middle panel of Fig. 2.9. It can be compared to a corresponding plot for a model computed with the Ledoux criterion for convection and a semiconvection parameter of $\alpha_{sc} = 1$, where the mixing is much more limited, and dX/dQ does increase only to values of about five (top panel of Fig. 2.9).

We compute the evolution of a $40\,M_\odot$ model which accreted $10\,M_\odot$ of unprocessed material near the end of its main sequence evolution, which may simulate the situation of a mass gainer in a close binary system (Braun and Langer, 1995), using again $\alpha_{sc} = 1$. The corresponding hydrogen profile is shown in the bottom panel of Fig. 2.9. As a result of the mass accretion, its convective core has grown in mass, which also gives rise to a very steep hydrogen profile.

Another process which steepens the hydrogen profile is hydrogen shell burning. However, this does not cause changes in dX/dQ which are as dramatic as those caused by the mixing processes discussed above. In the most extreme case this could cause an increase of $dX/dQ = 2$ to $dX/dQ = 4$, but the effect vanishes for large dX/dQ values (see Appendix C).

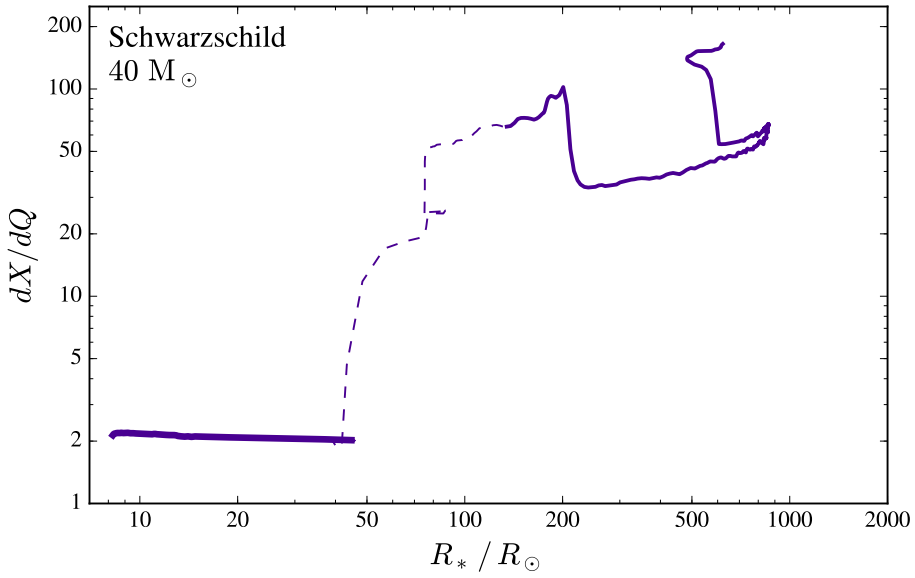

Figure 2.8: Evolution of the hydrogen slope dX/dQ of a 40 $M_\odot$ model as a function of stellar radius. As in Fig. 2.1 and Fig. 2.4, the hydrogen burning phase is shown with a thick solid line, the short-lived hydrogen shell burning phase with a dashed line and helium burning with a thin solid line. This sequence was computed adopting the Schwarzschild criterion for convection.

2.5.3 Connecting the hydrogen profile in SMC WR stars with their evolutionary history

WR stars, in particular the ones in the SMC discussed here, have lost most of their hydrogen-rich envelope. The high temperature of the hot majority of the SMC WR stars requires them to be in the stage of core helium burning. In the following, we discuss the various possibilities for how these stars could have lost their hydrogen-rich envelope, and, according to our discussion above, which slope for the hydrogen gradient we could expect in the corresponding scenario.

2.5.3.1 Single star mass loss

As shown above, the small dX/dQ values of the WR stars in binaries imply that their progenitors have been stripped in a compact stage (see also Sect. 2.5.3.2). The much higher dX/dQ values of the apparently single WR stars indicate that their progenitors strongly expanded before their envelopes were stripped (Sect. 2.5.2.2). Since envelope stripping is expected to produce WR stars also in wide binaries (Schneider, Izzard, Langer et al., 2015) — in about as many cases as in Case A or early Case B, given the Sana, de Mink, de Koter et al. (2012) orbital period distribution — we conclude that at least the majority of the apparently single WR stars lost their envelope due to a binary companion (cf. Sect 2.5.3.3.)

We may still ask the question whether a fraction of these stars might have lost their envelopes as single stars, that is, without the help of a companion. At present, they (apart from SMC AB4) are losing about $2\,M_\odot\,\mathrm{Myr}^{-1}$ through stellar winds. At this rate, which is higher than what is expected for the main sequence evolution, mass loss is not strong enough to expose hydrogen-depleted layers for reasonable initial masses. As stellar wind mass loss rates during the hot stages of evolution may currently even be overestimated at low metallicity (Hainich, Shenar, Sander et al., 2017), hot star winds can not have

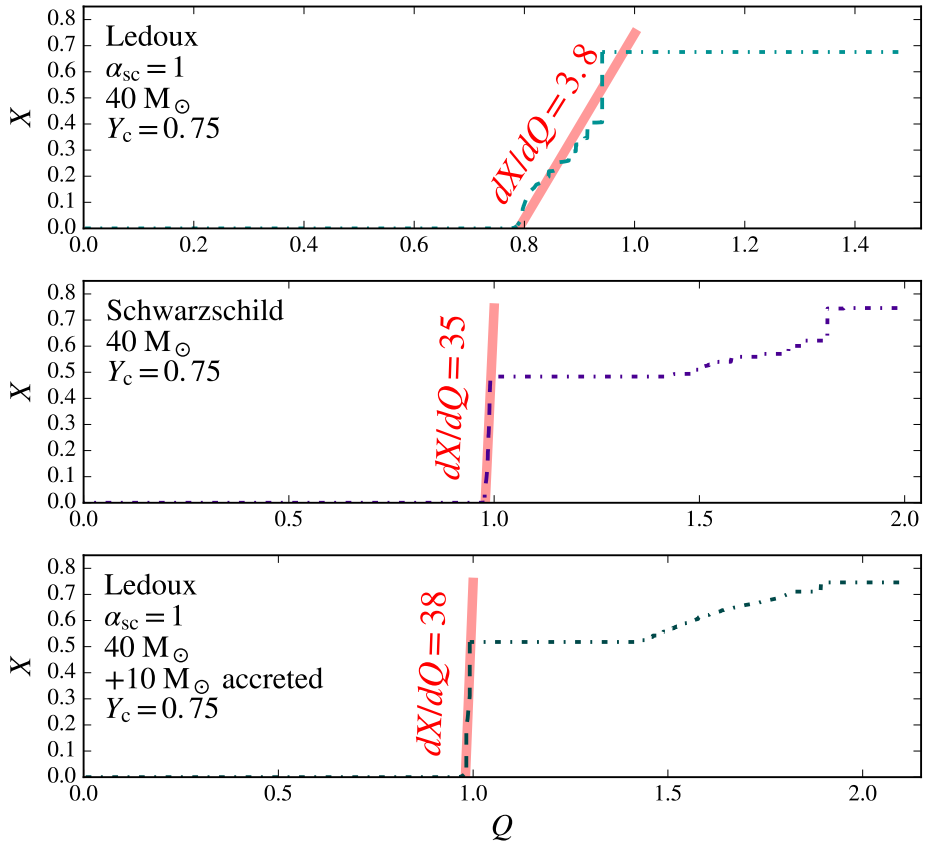

Figure 2.9: Same as Fig. 2.5, but showing core helium burning models with central helium mass fraction of Y_c = 0.75. Apart from the model with default assumptions (top), we also show a model where the Schwarzschild criterion for convection is assumed (middle) and a model which has accreted 10 $M_\odot$ near the end of the main sequence (bottom).

removed the hydrogen envelopes of the SMC WR stars.

Thus, the envelope stripping in any single star scenario would have to occur in the cool part of the HR diagram, possibly in the form of episodic luminous blue variable (LBV)-type mass loss, or in a yellow/red supergiant stage. Since the Small Magellanic Cloud does not host red supergiants with a luminosity as high as those of the bulk of the SMC WR stars (Blaha and Humphreys, 1989; Neugent, Massey, Skiff et al., 2010; Yang and Jiang, 2012) the loss of the hydrogen-rich envelope during a RSG phase is therefore unlikely. The LBV phenomenon, on the other hand, has been associated with the stellar Eddington limit (e.g., Lamers and Fitzpatrick, 1988; Sanyal, Grassitelli, Langer et al., 2015), which, at SMC metallicity, is located well above 10^6 $L_\odot$ (Ulmer and Fitzpatrick (1998) — see also Sanyal, Langer, Szécsi et al. (2017), their Fig. 2, for the inflation of TAMS stars which are at the Eddington limit). Therefore, in particular the apparently single SMC WR stars can not be expected to have hit the Eddington limit. However, as long as the LBV mass loss is not fully understood — for example, it has been proposed recently that the LBV phenomenon is caused by binary interaction (Smith and Tombleson, 2015) — a single star origin of *some* of the apparently single SMC WR stars can not be fully excluded.

Independent of the mass loss mechanism, also the luminosity distribution of the SMC WR stars appears not easily compatible with any single star WR formation channel. If such a channel exists, it

would work above a certain mass, or luminosity, threshold. As the binary channels work for all masses, we would expect both contributions above the threshold luminosity, but only WR binaries below it. However, observations show that the five most luminous SMC WR stars are all in binaries and the five least luminous ones are all apparently single (Table 2.2&2.1). We conclude that a single star origin of the apparently single SMC WR stars can not be firmly excluded, but does appear unlikely.

2.5.3.2 Stable Roche lobe overflow

When the initially more massive star in a close binary expands and fills its Roche lobe, mass transfer commences. For relatively small initial orbital periods (Case A and early Case B mass transfer), the mass transfer is stable in the sense that contact is avoided (Podsiadlowski, Joss and Hsu, 1992; Wellstein, Langer and Braun, 2001), and only stops after most of the hydrogen-rich envelope has been stripped off the mass donor. Since stable mass transfer also requires initial mass ratios close to one, the outcome would be a stripped star, that is, a nitrogen sqeuence WR (WN) star in close orbit with an O star of nearly equal or higher mass.

The WN binaries SMC AB3 and AB7 can be well explained in this way, and the WO+O binary SMC AB8 fits the same scenario, only that the system is further evolved (in agreement with Shenar, Hainich, Todt et al., 2016). Their short present-day orbital periods (in the range of 6-20 d, Table 2.2), indicate that they experienced binary interaction during or shortly after their main sequence evolution.

Interestingly, the WR stars in the WN+O binaries have, according to our analysis above, shallow hydrogen slopes with $dX/dQ \simeq 2$ (Fig. 2.7). Since in mass donors of Case A and early Case B binaries the mixing processes which can increase the slope of the hydrogen profile (see above) have not yet occurred by the time of mass transfer (see for example Fig. 2 of Wellstein and Langer, 1999), such shallow slopes are indeed expected for stable mass transfer systems. Such evolution appears therefore most likely for the WN+O binaries in the SMC.

We note that the binary SMC AB5 (HD 5980), which consists of two very hydrogen-deficient stars, cannot be explained well by stable mass transfer. As discussed by Koenigsberger, Morrell, Hillier et al. (2014), chemically homogeneous evolution, perhaps tidally induced (de Mink, Cantiello, Langer et al., 2009; Marchant, Langer, Podsiadlowski et al., 2016), can explain this binary best.

2.5.3.3 Common envelope evolution

Mass transfer in initially relatively wide binaries (late Case B, Case C), and/or with initial mass ratios very different from one does lead to contact and the formation of a common envelope (CE). The outcome of this will be a merger in many cases, which may lead back to the single star scenario discussed above. However, when the more evolved star has significantly expanded before the CE evolution sets in, the hydrogen-rich envelope may be bound loosely enough such that an envelope ejection occurs and the binary as such survives (Ivanova, Justham, Chen et al., 2013). The result will be a WN star with, most likely, a main sequence companion. Here, if the primary could expand sufficiently, the mass of the main sequence companion may even be rather small (Kruckow, Tauris, Langer et al., 2016).

This scenario could apply to the hot apparently single WR stars, that is, SMC AB1, and SMC AB9...12, since a low or intermediate mass companion might have been easily missed in the binary search of Foellmi, Moffat and Guerrero (2003). Furthermore, the large dX/dQ values which we found for all these stars imply that the WR progenitors did expand to large radii before they were stripped. In view of Fig. 3.6 we may even speculate that intermediate values of dX/dQ are rare because they would correspond to binaries of intermediate initial periods, where a merger is the most likely outcome.

2.5.3.4 Reverse mass transfer

In some binaries, a WR star may also form from the initially less massive star. For this to happen, the binary must have survived an earlier phase of, most probably, stable mass transfer (see above), and the initially more massive star (e.g., the WR star in the WR+O binaries discussed above) will likely be a compact object by the time reverse mass transfer starts. Due to the large mass ratio in this situation, the system will likely undergo CE evolution at this stage, out of which it may emerge as a WR binary with a compact companion (WR+cc).

Again, this scenario may apply to the apparently single WR stars, because for not too large compact object masses radial velocity variations may remain small. While the compact companion may accrete matter from the wind of the WR star and become a strong X-ray source, the X-ray emission may also be weak, in particular if the compact object is a black hole and when the formation of an accretion disk is avoided (Shapiro and Lightman, 1976). Since the secondary star has accreted substantial amounts during the first, stable, mass transfer phase, the resulting WR star can be expected to show a steep hydrogen profile (cf. Fig. 2.9, bottom).

Thus the hot apparently single WN stars in the SMC could also be well explained through this scenario. Since some of the WR+O binaries will merge or might break up when the first supernova occurs, the number of the WR+cc binaries is expected to be smaller than that of WR+O binaries. Nevertheless, the reverse mass transfer scenario offers the chance that among the apparently single WR stars in the SMC, we may soon detect the first direct double black hole progenitor with black holes as massive as those recently detected by LIGO (B. P. Abbott, Abbott, Abbott et al., 2016a; B. P. Abbott, Abbott, Abbott et al., 2016b; B. P. Abbott, Abbott, Abbott et al., 2017a).

2.5.4 The only hydrogen-free SMC WR star - SMC AB8

The fact that the only hydrogen-free star SMC WR star (SMC AB8) is of the type WO (i.e., it has also lost its pure helium envelope) could be seen as an indication for efficient semiconvection. As a result of semiconvective mixing, the CO core is able to grow and will be buried less deep in the He mantle, making it easier to expose. Given its current mass loss rate it would lose $\sim 6\,M_\odot$ during core helium burning. We find that for a scenario with inefficient semiconvection, only helium stars with $M < 15 - 20\,M_\odot$ develop sufficiently low mass helium envelopes above the CO core. This mass is well below the mass expected for its luminosity, which is around $40\,M_\odot$ (Gräfener, Vink, de Koter et al., 2011).

2.6 Conclusions

In this study, we have compared the observed parameters of Wolf-Rayet (WR) stars in the Small Magellanic Cloud (SMC) with a variety of models obtained with the detailed stellar evolution code MESA. This includes evolutionary models which undergo chemically (quasi-)homogeneous evolution (CHE) in both the core hydrogen and helium burning phase, as well as synthetic core helium burning stars with diverse hydrogen profiles which represent stripped stars. In particular, we have determined the average slope of the hydrogen abundance profile in the envelopes of the considered WR stars, which allowed us to identify the most likely evolutionary scenario for producing the WR stars individually.

We found that in particular the two WR components of SMC AB5 (HD 5980), but also the apparently single WN star SMC AB12, have properties which are consistent with CHE. SMC AB5 is in fact difficult to explain in any other way (Koenigsberger, Morrell, Hillier et al., 2014).

For the hot WR stars ($T_{\rm eff} > 60\,$kK), which are in the stage of core helium burning, we find a dichotomy in the slope of the hydrogen profiles, with one group showing shallow slopes, which are consistent with

those found in stellar models at core hydrogen exhaustion, and the second group showing much steeper slopes. A physical interpretation of this dichotomy, despite the small number of stars, appears reasonable because the WR stars of the first group have massive O star companions, while no companions have been found for any of the WR stars of the second group.

The WR stars with O star companions turn out to fit very well to models which undergo stable Roche lobe overflow. This concerns the binary properties, in particular the mass ratio and the orbital period. But it also holds for the properties of the WR stars, for which corresponding models do predict shallow hydrogen profile slopes with values very close to the ones we derived.

When studying the evolution of the hydrogen profile slope in post-main-sequence stellar evolution models, we found two possible ways for steep hydrogen profiles to develop. One is due to convective and semiconvective mixing in the hydrogen-rich envelope, which occurs during the post-main-sequence expansion of the star. The second is due to mass accretion during the main sequence stage, which leads to an increase of the convective core mass. We show that in the binary evolution context, both possibilities point to the formation of the WR star in a common envelope phase, with a main sequence star as the most likely companion in the first case, and — excitingly — a compact object in the second case.

A single star origin for the hot and apparently single SMC WR stars can not be firmly excluded. However, the high fraction of massive stars in close binaries (Sana et al. 2012), and the detailed properties of these WR stars render a common envelope evolution as the likely agent for removing their hydrogen-rich envelope (cf. Sect. 5.3). This would raise the WR binary fraction in the SMC from about 50% Foellmi, Moffat and Guerrero (2003) to near 100%, in line with the expectation for a very metal poor environment.

A previous common envelope phase of the hot apparently single WR stars would imply that they presently do have companions. The prospects of finding these companions are in fact good. Due to their relatively weak winds, absorption lines are present in the spectra of many of them (Marchenko, Foellmi, Moffat et al., 2007; Hainich, Pasemann, Todt et al., 2015), which may allow to push the current accuracy of the radial velocity measurements of $\sim$30 km s^{-1} to much smaller values, such that even quite low mass companions might become detectable.

Finding these companions would in fact be very valuable, as they would give us the very first observational benchmark for the efficiency of common envelope ejection in the stellar mass range of black hole progenitors. Some of the companions may even be black holes — this cannot be excluded from the current upper limits of their X-ray emission (Guerrero and Chu, 2008a; Guerrero and Chu, 2008b) — which would render such binaries as direct progenitors of massive double black hole systems.

Acknowledgements. The authors would like to thank Pablo Marchant for help and input and Nathan Grin and Thomas Tauris for fruitful discussions.

CHAPTER 3

Constraining internal mixing processes in massive stars in the Small Magellanic Cloud

A. Schootemeijer, N. Langer, N. J. Grin, & C. Wang
Argelander-Institüt für Astronomie, Universität Bonn, Auf dem Hügel 71, 53121 Bonn, Germany

To be submitted to *Astronomy & Astrophysics*

Abstract. *Context:* The evolution of massive stars is strongly influenced by internal mixing processes such as semiconvection, convective core overshooting, and rotationally induced mixing. None of these processes is currently well constrained.
Aims: We investigate models for massive stars in the Small Magellanic Cloud (SMC), for which stellar wind mass loss is less important than for their metal-rich counterparts. We aim to constrain the various mixing efficiencies by comparing model results to observations.
Method: For this purpose, we use MESA to compute more than 60 grids of detailed evolutionary models for stars with initial masses of $9 \ldots 100\,M_{\odot}$, assuming different combinations of mixing efficiencies of the various processes in each grid. Our models evolve through core hydrogen and helium burning, such that they can be compared with the massive main sequence and supergiant population of the SMC.
Results: We find that for most of the combinations of the mixing efficiencies, models in a wide mass range spend core-helium burning either only as blue supergiants, or only as red supergiants. The latter case corresponds to models that maintain a shallow slope of the hydrogen/helium (H/He) gradient separating the core and the envelope of the models. Only a small part of the parameter space ($\alpha_{\rm ov} \approx 0.33$, $\alpha_{\rm sc} \gtrsim 10$) leads to models which produce a significant number of blue and red supergiants. Interestingly, these models also contain steep H/He gradients, as is required to understand the hot, hydrogen-rich Wolf-Rayet stars in the SMC. We find that unless it is very fast, rotation has a limited effect on the H/He profiles in our models.
Conclusions: While our models use specific implementations for the considered mixing processes, they comprehensively probe the two first order structural parameters, the core mass and H/He gradient in the core-envelope interface. Future observational surveys of the massive stars in the SMC can therefore be used to derive these important quantities and thereby considerably reduce the uncertainties in massive star evolution models.

Key words. stars: massive – stars: early-type – stars: Wolf-Rayet – stars: interiors – stars: rotation – stars: evolution

3.1 Introduction

Massive stars play a central role in astrophysics. They dominate the evolution of star forming galaxies by providing chemical enrichment, ionizing radiation and mechanical feedback (e.g. Hopkins, Kereš, Oñorbe et al., 2014). Massive stars also produce a variety of transient phenomena, like supernovae (SNe), long-duration gamma-ray bursts (lGBRs) and merging black holes emitting gravitational waves (GWs). Excitingly, these events can be so bright that they are observable up to high redshift, allowing us to study the early universe. In fact, lGRBs (Graham and Fruchter, 2017) superluminous supernovae (Chen, Smartt, Yates et al., 2017; Schulze, Krühler, Leloudas et al., 2018), and likely also massive black hole mergers (Belczynski, Dominik, Bulik et al., 2010) appear predominantly in low-metallicity galaxies. The implication is that massive star evolution can proceed differently in the early universe compared to our neighborhood. However, at high redshift, massive star can not be observed individually until they explode.

It is therefore important to study the existing low-metallicity massive stars that are nearby, which are concentrated in star forming dwarf galaxies. A unique environment for this is provided by the Small Magellanic Cloud (SMC), which, at a distance of ~60 kpc, allows the detailed study of individual stars. With a metal content of about one fifth of the solar value (Venn, 1999; Korn, Becker, Gummersbach et al., 2000), it is representative of massive star forming galaxies at a redshift around 3.5 (Kewley and Kobulnicky, 2007).

Evolutionary models of massive stars are plagued by our ignorance of two physical ingredients, mass loss and internal mixing. In this respect, it is also beneficial to focus on the low metallicity environment of the SMC, where stellar winds appear to be significantly weaker than in the Miky Way (Mokiem, de Koter, Vink et al., 2007). E.g., current models predict that stars above ~ 25 $M_\odot$ in the Galaxy lose more than 10% of their initial mass by stellar winds during the main sequence evolution, while in the SMC this happens only for stars above ~60 $M_\odot$ (Brott, de Mink, Cantiello et al., 2011). With considering massive stars in the SMC, we want to exploit this feature, which allows us, at least below a certain threshold mass, to focus on internal mixing as the major uncertainty in massive single star evolution.

The evolution of massive stars is known to sensitively depend on a number of internal mixing processes (Langer, 2012). The most important one is certainly convection, and "convective overshooting", i.e., the mixing at the boundaries of convective regions (Maeder and Meynet, 1988; Alongi, Bertelli, Bressan et al., 1993), which affects the core masses and lifetimes of all phases of massive star evolution. Furthermore, semiconvection is an important but not well-understood process that determines the time scale of mixing in layers with a stabilizing gradient in the mean molecular weight (Langer, Fricke and Sugimoto, 1983). It regulates the chemical gradient at the core envelope interface in massive stars, thereby sensitively influencing their post-main sequence radius evolution (Langer, 1991; Stothers and Chin, 1992; Langer and Maeder, 1995). Finally, rotationally induced mixing may affect the evolution of massive stars, at least for the fraction of them that rotates rapidly (Maeder and Meynet, 2000; Heger, Langer and Woosley, 2000; Yoon, Langer and Norman, 2006). These mixing processes will not only affect the evolution of the surface properties of massive stars, but also determine their internal structure and are therefore important, e.g., for creating realistic pre-supernova models.

Unfortunately, the efficiency of these internal mixing processes is difficult to to gauge from first principle multi-dimensional calculations (Merryfield, 1995; Grossman and Taam, 1996; Canuto, 1999a; Zaussinger and Spruit, 2013). At the same time, even when the influence of mass loss on the evolution can be neglected, it also appears as a humongous task to derive solid observational constrains, as all three processes may act at the same time. We therefore combine our analysis with the results obtained by Schootemeijer and Langer (2018), who studied the Wolf-Rayet stars in the SMC. They found that the progenitor stars of apparently single Wolf-Rayet stars contain an about ten times steeper hydrogen/helium

(H/He) gradient than the one emerging during core hydrogen burning due to the retreating convective core.

Here, we computed 66 model grids with 11 initial masses per grid, i.e., a total of 726 evolutionary sequences. We varied the assumptions on the efficiency of overshooting, semiconvection, and, by choosing different initial rotational velocities, of rotationally induced mixing. We then explored which combinations of mixing efficiencies lead to models that are consistent with observational constraints.

In Sect. 3.2, we explain which method we used to obtain our results, which are presented in Sect. 3.3. In Sect. 3.4 we compare our results with earlier work. We interpret the further implications of observed blue and red supergiant populations on the efficiency of overshooting and semiconvection in Sect. 3.5. In Sect. 3.6 we discuss the robustness of our results and finally we present the conclusions of our work in Sect. 3.7.

3.2 Method

We used MESA (Paxton, Bildsten, Dotter et al., 2011; Paxton, Cantiello, Arras et al., 2013; Paxton, Marchant, Schwab et al., 2015; Paxton, Schwab, Bauer et al., 2018) to simulate our grid of stellar evolution models. MESA is a one-dimensional stellar evolution code that solves the stellar structure equations. For the physics assumptions we followed Schootemeijer and Langer (2018), who in turn have adopted a.o. the SMC chemical composition and wind mass loss recipe from Brott, de Mink, Cantiello et al. (2011). Below, we highlight the most important physics assumptions.

The wind mass loss recipe depends on the temperature $T_{\rm eff}$ and surface hydrogen mass fraction $X_{\rm s}$. For hot stars ($T_{\rm eff} > 25\,$kK) that are hydrogen rich ($X_{\rm s} > 0.7$) we adopted the prescription of Vink, de Koter and Lamers (2001). For hot hydrogen-poor stars ($X_{\rm s} < 0.4$) we used the wind of Hamann, Koesterke and Wessolowski (1995) divided by ten. We linearly interpolated between the predicted $\log \dot{M}$ given by both prescriptions in case $0.4 < X_{\rm s} < 0.7$. For cold stars we used the prescription from Nieuwenhuijzen and de Jager (1990). Due to its high opacity, iron is the main driver of stellar winds. Therefore, we scaled the winds to the iron abundance rather than the metallicity Z. The stellar winds thus scale as $\dot{M} \propto (X_{\rm Fe}/X_{\rm Fe,\odot})^{0.85}$, where the factor 0.85 is the metallicity dependence found by Vink, de Koter and Lamers (2001). Here, $X_{\rm Fe,\odot} = 0.00124$ (Grevesse, Noels and Sauval, 1996).

The initial composition of our models is based on various observations. The iron mass fraction $X_{\rm Fe,\,SMC}$ follows from Venn (1999), who found that $[{\rm Fe/H}]_{\rm SMC} = -0.4$. The mass fractions from the elements C, N, O, and Mg are those as listed in Brott, de Mink, Cantiello et al. (2011). The helium mass fraction (Y) is 0.252. Finally, the hydrogen mass fraction is calculated as $X = 1 - Y - Z$.

We adopted the Ledoux criterion for convection. In regions where convective mixing occurs, we employed standard mixing-length theory (Böhm-Vitense, 1958) with mixing-length parameter $\alpha_{\rm MLT} = 1.5$. In regions that are Schwarzschild unstable to convection but possess a stabilizing mean molecular weight (μ) gradient, we assumed semiconvective mixing to occur. The efficiency of semiconvective mixing in our models is controlled by the scaling factor $\alpha_{\rm sc}$ (Langer, Fricke and Sugimoto, 1983). We explore the range $\alpha_{\rm sc} = 0.01, \ldots, 300$. Mixing above hydrogen-burning convective cores is implemented via a step overshooting parameter. The mixing region extends $\alpha_{\rm ov}$ pressure scale heights above the convective core. Here, we explore the range $\alpha_{\rm ov} = 0.0, \ldots, 0.55$. The range of initial masses that we explored is $M = 9, \ldots, 100\,{\rm M}_\odot$.

We investigated which spatial and temporal resolution gives the most consistent results. We found that relatively high spatial resolution (`mesh_delta_coeff = 0.3` in MESA lingo) and relatively low time resolution (`varcontrol_target = 7d-4`) accomplish this. Our results appear to be not affected by the resolution in the non-rotating case. It is known that different numerical choices, for a.o. time resolution,

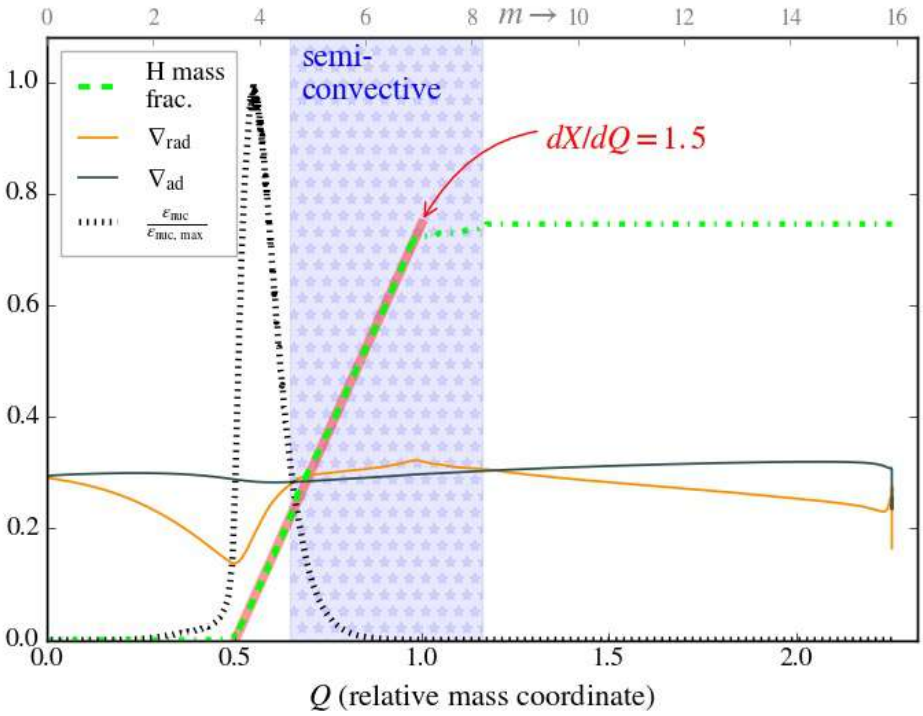

Figure 3.1: Various quantities of our 16 $M_\odot$ stellar model computed with $\alpha_{ov} = 0.11$ after core hydrogen depletion as function of the internal mass coordinate. The model is undergoing hydrogen shell burning, as indicated by the relative rate of nuclear energy production (black dotted line). The hydrogen mass fraction is shown in green. The part of the hydrogen profile that was used to fit the hydrogen gradient dX/dQ (see main text) is shown with a dashed line, the rest with a dot-dashed line. The resulting fit is shown as a straight red line. The semiconvective region, where the radiative temperature gradient ∇_{rad} exceeds the adiabatic temperature gradient ∇_{ad} in the presence of a stabilizing mean molecular weight gradient, is shaded in blue.

affect the exact amount of rotational mixing that takes place (Lau, Izzard and Schneider, 2014). Therefore, we choose the MESA standard value for our models including rotation (`varcontrol_target = 1d-4`.)

As an example of how we measure the slope of the H/He-gradient, we show a model from our grid in Fig. 3.1 that has just exhausted hydrogen in its core. The retreat of the convective core during the main sequence evolution has left a nearly linear hydrogen gradient, which is well represented by a slope with $dX/dQ = 1.5$. Here, Q is a relative mass coordinate with $Q = 1$ corresponding to the point where the slope dX/dQ reaches the initial hydrogen mass fraction of the star: $X = X_{ini}$ (red line in Fig. 3.1 – see Schootemeijer and Langer, 2018).

Our evolutionary sequences are discontinued upon core helium exhaustion ($Y_c = 0.01$). Stars in later, short-lived burning phases are not expected to constitute a significant fraction of massive star populations. While we do not compute binary models, we discuss the potential impact of this omission in Sect. 3.6.

3.3 Results

Below, we investigate in Sect. 3.3.1 the main effects that overshooting and semiconvection have on the evolution of massive star models in the Hertzsprung-Russell diagram (HRD). Subsequently, we discuss in more detail how overshooting, semiconvection and rotational mixing affect the internal chemical profiles

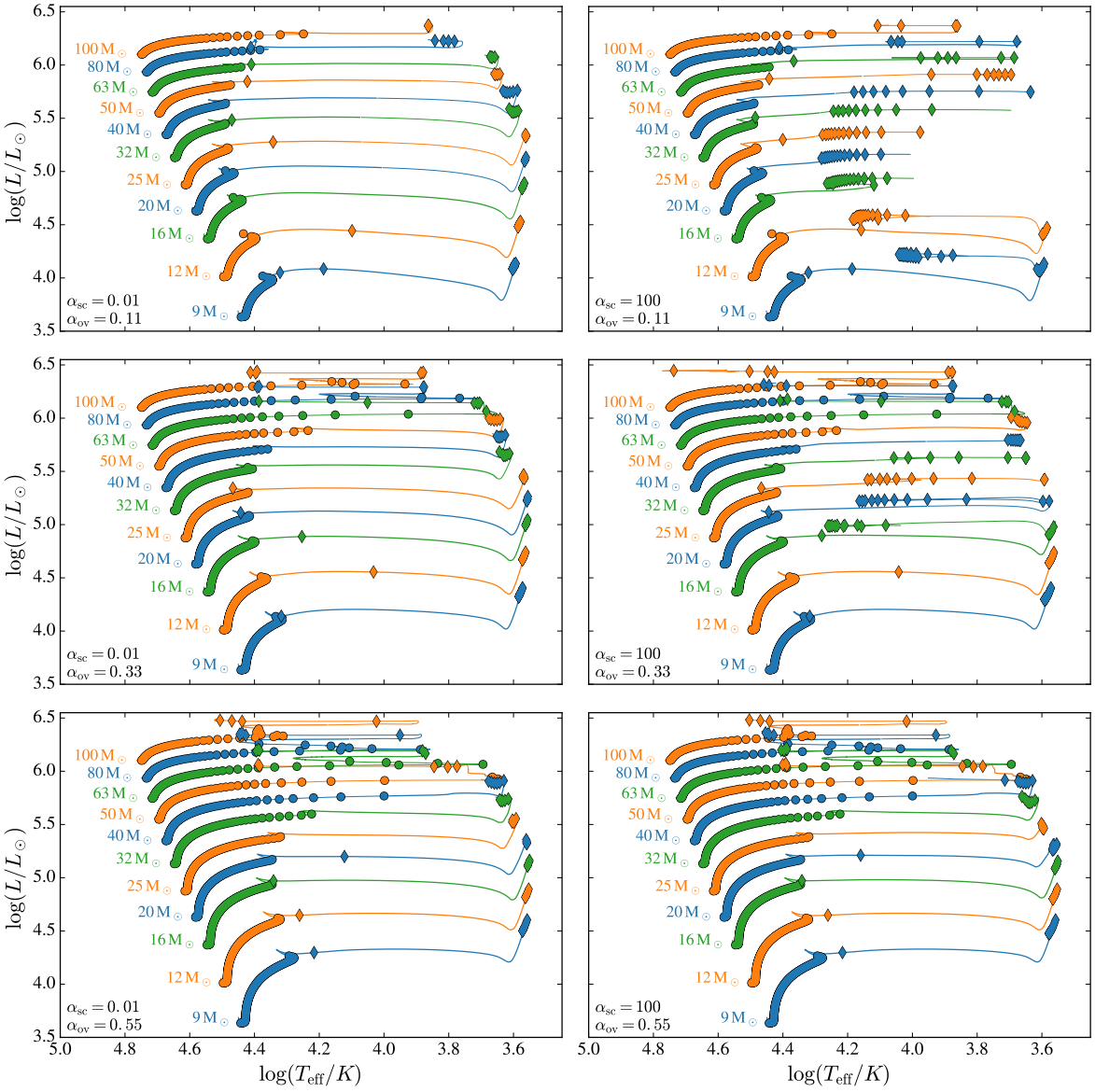

Figure 3.2: Evolutionary tracks in the Hertzsprung-Russell diagram for models computed with different efficiencies of overshooting and semiconvective mixing, from core hydrogen ignition to core helium exhaustion. The left panel shows models computed with inefficient semiconvective mixing (α_{sc} = 0.01) for three different overshooting parameters (α_{ov} = 0.11, 0.33, and 0.55), while the right panels show models computed with efficient semiconvection (α_{sc} = 100), for the same three different values of the overshooting parameter. The time difference between two neighboring markers on a track is 50 000 yr. Rotational mixing was not included in these models.

of our models in Sect. 3.3.2.

3.3.1 Effects of mixing on the evolution in the HR diagram

3.3.1.1 Main sequence evolution

The main mixing processes that play a role during the main sequence evolution are convection, overshooting, and rotational mixing. Semiconvection becomes important only after the main sequence stage (we elaborate on this in Sect. 3.3.2). As is well known (e.g., Cloutman and Whitaker, 1980), mixing of layers above the convective core increases the main sequence lifetime and allows stars to end core hydrogen burning at lower surface temperatures and higher luminosities. In most evolutionary models in the literature, such mixing is assumed to be due to core overshooting, but rotational mixing can have a similar effect (see e.g. Heger, Langer and Woosley, 2000). The effects of overshooting described above do emerge in Fig. 3.2, where the main sequence broadens as $\alpha_{\rm ov}$ is increased. In the same figure, it can be seen that the main sequence evolution is unaffected by the efficiency of semiconvection.

We further demonstrate the effects of overshooting and rotational mixing on the main sequence evolution in Fig. 3.3, where we display the terminal-age main sequence (TAMS) for evolutionary sequences with different initial rotation velocities (0, 225 and 375 $\mathrm{km\,s^{-1}}$). We see that rotation leads to slightly cooler TAMS temperatures, like overshooting. There are two reasons for this. First, the central mixing region is extended, although this effect is typically small in our models (cf., Sect. 3.2.4). Second, because of rotation, the temperatures decrease as a result of gravity darkening (von Zeipel, 1924). In our model sequences, this effect is stronger at the TAMS than at the zero-age main sequence (ZAMS), because during the main sequence evolution the ratio of rotational to critical rotational velocity increases. This effect is only reduced at for the highest considered masses, where stellar winds induce a spin-down of the models.

3.3.1.2 Post main sequence evolution

In many of our stellar models, the ratio of blue to red supergiant lifetime during core helium burning depends strongly on the efficiency of semiconvective mixing during the early stages of hydrogen shell burning. If such mixing is inefficient, the model sequences tend to favor red supergiant (RSG) solutions. This is illustrated in Fig. 3.2, where the left panels show that all model sequences with $\alpha_{\rm sc} = 0.01$ (i.e., very inefficient semiconvection) spend ∼all of helium core burning in a narrow effective temperature range as RSGs. In case semiconvection is very efficient ($\alpha_{\rm sc} = 100$, right panels in Fig. 3.2), the lifetime in the blue supergiant (BSG) regime is enhanced. In particular when efficient semiconvection is combined with low overshooting, our evolutionary sequences spend most of their core helium burning lifetimes as BSGs. For large values for $\alpha_{\rm ov}$, the difference between low and and high $\alpha_{\rm sc}$ vanishes, because then semiconvective regions do rarely develop in the deep hydrogen envelope. We discuss this in more detail in Sect. 3.3.2.2. Appendix B provides a figure similar to Fig. 3.2, but for more values of $\alpha_{\rm sc}$ and $\alpha_{\rm ov}$ (Fig. B1).

To further quantify how our core helium burning models spend their lives, we compute which fraction of it is spent as a RSG. Following Drout, Massey, Meynet et al. (2009), we adopt a temperature threshold for RSGs as $T < 4800\,\mathrm{K}$. The result is shown in Fig. 3.4. We find that if semiconvection is inefficient ($\alpha_{\rm sc} \leq 0.3$) or overshooting is high ($\alpha_{\rm ov} \geq 0.44$), our models tend to spend helium burning as RSGs. The only exception to this occurs at the highest masses: in that case, the more massive a star is and the larger the overshooting, the less time it spends as an RSG. The reason is that the stellar winds in these models (which become stronger with mass) are able to remove a significant fraction of the hydrogen envelope

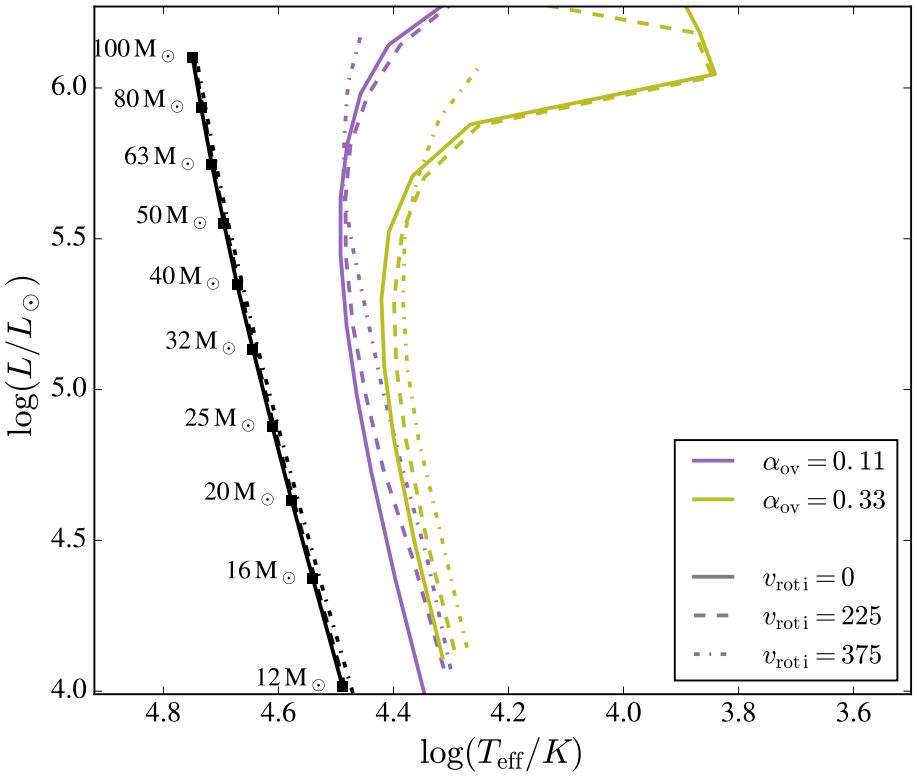

Figure 3.3: Hertzsprung-Russell diagram showing the terminal-age main sequences (TAMS) lines emerging from model grids computed with different combinations of overshooting α_{ov} and initial rotation velocity v_{roti} (in units of $\mathrm{km\,s^{-1}}$). The semiconvective mixing efficiency is fixed to $\alpha_{sc} = 1$, but the TAMS-lines are insensitive to this parameter. The black lines indicate the corresponding zero age main sequences.

(which becomes less massive with higher overshooting). If the mass of the hydrogen envelope becomes small enough, the models predict temperatures in the yellow supergiant (YSG) or BSG regime.

Models in the bottom right of the plots in Fig. 3.4, i.e., with low overshooting ($\alpha_{ov} \leq 0.22$) and efficient semiconvection, often fail to reach RSG temperatures during core helium burning. Models with efficient semiconvection and intermediate overshooting (around $\alpha_{ov} = 0.22$ or 0.33, depending om mass) spend helium burning partly as RSG and partly as BSG. This can happen in two different ways. The first possibility, which we see in models with initial masses up to $\sim 20\,M_\odot$, is that after becoming RSGs they experience a blue loop excursion. The second possibility is that stars remain blue after core hydrogen exhaustion, and only become cooler later on — as seen in some models with initial masses of $\sim 25\,M_\odot$ or more. Both behaviors are present in Fig. 3.2.

Fig. B2 in Appendix B compares the evolutionary tracks from selected model grids for models with initial rotational velocities of 225 km/s and 375 km/s. While minute differences can be seen, we find that rotation has no significant effect on the tracks for the majority of our models. We discuss this result further in Sect. 3.3.2.4.

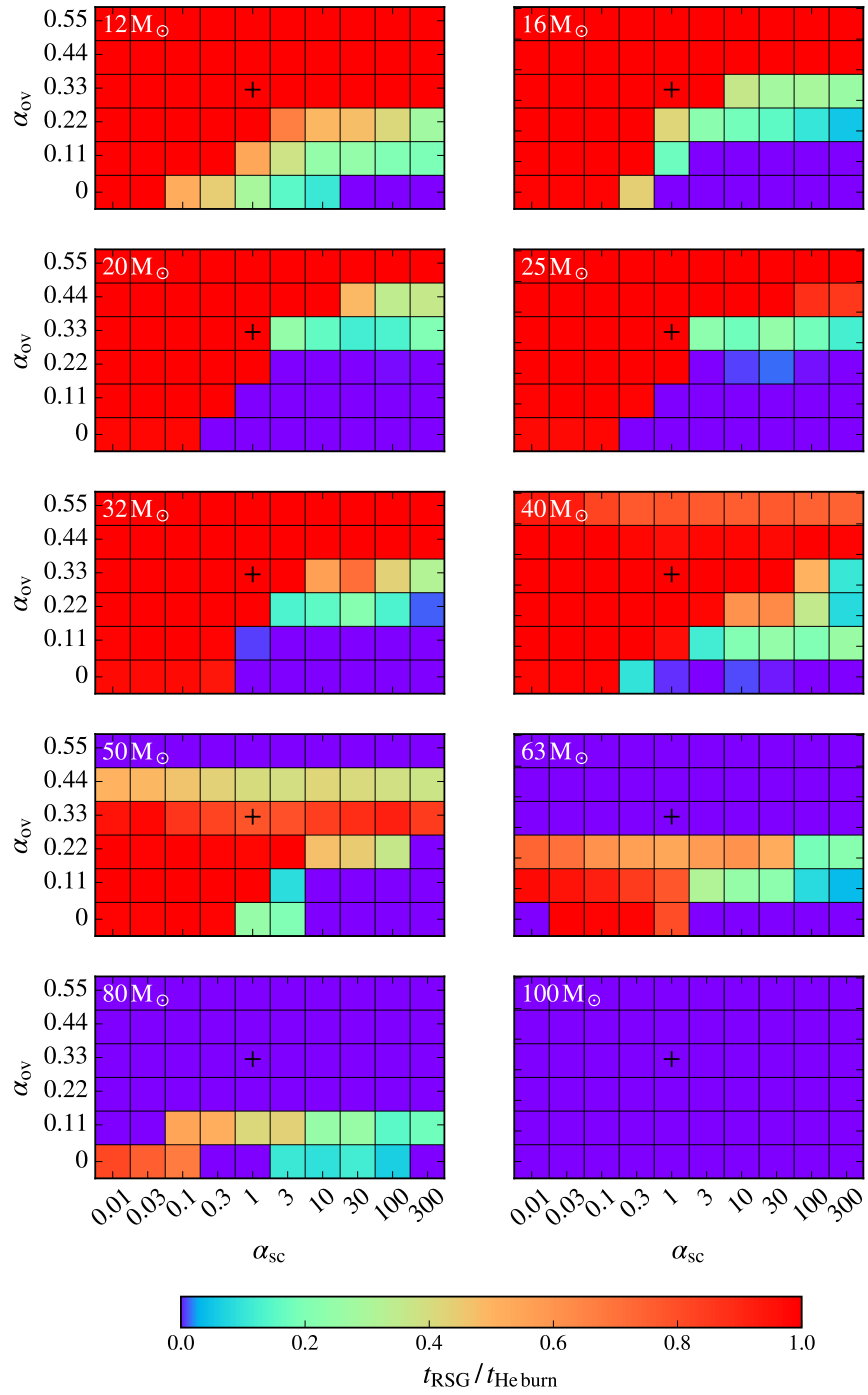

Figure 3.4: The fractional core helium burning lifetime that our model sequences spend as a red supergiant (color coded), as function of the adopted values of α_{sc} and α_{ov} in our model grids, for ten different considered initial masses. Each pixel represents one stellar evolution sequence. The cross indicates the parameters chosen in the models of (Brott, de Mink, Cantiello et al., 2011).

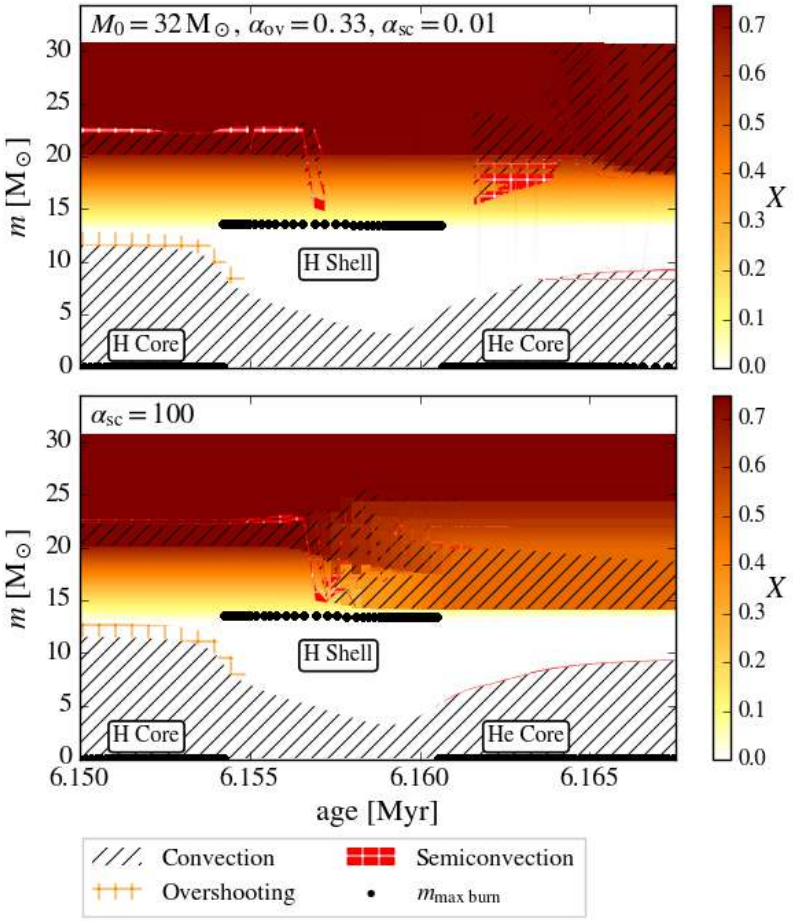

Figure 3.5: Kippenhahn diagram, showing the mass coordinate range's internal convection and semiconvection, as well as the overshooting region and the hydrogen mass fraction (color coded), as function of time, for two 32 $M_\odot$ evolutionary sequences. One is computed with inefficient semiconvective mixing (α_{sc} = 0.01; top panel), the other one computed with efficient semiconvective mixing (α_{sc} = 100; bottom panel). The displayed time interval starts near core hydrogen exhaustion and ends in the early stage of core helium burning. The overshooting parameter for both models is α_{ov} = 0.33, and rotation is not included. Black dots indicate the mass coordinate of the maximum specific nuclear energy generation.

3.3.2 The hydrogen/helium gradient

3.3.2.1 Semiconvective mixing

After core hydrogen exhaustion, massive star models show an overall contraction phase which leads to the ignition of hydrogen in a shell. At this time, which for two of our models occurs just before 6.155 Myr (Fig. 3.5, semiconvective regions form subsequently in the deep hydrogen envelope. The choice of α_{sc} determines the efficiency of this mixing process in our models. When semiconvective mixing is inefficient (top panel of Fig. 3.5, where α_{sc} = 0.01) there is no significant composition change arising in the semiconvective regions above the hydrogen burning shell. As a result, the hydrogen gradient in the deep hydrogen envelope (e.g., as shown in Fig. 3.1) remains almost unaltered this phase.

On the other hand, when semiconvective mixing is efficient (bottom panel of Fig. 3.5, α_{sc} = 100)

hydrogen gradients around mass coordinate $m = 15 \ldots 20\,M_\odot$ can quickly wash out. As a result, the criterion for semiconvection

$$\nabla_{ad} < \nabla_{rad} < \nabla_{ad} + f\,\nabla_\mu. \tag{3.1}$$

is no longer fulfilled. In the equation above, ∇_{ad} is the adiabatic temperature gradient $(d\log T/d\log P)_{ad}$, ∇_{rad} is the radiative temperature gradient and ∇_μ is the mean molecular weight gradient. Moreover, f is a factor that is equal to unity in case of an ideal gas, while it has a smaller but positive value when radiation pressure starts to play a role. We define it as $f = -\chi_\mu/\chi_T$, where $\chi_T = (d\log P/d\log T)_{\rho,\mu}$ and $\chi_\mu = (d\log P/d\log\mu)_{\rho,T}$. Ordinary convection can take place in these layers after ∇_μ has vanished. A consequence of rapid semiconvective mixing is that hydrogen-rich material is pushed close to the hydrogen-depleted core, thereby steepening the hydrogen gradient dX/dQ.

The top panel of Fig. 3.6 shows dX/dQ as a function of stellar radius R for models computed with various semiconvective efficiencies and a fixed overshooting parameter ($\alpha_{ov} = 0.33$). In sequences with the most efficient semiconvection ($\alpha_{sc} = 10, 100$) the hydrogen gradient starts to increase immediately when the star expands after the main sequence. In contrast, the model sequences with less efficient semiconvection ($\alpha_{sc} = 0.01, 0.1, 1$), have no noticeable change in their hydrogen profile right after the main sequence. During core helium burning the hydrogen gradient only increases slightly as the innermost hydrogen layers are converted into helium.

3.3.2.2 The role of overshooting

Similar to what we did in Sect. 3.3.2.1, we explore here how the efficiency of overshooting affects the evolution of the radius R and the hydrogen gradient dX/dQ. For this, we fix the semiconvection parameter to $\alpha_{sc} = 1$. The bottom panel of Fig. 3.6 shows two effects of an increasing α_{ov} on main sequence stars. First, dX/dQ becomes slightly larger (~3 instead of ~2), but not close to the dX/dQ values of ~10 or higher inferred for the apparently single WR stars in the SMC. Second, the stars can reach larger radii at the end of the main sequence. In the model sequence without overshooting, some semiconvective mixing can already occur during the main sequence, which causes a slight increase in dX/dQ.

A third effect of overshooting manifests itself after the main sequence evolution. In model sequences with large α_{ov} values, steep hydrogen gradients of $dX/dQ > 10$ do not develop. Overshooting plays a role here because it changes the shape of the hydrogen profile, which determines if and where the superadiabatic layers (i.e., where $\nabla_{rad} > \nabla_{ad}$, see Eq. 3.1) form that are required for semiconvective mixing. As found by Langer (1991), such layers are less likely to form in models with larger overshooting, and as a result, less semiconvective mixing takes place in these models.

This shows that overshooting has a strong effect on the amount of semiconvective mixing that takes place after core hydrogen exhaustion. Therefore, we consider the variation of both mixing processes simultaneously in the next section.

3.3.2.3 Semiconvection and overshooting

Here, we consider the same model grids as displayed in Fig. 3.4. Apart from the question *if* models produce steep hydrogen gradients, we also want to answer the question *when* they produce steep hydrogen gradients. This is especially important in the framework of binary interaction. Defining $(\Delta\log R)_{tot}$ as the total increase in $\log R$ from the ZAMS to the maximum stellar radius, we consider which part of this increase occurs while the hydrogen gradient fulfills the criterion $dX/dQ > 10$: $(\Delta\log R)_{dX/dQ>10}$. For example, the $\alpha_{sc} = 100$ model sequence shown in the top panel of Fig. 3.6 has a value of $(\Delta\log R)_{dX/dQ>10}\,/\,(\Delta\log R)_{tot} \approx 0.73$.

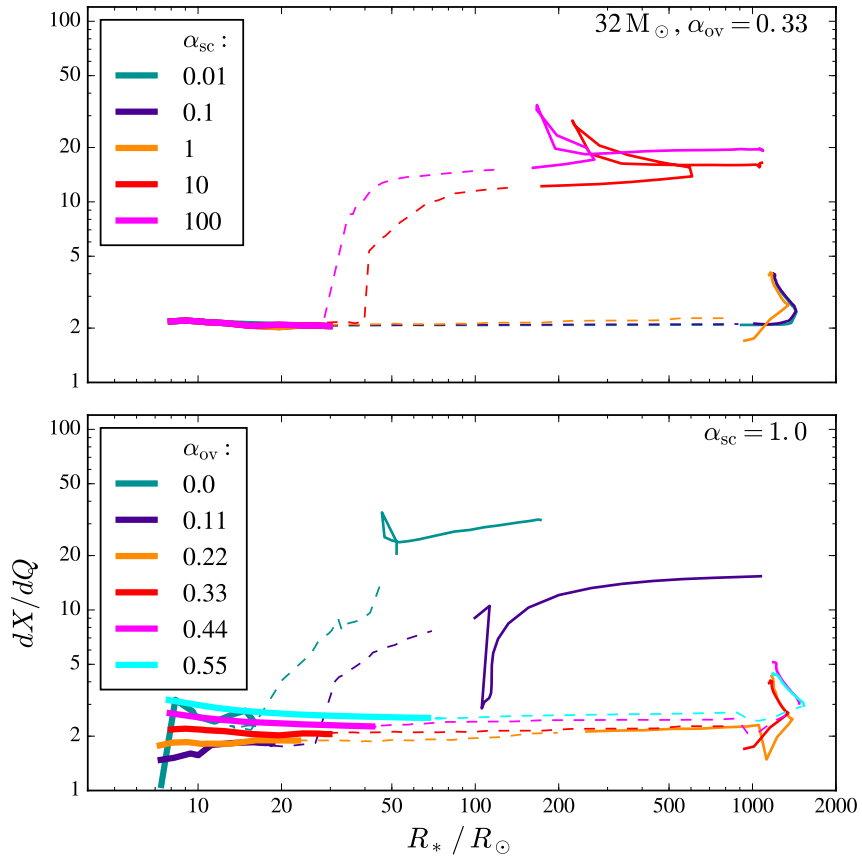

Figure 3.6: Hydrogen gradient dX/dQ (cf. Fig. 1 in Sect. 2) as a function of stellar radius for 32 $M_\odot$ sequences computed with various assumptions on internal mixing. Thick solid lines indicate core hydrogen burning, and thin solid lines indicate core helium burning. The short-lived in-between phase is displayed with a dashed line. In the top panel, $\alpha_{ov} = 0.33$ is adopted in all models while α_{sc} is varied. In the bottom panel, all models are computed with $\alpha_{sc} = 1$ while α_{ov} is varied.

Fig. 3.7 shows that the majority of model sequences either never develop a steep hydrogen gradient (blue pixels) – this is the case for practically all models with $\alpha_{sc} \leq 0.3$ as well as for almost all models with $\alpha_{ov} \geq 0.44$ – or they do so rather early during their post main-sequence expansion (red pixels). Only few sequences show an intermediate behavior.

Only the models with the lowest considered initial masses (12 $M_\odot$ and 16 $M_\odot$) behave significantly different from what is described above. None of these are able to produce hydrogen gradients of $dX/dQ > 10$ before core helium ignition. In some (for $\alpha_{sc} \geq 1$ and $\alpha_{ov} \leq 0.11$) such steep hydrogen gradients are reached during core helium burning, after the star has already expanded significantly – therefore, they represent an intermediate case. We note that masses of 16 $M_\odot$ and smaller are well below the inferred initial mass range of the SMC WR stars (Schootemeijer and Langer, 2018). Fig. 3.7 shows also that our most massive models are also less likely to develop steep hydrogen gradients.

We find that the parameter space described above, where model sequences develop steep hydrogen gradients, is strongly correlated with the parameter space where model sequences spend at least a significant fraction of their helium burning lifetime as objects hotter than RSGs (Sect. 3.3.1.2). This shows that the occurrence of the post-MS BSG phenomenon is tightly linked to internal mixing.

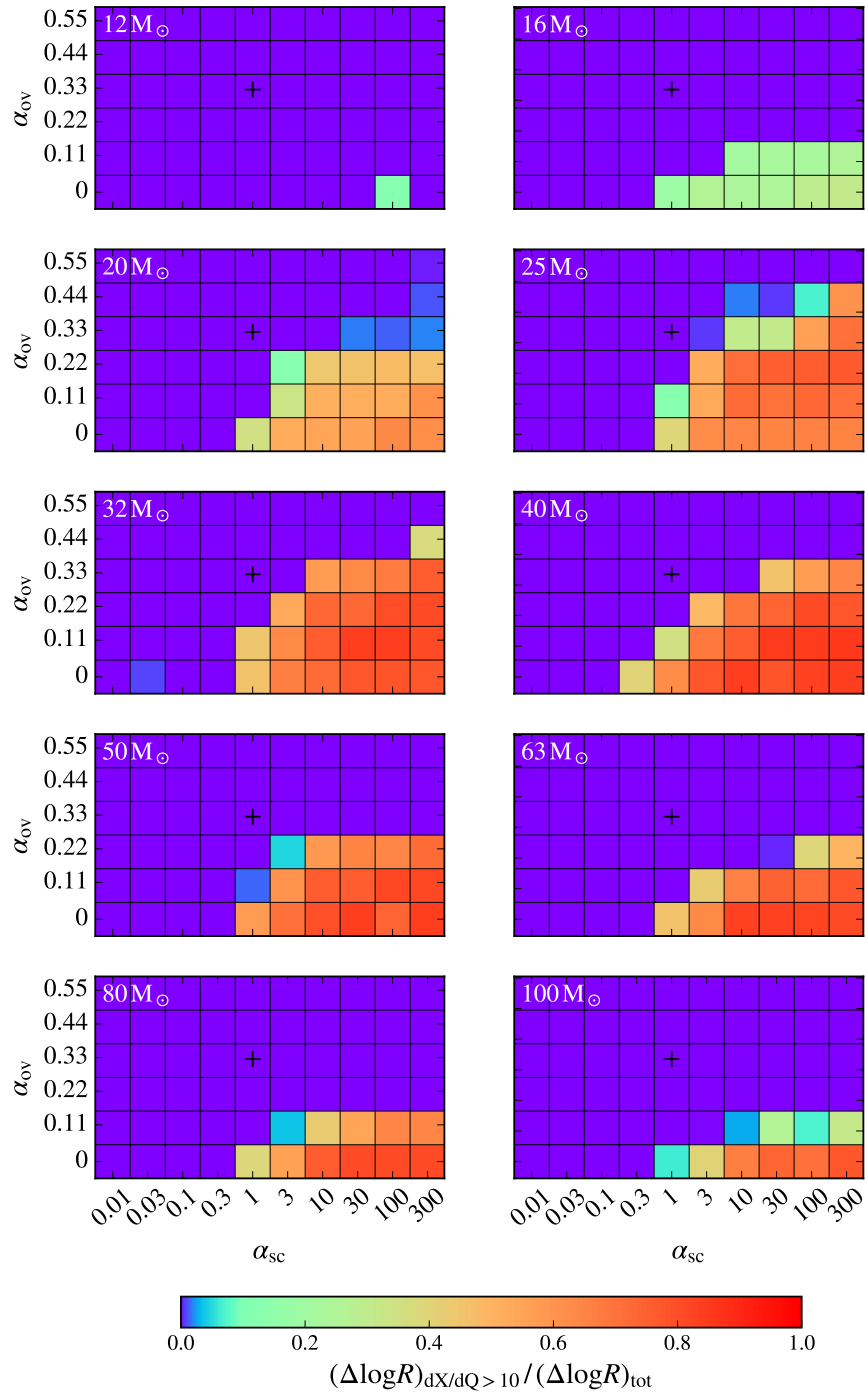

Figure 3.7: Same as Fig. 3.4, but now the color coding indicates during which fraction of the overall radius growth of a given sequence ($(\Delta \log R)_{tot}$) the internal hydrogen gradient dX/dQ exceeded a value of 10. Blue color indicates models in which the hydrogen gradient remains shallow, while red color indicates models where a steep hydrogen gradient is establshed early on.

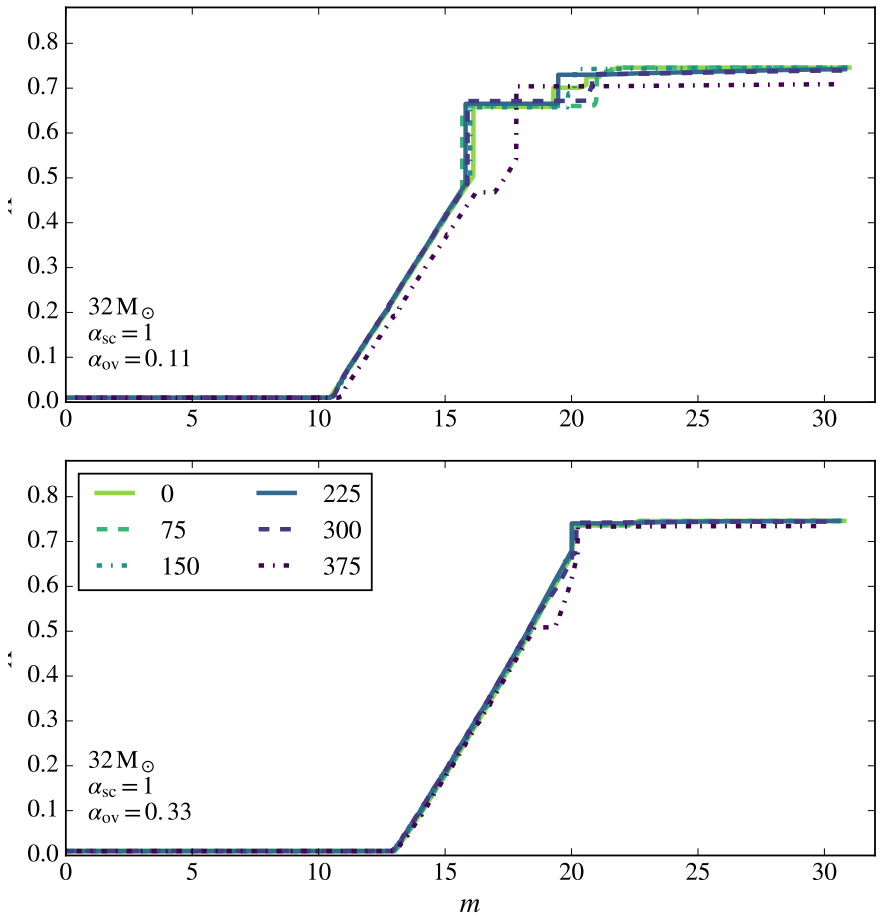

Figure 3.8: Hydrogen profiles of evolutionary models close to core hydrogen exhaustion, for six different initial rotation velocities (given in $\mathrm{km\,s^{-1}}$ in the legend). The top panel shows evolutionary models computed with an overshooting parameter of $\alpha_{\mathrm{ov}} = 0.11$, while $\alpha_{\mathrm{ov}} = 0.33$ for the models shown in the bottom panel.

3.3.2.4 Rotational mixing

Rotation is predicted to drive mixing processes in the envelopes of rapidly spinning stars (e.g. Maeder, 1987; Langer, 1992). As a result, these processes might have a non-negligible effect on the shape of the hydrogen profiles that we investigate. Therefore, we simulate a number of rotating model sequences to explore to what extent rotational mixing alters the hydrogen profile of our models.

In Fig. 3.8, we show the hydrogen profile of two sets of six models that are close to core hydrogen exhaustion ($X_{\mathrm{c}} = 0.01$). These $32\,\mathrm{M}_{\odot}$ models have initial rotation velocities of $v_{\mathrm{rot,\,i}} = 0, 75, \ldots, 375\,\mathrm{km\,s^{-1}}$, and are computed with an overshooting parameter of either $\alpha_{\mathrm{ov}} = 0.11$ (top) or $\alpha_{\mathrm{ov}} = 0.33$ (bottom). The hydrogen profiles for the same value of overshooting are very similar. Only for the highest considered rotation velocity, $v_{\mathrm{rot,\,i}} = 375\,\mathrm{km\,s^{-1}}$, a modest difference emerges.

O stars rotating with velocities of $375\,\mathrm{km\,s^{-1}}$ appear to be rare in the SMC. A study of 31 stars in the SMC cluster NGC 346 by Mokiem, de Koter, Evans et al. (2006) shows that less than only one in five stars has a projected rotational velocity above $v \sin i > 200\,\mathrm{km\,s^{-1}}$. Furthermore, extreme rotators are predicted to evolve quasi-chemically homogeneously (e.g. Yoon and Langer, 2005; Brott, de Mink,

Cantiello et al., 2011), in which case no sizable hydrogen gradient is expected. In conclusion, rotational mixing as implemented in our models does not appear to be a major factor in determining the shape of the chemical profile for the majority of stars and thus, it should not be a major factor in both the formation of steep hydrogen gradients and in post main sequence evolution. To illustrate the latter point, Fig. B2 in Appendix B compares HRDs in which the evolutionary models have different initial rotation velocities.

3.4 Comparison with earlier work

Many of our physics assumptions are similar to the ones used by Brott, de Mink, Cantiello et al. (2011), who adopted a semiconvection parameter of $\alpha_{\rm sc} = 1$, and who calibrated the overshooting parameter based on data from the FLAMES Survey of Massive Stars (Hunter, Lennon, Dufton et al., 2008) for stars of 16 $M_\odot$, for which they found $\alpha_{\rm ov} = 0.335$. Unsurprisingly, the post main sequence evolution of these models and ours with the same $\alpha_{\rm sc}$ and $\alpha_{\rm ov} = 0.33$ is very similar – both promptly ascend the red giant branch and do not experience blue loops. Also, in both sets of models, the smallest initial mass for which the TAMS bends to the coolest effective temperatures due to envelope inflation near the Eddington limit (Sanyal, Grassitelli, Langer et al., 2015) is about 60 $M_\odot$.

Often in previous evolutionary calculations of massive star models, the Schwarzschild criterion has been adopted for convection. This assumption implies that stabilizing mean molecular weight gradients are not taken into account, which is equivalent to semiconvection leading to mixing as efficient as convection. Therefore, such evolutionary models might behave similar to our models for which we have used the largest semiconvective efficiency, i.e., $\alpha_{\rm sc} = 300$. For example Charbonnel, Meynet, Maeder et al. (1993) and and Meynet, Maeder, Schaller et al. (1994) have published models using the Schwarzschild criterion, in combination with an overshooting parameter of $\alpha_{\rm sc} = 0.2$. Georgy, Ekström, Eggenberger et al. (2013) produced similar models, but adopted $\alpha_{\rm sc} = 0.1$. Below we compare the post main sequence evolution of their models low metallicity models with our results.

We find that the post-main sequence radius evolution of our $\alpha_{\rm sc} = 300$, $\alpha_{\rm ov} = 0.22$ models is indeed similar to that of the $\alpha_{\rm ov} = 0.2$ models of Charbonnel, Meynet, Maeder et al. (1993) and Meynet, Maeder, Schaller et al. (1994). In both cases, model sequences with initial masses up to $15 - 16\,M_\odot$ produce RSGs during core helium burning. This corresponds to an RSG upper luminosity of $\log\left(L/L_\odot\right) = 5.0$. More massive models, at least up to $30 - 40\,M_\odot$, never reach RSG temperatures, or only in the very final moments of helium core burning.

Georgy, Ekström, Eggenberger et al. (2013) provide models sequences ($\alpha_{\rm ov} = 0.1$) with and without rotation. Similar to what we describe above, the general behaviour of the non-rotating models is very similar to that of our $\alpha_{\rm sc} = 300$, $\alpha_{\rm ov} = 0.11$ model sequences.

A comparison of models including rotation is more difficult, as different implementations of the angular momentum and chemical transport processes are used in different groups. Following Heger, Woosley and Spruit (2005) and Suijs, Langer, Poelarends et al. (2008), we include the angular momentum transport by magnetic fields as suggested by Spruit (2002). As a consequence, our models remain close to rigid rotation during the main sequence evolution, making Eddington-Sweet circulations the dominant mixing process. A very similar treatment of rotation is implemented in the MESA code (Paxton, Cantiello, Arras et al., 2013). As we have shown above, except for a slight reduction of the slope of the hydrogen gradient, the effects of rotational mixing remain rather limited unless very fast rotation is considered.

Georgy, Ekström, Eggenberger et al. (2013), as well as Chieffi and Limongi (2013) and Limongi and Chieffi (2018) neglect magnetic fields. In their models, the shear instability dominates the transport of elements in radiative zones of the stellar models. Martins and Palacios (2013), Choi, Dotter, Conroy et al. (2016), Markova, Puls and Langer (2018) and and Limongi and Chieffi (2018) compare such models

with those of Brott, de Mink, Cantiello et al. (2011) for Galactic metallicity, and find that more helium is mixed out of the core into the hydrogen-rich envelope in this case. As a consequence, larger helium core masses are produced, similar to the effect of convective core overshooting, as well as shallower hydrogen gradients. The finding of Georgy, Ekström, Eggenberger et al. (2013) that their rotating and non-rotating models at $Z = 0.002$ remain BSGs during essentially all of core helium burning (see their Fig. 14) is consistent with their use of the Schwarzschild criterion for convection. The non-rotating models of Limongi and Chieffi (2018) appear to produce mostly RSGs, as they employ the Ledoux criterion and inefficient semiconvection. With increasing rotation, the fraction of their models spent in the BSG regime appears to increase in the mass range $15 \ldots 25\,M_\odot$ (cf., their Fig. 14), in line with the additional rotational mixing in semiconvection zones mimicking a larger semiconvective mixing efficiency.

While our analysis of the literature results must remain tentative, it does support the general idea that the core mass and the H/He-gradient at the core-envelope interface are the dominant factors in determining the post-main sequence radius evolution of massive star. This underlines the view that our results are meaningful beyond the particular parametrization of the individual mixing process chosen for the models of our new stellar evolution grids.

3.5 Observational constraints

Above, we have described in which way the various considered internal mixing processes affect the observable stellar properties, i.e., the evolution of the models in the HR diagram and the internal H/He gradient. In this section, we attempt to find observational constraints which allow to rule out certain classes of models, and thereby constrain the efficiency of the internal mixing processes.

3.5.1 Main sequence stars

The occurrence of semiconvection during the main sequence evolution of massive stars has been studied by, e.g., Chiosi and Summa (1970), Chiosi, Nasi and Sreenivasan (1978) and and Langer, El Eid and Fricke (1985), who showed that while semiconvection can occur prominently, the evolution of the models during this stage is hardly affected by the choice of the semiconvective mixing efficiency. Therefore, we concentrate here on the discussion of the effect of convective core overshooting, whose main effect is moving the location of the TAMS to cooler effective temperatures in the HR diagram (e.g. Maeder and Meynet, 1988; Prantzos, Doom, Arnould et al., 1986; Stothers and Chin, 1992).

To find valid constraints on convective overshooting for massive stars has proven difficult, since the isochrone method used for low and intermediate mass stars (Maeder and Meynet, 1991) can not be used due to a lack of populous young star clusters. Brott, de Mink, Cantiello et al. (2011) used the distribution of rotational velocities to conclude that around $16\,M_\odot$, the overshooting parameter should be close to $\alpha_{ov} = 0.33$.

By studying all the Galactic massive stars for which parameters have been determined through a detailed model atmosphere analysis, Castro, Fossati, Langer et al. (2014) could compare their observable parameters with the predictions of stellar evolution models. They confirmed a value of $\alpha_{ov} = 0.33$ near $16\,M_\odot$ from their data, but found that smaller values would be preferred for smaller initial masses, and larger ones for higher masses. Using their result, Grin et al. (in prep.) found that the best fit to the empirical TAMS of Castro, Fossati, Langer et al. (2014) is obtained for an increasing overshooting with mass such that $\alpha_{ov} = 0.2$ at $8\,M_\odot$ up to $\alpha_{ov} = 0.5$ at $20\,M_\odot$, with a constant value for higher masses.

In a recent study, Castro, Oey, Fossati et al. (2018) analyzed the population of SMC OB field stars as observed within the RIOTS4 survey (Lamb, Oey, Segura-Cox et al., 2016). They could derive a tentative

TAMS, which agrees well with that of the Brott, de Mink, Cantiello et al. (2011) SMC models using $\alpha_{ov} = 0.335$ while also finding some hints of a mass dependence.

Given the similarity between our models and the models of Brott, de Mink, Cantiello et al. (2011), we conclude that, for the considered mass range values of the overshooting parameter between $\alpha_{ov} = 0.2$ and $\alpha_{ov} = 0.5$ appear to be supported by observations.

3.5.2 Red supergiant luminosities

Both Levesque, Massey, Olsen et al. (2006) and Davies, R.-P. Kudritzki, Plez et al. (2013) show that the SMC RSG population extends up to a luminosity limit of $\log(L/L_\odot) \approx 5.3 - 5.4$. Earlier studies (e.g., Massey and Olsen, 2003) reported a higher luminosity cut-off. However, the inferred temperatures have since been revised upwards, resulting in smaller bolometric corrections and hence lower luminosities. The most recent SMC study of RSG luminosities by Davies, Crowther and Beasor (2018), who integrated photometric fluxes in a wide wavelength range to obtain the luminosity, also found a cutoff around $\log(L/L_\odot) \approx 5.4$. The latter study used a large sample including ~150 RSGs with $\log(L/L_\odot) > 4.7$). They found that evolutionary tracks of Georgy, Ekström, Eggenberger et al. (2013) predict an excess of luminous RSGs.

In Fig 3.9, we compare the distribution of Davies, Crowther and Beasor (2018) to our theoretical predictions for different α_{sc} and α_{ov} combinations, under the assumption that there are ~300 helium burning stars in the SMC with $\log(L/L_\odot) > 4.7$. We obtain this number by adding the number of 150 BSGs (see Sect. 3.5.3) in this luminosity range to the 150 RSGs in the sample of Davies, Crowther and Beasor (2018). Although uncertain, the real number should be accurate up to at least a factor of a few: it could be a lower due to foreground contamination, or a higher due to to incompleteness of the sample, in particular for the BSGs. Because of these uncertainties, we emphasize that a distribution shown in Fig. 3.9 can still be a good fit even if it needs to be scaled up or down be a reasonable amount. To be consistent with Davies, Crowther and Beasor (2018), we make the division between RSGs and hotter objects at 7 kK.

Fig. 3.9 shows that largest discrepancy between the observed RSG luminosity distribution and the predictions occurs for efficient semiconvection and the lowest overshooting, where hardly any RSGs are produced (see also Fig. 3.4). There, the RSG fraction $f_{RSG} = N_{RSG}/(N_{RSG} + N_{BSG})$ is of the order of a few up to ten per cent, which would imply that on the order of 1500-5000 BSGs would need to be present in the SMC given that 150 RSGs are observed. Such a large BSG population would rival the entire SMC in terms of total luminosity. Davies, Crowther and Beasor (2018) compare with tracks of Georgy, Ekström, Eggenberger et al. (2013) where the Schwarzschild criterion for convection (which translates into extremely efficient semiconvection) and $\alpha_{ov} = 0.1$ are assumed. Indeed, when we trace the progenitor evolution of the RSG models that were considered we find that ~5000 BSG progenitors of the 150 RSGs should be present based on lifetime arguments.

In model sequences where little semiconvective mixing occurs (i.e., where α_{sc} is low and/or α_{ov} is high), the mismatch in Fig. 3.9 between observations and model predictions is less striking. The steepness of the drop of the number of RSGs with increasing luminosity could be mostly reflecting the IMF, and can be well matched by the models. However, for luminosities above $\log(L/L_\odot) > 5.3$, essentially no RSGs are observed (Davies et al. list one RSG at $\log(L/L_\odot) \simeq 5.4$, and one more at $\log(L/L_\odot) \simeq 5.6$), most of our model grids predict some tens of RSGs.

However, there is a limited range of mixing parameters which might be compatible with the observed paucity of luminous RSGs. We see in Fig. 4 that the in the mass range from 12 to 25 $M_\odot$ for efficient semiconvection, that the pure BSG solutions prevails for larger overshooting at higher mass. Therefore, if nature had chosen for, e.g., $\alpha_{ov} = 0.22$ and $\alpha_{sc} = 100$, there would be a gap in the luminosity distribution

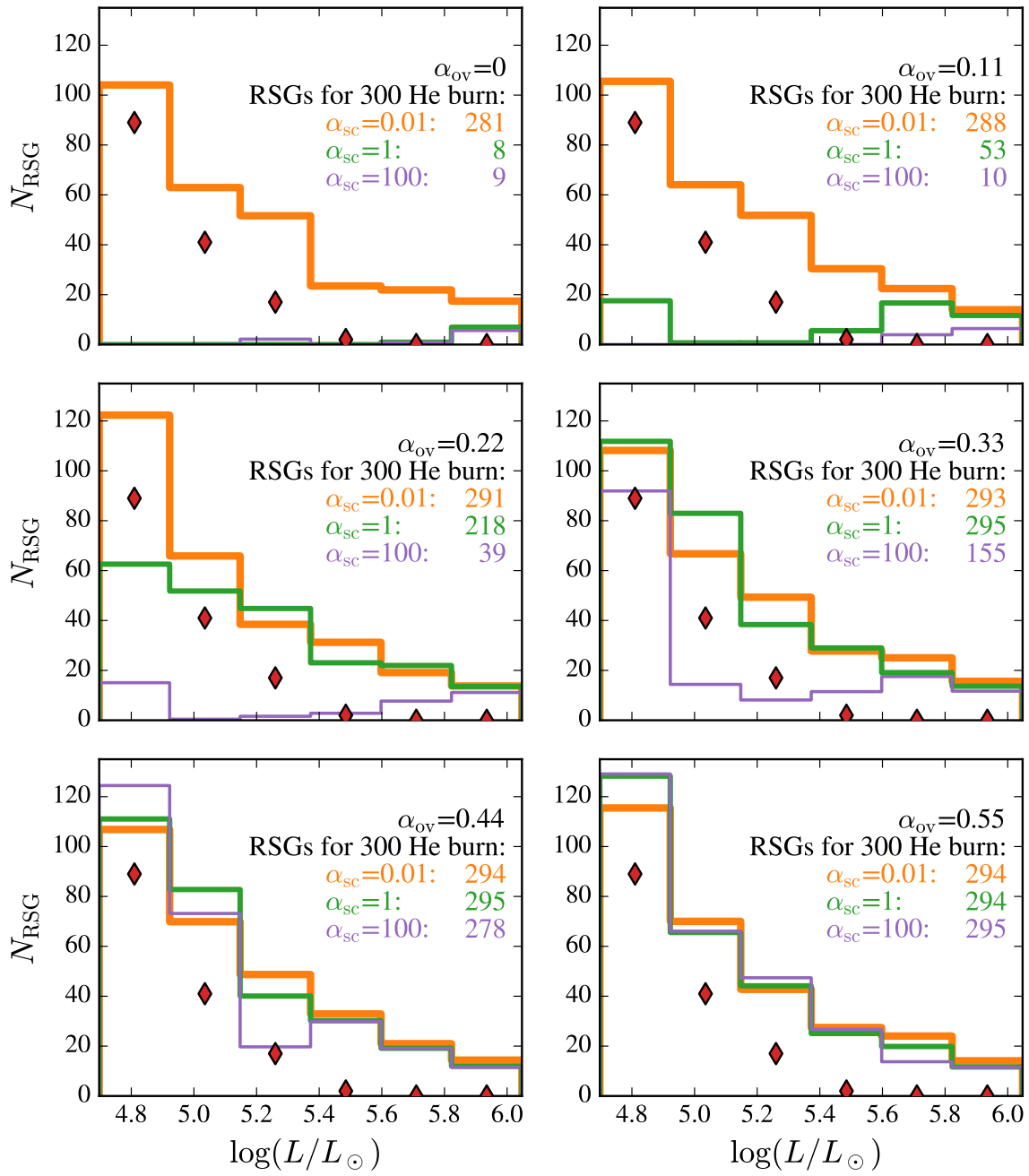

Figure 3.9: Diagrams showing the predicted luminosity distribution of red supergiants in the SMC. Each of the six diagrams has a different value for the overshooting parameter α_{ov}. The red diamonds indicate the number of red supergiants observed by Davies, Crowther and Beasor (2018).

of RSGs, because stars with initial masses above 20 $M_\odot$ would never become RSGs. Fig. B1 shows several such luminosity gaps for low overshooting and high semiconvection parameters, and Fig. B2 shows that such gaps also prevail in our models which include rotational mixing.

In most of our grids, we find models above ~40 $M_\odot$ to evolve to cool effective temperatures. However, corresponding stars in that state might be rare, due to lifetime and IMF effects, and they do not populate the classical RSG branch but are somewhat hotter. Also, we consider the mass loss rates for such objects as very uncertain, such that changes in the mass loss rates might also remove such very bright and cool models.

It remains remarkable that the range in mixing parameters which offers a tentative solution of the RSG luminosity problem described in Davies, Crowther and Beasor (2018) has a significant overlap with the parameter ranges favored by other observational constraints.

3.5.3 Blue supergiants

The shape and size of the the BSG population in the SMC appears to be more uncertain than for the case of the RSG population. For our analysis, we combine the two samples of ~100 A-type supergiants from Humphreys, R. P. Kudritzki and Groth (1991) and ~50 B-type supergiants of Kalari, Vink, Dufton et al. (2018). These samples should in principle span the entire temperature range of BSGs. We consider the same luminosity range as for RSGs (Sect. 3.5.2). However, observational studies presented by Blaha and Humphreys (1989) and Evans, Lennon, Smartt et al. (2006) also contain some tens of objects in our temperature range of interest – thus, depending on the amount of overlap and other biases, the above number of BSGs could be seen as a lower limit.

Fig. 3.10 shows that in synthetic populations where efficient semiconvective mixing does not take place (e.g., if $\alpha_{sc} = 0.01$ or $\alpha_{ov} \geq 0.44$), the BSG population is negligible. This seems to be at odds with aforementioned observations. For the opposite case, e.g., where $\alpha_{sc} = 100$ and $\alpha_{ov} \leq 0.22$, almost all helium burning stars should be BSGs. While, given the uncertainties described above, this evolutionary scenario could still agree with the observed BSG population, it is clearly challenged by the presence of the observed RSG population (Sect. 3.5.2). For constant overshooting, we conclude that the synthetic population with $\alpha_{sc} = 100$ and $\alpha_{ov} = 0.33$ performs best on simultaneously explaining the RSG and BSG populations in the SMC.

While these values might provide the most satisfying match between observations and theory, there could be a mismatch at luminosities below the range that we discussed above. The evolutionary sequences with $M_{ini} = 12\,M_\odot$ and below do not experience blue loops, while some A- and B-type supergiants are observed in the associated luminosity range. We note that for these relatively faint stars, detection biases are larger. A possible explanation is that the extent of overshooting is lower at lower initial masses, as proposed by Grin et al. (in prep. – see also Sect. 3.5.1). If that is the case, stars with lower initial masses also become BSGs (Fig. 3.2 and B1). Alternatively, these objects could have a binary origin – we discuss this in Sect. 3.6. To be able to draw any strong conclusion, a more complete observational picture is warranted.

3.5.4 Surface abundances

The nitrogen abundance at the surface of a star can be used as a probe for its evolutionary history. We illustrate this in Fig. 3.11. For stars that are approaching the red giant branch from hotter temperatures, no nitrogen enhancements are predicted by our evolutionary sequences. However, for stars that are on a blue loop excursion, it is predicted that CNO-processed material is dredged up via deep convective envelopes during the prior RSG phase. As a result, the mass fractions of helium and nitrogen on the

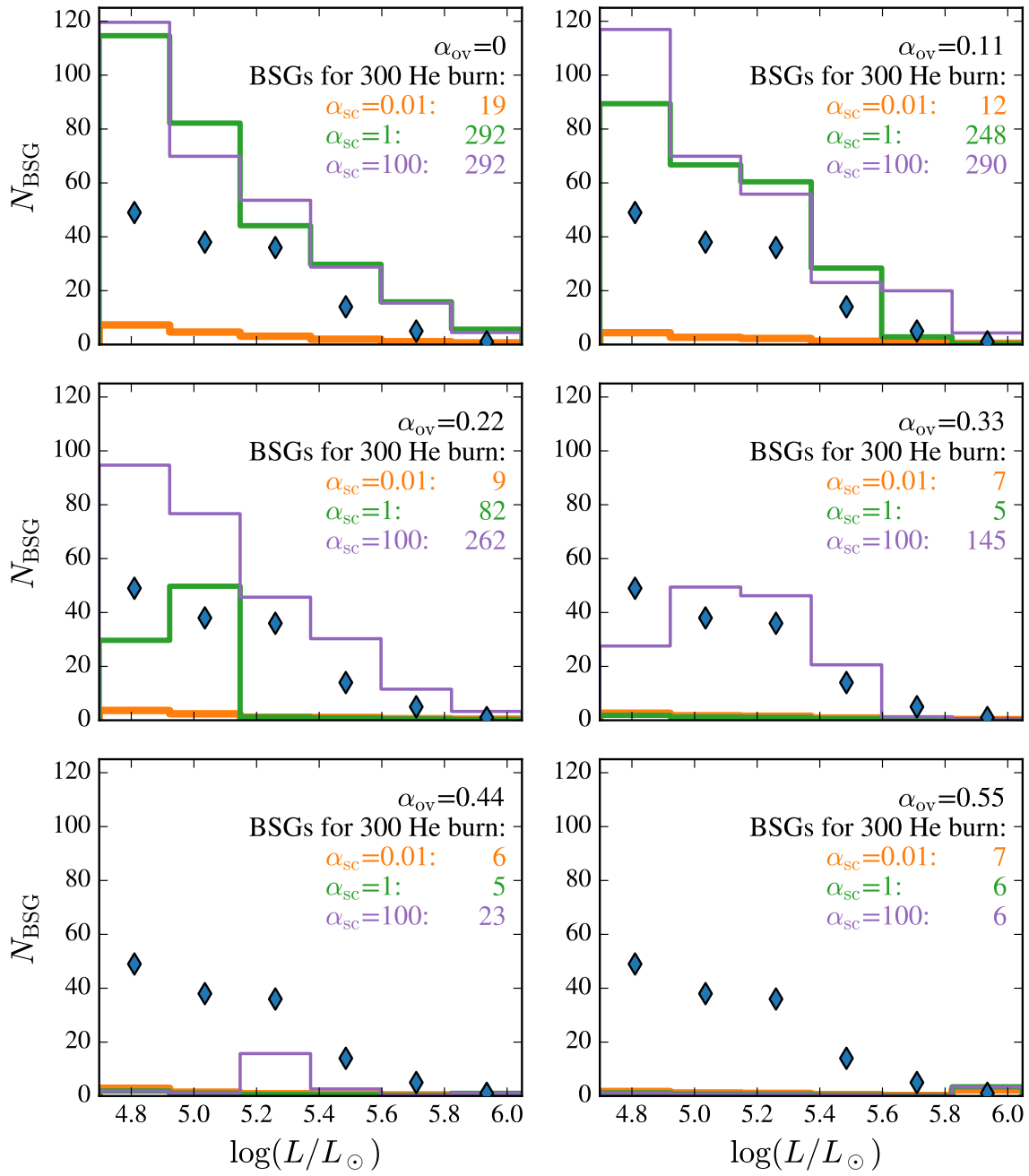

Figure 3.10: Same as Fig. 3.9, but this diagram is showing the luminosity distribution of blue supergiants. Here, blue diamonds indicate the combined number of blue supergiants observed in the SMC by Humphreys, R. P. Kudritzki and Groth (1991) and Kalari, Vink, Dufton et al. (2018).

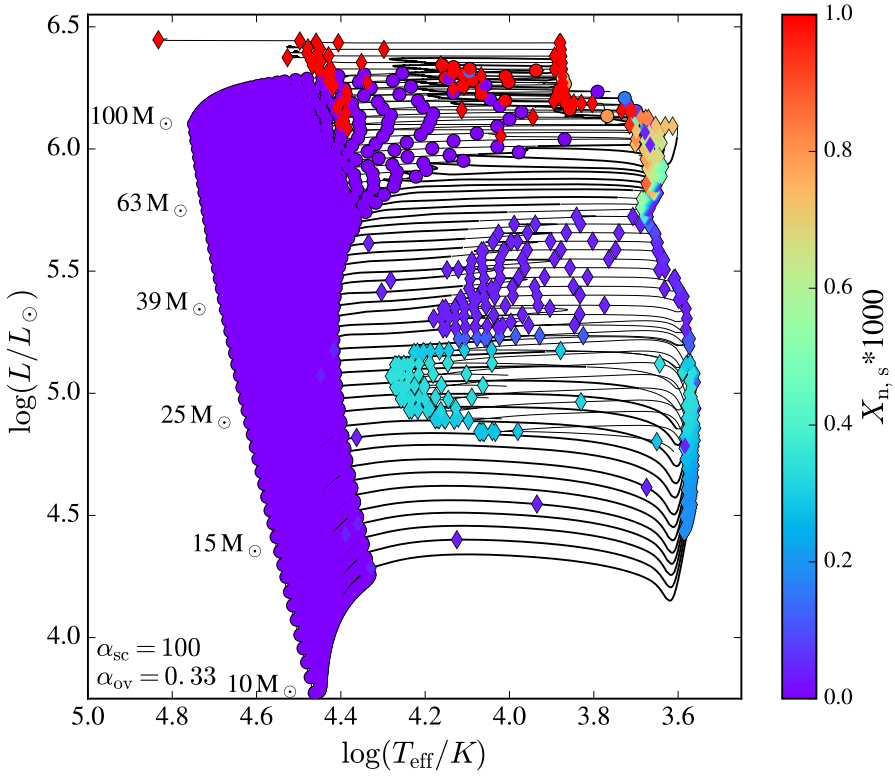

Figure 3.11: Hertzsprung-Russell Diagram showing the nitrogen surface mass fraction of our evolutionary sequences with α_{sc} = 100 and α_{sc} = 0.33. The initial masses of the shown stellar tracks are, logarithmically, evenly spaced every 0.02 dex.

surface are enhanced. This applies to the blue points in Fig. 3.11 around $\log\left(L/L_\odot\right) \approx 5$ which are also hotter than the stars on the red giant branch. The evolutionary tracks we show are those where α_{sc} = 100 and α_{ov} = 0.33, which could best explain the RSG and BSG populations.

In practice, using nitrogen abundances to constrain the evolutionary history of stars is tricky, because even on the main sequence a large fraction of stars show nitrogen enrichment (Hunter, Brott, Lennon et al., 2008; Grin, Ramirez-Agudelo, de Koter et al., 2017). This nitrogen enrichment does not, or not clearly, correlate with rotation velocity. Therefore, the origin of this nitrogen enrichment in at least a part of the main sequence stars is unknown. Thus, given that many of the main sequence progenitors of the helium burning models shown in Fig. 3.11 are somehow enriched in nitrogen, no conclusions can be drawn about a previous red giant phase (which should increase the nitrogen surface abundance through convective mixing) if their more evolved counterparts often also show nitrogen enrichment. However, the argument *does* work the other way around: stars unenriched in nitrogen should practically not be observed at temperatures below ~20 kK at luminosities lower than $10^{5.2}$ $L_\odot$ (Fig. 3.11 – the ascension of the RSG branch is about 100 times shorter lived than the blue loop phase). If stars without nitrogen enrichment would be observed in this part of the HRD, it would mean that the evolutionary models that we show in Fig. 3.11 are not valid for at least this range of temperatures and luminosities. The lack of enrichment could then be explained by internal mixing taking place – this makes for example the model sequences with lower overshooting and efficient semiconvection ascend the RSG branch more slowly (in the temperature and luminosity range discussed here – see Fig. B1). Thus, the models could be reliably

tested by measuring nitrogen abundances.

3.5.5 The most massive stars

We paid less attention to the predictions of our models for the most luminous stars. The reason is that such stars are expected to be quite rare, and there are very few solid observational constraints available at this time. In addition, even though the SMC offers the advantage of mass loss rate uncertainties being less important, this is not the case any more if we consider initial stellar masses of $60\,M_\odot$ and higher. Therefore, even when picking the model grid with the most promising mixing parameters, the models for the highest masses are not likely to be close to reality.

An exception is perhaps the core hydrogen burning phase of evolution, for which the mass loss rates are the best understood. In this respect, our prediction that the TAMS bends to very cool temperatures at luminosities below $\sim \log\left(L/L_\odot\right) = 6$ for what we identified as the most likely mixing parameters appears relatively robust. As shown in Fig. B2, this should lead to a continuous effective temperature distribution of the most luminous stars, rather than showing a pronounced post main sequence gap as visible in the grids computed with the smallest overshooting parameters.

Finally, we want to point out that with the mass loss rates assumptions adopted for our models, which are state-of-the-art but are surely uncertain for low effective temperature models, there are essentially no hydrogen-poor or hot Wolf-Rayet stars produced independent of what we assumed for internal mixing.

3.6 Discussion

3.6.1 Summarizing our results

In the sections above, we have worked out the systematic trends that occur in massive star evolution models with an SMC initial chemical composition as function of the assumption on internal mixing processes. We have seen that these mixing processes determine the core mass increase and the slope of the H/He-gradient at the core-envelope interface, which are the internal structure parameters ruling the evolution of the stars in the HRD.

We have then confronted these evolutionary models with various observational constraints. We found that for the overshooting parameter $\alpha_{\rm ov}$ – which determines the increase of the core masses – and the semiconvection parameter $\alpha_{\rm sc}$ – which is the key parameter for determining the H/He gradient – only a limited range of combinations is compatible with those observational constraints.

We have seen that the constraints on the main sequence imply a convective core overshooting corresponding to $\alpha_{\rm ov} = 0.2 \ldots 0.3$ in the considered mass range. Interestingly, larger overshooting has the consequence that the stellar tracks produce essentially no BSGs with luminosities of $\log\left(L/L_\odot\right) \lesssim 5.5$ and temperatures $\log T_{\rm eff} \lesssim 4.3$ (cf., Fig. B1). Since plenty of such stars are observed in the SMC (e.g. Blaha and Humphreys, 1989), an overshooting parameter of $\alpha_{\rm ov}$ significantly above 0.3 is excluded by two independent constraints. When the requirement of a large H/He-gradient from Schootemeijer and Langer (2018) is folded in, such a large overshooting is again ruled out. Similarly, $\alpha_{\rm ov} = 0 \ldots 0.1$ yields only BSGs for a wide range of initial masses for models where semiconvection is reasonably efficient.

Conversely, Fig. B1 shows that inefficient semiconvection ($\alpha_{\rm sc} \lesssim 1$) can be ruled out, because – independent of the amount of overshooting – far too few BSGs are produced. Again, this conclusion is reinforced by the fact that $\alpha_{\rm sc} < 1$ does not allow for steep H/He-gradients. In fact, the nearly complete overlap in the parameter space of only shallow H/He-gradients (Fig. 3.7) with the parameter space where only RSGs are produced (Fig. 3.4) reinforces the conclusion of Schootemeijer and Langer (2018) that steep H/He-gradients are observationally required and generalizes it to a wider mass range. Finally, we

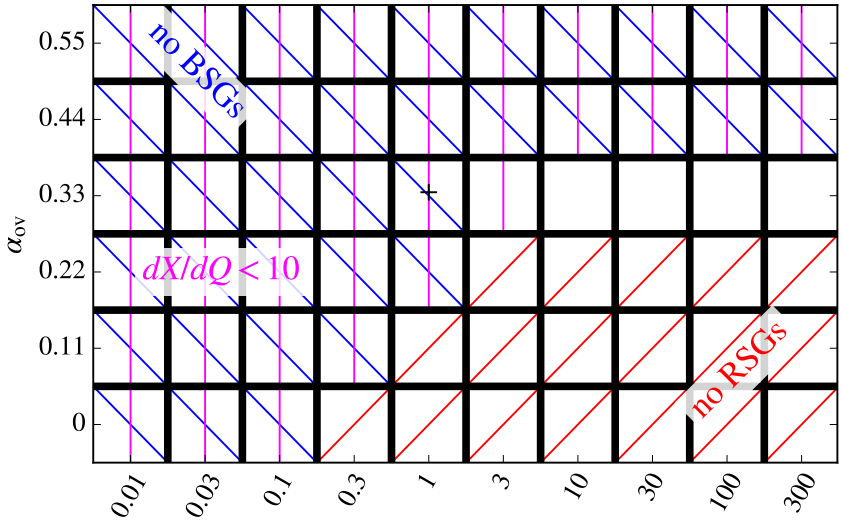

Figure 3.12: Schematic diagram indicating which part of the α_{sc} and α_{ov} parameter space is at odds with our three different criteria. These criteria are 1) the ability to produce steep hydrogen gradients (Sect. 3.3.2, purple vertical lines), 2) stars spending less that a few per cent of their helium burning lifetime as BSGs (blue diagonal lines) and 3) the ability to become RSG stars at and below 20 $M_\odot$ (red diagonal lines).

have seen in Sect. 3.5.2 that the parameter range which offers a solution to the problem of the paucity of luminous RSGs falls within the range which is compatible with all other observational constraints.

The situation is summarized in Fig. 3.12. We see that the parameter subspace where all observational tests are passed is rather small. In fact, the overshooting parameter seems to be well constrained to the interval $0.2 \lesssim \alpha_{sc} \lesssim 0.35$. Semiconvection, on the other hand, is required to be efficient in the sense that $\alpha_{sc} > 1$. Here it is to be mentioned that the allowed parameter space for the semiconvection parameter may appear larger than it is, since for $\alpha_{sc} \gtrsim 10$ our models behave very similar.

Importantly, Fig. 3.12 shows the existence of a subspace of the considered parameter space which appears to be compatible with all observational constraints. We note that a priori there is no guarantee of this outcome, which gives the hope that our problem is well posed, in the sense that the adopted physical descriptions allow for a representation of the real stars — despite the caveats discussed below. Further tests may show whether or not this turns out to be an illusion. For example, a study similar to this one needs to be done for Galactic and LMC composition, although the higher metallicity of these environments may introduce additional uncertainties through the increased importance of stellar winds. The concept of this work may also be extended to intermediate mass stars. However, it is already clear that a consideration of a mass dependence of the mixing parameters can not be avoided in this case (see below).

3.6.2 Caveats

Figure 3.12 gives an overview of our findings, without subdividing the mass range we consider (9. . . 100 $M_\odot$). However, in the discussion above, we had already to specify smaller initial mass ranges when discussing specific observational constraints. Indeed, the physical situation in our models changes significantly, with our 9 $M_\odot$ models being dominated by ideal gas pressure, while radiation pressure is more important in our 100 $M_\odot$ models.

In fact, when considering the overshooting parameter, it already appears evident that it can not be constant for all core hydrogen burning stars. For intermediate and low mass stars, good constraints exist pointing to values of $\alpha_{ov} \lesssim 0.2$. On the other hand, the results of Castro, Fossati, Langer et al. (2014) strongly argue for an increase of α_{ov} with mass (Grin et al., in prep.). Furthermore, as discussed in Sect. 3.5.3, a lower overshooting than indicated by Fig. 3.12 may yield better agreement with the blue-to-red supergiant ratio at the lowest considered masses.

Such a mass dependence would actually not be surprising, since α_{ov} is an ad hoc parameter, which is not backed up by any physical theory. The semiconvection parameter, on the other hand, is based on a local, linear stability analysis (Kato, 1966; Langer, Fricke and Sugimoto, 1983), which fully accounts for a mixture of gas and radiation pressure. Therefore, we may hope that the mass dependence of this parameter is weaker or absent.

Furthermore, our discussion of the chemical structure of massive stars remained limited, since we only considered the parameters core mass and hydrogen gradient. Clearly, as indicated by Fig. 3.8, hydrogen and helium profiles can be quite complex and may need more than two parameters to describe them. Obviously, the inclusion of additional parameters would hardly be feasible at the moment. In any case, its necessity has not yet been shown, and the convergence of the viable part of the parameter space from multiple constraints is not arguing for it.

On the other hand, we know that even for a fixed initial chemical composition, the initial stellar mass is not the only parameter describing its future evolution. Rotation and binarity are widely discussed as initial parameters affecting the evolution of massive stars (Maeder and Meynet, 2012; Langer, 2012). However, while for massive stars living in a binary is the rule rather than the exception (Sana, de Mink, de Koter et al., 2012), the fraction of isolated massive stars whose evolution is significantly affected by rotation is unclear. As discussed in Sect. 3, we find the effects of rotation on our models to be quite limited — except for extreme rotation, which allows for chemically homogeneous evolution Yoon, Langer and Norman (2006) and and Brott, de Mink, Cantiello et al. (2011), but is thought to be very rare. However, in the framework of models which allow for a significant redistribution of hydrogen and helium for average rotation rates (cf., Sect. 3), rotation would need to be considered as an important third parameter.

Our neglect of binarity, however, is harder to justify, except for feasibility reasons. The two additional, necessary initial parameters (initial secondary mass, and initial separation) tremendously blow up the initial parameter space to consider. However, now that our analysis of single star models has narrowed the viable parameter space for the mixing parameters, it will be our next step to compute binary evolution grids with the current best guess for these, and see whether the binary results affect our conclusions.

On the other hand, that binarity may be omnipresent in massive stars does not imply that it is clearly important for our discussion. Considering main sequence stars, of the order of 10% and 15% may be merger products or mass gainers in post mass transfer systems, respectively (de Mink, Sana, Langer et al., 2014). However, if these would be fully rejuvenated, they might be rather indistinguishable from ordinary single stars and evolve further on as such. In fact, the very efficient semiconvective mixing advocated by our results would imply that rejuvenation occurs in the vast majority of cases (Braun and Langer (1995)). On the other hand, it has been suggested that stellar mergers produce strong magnetic fields (Ferrario, Pringle, Tout et al., 2009; Langer, 2012; Schneider, Podsiadlowski, Langer et al., 2016), in which case the evolution on the main sequence and beyond could be strongly affected (Petermann, Langer, Castro et al., 2015). As about 7% of the massive main sequence stars are found to be magnetic (Fossati, Castro, Schöller et al., 2015; Grunhut, Wade, Neiner et al., 2017), this may affect our analysis at this level.

The only other branch of massive binary evolution which may be of relevance here (as, e.g., common envelope evolution or binaries involving compact objects produce exotic, easily identifiable types of stars) are post-main sequence stellar mergers. Such mergers produce stars whose core mass is smaller compared to that of a single star of the same mass. Such objects are known to spend nearly all of core helium

burning as BSGs (Braun and Langer, 1995); Justham, Podsiadlowski and Vink (2014). The fraction of massive binaries which produce such stars is again estimated to be of the order of 10% (Podsiadlowski, Joss and Hsu, 1992); however, the uncertainty of this number is considerably (de Mink, Sana, Langer et al., 2014) and not independent of the mixing parameters which we discuss here.

In summary, there is much more work to do to consolidate or modify our conclusion. Yet, there appears to be no reason at present to assume that our results will have to be revised significantly.

3.7 Conclusions

In this study, we have computed a large number of grids of massive star model sequences to explore the effects of the most relevant internal mixing processes on their hydrogen burning and post main sequence evolution. We chose to focus on models with an initial chemical composition of that of the Small Magellanic Cloud (SMC), such that uncertain mass loss rates affect our conclusions as little as possible.

We compared the predictions of our models to a multitude of observational constraints, including the observed widths of the main sequence band in the Hertzsprung-Russell diagram, the presence of both blue and red supergiants for a considerable range of luminosities, the empirical upper luminosity limit of red supergiants, and the requirement of a steep H/He-gradient at the core-envelope interface. As summarized in Sect.3.6.1, we find a small but clear subspace of the mixing parameters where all constraints can be reasonably satisfied. Conversely, we can exclude most of the considered parameter space. In terms of the formulation of the mixing process used in our models, we find that semiconvective mixing needs to be efficient ($\alpha_{\rm sc} \gtrsim 1$) and convective core overshooting is restricted to intermediate values ($0.22 \lesssim \alpha_{\rm ov} \lesssim 0.33$), where some trend with mass appears likely. Rotational mixing in our models was found of limited importance.

In terms of structural parameters, which are relevant beyond our chosen mathematical formulation of the mixing processes, we find a necessity of a moderate core mass increase over the canonical value, which may be produced by convective core overshooting or otherwise, and as well a H/He-gradient which is at least five times steeper than the one which emerges naturally from the retreating convective core during core hydrogen burning. While the latter has been concluded previously for stars above $\sim$40 $M_\odot$, we find this here to be valid stars down to $\sim$9 $M_\odot$.

Since our results could only be derived with various caveats (cf., Sect.3.6.2), more theoretical work is needed to consolidate them, in particular to include models of close binary evolution. In any case, much more stringent observational tests would be possible if we had a complete set of spectroscopic data of all the massive stars in this key galaxy, the SMC, which is currently available only very fragmentary.

CHAPTER 4

Synthetic color magnitude diagrams of massive stars in the Small Magellanic Cloud

A. Schootemeijer, N. Langer, N. Castro & C. Wang

Argelander-Institüt für Astronomie, Universität Bonn, Auf dem Hügel 71, 53121 Bonn, Germany

To be submitted to *Astronomy & Astrophysics*

Abstract. *Context:* The evolution of massive stars depends sensitively on a number of internal mixing processes. Earlier, we have provided testable predictions for these mixing processes in massive stars in the Small Magellanic Cloud, but comprehensive spectroscopic surveys are lacking.
Aims: We aim to use a combination of existing photometry data sets of Massey (2002), and the recently released GAIA DR2 to compare with our predictions. This catalog should be largely complete for our targeted magnitude range. In particular, we aim to find out whether or not a population of blue supergiants, that is predicted for a certain set of assumed mixing efficiencies, exists.
Method: To translate the temperatures and luminosities of our evolutionary models into colors and magnitudes, we used two different approaches: the black body approximation and synthetic spectra. Using parallaxes of GAIA DR2, we clean the Massey (2002) catalog of foreground contamination and extend the photometric data with the GAIA colors and magnitudes.
Results: In the GAIA color-magnitude diagram, we identify a band of blue sources next to the main sequence at a color value that matches the expected color of a blue supergiant population. This feature is only discernible at the high magnitude end. To explain these stars with internal mixing, overshooting cannot exceed $\alpha_{\rm ov} = 0.2$ in the mass range around ten solar masses. Below that, we cannot make a comparison because we do not have models of intermediate mass stars. In classical UBV data, this blue band does not manifest itself as clearly.
Conclusions: The blue sources next to the main sequence could be seen as an indication for internal mixing, but their origin could also be binary interaction or perhaps disk emission as a result of rapid rotation. Also, to do a full assesment, it would be necessary to extend the synthetic population to intermediate masses.

Key words. stars: massive – stars: early-type – stars: interiors – stars: evolution

4.1 Introduction

Understanding massive stars is crucial for understanding a grand variety of objects and phenomena observed in the sky. In galaxies, massive stars dominate their environment by providing feedback in the form of ionizing radiation, mechanical energy injection en chemical enrichment (Hopkins, Kereš, Oñorbe et al., 2014). Among the transient phenomena that they precede are long duration gamma ray bursts (lGRBs: Yoon, Langer and Norman, 2006; Woosley and Heger, 2006), supernovae (SNe, including the recently discovered subgroup of superluminous SNe: Smartt, 2009) and gravitatonal wave transients (GWs: see e.g. B. P. Abbott, Abbott, Abbott et al., 2016a).

Although progress has been made in last decades, many uncertainties in the evolution of massive stars remain. A prime example of these uncertainties is internal mixing, as was discussed in Chapter 3. Rotational mixing (Maeder, 1987; Langer, 1992; Heger, Langer and Woosley, 2000) could transport material from inner layers to the surface of a star already during the main sequence. Semiconvective mixing – which can occur in layers that would be unstable to convection had they not been stabilized by a mean molecular weight gradient – could strongly affect the chemical structure of a star after the main sequence evolution. However, the efficiency of semiconvective mixing processes is poorly understood. Both theoretical predictions (e.g. Merryfield, 1995; Zaussinger and Spruit, 2013) and observational campaigns have not been able to provide strong constraints. A key aspect of semiconvective mixing is that it can influence the post main sequence radius evolution of a star. Not only does this strongly affect the population of evolved stars (do they burn helium as blue supergiants (BSGs) or red supergiants (RSGs)?), it can also be expected to significantly affect binary evolution. A star that expands more slowly is stripped of its mass more slowly, possibly giving the accretor star more time to adjust its structure after accepting mass from its companion, which in turn is likely to affect the mass transfer efficiency and later evolution of the system. Thus, to understand where the transient phenomena mentioned above (lGRBs, SNe, GWs) come from, it is important to put constraints on these internal mixing processes.

In this chapter, we expand upon work done earlier in this thesis, related to the greater goal of putting constraints on aforementioned internal mixing processes. In Chapter 2 we inferred steep hydrogen gradients in the envelopes of apparently single Wolf-Rayet stars in the Small Magellanic Cloud (SMC). In contrast, in binary Wolf-rayet stars fitted to models where the shallow hydrogen gradient, left by the retreating convective core, was still intact. We found that the steep hydrogen gradients in apparently single WR stars can be explained by efficient semiconvection taking place upon radial expansion after the main sequence. We discussed also that alternatively, these steep gradients could be formed in accretor stars where the convective core grows upon mass accretion – although it would be questionable if this could be the evolutionary history of all apparently single SMC WR stars. For more details we refer to Sect. 2.5.3.4.

In Chapter 3, we made theoretical predictions for populations of massive stars in the SMC under different assumptions for the effictiveness of overshooting and semiconvective mixing. This included predictions for which regions in the Herzsprung-Russell diagram (HRD) are the most populated, as well as for luminosity distributions of BSGs and RSGs. However, apart from the RSGs (Levesque, Massey, Olsen et al., 2006; Davies, Crowther and Beasor, 2018), no systematic spectroscopic analysis has been done of the massive star population in the SMC. Given that every star would have to be analyzed spectroscopically, such systematic study would be expensive in telescope time. Thus, in this chapter we attempt to resort to a cheaper alternative that we describe below: photometry.

In photometic studies, the fluxes in different filters can be measured for a large number of sources, which are then typically put in a color-magnitude diagram (CMD). This diagram is similar to the Hertzsprung-Russell diagram (HRD) presented in the two previous chapters – but with slightly different axes. First, instead of temperature, the color is displayed on the x-axis. Here, color is defined as the

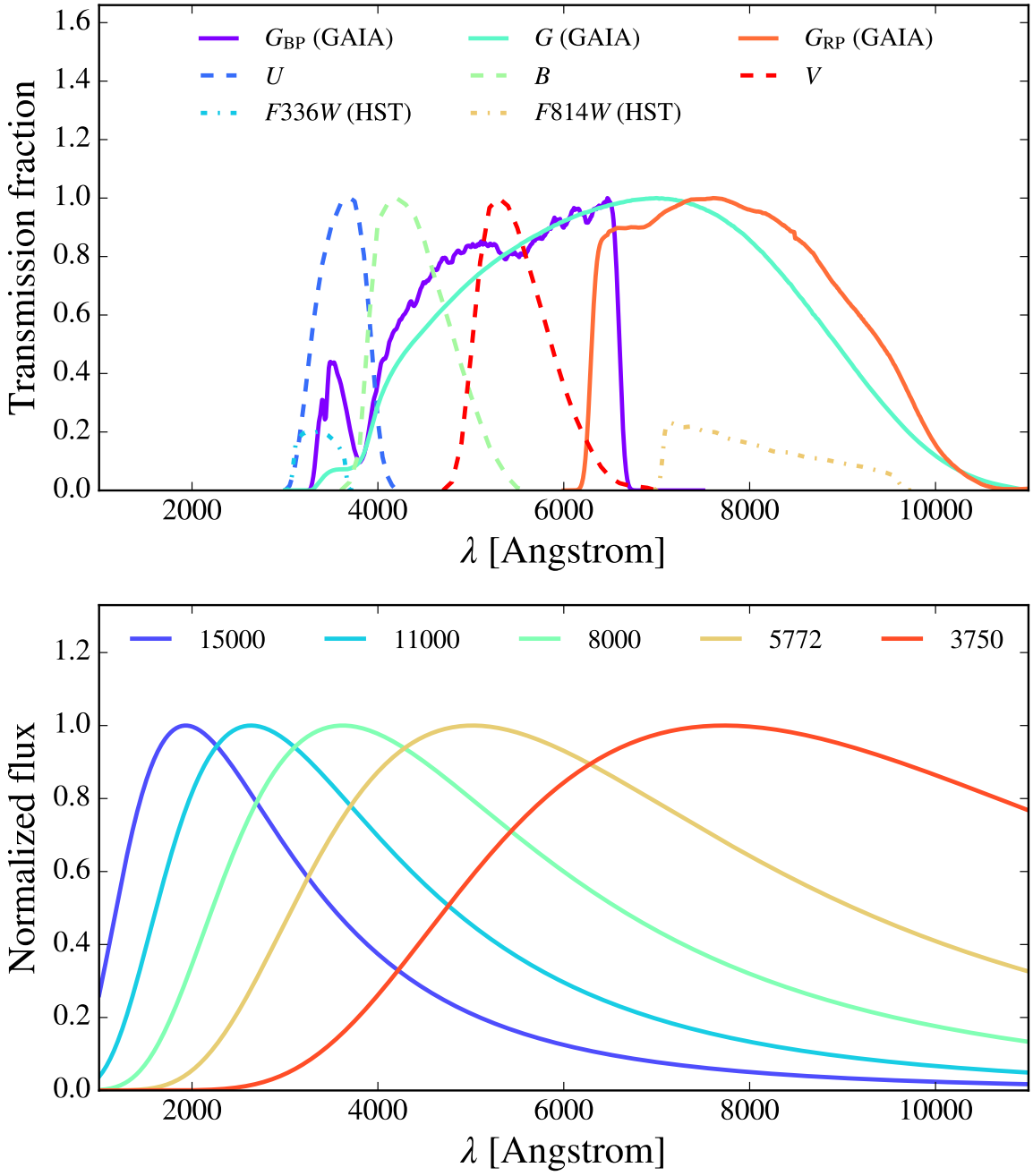

Figure 4.1: **Top:** transmission fractions of a variety of filters as a function of wavelength. **Bottom:** normalised fluxes of black bodies with different effective temperatures, which are indicated by the numbers in the top of the plot in units of Kelvin. The line with $T_{\rm eff}$ = 5772 K corresponds to the Solar effective temperature.

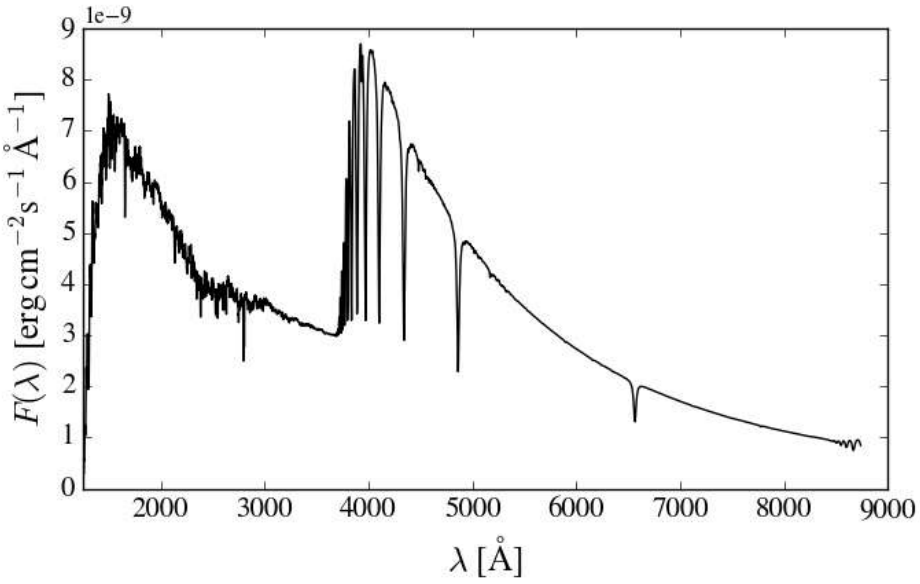

Figure 4.2: The spectrum of the standard star Vega.

magnitude difference between a blue and a red filter. Fig. 4.1 shows the transmission function of a variety of different filters in the top panel, and for reference, at the bottom, the flux distributions of black bodies with different temperatures. A traditionally often-used color is $B - V$, i.e., the 'blue' band magnitude minus the 'visible' band magnitude. The lower the value, the 'bluer' (and therefore, hotter) the star. Later on in Fig. 4.8 we show the relation between the color and temperature for different filter combinations. Second, on the y-axis the magnitude through one filter is displayed, rather than the bolometric luminosity (i.e., the luminosity emitted in all wavelengths).

Apart from the traditional UBV magnitudes, we also consider two different sets of filters. The first are the $F336W$ and $F814W$ filters, which are a part of the Hubble Space Telescope (HST). HST's advantage is that as a space instrument, it is not hindered by the Earth's atmoshere, which becomes opaque for short-wavelength photons in the ultraviolet part of the spectrum. Thus, it can observe at wavelengths that are inaccesible for ground-based telescopes. Also, its observations are not affected by atmospheric distortion. The second set of filters is used in the recently launched GAIA space telescope. In this revolutionary mission, the fluxes and positions of billions sources over the entire sky are monitored, with extreme precision in the angular resolution. As a result, by measuring the parallax (change of position in the sky as a result of Earth's motion around the Sun) the GAIA mission provides a very large stellar catalog with measured distances. As such, the contamination of foreground sources can be strongly reduced for the Small Magellanic Cloud, which is the target environment in our study.

To obtain the colors and magnitudes of our stellar models, we use two different approaches. The simplest approach is to assume that a star emits light like a black body – in this case, its spectrum can be obtained with a formula that depends only on effective temperature (see Sect. 4.2.1 for details – see also Fig. 4.1), so no extra modelling is required. However, this might be inaccurate to some extent because strong absorption features are common in spectra of stars. To illustrate this, we show the spectrum of the standard star Vega in Fig. 4.2 (Bohlin, 2007)[1]. This is a synthetic spectrum that is claimed to be

[1] This spectrum is publicly available on the website of the Space Telescope Science Intitute: `ftp://ftp.stsci.edu/cdbs/calspec/alpha_lyr_stis_008.fits`

accurate to within 1-2% over most of the wavelength range. The figure clearly shows strong Balmer lines: e.g., Hα at 6560 Å, Hβ at 4860 Å, towards shorter wavelengths climaxing in a very strong Balmer jump around 3650 Å. The latter is the wavelength of a photon that carries the amount of energy required to ionise a hydrogen atom that is in the first excited state. We note that Vega is an extreme case because as an A-type star, it per definition shows the strongest hydrogen lines of all. The temperature of Vega is at the lower end of the temperature range of the stars we focus on. Most other stars are hotter and have weaker hydrogen lines. Also, not all filters are affected by the Balmer jump (Fig. 4.1). Still, a glance at Vega's spectrum makes it evident that it is worth investigating how well the black body approximation holds for the relevant models (in our case, SMC models, in particular those that are hot). We do so using a set of synthetic spectra. We note that the relation between colors and effective temperatures has been a topic of numerous studies (see e.g. Girardi, Bertelli, Bressan et al., 2002; Worthey and Lee, 2011). We can make a direct comparison with the latter, where we find good agreement in the color-temperature relations.

The stucture of this chapter is as follows. In Sect. 4.2, we explain how we made the synthetic CMDs. Then, we show the CMDs obtained using the black body approximation in Sect. 4.3.1. After that, we test how well the black body approximation holds in Sect. 4.3.2 and compare our modeled population to observational data in Sect. 4.3.3. Finally, we draw our conclusions in Sect. 4.4.

4.2 Method

The model sequences described in Chapter 3 are the starting point of this work. These are simulated with the detailed stellar evolution code MESA (Paxton, Bildsten, Dotter et al., 2011; Paxton, Cantiello, Arras et al., 2013; Paxton, Marchant, Schwab et al., 2015; Paxton, Schwab, Bauer et al., 2018), which is a detailed one-dimensonal code solving the stellar structure equations. In this model grid, we explored how different assumptions for internal mixing affect the evolution of massive stars. The parameter space we explored covered for the semiconvection parameter $\alpha_{\rm sc} = 0.01, \ldots, 300$. We simultaneously varied the core overshooting parameter between $\alpha_{\rm ov} = 0$ and $\alpha_{\rm ov} = 0.55$ with 60 combinations in total. We did this for stars with masses between 10 and 100 solar masses. For these model sequences, we used an initial composition appropriate for the SMC, and a wind mass loss recipe plus a number of other physics assumptions that are based on the earlier work by Brott, de Mink, Cantiello et al. (2011). For details we refer to Sect. 3.2.

We used two different approaches to convert the temperatures and luminosities of our MESA models into colors and magnitudes. We describe these in Sect. 4.2.1 (blackbody approximation) and Sect. 4.2.2 (synthetic spectra).

4.2.1 Black body approximation

The first approach to calculate the magnitudes of our MESA models is to use the black body approximation. This implies that we assume that stars radiate as is dictated by Planck's law:

$$B_\lambda(\lambda, T) = \frac{2hc^2}{\lambda^5} \frac{1}{e^{hc/(\lambda k_{\rm b} T)} - 1}, \tag{4.1}$$

where B_λ is the spectral radiance in units of erg s^{-1} cm^{-2} Å^{-1}, λ is the wavelength, T is the temperature of the black body, h is Planck's constant, c is the speed of light and $k_{\rm b}$ is Boltzmann's constant. Examples of such black body spectra are given in Fig. 4.1. We note that these are normalised to the maximum value of the spectral radiance to show at which wavelengths they peak. In reality, for a black body with

a higher temperature B_λ is always higher at any wavelength. To calculate the apparent magnitude of a stellar model in a filter, we take the following steps:

1. Calculate the spectral energy distribution of its flux at Earth by integrating the spectral radiance, as dicated by Eq. 4.1, over the surface of the star (as seen from Earth, a disk with surface $\pi \cdot R^2$) and correcting for the distance to the SMC, for which we adopt $d = 60.6\,\mathrm{kpc}$ (Hilditch, Howarth and Harries, 2005).
$$f_{\lambda,\oplus}(\lambda, T, R, d) = \frac{B_\lambda(\lambda, T)\pi R^2}{d^2}. \tag{4.2}$$
2. Integrate the product of this spectral energy distribution and the transmission function of the filter $T(\lambda)$: $\int_0^\infty f_{\lambda,\oplus}(\lambda, T, R, d)\, T(\lambda)\, d\lambda$. This is the transmitted flux at Earth in $\mathrm{erg\,s^{-1}\,cm^{-2}}$. The relevant transmission functions[2] are shown in the top panel of Fig. 4.1.
3. Divide this flux at Earth by the equivalent width of the filter: $\int_0^\infty T(\lambda)\, d\lambda$ (in units of Å). Now, we have the following term that we call F, which is in units of $\mathrm{erg\,s^{-1}\,cm^{-2}\,Å^{-1}}$:
$$F = \frac{\int_0^\infty T(\lambda) f_{\lambda,\oplus}(\lambda, T, R, d)\, d\lambda}{\int_0^\infty T(\lambda)\, d\lambda}. \tag{4.3}$$
4. Next, F is compared to the zero point ZP, that is defined as the observed flux at Earth of the standard star Vega divided by the equivalent width of the filter:
$$ZP = \frac{\int_0^\infty T(\lambda) f_{\lambda,Vega}(\lambda)\, d\lambda}{\int_0^\infty T(\lambda)\, d\lambda}. \tag{4.4}$$
5. The ratio of F and ZP is then easily translated into an apparent magnitude via the following formula:
$$m = -2.5 \log_{10}\left(\frac{F}{ZP}\right). \tag{4.5}$$

As can be deduced from Eq. 4.5, the apparent magnitude of Vega is zero per definition in all wavelength bands (with the exception of the visual band where $m_{\mathrm{Vega}} = 0.03$ is adopted – see e.g. Girardi, Bertelli, Bressan et al., 2002).

To test our method, we calculate the visual magnitude and color of the Sun. Adopting an effective temperature of 5772 K[3] We find an apparent visual (i.e., V band) magnitude of the Sun of $m_V = -26.66$, which is in good agreement with the commonly known value of $m_V = -26.7$. We obtain a color of $B - V = 0.61$, which is close to the Solar value of 0.63 for a G2V star (Croft, McNamara and Feltz, 1972; Bessell, 1990).

4.2.2 Synthetic spectra

The second approach we used to calculate the MESA models' magnitudes and colors uses synthetic spectra. These synthetic spectra were created by Castro, Oey, Fossati et al. (2018) and were designed to

[2] These transmission functions are publicly available at `http://svo2.cab.inta-csic.es/svo/theory/fps/`

[3] Obtained using the official International Astronomical Union's values for the Solar radius, $R = 6.957 \cdot 10^{10}$ cm, the Solar luminosity, $L = 3.828 \dot{1}0^{33}\,\mathrm{erg\,s^{-1}}$ (both from Mamajek, Prsa, Torres et al., 2015), and the Stefan-Boltzmann law that dictates that $T_{\mathrm{eff}} = (L/(4\pi R^2 \sigma))^{0.25}$, where $\sigma = 5.67 \cdot 10^{-5}\,\mathrm{erg\,s^{-1}\,cm^{-2}\,K^{-4}}$.

be compared with an SMC sample of 331 O- and B-type stars. The majority, 225, of these stars come from the RIOTS4 spectral catalog of hot SMC field stars (Lamb, Oey, Segura-Cox et al., 2016). The other 106 OB stars were taken from the 2dF survey (Evans, Howarth, Irwin et al., 2004). Because the stars in this sample are both hot and, being SMC stars, metal poor, Castro, Oey, Fossati et al. (2018) noticed that at the considered low spectral resolution, they show only few significant absorption lines that are not from H I, He I or He II. Therefore, the large grid of synthetic spectra that they calculated includes only hydrogen and helium lines. The models cover a range of effective temperatures between 9 kK and 67 kK (with a 1 kK interval) and surface gravities between $\log g = 0.8$ and $\log g = 5$ (with a 0.1 dex interval). Thus, the effective temperatures do not cover the entire temperature range of our evolutionary models described in Chapter. 3, but the main sequence and most of the blue supergiant temperature range are covered. From here, the approach to obtain the apparent magnitude of a MESA stellar model is very similar to the method described in Sect. 4.2.1 – the only difference is that instead of a blackbody spectrum, we use the synthetic spectrum in the grid of Castro, Oey, Fossati et al. (2018) that is closest in effective temperature and $\log g$.

4.2.3 Comparison with observations

To compare our theoretical predictions with observations, we combined two catalogs. The first is the *UVBR* catalog of massive stars in the Magellanic clouds from Massey (2002). The second is the recently released GAIA data release 2 (DR2) catalog (Gaia Collaboration, Brown, Vallenari et al., 2018), which we use for two purposes: i) to extend the available observational color (with $G_{\rm BP} - G_{\rm RP}$) and magnitude (with G) data, and ii) to discriminate between foreground stars and SMC members by applying criteria to the parallax and proper motion of candidate objects. In practice, our method to compile the observational data set looks at follows.

1. For each source in the catalog of Massey (2002), we search for a counterpart within a 3" radius.
2. If more than one counterpart is found, we take the source with the G magnitude closest to the V magnitude in Massey's catalog. If the difference is larger than 1 magnitude, the source is discarded.
3. We restrict our search to sources with magnitudes of $G < 15$.
4. Sources with a parallax of $\pi < 0.25$ milli-arcseconds (mas) – this corresponds to 4 kpc, while the SMC is at a distance of roughly 60 kpc – are considered to be foreground stars and are eliminated from the sample.
5. Sources with proper motions[4] of $\mu > 5\,\mathrm{mas\,yr^{-1}}$, which corresponds to a tangential velocity of $\sim$1500 $\mathrm{km\,s^{-1}}$ at the distance of the SMC, are also eliminated.

Estimates for extinction, $A_{\rm G}$, and reddening, $E(G_{\rm BP} - G_{\rm RP})$, are available but only for a small minority of the sources that ended up in our final data set – therefore, we do not use them. We discuss the impact of extinction and reddening when when we examine the results in Sect. 4.3.3.

[4] Calculated as $\mu = (\mu_\delta^2 + \cos^2(\delta)\mu_r^2)^{1/2}$, where δ refers to declination and r to right ascension

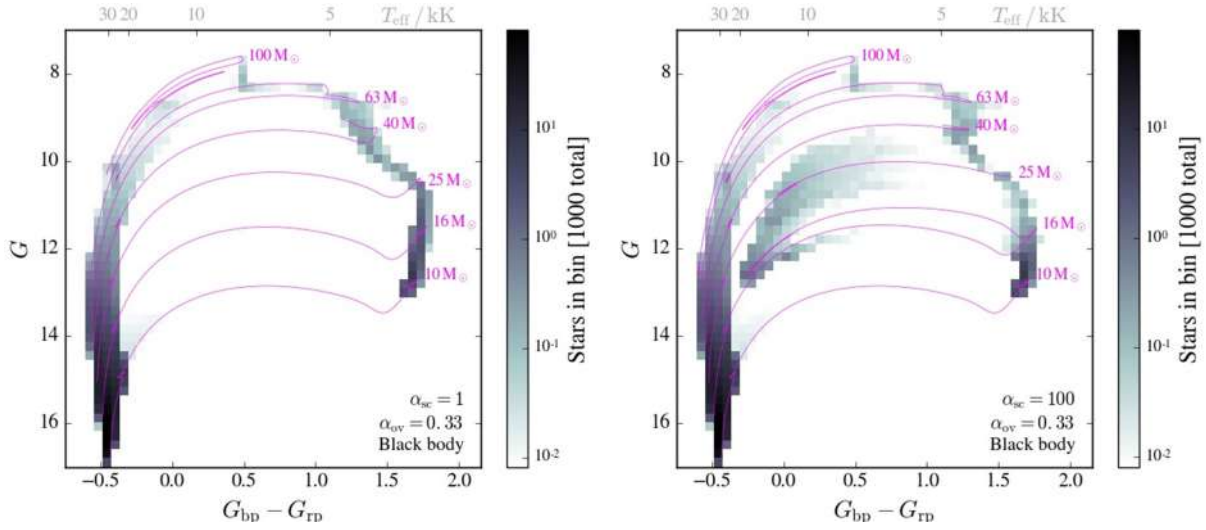

Figure 4.3: Synthetic color-magnitude diagrams, constructed with stellar models with a chemical composition appropriate for the Small Magellanic Cloud. These have initial masses between 10 $M_\odot$ and 100 $M_\odot$. The color of each pixel represents the number of stars it contains, given that there would be 1000 stars present in the aforementioned mass range. The purple lines are the evolutionary tracks in the color magnitude diagram for a subset of evolutionary sequences. Their initial masses are indicated in purple. On the axes we show the GAIA color $G_{\rm BP} - G_{\rm RP}$ (x-axis) and magnitude G (y-axis). In both panels we adopt $\alpha_{\rm ov} = 0.33$ for overshooting. **Left:** a semiconvection efficiency of $\alpha_{\rm sc} = 1$ is assumed for all evolutionary sequences. The shown models have identical mixing parameters to those shown in the center left Hertzsprung-Russell diagram in Fig. 3.2. **Right:** a semiconvection efficiency of $\alpha_{\rm sc} = 100$ is assumed for all evolutionary sequences. These models have identical mixing parameters to those shown in the center right Hertzsprung-Russell diagram in Fig. 3.2.

4.3 Results and discussion

Here, we present the populations of our MESA models in CMDs. In each diagram, there are one thousand stars in the synthetic population. Our evolutionary sequences have initial masses of $10 \leq M / M_\odot \leq 100$. The total number of evolutionary sequences is 51, evenly separated in log mass. The color of each pixel, which indicates the number of stars it contains, is calculated for constant star formation and assuming a Salpeter initial mass function (Salpeter, 1955).

4.3.1 Color-magnitude diagrams obtained with the blackbody approximation

In this section, we present the CMDs that we constructed while using the black body approximation. Because in this case the colors only depend on the effective temperatures of the stars, we can show these in gray at the top of the plots for reference.

For different colors and magnitudes, we compare the shapes of the populations calculated with a semiconvection efficiency of $\alpha_{\rm sc} = 1$ to to those with a semiconvection efficiency of $\alpha_{\rm sc} = 100$. In both cases, the size of the overshooting region above the hydrogen burning core is set to 0.33 pressure scale heights: $\alpha_{\rm ov} = 0.33$. At this value for $\alpha_{\rm ov}$, the $\alpha_{\rm sc} = 1$ population is representative for a stellar population in which no efficient semiconvection takes place (left panel of Fig. 4.3 and see Chapter 3). On the other hand, evolution after the main sequence in the $\alpha_{\rm sc} = 100$ population is strongly influenced by semiconvective mixing. In Chapter 2, we conluded that the scenario with efficient semiconvective mixing is preferred to form the steep hydrogen gradients inferred for apparently single hot Wolf-Rayet stars in

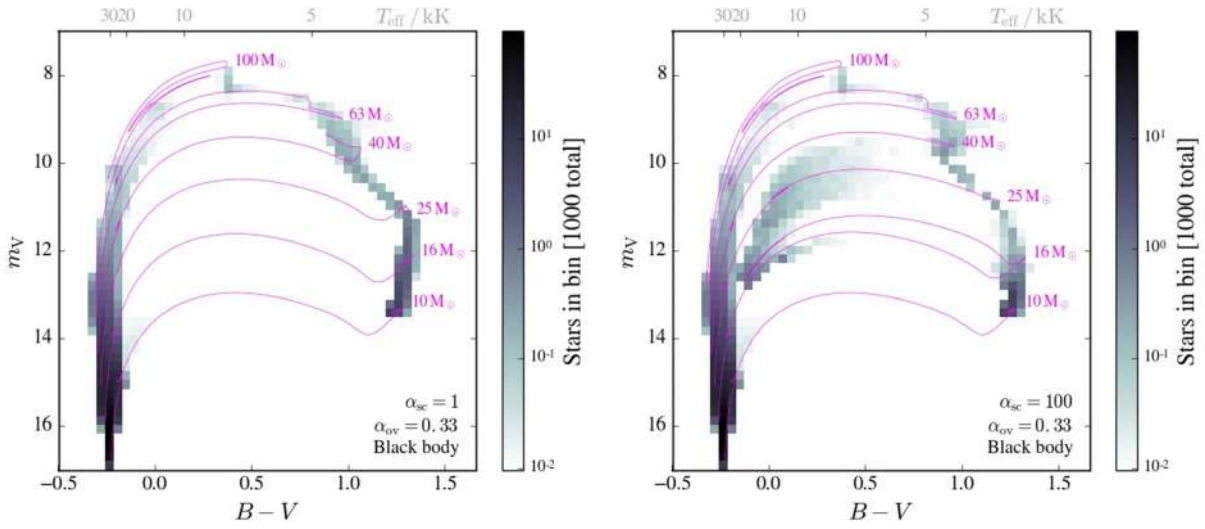

Figure 4.4: Same as Fig. 4.3, but now with the classical $B - V$ color and V magnitude on the x-axis and y-axis, respectively.

the SMC; in Chapter 3, we found that efficient semiconvection is preferred because it tends to lead to stars being BSGs for a non-negligible time. This results in a seemingly better agreement of the evolutionary models with both the BSG population (observed by Blaha and Humphreys, 1989; Kalari, Vink, Dufton et al., 2018) and RSG population (observed by Levesque, Massey, Olsen et al., 2006; Davies, Crowther and Beasor, 2018).

We find that in this population of stars, where $10 \leq M \,/\, \mathrm{M}_\odot \leq 100$, $\alpha_{\rm ov} = 0.33$ and $\alpha_{\rm sc} = 100$, the blue-to-red supergiant ratio is about 1:2.5. This seems to be at odds with the number distributions we showed of BSGs and RSGs in Chapter 3, where we found that in the case of $\alpha_{\rm ov} = 0.33$ and $\alpha_{\rm sc} = 100$ this ratio is close to unity. The explanation for this apparent discrepancy is that there, we only considered a subset of this population with $4.70 \leq \log\left(L \,/\, \mathrm{L}_\odot\right) \leq 6.05$ (we did this to be consistent with Davies, Crowther and Beasor (2018), who considered the same luminosity range). Importantly, this excluded stars with initial masses near $10\,\mathrm{M}_\odot$, which contribute heavily in population statistics because they are favored by the initial mass function and they live for a long time.

The difference in evolution between the $\alpha_{\rm sc} = 1$ and $\alpha_{\rm sc} = 100$ populations also shows in the CMDs we present in this section. Below we discuss these CMDs individually.

GAIA: In the left panel of Fig. 4.3, which shows the GAIA colors and magnitudes of the $\alpha_{\rm sc} = 1$ population, stars are expected to be observed almost exclusively in two narrow bands: the main sequence at $G_{\rm BP} - G_{\rm RP} \approx -0.5$ and the red giant branch at $G_{\rm BP} - G_{\rm RP} \approx 1.5$. In the right panel of Fig. 4.3 ($\alpha_{\rm sc} = 100$), there is also a population of helium burning BSGs which is close to the main sequence, but could ideally be observed as a seperate population.

In both panels, the evolutionary tracks do not cover the mid-bottom and bottom right of the plot. The reason for this is that we only show stars of $M > 10\,\mathrm{M}_\odot$, which all have a relatively high temperature at the beginning of their hydrogen-burning lifetime ($T_{\rm eff} \gtrsim 25$ kK, see Chapter 3) – compared to when they are more evolved. They emit most of their radiation in the ultraviolet range of the spectrum, which does not pass through the GAIA filters. This is illustrated in Fig. 4.1. Thus, the stars begin their evolution with high G-band magnitudes (i.e., they are dim in the G band) and as they evolve and cool down, they move towards lower G-band magnitudes. Once they reach very low temperatures, the G-band magnitude can increase again because the spectrum shifts towards the infrared, which is only marginally transmitted by

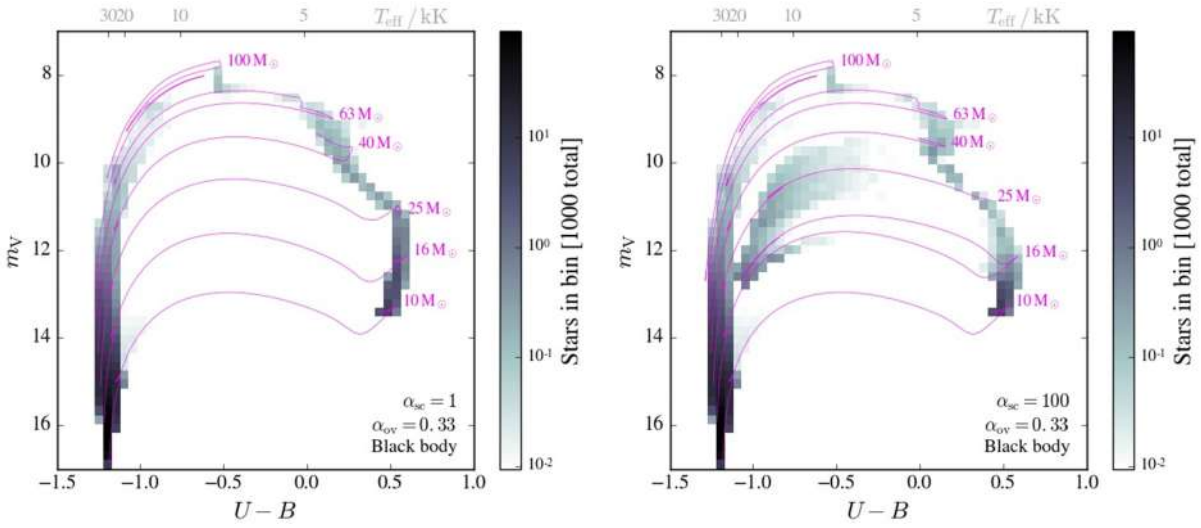

Figure 4.5: Same as Fig. 4.3, but now with the classical $U - B$ color and B magnitude on the x-axis and y-axis, respectively.

this filter.

When CMDs are constructed using other filters our evolutionary models show, in general, similar behaviour. We discuss the similarities and differences below for the CMDs constructed using classical UBV and Hubble filters.

B-V: In the right panel of Fig. 4.4, an identifiable BSG population is also visible. However, the $B - V$ color at the hot end is somewhat less sensitive to the effecive temperature of the star (when compared to the $G_{\rm BP} - G_{\rm RP}$ color). The main sequence and BSG populations are closer to each other and merge for the least luminous BSGs.

U-B: The $U - B$ CMD looks similar to the $B - V$ CMD, although the color is slightly less sensitive to changes in the temperature (for the black body approximation, at least). However, there seem to be no advantage compared to using the $B - V$ color because the $U - B$ color can be expected to have a larger error. The reason for this is that extinction is stronger at shorter wavelengths (Gordon, Clayton, Misselt et al., 2003).

U-V: Fig. 4.6 that the $U - V$ color is more sensitive to changes in effective temperature than the $B - V$ and $U - B$ colors, which both span about 1.5 magnitude. This is not surprising, as this color is simply the sum of the two other colors: $(U - B) + (B - V) = U - V$. As such, it spans around three magnitudes, which makes it more easy to distinguish between the main sequence and BSG populations.

F336W - F814W: Because the $F336W$ and $F814W$ filters are relatively narrow and far apart, this CMD with HST colors and magnitudes (Fig. 4.7) has the largest spread in color. This is advantageous in case precise measurements (and in a large enough quantity) could be obtained. However, in the $F336$ filter the magnitudes obtained from the black body approximation and the synthetic spectra show the largest discrepancies, because its entire wavelength range is in the Balmer jump (Fig. 4.2 and Fig. 4.1). Unfortunately, we do not have synthetic colors and magnitudes of these HST filters, so we do not discuss them later on.

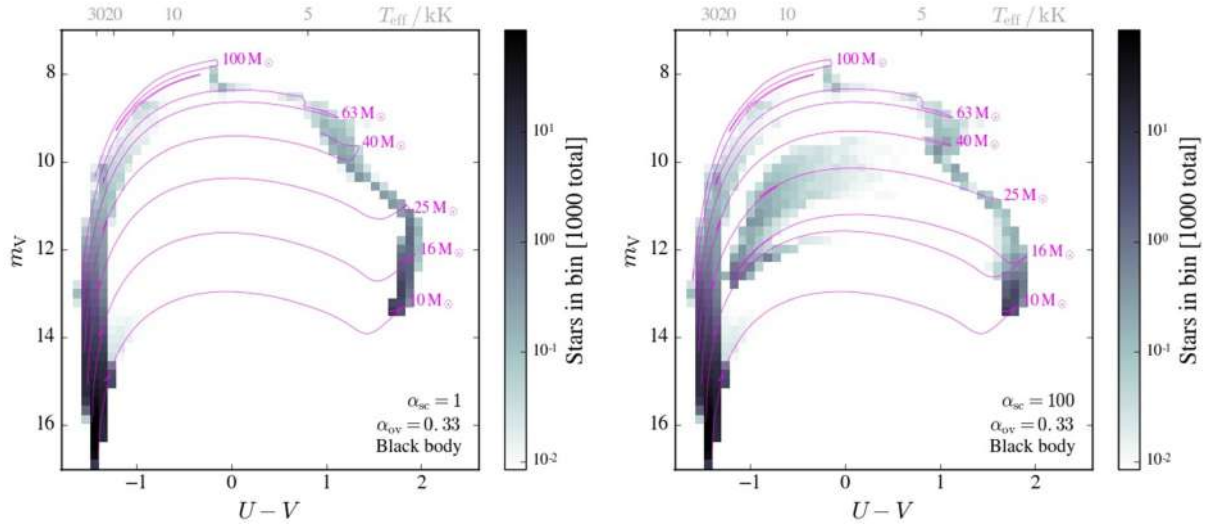

Figure 4.6: Same as Fig. 4.3, but now with the classical $U - V$ color and V magnitude on the x-axis and y-axis, respectively.

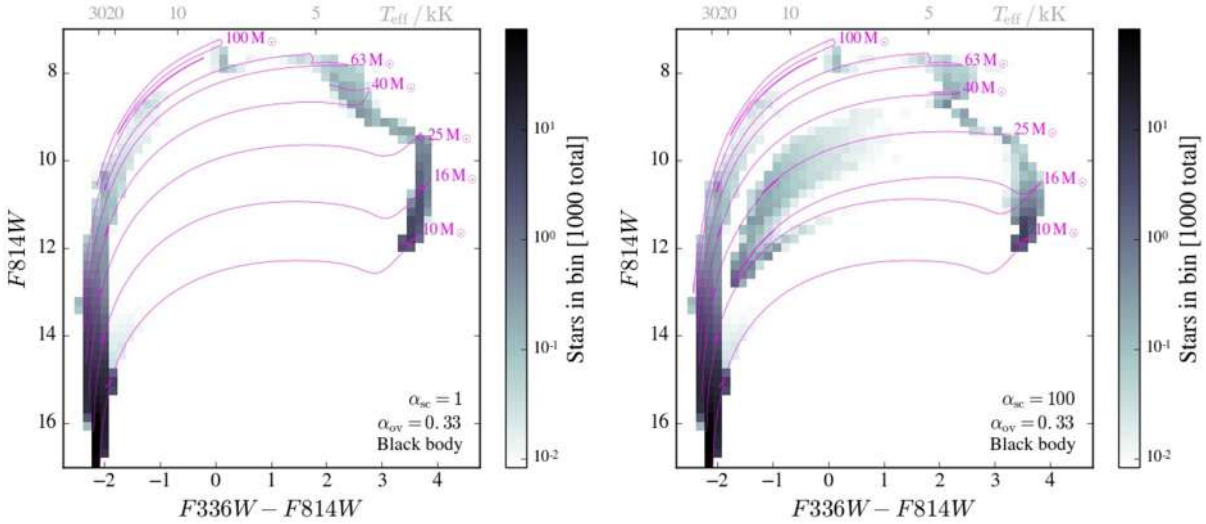

Figure 4.7: Same as Fig. 4.3, but now with the Hubble Space Telescope $F\,336W - F\,814W$ color and $F\,814W$ magnitude on the x-axis and y-axis, respectively.

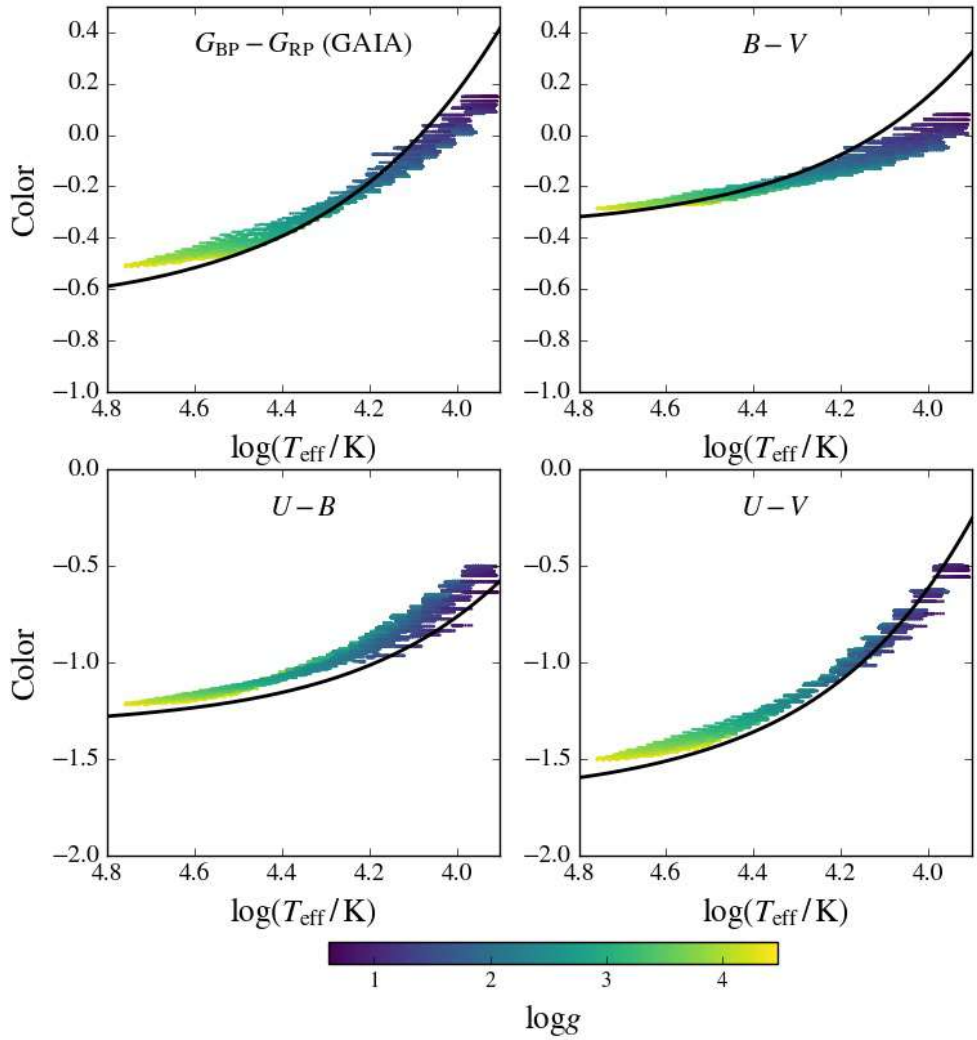

Figure 4.8: The relation between color and effective temperature, calculated using the synthetic atmosphere models. We show this for the GAIA color $G_{BP} - G_{RP}$ and for the possible combinations of the classical UBV filters. The color indicates the logarithm of a model's surface gravity in units of cm s^{-2}. For reference, we also show (with black lines) the relation between effective temperature and color when the black body approximation is used.

4.3.2 Color-magnitude diagrams obtained with synthetic spectra

To explore how well the blackbody approximation holds, we compare the colors predicted by this method to the colors that are obtained from the synthetic spectra of Castro, Oey, Fossati et al. (2018). We start by comparing the temperature - color relations that are obtained by both methods, as shown in Fig. 4.8. The black line shows the result from the blackbody approximation, which provides a unique solution because for this method the color depends on effective temperature only. In reality, it also depends on surface gravity (Worthey and Lee, 2011), which is also the case for the scatter points shown in Fig. 4.8. There, these scatter points all represent a color that is derived from the temperature and log g of a model in our MESA grid using synthetic spectra.

In general, the blackbody method and synthetic spectra method yield very similar results. Typically,

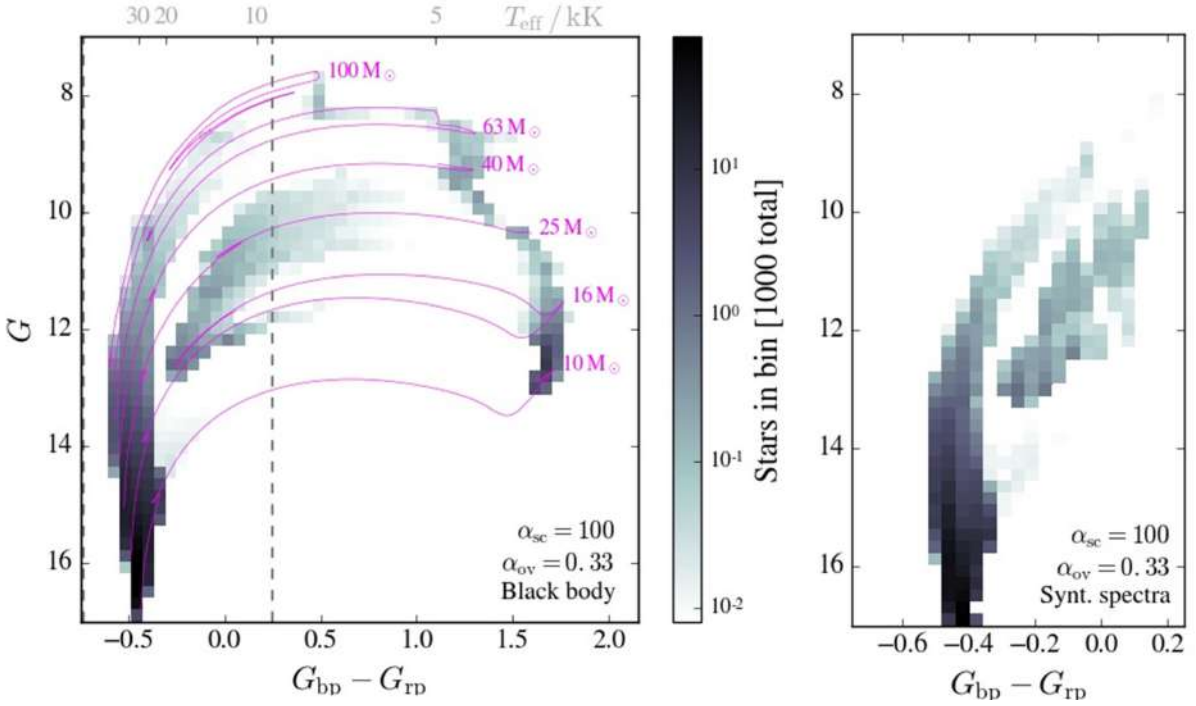

Figure 4.9: Same as Fig. 4.3, but here we show on the left the color magnitude diagram where we assume a semiconvection efficiency $\alpha_{\rm sc} = 100$ for our evolutionary sequences, where the colors are again obtained using the black body approximation. On the right, we show a zoomed-in version of exactly the same plot but where the colors are obtained with synthetic spectra.

both predict colors within 0.1 magnitude from each other. Exceptions occur at the lowest temperatures that are covered by the grid. This is in agreement with what would naively be expected from theory – ~10 kK is in the temperature range of A-type stars, which per definition have the strongest hydrogen absorption lines (Sect. 4.1 and Fig. 4.2). For example, the synthetic spectra method predicts a higher value (i.e., it is 'redder') for the $U - B$ color around 10 kK. This can be interpreted as the result of Balmer jump absorption reducing the flux in the bluer U band, while the flux in the B band is more or less unaffected by the Balmer jump and might even be increased through the line blanketing effect[5].

At the hot side of in particular the $G_{\rm BP} - G_{\rm RP}$ color, the synthetic spectra method predicts a slightly redder color than the black body method. The highest temperatures are associated with the most massive stars that are still close to the zero age main sequence. A possible explanation could be that in a relatively dense wind (compared to the less luminous and/or larger stars), free-free emission (becoming stronger towards the infrared) makes the spectrum slightly more red (Wright and Barlow, 1975). Alternatively, this could also be caused by line blanketing. In that case, significant absorption takes place in the stellar wind, which causes the spectral energy distribution to shift to lower wavelengths and make the spectral energy distribution of the star appear to have a lower effective temperature (Herrero, Puls and Najarro, 2002; Bianchi and Garcia, 2002; Markova, Puls, Repolust et al., 2004).

Next, we discuss how these seemingly modest differences affect the appearance of stellar populations in the CMDs that we presented in Sect. 4.3.1. We again focus on the BSGs that are present in the synthetic population where $\alpha_{\rm sc} = 100$ and $\alpha_{\rm ov} = 0.33$. We remind the reader that the synthetic grid only covers

[5] Line blanketing is the re-emission of light at higher wavelength after a photon is absorbed, thereby shifting the spectrum to the red (Milne, 1928; Hubeny and Lanz, 1995).

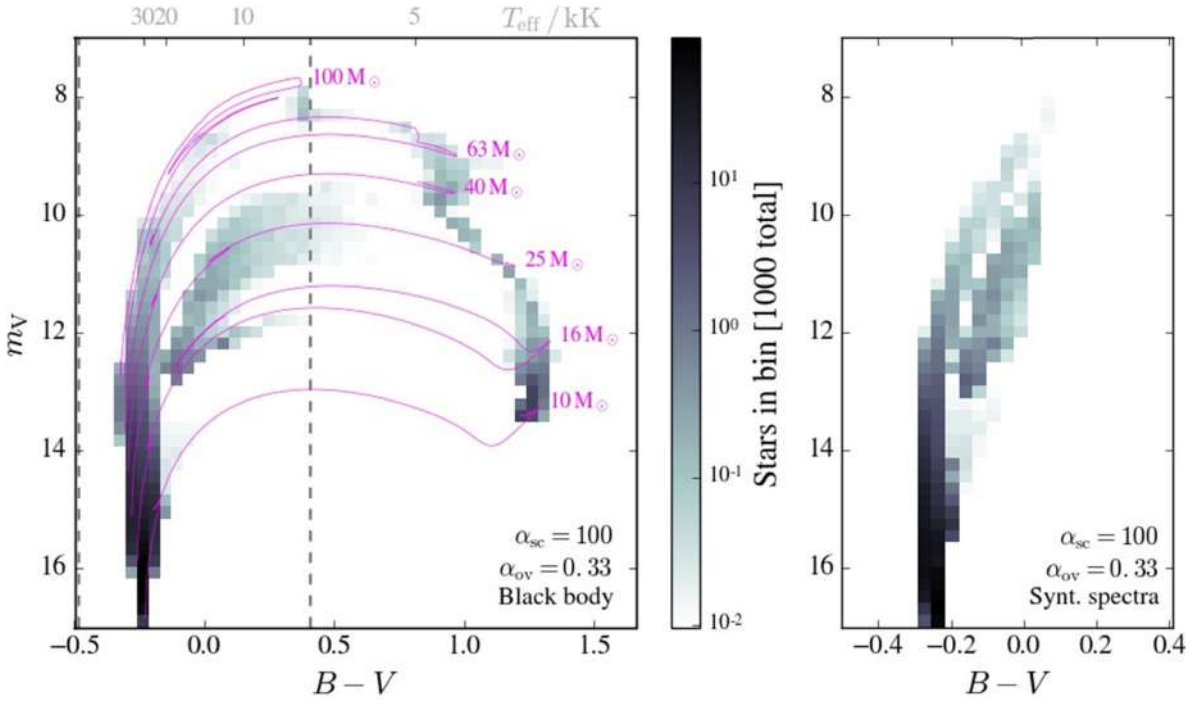

Figure 4.10: Same as Fig. 4.9, but now with the classical $B-V$ color and V magnitude on the x-axis and y-axis, respectively.

temperatures down to 9 kK– therefore, the coolest BSGs and the RSGs do not appear in the CMDs constructed with the synthetic spectra method. The main purpose of doing this comparison is to test if the predictions from Sect. 4.3.1, i.e., that there are identifiable BSG populations in the different CMDs, still holds. Below, we discuss individual CMDs:

GAIA: Fig. 4.8 has shown that the $G_{\rm BP} - G_{\rm RP}$ color obtained by synthetic spectra is similar to the blackbody color but with a slightly less steep correlation. This feature emerges as well in the CMD shown in Fig. 4.9, where similar colors are predicted by both methods. Also the G magnitudes are comparable. As a result, the general shape of both the main sequence and the BSG population remain the same, although it becomes a little more difficult to discriminate between both. In particular, at the low magnitude end around $G \approx 10$, the gap between both at $G_{\rm BP} - G_{\rm RP} \approx -0.1$ (corresponding to $T_{\rm eff} \approx 15$ kK) is almost closed. Still, the presence of a BSG population should be a well-discernable feature if observational data with high enough quality can be obtained.

B-V: A prominent difference between the synthetically derived color - temperature relations for the $G_{\rm BP} - G_{\rm RP}$ and $B-V$ colors is that the value of the $B-V$ color is less sensitive to the temperature (Fig. 4.8). This results in the $B-V$ values of the main sequence and BSG populations being in a very narrow range and nearly overlapping. Thus, identifying the BSG population using the $B-V$ color CMD shown in Fig. 4.10 would likely prove to be difficult. For the V magnitudes derived with both methods we find good agreement. Thus, this is also true for the other two CMDs with UBV colors, where we also show the V magniture on the y-axis.

U-B: For the $U-B$ color, the situation appears to be more hopeful than for the $B-V$ color because the synthetic spectra method predicts the $U-B$ color to span a range of about 0.8 magnitude in the considered temperature range, whereas this number was only about a third of a magnitude for $B-V$. A cause for this is that the rise of the Balmer jump towards temperatures of ∼10 kK (lowering the U

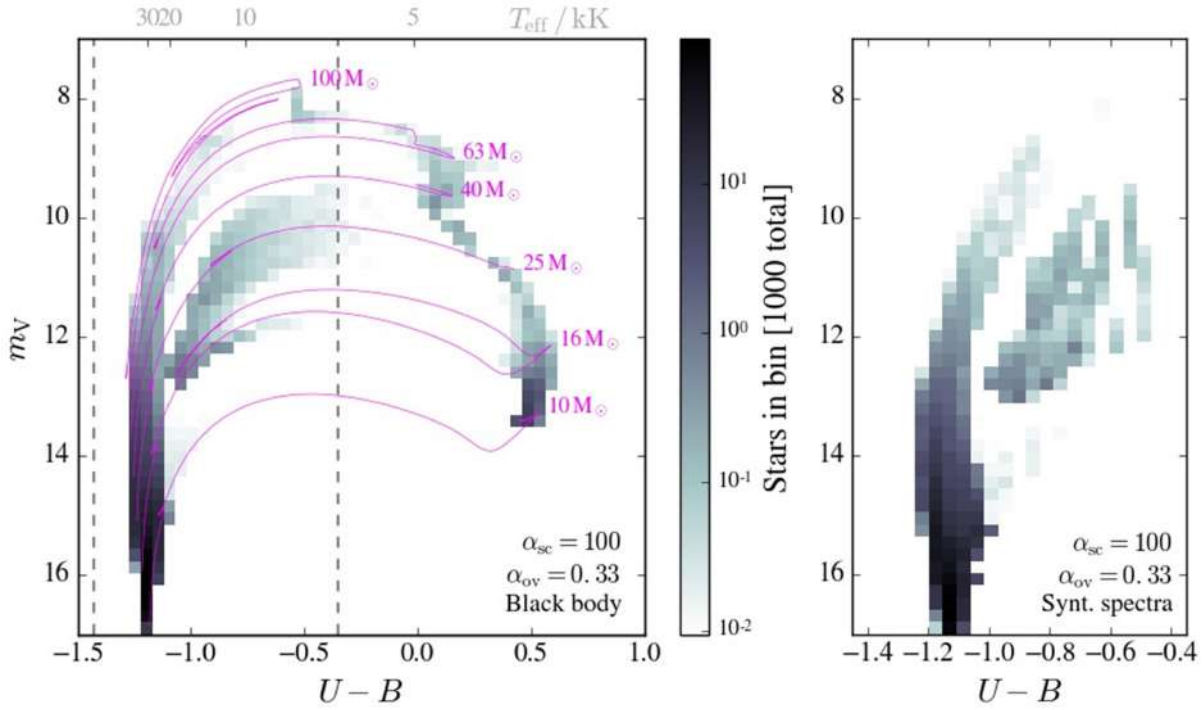

Figure 4.11: Same as Fig. 4.9, but now with the classical $U-B$ color and B magnitude on the x-axis and y-axis, respectively.

magnitude) expedites the $U-B$ color becoming more red with decreasing temperature. As a consequence, the right panel of Fig. 4.11 shows a BSG population which should in principle be observable.

U-V: The $U-V$ color, which as previously mentioned corresponds to the sum of the $U-B$ and $B-V$ colors, is the classical UBV color that is the most sensitive to the effective temperature. To identify a possible BSG population it seems to be even slightly more suitable than the $U-B$ CMD because, although the shape of the populations looks comparable, the $U-V$ color spans a somewhat larger magnitude range (Fig. 4.8 and Fig. 4.12).

In conclusion, for the colors obtained with the synthetic spectra method we consider the $G_{\rm BP}-G_{\rm RP}$ and $U-V$ colors to be the most promising for identifying a possible BSG population. The $B-V$ color should probably be disregarded for this purpose.

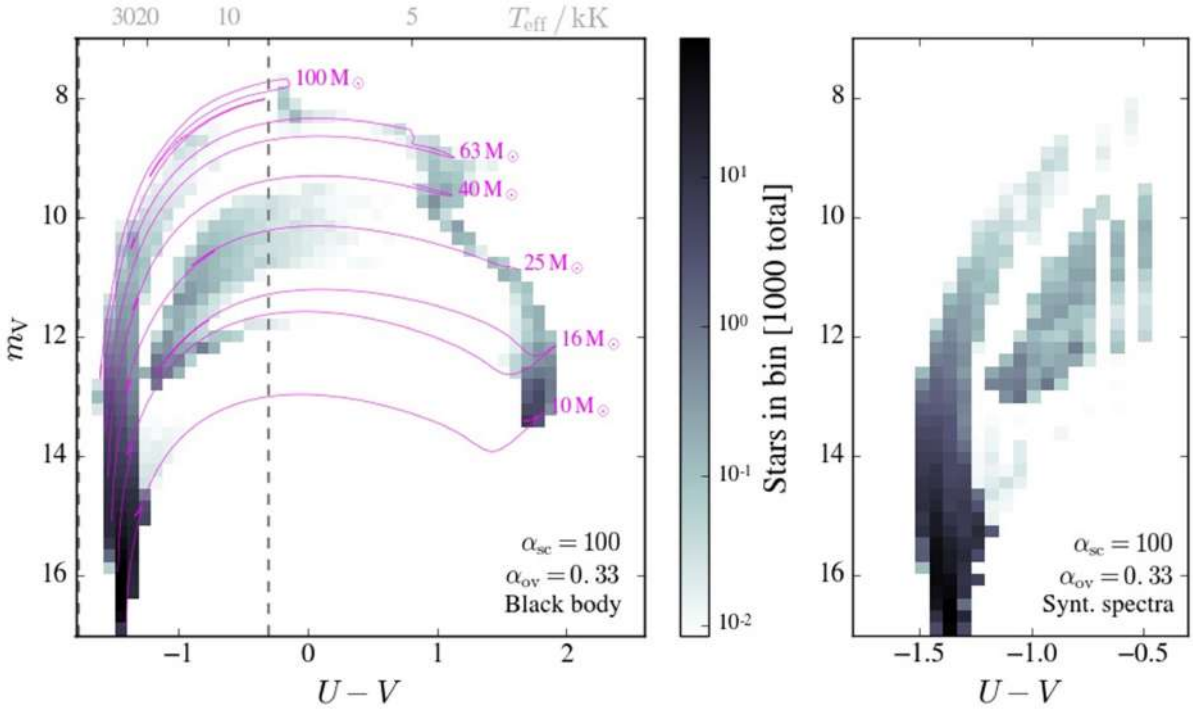

Figure 4.12: Same as Fig. 4.9, but now with the classical $U-V$ color and V magnitude on the x-axis and y-axis, respectively.

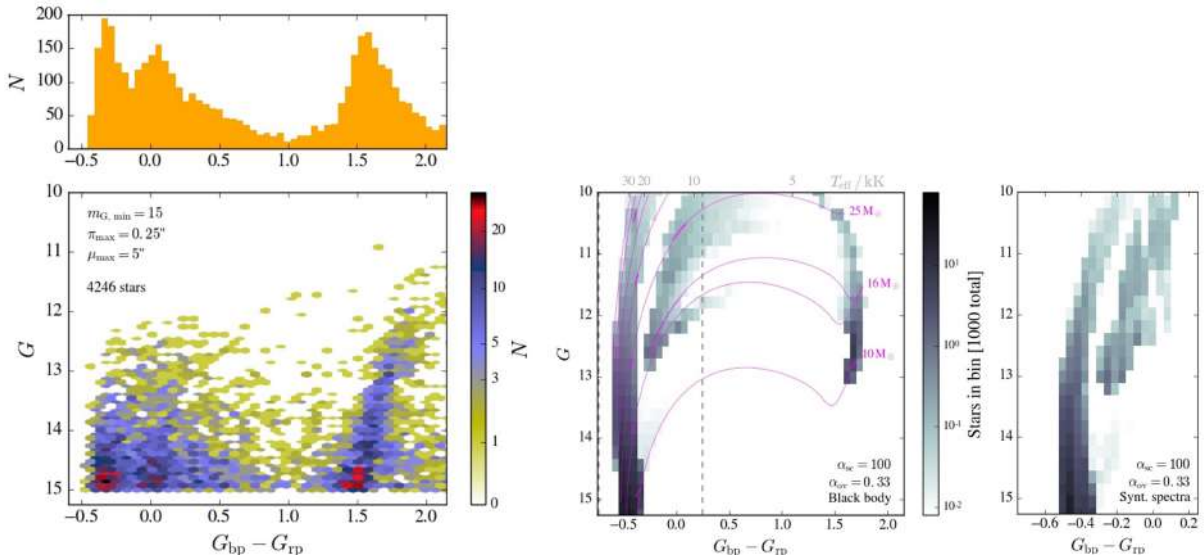

Figure 4.13: **Bottom left:** color magnitude diagram showing the observed population of stars in the Small Magellanic Cloud with a G magnitude lower than 15. In the top left of this panel, π_{max} and μ_{max} indicate the parallax and proper motion criteria that are set on the stars to be considered members of the Small Magellanic Cloud. The color indicates the number of stars observed in each hexagon. **Top left:** number distribution of the $G_{BP} - G_{RP}$ color of the stars shown in the bottom left panel. **Right:** the color magnitude diagram obtained using the black body approach (right panel of Fig. 4.3) and assuming efficient semiconvection ($\alpha_{sc} = 100$) is shown again for comparison.

4.3.3 Comparison with observations

In this section, we compare our synthetic populations with observed populations of bright stars in the SMC. One thing that we focus on is finding out if the BSG population, that is predicted by the $\alpha_{sc} = 100$ evolutionary models, exists. The observed population that we use is the combined Massey (2002) and GAIA catalog described in Sect. 4.2.3.

The distance estimates from GAIA allow us to identify sources that are likely foreground stars by discarding those with a parallax of $\pi > 0.25$ mas and/or with a very high proper motion of $\mu > 5$ mas. It turns out that such objects are numerous in the Massey (2002) catalog: without these selection criteria, we find that Fig. 4.13 would contain 6474 sources instead of the 4246 that are now in the plot. Most of those 2228 supposedly foreground stars are yellow stars with a typical color of $G_{BP} - G_{RP} \approx 1$ (which corresponds to a temperature roughly comparable to the Solar temperature). Yellow stars are predicted to be very rare at high luminosities, because such stars spend their main sequence lifetimes as blue objects and do helium burning as either blue or red supergiants, with a very short time in between. Thus, GAIA allows us to get a much better agreement between the theoretically predicted population and the observed population. Below we again discuss the different CMDs individually.

GAIA: We identify three features that emerge in the observational CMD shown in Fig. 4.13:

I. Around $G_{BP} - G_{RP} \approx -0.35$ a band of stars appears that we interpret as the main sequence. In the top left panel of Fig. 4.13, this band of stars appears as the most left peak in the number distribution of observed stars. This peak is somewhat redder than what the main sequence in the synthetic population predicts (where the peak is at $G_{BP} - G_{RP} \approx -0.5$) – we discuss this in more detail below.

II. The second feature is a peak in the number of stars at $G_{\rm BP} - G_{\rm RP} \approx 0$. Excitingly, this is close to the value where the evolutionary models with $\alpha_{\rm sc} = 100$ predict the blue supergiant population to reside. However, the G magnitude range does not seem to match. We again discuss this in more detail below. It is important to note that Castro, Oey, Fossati et al. (2018) find hints that in the population of stars that are in their sample of the RIOTS4 and 2dF surveys, there also seems to be a group of stars that resides at temperatures cooler than the main sequence – at a luminosity where the coolest main sequences stars are 30 kK, these color stars form a band around 15-20 kK. The vast majority of this group shows emission features, which might be associated to the presence of a disk that could affect photometric colors. To what extent i) this is also the case for stars in our sample and ii) this affects our theoretical predictions, remains to be understood.

III. Finally, there is a third concentration of stars at $G_{\rm BP} - G_{\rm RP} \approx 1.6$, which corresponds well to the predicted red supergiant population. The only major difference between observations and theory here is that theory predicts a population of luminous RSGs ($G \lesssim 11$ and a $G_{\rm BP} - G_{\rm RP}$ value of about 1 to 1.5) that is absent in the observed population. Although puzzling, this is in agreement with previous observations of RSGs in the SMC (Davies, Crowther and Beasor, 2018). These have shown that the upper luminosity limit of RSGs, which is around $\log\left(L \,/\, \mathrm{L}_{\odot}\right) \approx 5.35$, indicates that the SMC does not contain RSGs significantly more massive that $20\,\mathrm{M}_{\odot}$. This is a feature that cannot be explained with IMF and lifetime effects alone. We discussed this in detail in Chapter 3.

IV. Between features II and II, there is a pronounced gap centered at $G_{\rm BP} - G_{\rm RP} \approx 1$. This gap is reproduced by the models very well.

Generally speaking, for GAIA photometry we find similar features in the theoretical and observational CMDs. The indications we find for the existence of a BSG population could imply that an internal mixing process such as semiconvection is efficient: in case there is no mixing in the deep hydrogen envelope, practically no blue supergiants should exist (Chapter 3). However, a word of caution is necessary here. It is known that products of binary interaction can also manifest themselves as BSGs after mass accretion (Braun and Langer, 1995) or a stellar merger (Podsiadlowski and Joss, 1989). How many BSGs could be produced by binary interaction is unknown, but products of binary interaction in general are expected to be prevalent (de Mink, Sana, Langer et al., 2014).

Between the theoretical and observational CMDs, some differences are also visible. We discuss these below. The first difference between the observational CMD and the synthetic CMD is that the observed main sequence (and BSG population) is about ~0.15 magnitude redder than expected from theory and the BSGs population being significantly dimmer than the theoretical one. As already briefly mentioned, the colors and magnitudes can be affected by extinction. Here, we briefly attempt to quantify how much the colors and magnitudes are affected. Because the extinction $A(\lambda)$ is strongest at shorter wavelengths (Fig. 4.14), stars appear redder than they are intrinsically. For example, Gordon, Clayton, Misselt et al. (2003) find an average difference in extinction, i.e., reddening, of $A(B) - A(V) = E(B-V) \approx 0.2$ for SMC sources. While this study does not provide any numbers for extinction in the GAIA bands[6], we can still use the $A(\lambda)/A(V)$ relation of Gordon, Clayton, Misselt et al. (2003) to obtain an estimate. For this, we first need a value for $A(V)$. Given the measured relation $R(V) = A(V) \,/\, E(B-V) \approx 2.75$[7] which is typical for SMC sources (again Gordon, Clayton, Misselt et al., 2003), rearranging the equation and filling in both known values yields $A(V) \approx 0.55$. Next, we are going to make the assumption that the extinction measured by Gordon, Clayton, Misselt et al. (2003) at wavelength λ equals the extinction of a GAIA filter

[6] This study was conducted ten years before the launch of the GAIA satellite.

[7] $R(V)$ is a measure for the slope of the extinction. If there is no wavelength dependence of the extinction, there is also no reddening.

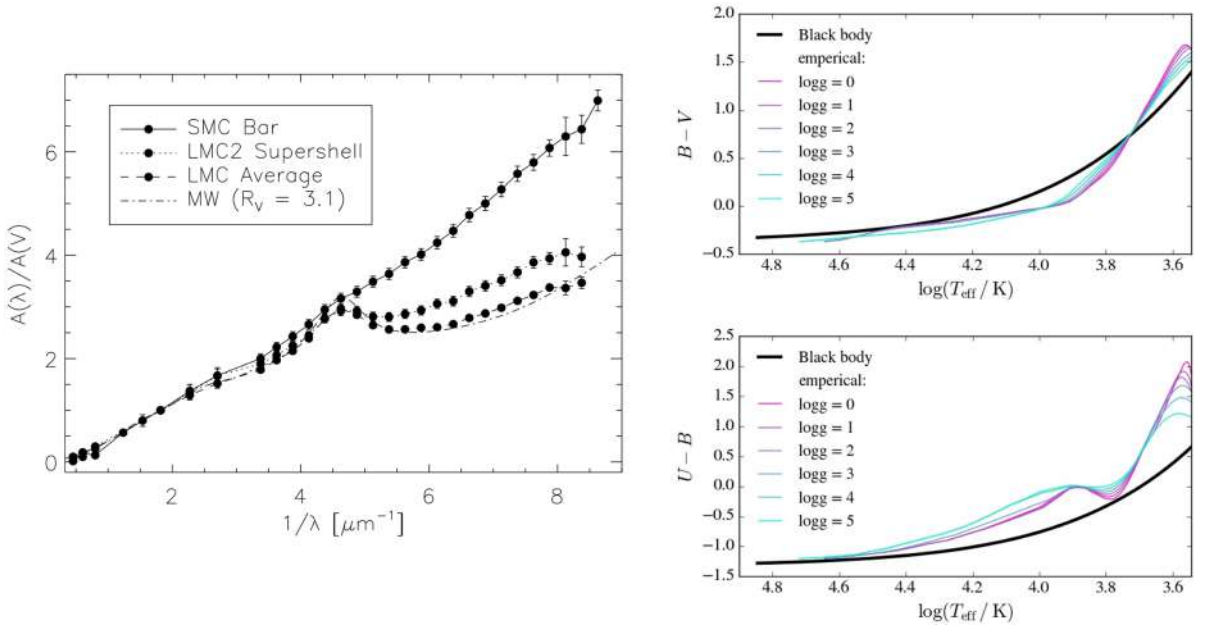

Figure 4.14: **Left:** figure showing the wavelength dependence of the average relative extinction for a.o. Small Magellanic Cloud sources. This figure was taken from Gordon, Clayton, Misselt et al. (2003). **top right:** Emperical $B-V$ color-temperature relations from Worthey and Lee (2011) for different values of the surface gravity $\log g$. For comparison, we also show the result for our black body approximation. **top right:** same as the top right panel, but now we show the temperature dependence of the $U-V$ color.

centered at this wavelength λ[8]. Then, the extinction magnitudes that we obtain are the following. For G, which is centered around $\lambda = 6500$ Å (Fig. 4.1) where $A(\lambda) = 0.8A(V)$ (their Fig. 10 and Table 4), we get $A(G) \approx 0.45$. The $G_{\rm BP}$ filter is centered around the same λ as the V filter, so we adopt $A(G_{\rm BP}) = 0.55$. Finally, $G_{\rm RP}$ is centered around $\lambda = 8000$ Å where $A(\lambda) = 0.57A(V)$ and thus $A(G_{\rm RP}) \approx 0.31$. Using the last two values, we obtain a reddening of $A(G_{\rm BP}) - A(G_{\rm RP}) = E(G_{\rm BP} - G_{\rm RP}) = 0.24$ magnitude. The value for reddening of $E(G_{\rm BP} - G_{\rm RP}) = 0.24$ is in reasonable agreement with the slight offset we found between the theoretical en observed populations, where the latter were about 0.15 magnitude shifted to the red. Considering this our estimate of $E(G_{\rm BP} - G_{\rm RP}) = 0.24$ might, if anything, slightly overestimate the reddening. An extinction value of $A(G) = 0.45$ shifts the observed population to somewhat lower magnitudes (i.e, more bright) but by far not enough to single-handedly account for the difference described above. Although for hot stars the extinction in the G band might be slightly larger than the estimated value of $A(G) = 0.45$ because relatively more light is emitted at short wavelengths (where extinction is stronger), we do not expect this difference to be dramatic. The reason is the following: even in the extreme case that *all* radiation is emitted at the short wavelength end of the filter at 4000 Å, the extinction would be only moderately higher: of the order of $1.374\,A(V) = 0.76$ (adopting values from Gordon, Clayton, Misselt et al., 2003). This, however, is not a realistic scenario (Fig. 4.1, bottom).

Another difference between the observational CMD and the synthetic CMD is the G magnitude distribution of the population with color $G_{\rm BP} - G_{\rm RP} \approx 0$. Here, the G magnitude range of the observed population does not match the theoretical predictions. There are a few reasons for this. First, we have

[8] For wide-band filters such as $G_{\rm BP}$, $G_{\rm RP}$ and expecially G (see Fig. 4.1), this could be a somewhat crude assumption because the flux distribution can be shifted towards shorter or longer wavelengths, resulting in a difference in extinction. The narrower the filter, the less of a problem this is.

simulated only stars with initial masses of $10\,M_\odot$ and above – this results in the bottom-center and bottom-right part of the synthetic CMD remaining empty (Sect. 4.3.1). Still, the theoretically predicted upper magnitude limit for BSGs is rather high at $G \approx 13$ because model sequences in Fig. 4.13 below $\sim 16\,M_\odot$ do not experience blue loops. These blue loops do occur in case of lower overshooting (Chapter 3). Thus, a possible explanation for the observed BSG population at high G magnitudes is that overshooting becomes smaller below $\sim 16\,M_\odot$. For this we consider Fig. 4.18, which contains six CMDs like the one in the middle of Fig. 4.13, but with different values for the overshooting parameter α_{ov}. This figure shows that in synthetic populations with lower overshooting, the separate BSG population would extend to $G \approx 14$. Apart from the $10\,M_\odot$ track for the case of $\alpha_{ov} = 0.22$, all of these become BSGs during to their evolution down to the lowest mass that is simulated[9].

The trend of overshooting decreasing with mass below $16\,M_\odot$ would be in remarkable agreement with the result of Grin et al. (to be submitted), who fitted the theoretical terminal age main sequence to the one observed by Castro, Fossati, Langer et al. (2014) through varying the overshooting parameter. Their result is that the overshooting parameter increases roughly linearly between $8\,M_\odot$ (where it would have a value of $\alpha_{ov} = 0.2$) and $15\,M_\odot$ and then stays constant. However, they find that the overshooting parameter increases to up to $\alpha_{ov} = 0.5$ at masses around $15\,M_\odot$ to $25\ M_\odot$. This value is higher than the prefered value found in Chapter 3, because it would result in the BSG phase being only very short lived (Fig. 3.10). A second reason for the the theoretical populations to have smaller G magnitudes is that the observed population should be affected by extinction. However, the value for the extinction that we calculated above only would have an only moderate effect: it would decrease the G magnitude by at most half a magnitude. This means that the synthetic population would move at most half a magnitude to the south in the CMD after correction for extinction.

Thus, in case of low overshooting below $16\,M_\odot$and accounting for extinction, we find that there is a distinguishable BSG population in our synthetic CMD up to $G \approx 14.5$. In the observational CMD (bottom left panel of Fig. 4.13), that overlaps only slightly with the magnitude range where one can argue that the GAIA data show distinct main sequence and BSG populations. Therefore, without the densely populated part in the observational CMD (up to $G = 15$) covered in the synthetic CMD as well, care has to be taken before drawing strong conclusions. Currently, one can argue that the presence of a second population in the GAIA CMD is an *indication* for the presence of a BSG population caused by internal mixing.

Another explanation could be that a population of rapidly rotating stars is causing a bifurcation in the GAIA CMD. Such a feature has been observed before as a red and blue main sequence (e.g. Milone, Marino, Di Criscienzo et al., 2018, who observed clusters in the Magallanic clouds). Marino, Przybilla, Milone et al. (2018) found spectroscopic evidence that faster rotating stars resided in the red main sequence, appearing cooler as a result of gravity darkening (von Zeipel, 1924) as proposed by Bastian and de Mink (2009). However, this effect cannot be expected to cause a color shift which is as large as the difference between the main sequence and the BSG populations in the GAIA CMD, which suggests an effective temperature difference of the order of 10 kK. Thus, we conclude that gravity darkening is unlikely to cause this bifurcation. A more likely possibility would be that disk emission, also related to rapid rotation (Rivinius, Carciofi and Martayan, 2013) would cause excess emission at longer wavelengths. In fact, as mentioned before, Castro, Oey, Fossati et al. (2018) did in fact find emission features in most of the stars in the population right to the main sequence. Whether that could lead to these star + disk systems having a small spread in their color as is observed around $G_{BP} - G_{RP} \approx 0$ (despite a suspected scatter caused by random inclination angles and various accretion disk masses) would need to

[9] If a very small ($\alpha_{ov} = 0.11$) to non-existent overshooting region is assumed, RSGs are no longer formed around $G = 12$, which would be in conflict with observations.

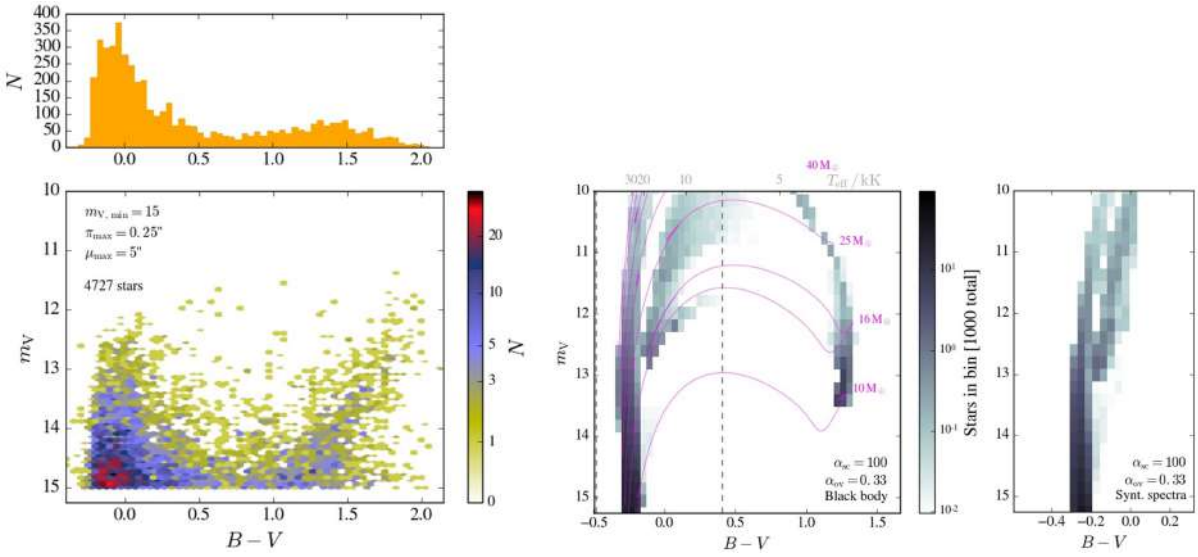

Figure 4.15: Same as Fig. 4.13, but now with the classical $B-V$ color and V magnitude on the x-axis and y-axis, respectively.

be investigated. Alternatively, the BSGs could be descendants of binary interaction (e.g. Podsiadlowski and Joss, 1989), which is expected to be a major evolutionary channel for massive stars (Sana, de Mink, de Koter et al., 2012).

B-V: The CMD with the $B-V$ color and V magnitude (Fig. 4.15), composed of observations of Massey (2002) (but again cleaned of foreground stars using the GAIA parallaxes and proper motions), shows two major differences to the GAIA CMD.

The first difference is that the peak in the number distribution that corresponds to red supergiants is much more spread out than the in the GAIA CMD. This could be an indication that the observational errors for the $B-V$ color are larger, since theory predicts a narrow RSG branch also for $B-V$. A possible reason for this is that GAIA, aided by the fact that as a space telescope is not hindered by atmospheric distortions, has less crowding issues given its superior angular resolution. Also, the wavelength range of the filters could be a factor: the GAIA bands are i) broader, and thus less sensitive to individual features in the spectra, and ii) located at longer wavelengths, where extinction is weaker. However, relatively large errors do not seem to be in agreement with the typical $B-V$ errors mentioned in the Massey (2002) catalog for the sources shown in Fig. 4.15: these have a not-too-alarming root mean square (RMS) value[10] of $\sigma_{(B-V),\,\mathrm{RMS}} = 0.023$. The spread in RSG colors could be considered to be an indication that the errors provided in the catalog of Massey (2002) might be underestimated in at least some cases. Care has to be taken to draw such a conclusion, however, since there could be other explanations. Such an other option is that at relatively low temperatures, the black body approach is inaccurate for in particular $B-V$ photometry. To check this, we employ color - temperature relations from Worthey and Lee (2011) which also cover RSG temperatures (in contrast to our synthetic model spectra, which go down to only $T_{\mathrm{eff}} = 9\,\mathrm{kK}$). These empirical relations for SMC metallicity are shown in the top right panel of Fig. 4.14. They show that at around RSG temperatures (i.e. $T_{\mathrm{eff}} \lesssim 3.7$), the colors are indeed more sensitive on temperature than what is predicted by the black body method – but the difference is small. To better assess the cause of this spread, it would be mandatory to extend the model parameter space to lower masses, to cover the magnitude range where most RSGs are observed.

[10] Calculated as $\sigma_{\mathrm{RMS}} = N^{-1}\,(\Sigma_{i=1}^{N}\sigma_i^2)^{0.5}$.

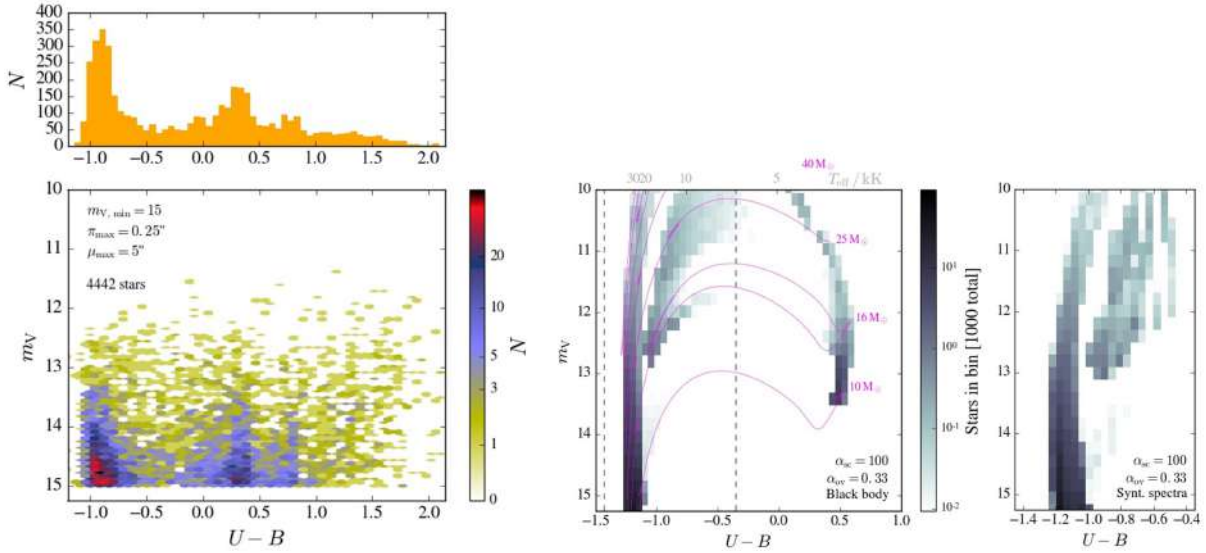

Figure 4.16: Same as Fig. 4.13, but now with the classical $U-B$ color and V magnitude on the x-axis and y-axis, respectively.

The second difference between the $B-V$ and GAIA CMDs, which is the more relevant one for this study, is that there are no longer two peaks in the number distribution at the blue end, as was the case for the GAIA CMD. Instead, one broad peak is present. With a width of around half a magnitude, this peak is much broader than the main sequence in the synthetic CMDs shown in Fig. 4.15. The $B-V$ color is not very sensitive to the temperature, especially when the colors are derived with synthetic spectra method (right panel of Fig. 4.15). In that case, the models from the hottest main sequence stars to the 9 kK BSGs span a color range of only 0.3 to 0.4 magnitudes. We identify two possible scenarios that could explain the shape of this peak in the number distribution. The first scenario would be that the broad peak centered around $B-V \approx 0$ contains both the main sequence and the BSG population, where both have merged into one feature due to low temperature sensitivity of the $B-V$ color, even for small errors on individual colors. The errors on indivudual colors might smear out stars enough to conceal the already very narrow to non-existing gap between the main sequence and the BSG population. If the relatively small errors of $\sigma_{(B-V),\mathrm{RMS}} = 0.023$ are accurate, this scenario might be prefered: the main sequence (width of about 0.1 to 0.15 magnitude) alone could not explain the observed $B-V$ peak width of ~0.5 magnitude. In the low overshooting CMDs shown in Fig. 4.19, the total width of the main sequence plus BSG population is of the order of half a magnitude as well. Alternatively, the second scenario (considering only the $B-V$ CMD) would be that the BSG popululation does not exist, and the main sequence is wider than expected because of underestimated errors or individual differences in reddening between different sources. Currently, we are not able to discriminate between both scenarios. Because of this, we are not able to draw conclusions about the existence of a BSG population from the information that the $B-V$ CMD provides.

U-B: In principle, as discussed in Sect. 4.3.2, the $U-B$ CMD should be more suitable for identifying a possible BSG population than the $B-V$ counterpart because this color is more sensitive to the stellar temperature. This prevents the main sequence and BSG populations from merging (right panel of Fig. 4.15 vs. right panel of Fig. 4.16). However, the U filter is plagued by extinction more than shorter-wavelength B and V filters – according to Gordon, Clayton, Misselt et al. (2003), the extinction ratios $A_V : A_B : A_U$ are $1 : 1.4 : 1.7$. This trend is in line with the larger RMS error of the $U-B$

color of the sources shown in the bottom left panel in Fig. 4.16, which in the Massey (2002) catalog have a RMS error of $\sigma_{(U-B),\mathrm{RMS}} = 0.053$ – i.e., more than two times higher than $\sigma_{(B-V),\mathrm{RMS}}$. The observational CMD is not corrected for reddening, which should be around the same as for the $B-V$ color: $E(U-B) \approx E(B-V) \approx 0.2$, calcutated using again extinction values of Gordon, Clayton, Misselt et al. (2003).

In the observed $U-B$ CMD (left in Fig. 4.16), it seems that a main sequence population is present centered at $U-B \approx -0.9$. This is in good agreement with the theoretically predicted main sequence around $U-B = -1.1$ reddened by an expected 0.2 magnitude. A second peak, as observed by GAIA, is again absent as is the case for the $B-V$ CMD. Surprisingly, the peak in the number distribution around $U-B = -0.9$ is about half as wide as the blue peak for $B-V$. This is not expected because i) the $U-B$ color is more sensitive to the temperature and ii) the errors are larger for $U-B$. In fact, the peak can easily be explained by a 0.2 magnitude wide main sequence slightly widened by the errors of $\sigma_{(U-B),\mathrm{RMS}} = 0.053$. For the synthetic populations shown in Fig. 4.16 the separation between the bluest part of the main sequence and the coolest helium burning BSGs seems to be half a magnitude. We see the same separation for evolutionary models around $m_V \approx 13.5$ with low overshooting (which do not burn helium for a significant time as BSGs for the standard set of mixing assumptions) in Fig. 4.20). This is two times wider than the blue peak that is observed. The consequence of this is that it is not possible that two peaks in the number distribution would be present intrinsically (as for the GAIA CMD, Fig. 4.13, left) but large individual errors merge both peaks in one peak – this would never result in a peak that is narrower than the separation of both peaks. Thus, it appears that in the case of the $U-B$ CMD, the observed blue peak is in line with the presence of only a main sequence population. The BSG population, if present, would not be recognizable as a peak in the number distribution but would be smeared out around the interval $-1.0 < U-B < 0$. Corrected for an extinction of $A(V) = 0.55$ (see above), this low α_{ov} BSG population would extend not further than to an m_V magnitude of 14.5. Thus, the synthetic CMD offers again no population to compare with at the dim end. Also, number comparisons cannot be done because of this incompleteness. Therefore, to identify or discard the presence of a BSG population it would seem necessary to also include lower mass models to be able to make comparisons using two fully populated CMDs.

At the red side of the CMD, the $U-B$ number distribution does show a modest peak near the theoretical value of the RSG branch ($U-B \approx 0.5$) around $U-B \approx 0.3$. Apart from that there is a 'cloud' of could stars that do not lie in the predicted narrow color range. For the bump at $U-B \approx 0.3$, we do indeed expect it there because $E(U-B) \approx 0.2$ (see above). However, when we employ the empirical temperature-color relations, these indicate that the $U-B$ color around the RSG temperature range is rather strongly shifted to the red compared to the black body predictions (bottom right panel of Fig. 4.14). This can be as much as 1.5 magnitude (emperical relations predict $U-B = 2.0$ and black body predicts $U-B = 0.5$) for stars with T_{eff} just below $10^{3.6}$ K, which is the temperature of our red giant models. Thus, the peak in the number distribution around $U-B \approx 0.3$ is in line with the black body prediction but not with the emprerical relations. This is rather puzzling as the black body approach can be expected to be inaccurate in temperature regimes where there are significant amounts of absorption in the stellar spectra. Alternatively, if we believe the emperical relations, it could be that the group of sources at $U-B = 0.3$ is an artifact and that RSG population is represented by the 'cloud' at the reddest colors.

U-V: The $U-V$ color is the sum of the $B-V$ and $U-B$ colors. Thus, the expected reddening $E(U-V)$ equals $E(B-V) + E(U-B) \approx 0.2 + 0.2 \approx 0.4$. For the main sequence band, this seems in line with the observations, as the largest density of stars in the observational CMD at $U-V \approx -1.0$ is ~0.4 magnitude further to the red than predicted by the synthetic population (Fig. 4.17), where the largest population inhabits the area where $U-V \approx -1.4$. Assuming that the errors on $B-V$ and $U-B$ are not correlated, we expect from error propagation a typical error of $\sigma_{(U-V),\mathrm{RMS}} = (\sigma^2_{(U-B),\mathrm{RMS}} + \sigma^2_{(B-V),\mathrm{RMS}})^{0.5} = 0.058$

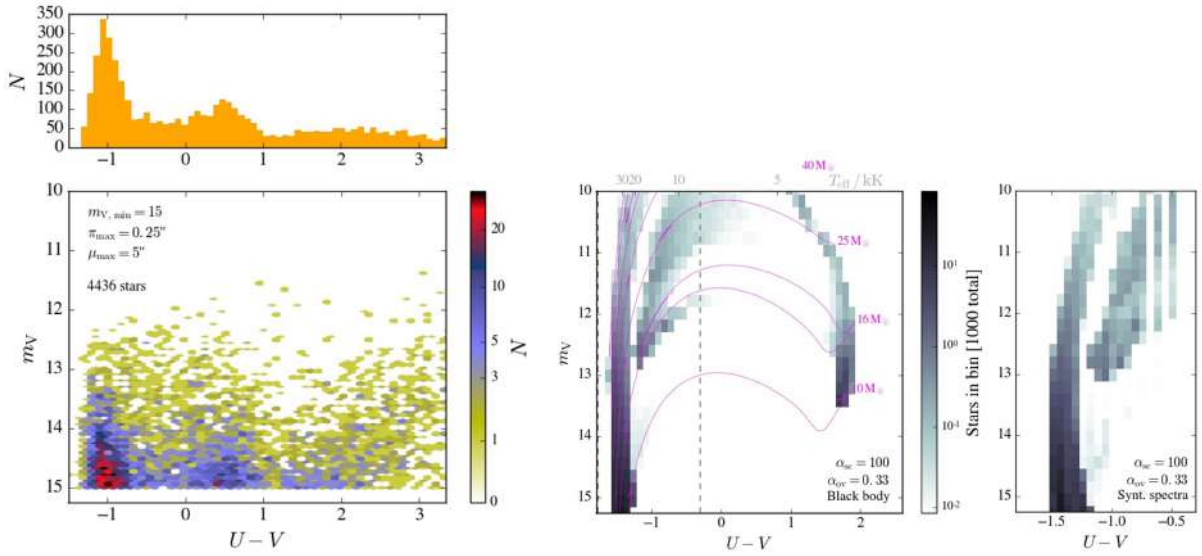

Figure 4.17: Same as Fig. 4.13, but now with the classical $U-V$ color and V magnitude on the x-axis and y-axis, respectively.

magnitude.

In the observed $U-V$ CMD (Fig. 4.17, left), features appear that are similar to those discussed above in the other two classical UBV CMDs, in particular the $U-B$ CMD. First, there is again no distinguishable BSG population – there is only a relatively narrow peak at the $U-V$ color where the main sequence is expected (after correcting for reddening). As for the $U-B$ CMD, this peak is significantly narrower than the magnitude spread of the main sequence plus BSG populations. It could again be explained by just a main sequence population with a bit of scatter due to intrinsic errors. Both in case of intermediate overshooting (synthetic CMDs shown in Fig. 4.17) and high-magnitude stars with low overshooting (Fig. 4.21), this color range is about a magnitude. Thus, the BSG population in the $U-V$ CMD, if present, does not manifest itself as a peak in the number distribution. Instead, it could be smeared out around the color interval $-1 < U-V < 0$.

Second, the RSG peak is not distinguishable as a peak – instead, the reddest stars span a much larger color range than what the synthetic population predicts. Finally, there is a significant population of 'yellow' stars around $U-V \approx 0.5$. Correcting for reddening, this corresponds to a central value of 5 kK (with the blackbody approach) or 6 kK (emperical relations). It does not correspond to the RSG temperature which is typically just below 4 kK– this is related to a color more than a magnitude further to the red. It is also a magnitude too red to correspond to the predicted BSG population.

However, the presence of a significant yellow supergiant (YSG) population is not expected on theoretical grounds due to lifetime effects (Langer, 2012). Also observationally, the YSG population in the SMC has been found to be of modest size (Neugent, Massey, Skiff et al., 2010). This seemed to be confirmed by the observed GAIA (Fig. 4.13, left) and $B-V$ (Fig. 4.15, left) CMDs. Thus, it seems more likely that there is a problem in our understanding of the $U-V$ color-temperature relations, or that there are perhaps observational biases. For a full assessment of this problem, however, we would once again need to fully explore the high magnitude range with theoretical models extending to lower masses.

4.4 Conclusions

In this chapter, we have made an attempt to compare theoretical models that were presented in Chapter 3 to observations. Because no complete spectral analysis of massive stars in the Small Magellanic Cloud is available, we used existing systematic photometric studies. These should in principle be nearly complete for stars above a certain magnitude limit. One of the major goals was to find out if a population of helium burning blue supergiants, at cooler temperatures than the main sequence, exists. This population is predicted to exist for a certain set of overshooting and semiconvective mixing efficiencies, on which we hope put constraints this way.

For this comparison we needed to translate the temperatures and luminosities of our stellar models into colors and magnitudes. We used two approaches to achieve this. First, we calculated these using the black body approximation. Second, we also calculated the colors and magnitudes using existing synthetic spectra of Castro, Oey, Fossati et al. (2018). This way, we were able to construct synthetic color-magnitude diagrams that could be compared to a combined GAIA DR2 and Massey (2002) UBV catalog. We found that that color-temperature relations of the black body and synthetic spectra predict comparable color values (typically within 0.1 magnitude). This is true especially for the hottest stars. Exceptions are the colors predicted at lower temperatures of around 10 kK, where the Balmer jump begins to distort the synthetic spectra. Even lower temperatures could not be probed because the computational method is not suitable for that purpose.

From the comparison between the observed and the synthetic color-magnitude diagrams, we emphasize that a full assessment is not possible without invoking evolutionary models of intermediate mass stars[11]. The reason is that the massive stars that are the subject of this study do, in certain temperature ranges, not cover the highest magnitude range in the observed color magnitude diagram. Only considering brighter stars (i.e., using a lower magnitude cut-off) is suboptimal because then the number of sources drops dramatically. To identify populations of stars, high-number statistics are mandatory.

Nevertheless, there are some insights obtained from the analysis. We find that the population observed by GAIA shows more identifiable features than the population of stars compiled using UBV colors and magnitudes, which seem to be more scattered. Thus, below we focus on the GAIA data. For this work, the most important feature in the GAIA color magnitude diagram is that it clearly shows a distinguishable band of observed blue stars next to the main sequence. This structure stands out most in the magnitude range where our standard set of evolutionary models do not predict helium burning blue stars. We show that around magnitude $G \approx 14.5$, this population can consist of $\sim$10 $M_\odot$ stars that are going through a blue loop excursion after experiencing semiconvective mixing. However in that case they need to have a lower core overshooting value of $\alpha_{ov} < 0.22$ pressure scale heights. At higher magnitudes of $G \approx 15$, lower mass models are required before a comparison can be done. The GAIA observations also indicate that overshooting cannot be as small as $\alpha_{ov} \leq 0.22$ in the mass range $16 \leq M/M_\odot \leq 20$ because then there would be virtually no stars in the red giant branch around $G = 11$ or 12 – but such stars are observed. This confirms the result of Chapter 3. Thus, either overshooting is dependent on initial mass (cf. the results of Grin et al., in prep) or another mechanism is responsible for creating the blue band of stars to the right of the main sequence. Plausible mechanisms could be binary interaction and/or disk emission towards the infrared caused by near-critical rotation[12].

[11] The lowest initial mass explored in this work is 10 $M_\odot$.
[12] Where the spin-up could also be the result of binary interaction.

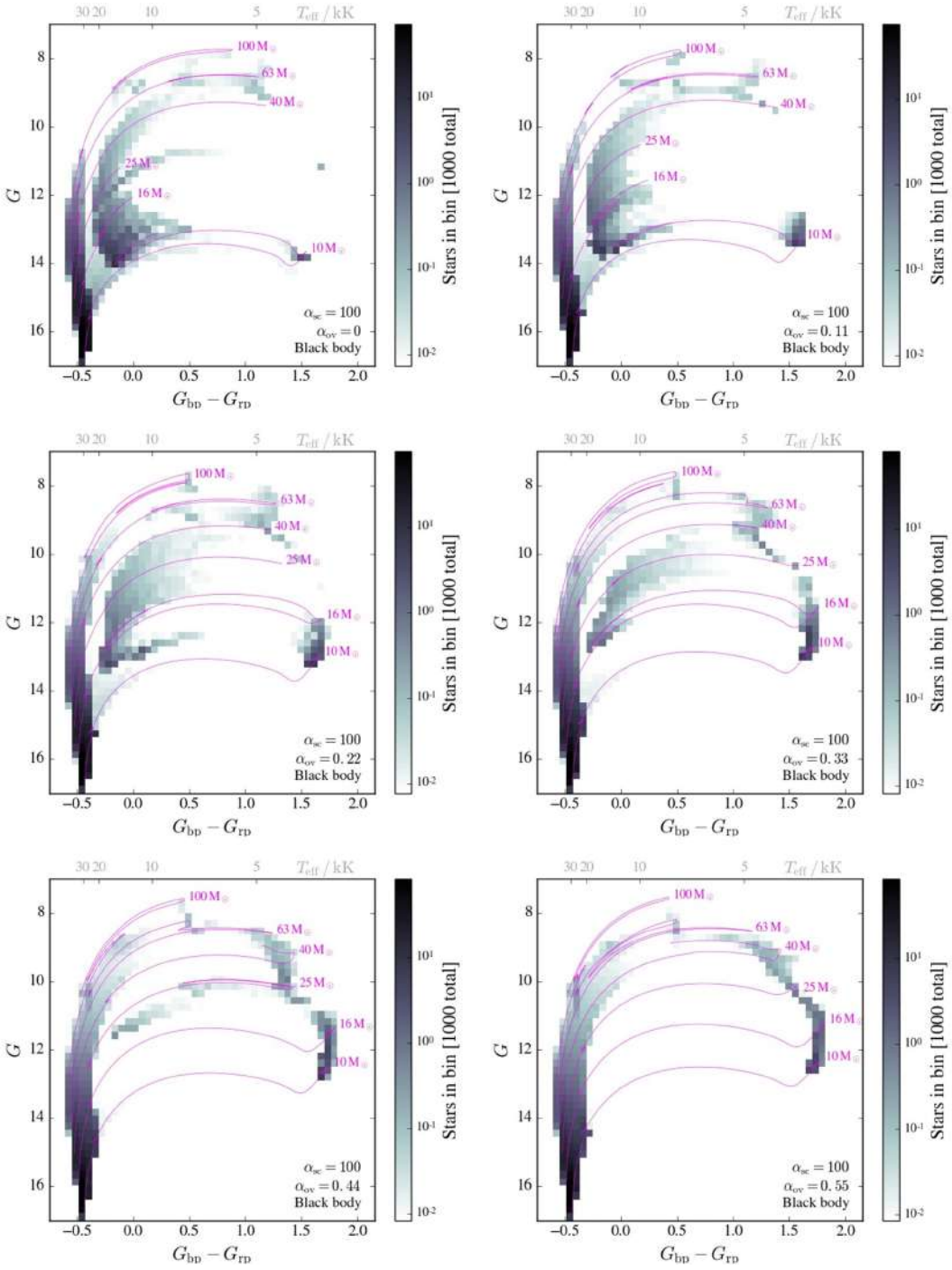

Figure 4.18: Six different color magnitude diagrams, which all have a different value for the the core overshooting parameter $\alpha_{\rm ov}$. For the models shown in each panel, the efficiency of semiconvection was $\alpha_{\rm sc} = 100$ and the black body approach was used to obtain the colors and magnitudes.

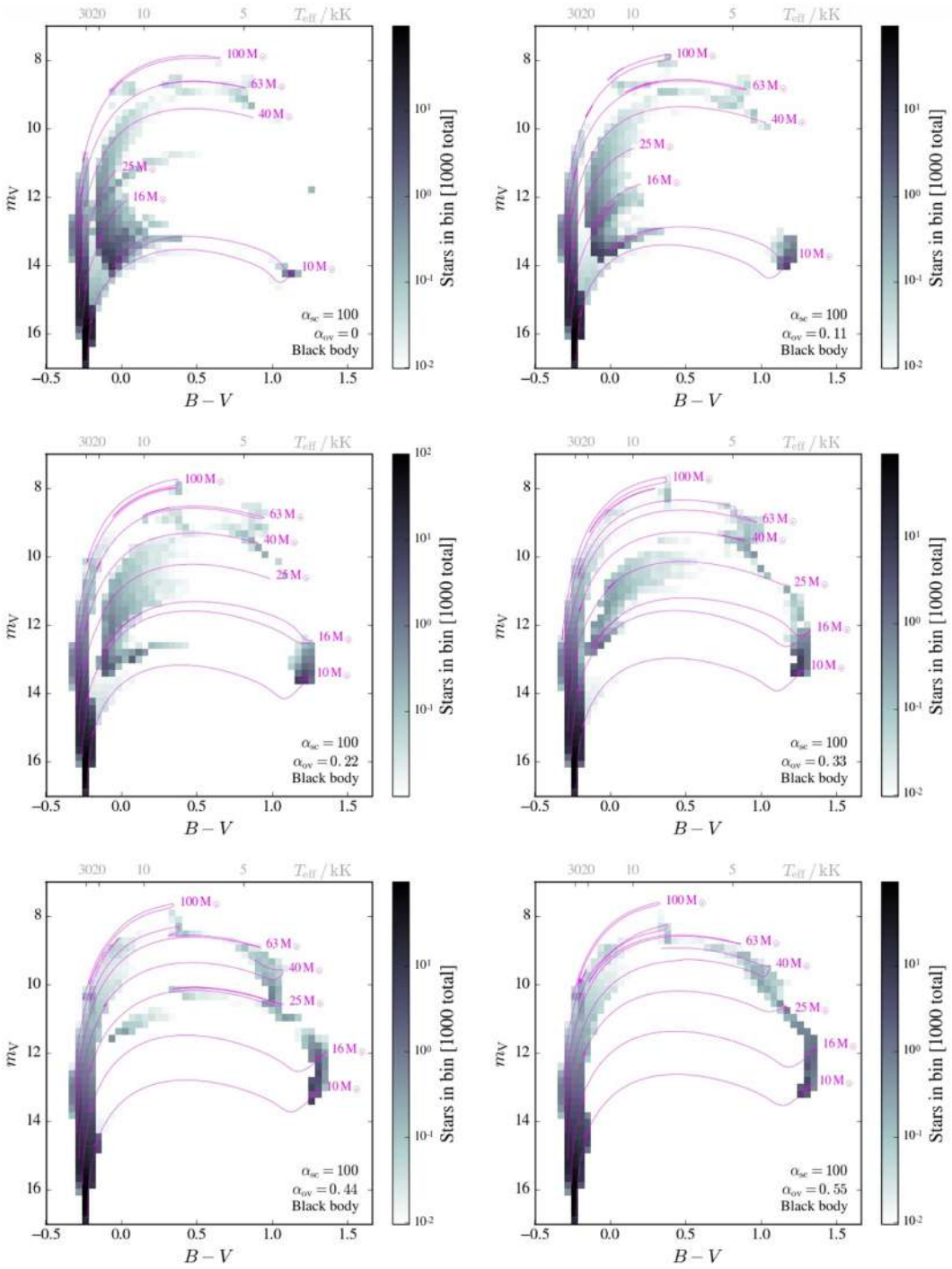

Figure 4.19: Six different color magnitude diagrams, which all have a different value for the the core overshooting parameter $\alpha_{\rm ov}$. For the models shown in each panel, the efficiency of semiconvection was $\alpha_{\rm sc} = 100$ and the black body approach was used to obtain the colors and magnitudes.

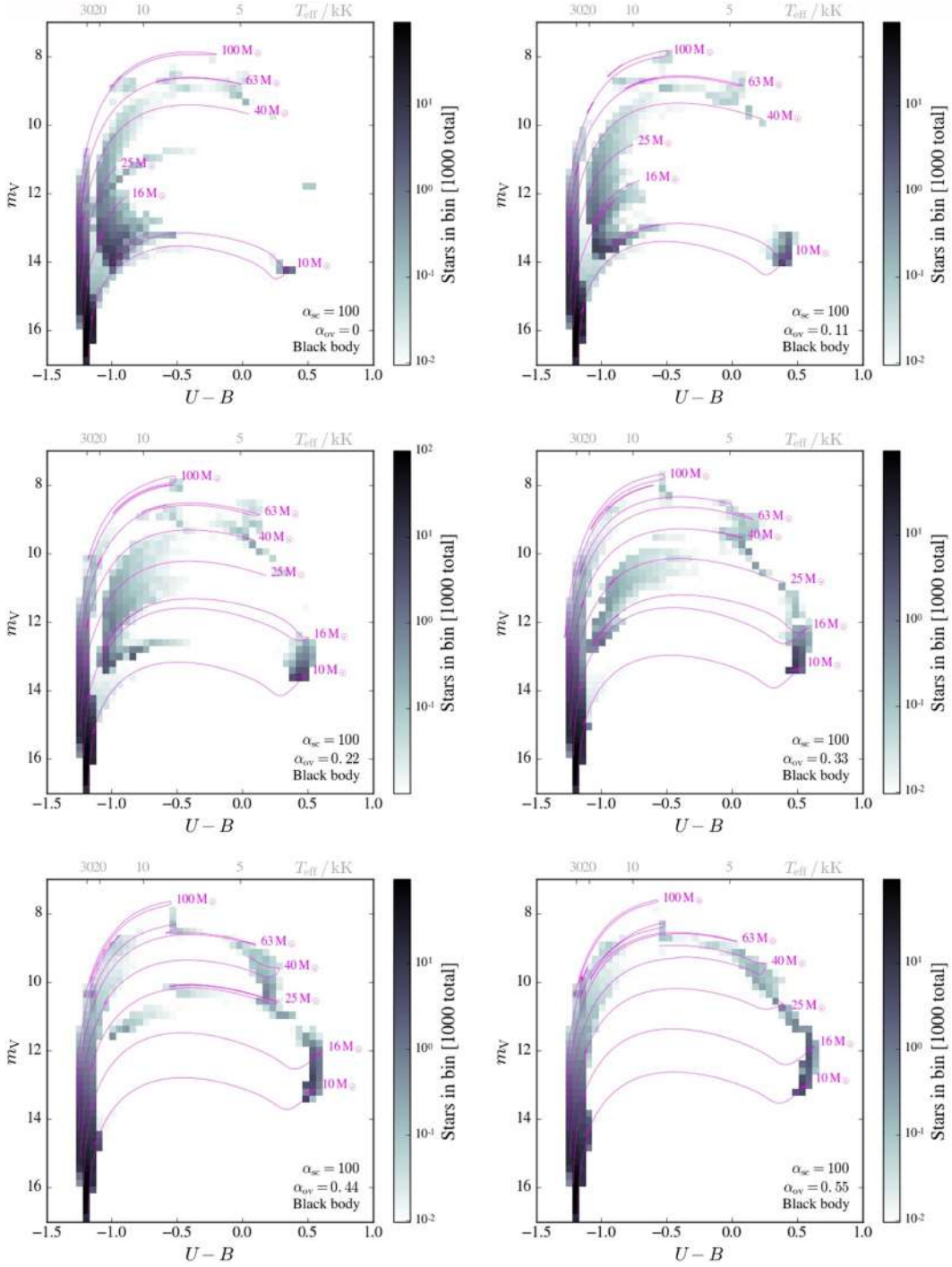

Figure 4.20: Six different color magnitude diagrams, which all have a different value for the the core overshooting parameter $\alpha_{\rm ov}$. For the models shown in each panel, the efficiency of semiconvection was $\alpha_{\rm sc} = 100$ and the black body approach was used to obtain the colors and magnitudes.

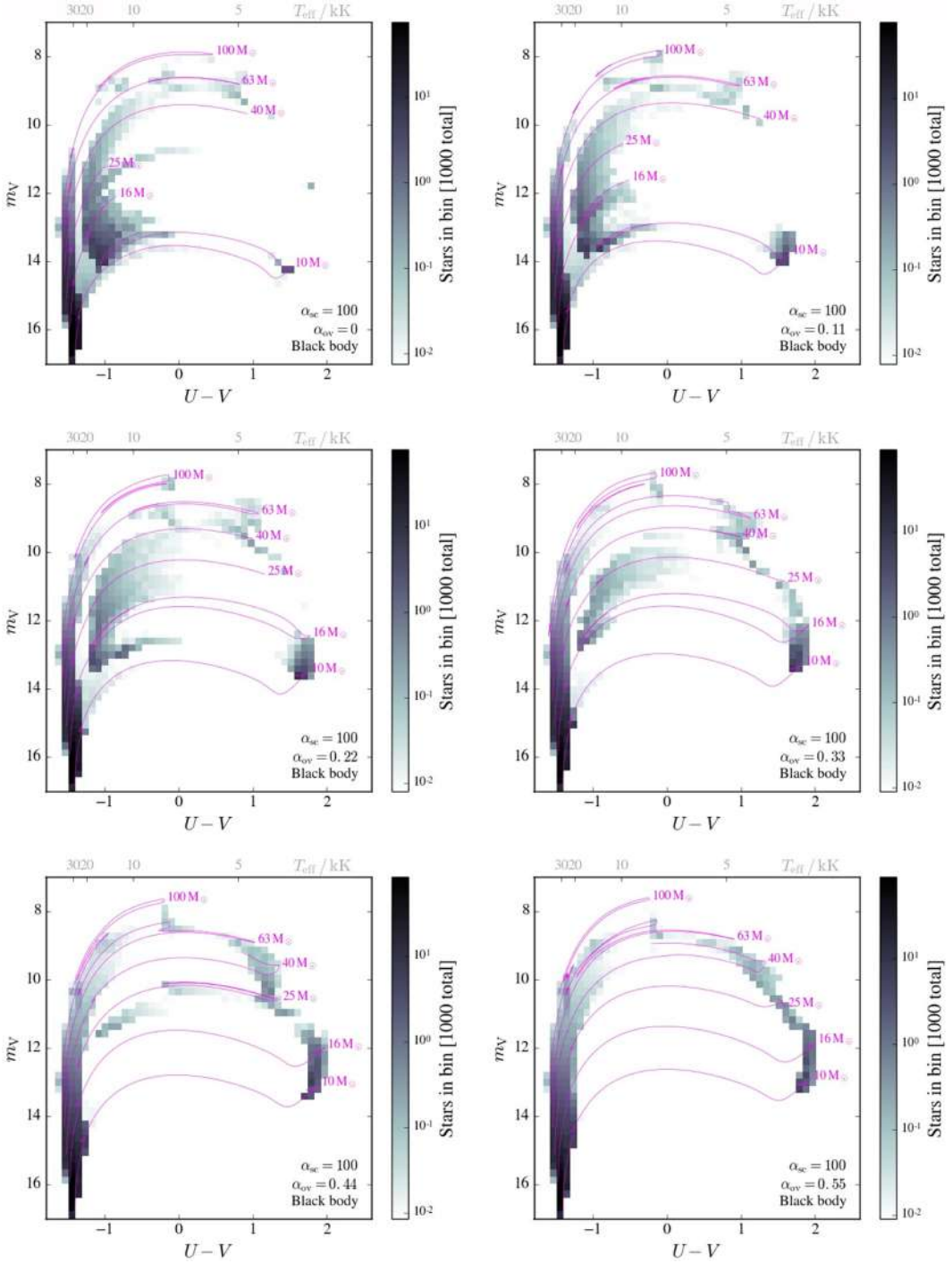

Figure 4.21: Six different color magnitude diagrams, which all have a different value for the the core overshooting parameter $\alpha_{\rm ov}$. For the models shown in each panel, the efficiency of semiconvection was $\alpha_{\rm sc} = 100$ and the black body approach was used to obtain the colors and magnitudes.

CHAPTER 5

Outlook

The year 2018 is in the middle of an exciting time for the field of massive stars – not only because of the increasing knowledge about massive stars themselves, but also because of the rapid developments in closely related fields. An example is the recently identified supernova class of superluminous supernovae (Gal-Yam, 2012), which can be a hundred times brighter than a typical supernova. Even more attention has been directed towards the rise of gravitational wave astronomy, with the first detection three years ago in 2015 (B. P. Abbott, Abbott, Abbott et al., 2016a) by the Laser Interferometer Gravitational-Wave Observatory (LIGO). Also high above the Earth's surface, there are (or will be) new observatories from which we can expect great contributions in the near future – e.g., the recently launched GAIA satellite, which focuses on mapping the positions and movements of billions of stars, and the soon-to-be-launched James Webb Space telescope (JWST). This telescope will observe around infrared wavelengths, making it especially suitable to observe the early universe. Below, we discuss how these (and other) developments can help us understand important phenomena in our universe – in particular, in relation to the work that we presented in this thesis.

As we have explained before in this thesis, individual stars in the early universe can (at least up to the foreseeable future) not be observed individually because they are extremely distant. However, in an ideal scenario where we would able to understand the evolution of massive stars in the Small Magellanic Cloud (SMC – a nearby satellite galaxy of the Milky Way with one fifth of the Solar metal content, that was the target environment of this work), we would be able to understand massive stars at a redshift of $\sim$3.5, which reside in an environment with a similar composition. This corresponds to a period in time almost twelve billion years ago, when the universe was just over two billion years old (Bergström and Goobar, 2004, their Eq. 4.77).

An important question is if stars can blow away their hydrogen-rich envelopes via stellar winds in metal-poor environments, where stellar winds are expected to be weaker. Whether or not they can do so has large consequences for the source of ionizing radiation in the early universe, as well as the morphology of exploding stars from there that we observe as supernovae. In Chapter 2, we have studied a group of hot, luminous stars with intermediate amounts of hydrogen on their surfaces. For this particular group of stars we have eliminated rotational mixing as one of their three possible formation channels (stellar winds, binary interaction, and chemically homogeneous evolution induced by rotation). Thus, the last step towards determining their formation channel is differentiating between wind mass loss and binary interaction. Given that better instruments such as the Very Large Telescope (VLT) have become available since the last observational study of their radial velocities to hunt for binary companions (Foellmi, Moffat and Guerrero, 2003; Foellmi, 2004), this should be very much feasible. In our group we have done a theoretical analysis of how much lower the error of the in radial velocity variation can be pushed. The

results were promising: they indicated that it might be possible to reduce the errors from 30 km s^{-1} all the way down to 2 km s^{-1}. In that case, performing such a study would lead to a win-win situation. Either, non-detection of binary components would prove that low-metallicity massive stars can shed their own hydrogen envelopes via stellar winds; or the first constraints on common-envelope evolution at low metallicity can be obtained if binary companions are detected, in parallel to the finding that such stars are unlikely to shed their hydrogen-rich envelope without the aid of a companion.

In relation to this, we might expect some developments from the field of high-resolution imaging. It happened only very recently that images of stars other than the Sun have been resolved (e.g., Betelgeuse and Antares – see O'Gorman, Kervella, Harper et al., 2017; Ohnaka, Weigelt and Hofmann, 2017, respectively), rather than seen as a point source. These observations have shown vigorous bulk motions and denser-than-expected material around the stars. Hopefully, this kind of studies will help us to understand the mechanisms responsible for mass loss of evolved stars (e.g., is it dust driven or driven by pulsations? Both depend differently on metallicity). In turn, this will allow us to have a better idea of how late-evolution mass loss operates in the early universe – especially if we are able to identify if mass loss or binary interaction is responsible for forming the Wolf-Rayet stars in the SMC. As we might observe the very first supernovae in the near future with the JWST (Hartwig, Bromm and Loeb, 2018), constraints on late-evolution mass loss in the early universe could prove to be crucial. Note, however, that red giant mass loss might or might not be relevant to extremely metal-deficient massive stars – whether or not they become red giants during their evolution depends on internal mixing processes (Limongi and Chieffi, 2018).

Speaking of internal mixing processes in massive stars – this brings us to a possible follow-up on Chapter. 3. There we provided testable predictions for populations of massive stars, for different assumptions concerning internal mixing. If internal mixing is efficient, single stars spend a significant amount of their helium burning lifetime as blue stars; if not, they do not. Comparing these predictions to a complete spectroscopic data set could be an important step forward in constraining internal mixing in massive stars. So far, only a small fraction of these blue supergiants (BSGs, by which we mean helium burning stars that tend to be colder than main sequence stars but significantly hotter than red supergiants) has been analyzed spectroscopically. Therefore, we strongly encourage such an observational campaign to learn about the properties of in particular the BSG population in the SMC. With a spectroscopic analysis, additional information could be extracted from nitrogen surface abundance measurements. While nitrogen enrichment of evolved stars might not yield conclusive evidence about their evolutionary history – because main sequence stars are often already enriched via an unknown mechanism – observing the *absence* of nitrogen enrichment could prove very valuable. For some sets of internal mixing efficiencies, ~all BSGs are predicted to be nitrogen-enriched; these sets could be ruled out by observations. An advantage of this approach is that (for once) binaries could most likely not be an alternative explanation, because mass transfer or merging should lead to some kind of nitrogen enhancement.

What could also be done in the future is to extend our theoretical models to metallicities of the Large Magellanic cloud (LMC) and our own galaxy. This way we can explore how the blue-to-red supergiant ratio scales with metallicy for our entire range of mixing efficiences. Then, it could become clear whether internal mixing can explain metallicity dependence of blue-to-red supergiant ratios or that other mechanisms such as binary interaction need to be invoked. Together with a parallel study about populations of binary stars that is currently being carried out in our group, the above would contribute to get a more complete picture of the evolution of evolved stars. We note that an important role will likely be in store for GAIA, since it can not only purify the populations of SMC and LMC stars by removing foreground stars, but also provide direct distance estimates for Galactic stars. For at least a subset of the Milky Way stars, it could also shed light on binary properties through astrometry.

A less time-demanding way to study massive star populations is by studying color-magnitude diagrams

(CMDs) obtained via photometry, as discussed in Chapter 4. One of the issues with the shown CMDs (constructed with the complete data sets that are currently available) is that they have measured colors in the visible part of the wavelength spectrum – these colors are relatively insensitive to temperature changes above 10 to 15 kK, which are the temperatures of interest for our BSG populations. This makes it hard to tell them apart from main sequence stars. If observations at shorter wavelengths could be carried out, this could allow for much more robust results about the number of BSGs and some of their properties. A unique instrument suited for such observations is the Hubble Space Telescope.

As already briefly mentioned, we are currently seeing the dawn of gravitational wave astronomy. Given that the sensitivity of the LIGO detectors can be increased by a factor ~ten compared to the first run, the volume (and thus the detection rate) could be boosted by a factor as high as one thousand. With a high enough number of detections, which we can expect to have within the timescale of a few years, it has been predicted that constraints can be put on the evolution of massive binary stars (Barrett, Gaebel, Neijssel et al., 2018). In this light, it would be interesting to explore how the formation of close compact object binaries would be affected by internal mixing in their progenitor stars. We have seen in Chapter 3 that the radius evolution sensitively depends on internal mixing. This can in turn can change the evolutionary state of the donor star at the onset of mass transfer, and at what timescale the envelope of the donor star gets stripped. Therefore, the efficiency of internal mixing might have significant consequences.

Above we have discussed a number of specific open questions, related to our work, that might be addressed in the near future. From a broader perspective, there is much more to be expected. Below, we highlight a few observatories of which we expect some of the most groundbreaking work in the coming years.

Within half a year (i.e., early 2019) after this thesis is written, LIGO will detect the coalescence of massive star remnants at greatly improved sensitivity – during an entire year, whereas the first observing run was just 3.5 months. Thus, given the already exciting discoveries from the first and second run, LIGO is likely to become a fountain of knowledge for gravitational-wave astronomy.

In three years, the long-anticipated launch of JWST will take place. Observing mostly in the infrared, it is mainly built to study the early universe: e.g., by pushing further the observational limit to high redshift galaxies (which are not unrelated to the field of low-metallicy massive stars, as we have explained above). However, it can also directly be used to observe massive stars or their explosions: e.g., it could study red supergiants, stars that in the process of being formed, and highly redshifted supernovae.

In six years time, observational astronomy will take another giant leap when the European-Extremely Large Telescope (E-ELT) starts its operations. With a mirror almost fourty meters in diameter, it will collect over ten times more photons than the largest optical telescope at Earth today. This will allow us to study individual stars in galaxies other than the Milky way or its satellites, greatly expanding the environments in which we can probe massive star evolution.

In conclusion, the future looks bright for the field of massive stars. Rapid developments can be expected from the observational side – this means that also we, the astronomers on the theoretical side, are not about to get bored anywhere in the foreseeable future.

Bibliography

Abbott, B. P. et al. (2016a). *Observation of Gravitational Waves from a Binary Black Hole Merger*. Physical Review Letters **116** 061102. arXiv: 1602.03837 [gr-qc] (cit. on pp. 6, 7, 22, 39, 66, 95).

– (2016b). *GW151226: Observation of Gravitational Waves from a 22-Solar-Mass Binary Black Hole Coalescence*. Physical Review Letters **116** 241103. arXiv: 1606.04855 [gr-qc] (cit. on p. 39).

Abbott, B. P. et al. (2017a). *GW170104: Observation of a 50-Solar-Mass Binary Black Hole Coalescence at Redshift 0.2*. Physical Review Letters **118** 221101. arXiv: 1706.01812 [gr-qc] (cit. on pp. 6, 39).

– (2017b). *Multi-messenger Observations of a Binary Neutron Star Merger*. Astrophysical Jounal Letters **848** L12. arXiv: 1710.05833 [astro-ph.HE] (cit. on p. 6).

Abbott, D. C. (1982). *The theory of radiatively driven stellar winds. II - The line acceleration*. Astrophysical Jounal **259** 282 (cit. on p. 22).

Almeida, L. A. et al. (2015). *Discovery of the Massive Overcontact Binary VFTS352: Evidence for Enhanced Internal Mixing*. Astrophysical Jounal **812** 102. arXiv: 1509.08940 [astro-ph.SR] (cit. on p. 22).

Alongi, M. et al. (1993). *Evolutionary sequences of stellar models with semiconvection and convective overshoot. I - Z = 0.008*. Astronomy & Astrophysics Supplement **97** 851 (cit. on p. 42).

Asplund, M. et al. (2009). *The Chemical Composition of the Sun*. Annual Review of Astronomy and Astrophysics **47** 481. arXiv: 0909.0948 [astro-ph.SR] (cit. on p. 7).

Azzopardi, M. and J. Breysacher (1979). *A search for new Wolf-Rayet stars in the Small Magellanic Cloud*. Astronomy & Astrophysics **75** 120 (cit. on p. 23).

Baade, W. and F. Zwicky (1934). *Cosmic Rays from Super-novae*. Proceedings of the National Academy of Science **20** 259 (cit. on p. 5).

Banerjee, S., H. Baumgardt and P. Kroupa (2010). *Stellar-mass black holes in star clusters: implications for gravitational wave radiation*. Monthly Notices of the Royal Astronomical Society **402** 371. arXiv: 0910.3954 [astro-ph.SR] (cit. on p. 6).

Barrett, J. W. et al. (2018). *Accuracy of inference on the physics of binary evolution from gravitational-wave observations*. Monthly Notices of the Royal Astronomical Society **477** 4685. arXiv: 1711.06287 [astro-ph.HE] (cit. on p. 97).

Bartzakos, P., A. F. J. Moffat and V. S. Niemela (2001). *Magellanic Cloud WC/WO Wolf-Rayet stars - I. Binary frequency and Roche lobe overflow formation*. Monthly Notices of the Royal Astronomical Society **324** 18 (cit. on p. 22).

Bastian, N. and S. E. de Mink (2009). *The effect of stellar rotation on colour-magnitude diagrams: on the apparent presence of multiple populations in intermediate age stellar clusters*. Monthly Notices of the Royal Astronomical Society **398** L11. arXiv: 0906.1590 (cit. on p. 84).

Belczynski, K., M. Dominik et al. (2010). *The Effect of Metallicity on the Detection Prospects for Gravitational Waves*. Astrophysical Jounal Letters **715** L138 (cit. on p. 42).

Belczynski, K., D. E. Holz et al. (2016). *The first gravitational-wave source from the isolated evolution of two stars in the 40-100 solar mass range*. Nature **534** 512. arXiv: 1602.04531 [astro-ph.HE] (cit. on p. 6).

Benacquista, M. (2013). *An Introduction to the Evolution of Single and Binary Stars* (cit. on p. 17).
Bennett, P. D. (2010). "Chromospheres and Winds of Red Supergiants: An Empirical Look at Outer Atmospheric Structure". *Hot and Cool: Bridging Gaps in Massive Star Evolution*. Ed. by C. Leitherer et al. Vol. 425. Astronomical Society of the Pacific Conference Series 181. arXiv: 1004.1853 [astro-ph.SR] (cit. on p. 13).
Bergström, L. and A. Goobar (2004). *Cosmology and Particle Astrophysics* (cit. on p. 95).
Bessell, M. S. (1990). *UBVRI passbands*. Publications of the ASP **102** 1181 (cit. on p. 70).
Bianchi, L. and M. Garcia (2002). *The Effective Temperatures of Mid-O Stars*. Astrophysical Jounal **581** 610 (cit. on p. 77).
Blaha, C. and R. M. Humphreys (1989). *A comparison of the luminosity functions in U, B, and V and their relationship to the initial mass function for the Galaxy and the Magellanic Clouds*. Astrophysical Journal **98** 1598 (cit. on pp. 37, 58, 61, 73).
Bohlin, R. C. (2007). "HST Stellar Standards with 1% Accuracy in Absolute Flux". *The Future of Photometric, Spectrophotometric and Polarimetric Standardization*. Ed. by C. Sterken. Vol. 364. Astronomical Society of the Pacific Conference Series 315. eprint: astro-ph/0608715 (cit. on p. 68).
Böhm-Vitense, E. (1958). *Über die Wasserstoffkonvektionszone in Sternen verschiedener Effektivtemperaturen und Leuchtkräfte. Mit 5 Textabbildungen*. Zeitschrift fuer Astrophysik **46** 108 (cit. on pp. 25, 43).
Bolton, C. T. (1972). *Identification of Cygnus X-1 with HDE 226868*. Nature **235** 271 (cit. on p. 6).
Bouret, J.-C., T. Lanz, D. J. Hillier et al. (2003). *Quantitative Spectroscopy of O Stars at Low Metallicity: O Dwarfs in NGC 346*. Astrophysical Jounal **595** 1182. eprint: astro-ph/0301454 (cit. on p. 22).
Bouret, J.-C., T. Lanz, F. Martins et al. (2013). *Massive stars at low metallicity. Evolution and surface abundances of O dwarfs in the SMC*. Astronomy & Astrophysics **555** A1. arXiv: 1304.6923 [astro-ph.SR] (cit. on p. 30).
Braun, H. and N. Langer (1995). *Effects of accretion onto massive main sequence stars.* Astronomy & Astrophysics **297** 483 (cit. on pp. 17, 35, 63, 64, 82).
Bressan, A. G., C. Chiosi and G. Bertelli (1981). *Mass loss and overshooting in massive stars*. Astronomy & Astrophysics **102** 25 (cit. on p. 10).
Breysacher, J. and B. E. Westerlund (1978). *Wolf-Rayet stars in the Small Magellanic Cloud*. Astronomy & Astrophysics **67** 261 (cit. on p. 23).
Brott, I. et al. (2011). *Rotating massive main-sequence stars. I. Grids of evolutionary models and isochrones*. Astronomy & Astrophysics **530** A115. arXiv: 1102.0530 [astro-ph.SR] (cit. on pp. 10, 24, 25, 42, 43, 48, 53–56, 63, 69).
Canuto, V. M. (1999a). *Overshooting in Massive Stars: Conceptual Problems and Suggested Solution*. Astrophysical Jounal Letters **518** L119 (cit. on pp. 10, 42).
– (1999b). *Turbulence in Stars. III. Unified Treatment of Diffusion, Convection, Semiconvection, Salt Fingers, and Differential Rotation*. Astrophysical Jounal **524** 311 (cit. on p. 10).
Casares, J. (2007). "Observational evidence for stellar-mass black holes". *Black Holes from Stars to Galaxies – Across the Range of Masses*. Ed. by V. Karas and G. Matt. Vol. 238. IAU Symposium 3. eprint: astro-ph/0612312 (cit. on p. 6).
Casares, J. and P. G. Jonker (2014). *Mass Measurements of Stellar and Intermediate-Mass Black Holes*. Space Science Reviews **183** 223. arXiv: 1311.5118 [astro-ph.HE] (cit. on p. 6).
Castor, J. I., D. C. Abbott and R. I. Klein (1975). *Radiation-driven winds in Of stars*. Astrophysical Jounal **195** 157 (cit. on p. 13).
Castro, N., L. Fossati et al. (2014). *The spectroscopic Hertzsprung-Russell diagram of Galactic massive stars*. Astronomy & Astrophysics **570** L13. arXiv: 1410.3499 [astro-ph.SR] (cit. on pp. 55, 63, 84).

Castro, N., M. S. Oey et al. (2018). *The spectroscopic Hertzsprung-Russell diagram of hot massive stars in the SMC*. ArXiv e-prints. arXiv: 1810.04682 [astro-ph.SR] (cit. on pp. 55, 70, 71, 76, 82, 84, 89).

Charbonnel, C. et al. (1993). *Grids of Stellar Models - Part Three - from 0.8 to 120-SOLAR-MASSES at Z=0.004*. Astronomy & Astrophysics Supplement **101** 415 (cit. on p. 54).

Chen, T.-W. et al. (2017). *Superluminous supernova progenitors have a half-solar metallicity threshold*. Monthly Notices of the Royal Astronomical Society **470** 3566 (cit. on p. 42).

Chieffi, A. and M. Limongi (2013). *Pre-supernova Evolution of Rotating Solar Metallicity Stars in the Mass Range 13-120 M _ and their Explosive Yields*. Astrophysical Jounal **764** 21 (cit. on p. 54).

Chiosi, C., E. Nasi and S. R. Sreenivasan (1978). *Massive stars evolution with mass-loss. I - 20-100-solar-mass models*. Astronomy & Astrophysics **63** 103 (cit. on p. 55).

Chiosi, C. and C. Summa (1970). *On the Evolution of OB Stars from the Main Sequence to the Helium Exhaustion Phase*. Astrophysics and Space Science **8** 478 (cit. on p. 55).

Choi, J. et al. (2016). *Mesa Isochrones and Stellar Tracks (MIST). I. Solar-scaled Models*. Astrophysical Jounal **823** 102. arXiv: 1604.08592 [astro-ph.SR] (cit. on p. 54).

Chu, Y.-H. and R. C. Kennicutt Jr. (1994). *Kinematic structure of the 30 Doradus giant H II region*. Astrophysical Jounal **425** 720 (cit. on p. 8).

Cloutman, L. D. and R. W. Whitaker (1980). *On convective and semiconvective mixing in massive stars*. Astrophysical Jounal **237** 900 (cit. on p. 46).

Conti, P. S., C. D. Garmany and P. Massey (1989). *Spectroscopic studies of Wolf-Rayet stars. V - Optical spectrophotometry of the emission lines in Small Magellanic Cloud stars*. Astrophysical Jounal **341** 113 (cit. on p. 23).

Conti, P. S. and R. McCray (1980). *Strong stellar winds*. Science **208** 9 (cit. on p. 7).

Croft, S. K., D. H. McNamara and K. A. Feltz Jr. (1972). *The (B-V) and (U-B) Color Indices of the Sun*. Publications of the ASP **84** 515 (cit. on p. 70).

Crowther, P. A. (2007). *Physical Properties of Wolf-Rayet Stars*. Annual Review of Astronomy and Astrophysics **45** 177. eprint: astro-ph/0610356 (cit. on p. 23).

Davies, B., P. A. Crowther and E. R. Beasor (2018). *The luminosities of cool supergiants in the Magellanic Clouds, and the Humphreys-Davidson limit revisited*. Monthly Notices of the Royal Astronomical Society **478** 3138. arXiv: 1804.06417 [astro-ph.SR] (cit. on pp. 56–58, 66, 73, 82).

Davies, B., R.-P. Kudritzki et al. (2013). *The Temperatures of Red Supergiants*. Astrophysical Jounal **767** 3. arXiv: 1302.2674 [astro-ph.SR] (cit. on p. 56).

de Mink, S. E., M. Cantiello et al. (2009). *Rotational mixing in massive binaries. Detached short-period systems*. Astronomy & Astrophysics **497** 243. arXiv: 0902.1751 [astro-ph.SR] (cit. on pp. 6, 38).

de Mink, S. E. and I. Mandel (2016). *The chemically homogeneous evolutionary channel for binary black hole mergers: rates and properties of gravitational-wave events detectable by advanced LIGO*. Monthly Notices of the Royal Astronomical Society **460** 3545. arXiv: 1603.02291 [astro-ph.HE] (cit. on p. 6).

de Mink, S. E., O. R. Pols and R. W. Hilditch (2007). *Efficiency of mass transfer in massive close binaries. Tests from double-lined eclipsing binaries in the SMC*. Astronomy & Astrophysics **467** 1181. eprint: astro-ph/0703480 (cit. on p. 17).

de Mink, S. E., H. Sana et al. (2014). *The Incidence of Stellar Mergers and Mass Gainers among Massive Stars*. Astrophysical Jounal **782** 7. arXiv: 1312.3650 [astro-ph.SR] (cit. on pp. 17, 63, 64, 82).

Drout, M. R. et al. (2009). *Yellow Supergiants in the Andromeda Galaxy (M31)*. Astrophysical Jounal **703** 441. arXiv: 0907.5471 [astro-ph.SR] (cit. on p. 46).

Eddington, A. S. (1920). *The Internal Constitution of the Stars*. The Scientific Monthly **11** 297 (cit. on p. 2).

Eddington, A. S. (1925). *Circulating currents in rotating stars*. The Observatory **48** 73 (cit. on p. 12).
Eichler, D. et al. (1989). *Nucleosynthesis, neutrino bursts and gamma-rays from coalescing neutron stars*. Nature **340** 126 (cit. on p. 7).
Ekström, S. et al. (2012). *Grids of stellar models with rotation. I. Models from 0.8 to 120 M_ at solar metallicity (Z = 0.014)*. Astronomy & Astrophysics **537** A146. arXiv: 1110.5049 [astro-ph.SR] (cit. on p. 15).
Evans, C. J., I. D. Howarth et al. (2004). *A 2dF survey of the Small Magellanic Cloud*. Monthly Notices of the Royal Astronomical Society **353** 601. eprint: astro-ph/0406409 (cit. on p. 71).
Evans, C. J., D. J. Lennon et al. (2006). *The VLT-FLAMES survey of massive stars: observations centered on the Magellanic Cloud clusters NGC 330, NGC 346, NGC 2004, and the N11 region*. Astronomy & Astrophysics **456** 623. eprint: astro-ph/0606405 (cit. on p. 58).
Evans, C. J., S. J. Smartt et al. (2005). *The VLT-FLAMES survey of massive stars: Observations in the Galactic clusters NGC 3293, NGC 4755 and NGC 6611*. Astronomy & Astrophysics **437** 467. eprint: astro-ph/0503655 (cit. on p. 25).
Ferrario, L. et al. (2009). *The origin of magnetism on the upper main sequence*. Monthly Notices of the Royal Astronomical Society **400** L71 (cit. on p. 63).
Foellmi, C. (2004). *Another single hydrogen-rich Wolf-Rayet star in the SMC?* Astronomy & Astrophysics **416** 291. eprint: astro-ph/0310153 (cit. on pp. 22–24, 95).
Foellmi, C., A. F. J. Moffat and M. A. Guerrero (2003). *Wolf-Rayet binaries in the Magellanic Clouds and implications for massive-star evolution - I. Small Magellanic Cloud*. Monthly Notices of the Royal Astronomical Society **338** 360 (cit. on pp. 22–24, 38, 40, 95).
Fossati, L. et al. (2015). *B fields in OB stars (BOB): Low-resolution FORS2 spectropolarimetry of the first sample of 50 massive stars*. Astronomy & Astrophysics **582** A45. arXiv: 1508.00750 [astro-ph.SR] (cit. on p. 63).
Fowler, W. A. and F. Hoyle (1964). *Neutrino Processes and Pair Formation in Massive Stars and Supernovae*. Astrophysical Journal Supplement **9** 201 (cit. on p. 6).
Friend, D. B. and D. C. Abbott (1986). *The theory of radiatively driven stellar winds. III - Wind models with finite disk correction and rotation*. Astrophysical Jounal **311** 701 (cit. on p. 25).
Gaia Collaboration, A. G. A. Brown et al. (2018). *Gaia Data Release 2. Summary of the contents and survey properties*. Astronomy & Astrophysics **616** A1. arXiv: 1804.09365 (cit. on pp. 3, 19, 71).
Gaia Collaboration, T. Prusti et al. (2016). *The Gaia mission*. Astronomy & Astrophysics **595** A1. arXiv: 1609.04153 [astro-ph.IM] (cit. on p. 3).
Gal-Yam, A. (2012). *Luminous Supernovae*. Science **337** 927. arXiv: 1208.3217 (cit. on pp. 5, 95).
Gamow, G. (1943). *On WC and WN Stars.* Astrophysical Jounal **98** 500 (cit. on p. 7).
Georgiev, L. et al. (2011). *Wind Structure and Luminosity Variations in the Wolf-Rayet/Luminous Blue Variable HD 5980*. Astrophysical Journal **142** 191 (cit. on p. 28).
Georgy, C. et al. (2013). *Grids of stellar models with rotation. III. Models from 0.8 to 120 M_ at a metallicity Z = 0.002*. Astronomy & Astrophysics **558** A103. arXiv: 1308.2914 [astro-ph.SR] (cit. on pp. 14, 54–56).
Girardi, L. et al. (2002). *Theoretical isochrones in several photometric systems. I. Johnson-Cousins-Glass, HST/WFPC2, HST/NICMOS, Washington, and ESO Imaging Survey filter sets*. Astronomy & Astrophysics **391** 195. eprint: astro-ph/0205080 (cit. on pp. 69, 70).
Gordon, K. D. et al. (2003). *A Quantitative Comparison of the Small Magellanic Cloud, Large Magellanic Cloud, and Milky Way Ultraviolet to Near-Infrared Extinction Curves*. Astrophysical Jounal **594** 279. eprint: astro-ph/0305257 (cit. on pp. 74, 82, 83, 86, 87).

Gotberg, Y., S. E. de Mink and J. H. Groh (2017). *Ionizing spectra of stars that lose their envelope through interaction with a binary companion: role of metallicity*. ArXiv e-prints. arXiv: 1701.07439 [astro-ph.SR] (cit. on p. 17).

Gräfener, G. et al. (2011). *The Eddington factor as the key to understand the winds of the most massive stars. Evidence for a Γ-dependence of Wolf-Rayet type mass loss*. Astronomy & Astrophysics **535** A56. arXiv: 1106.5361 [astro-ph.SR] (cit. on p. 39).

Graham, J. F. and A. S. Fruchter (2017). *The Relative Rate of LGRB Formation as a Function of Metallicity*. Astrophysical Jounal **834** 170 (cit. on p. 42).

Grevesse, N., A. Noels and A. J. Sauval (1996). "Standard Abundances". *Cosmic Abundances*. Ed. by S. S. Holt and G. Sonneborn. Vol. 99. Astronomical Society of the Pacific Conference Series 117 (cit. on pp. 24, 25, 43).

Grevesse, N. and A. J. Sauval (1998). *Standard Solar Composition*. Space Science Reviews **85** 161 (cit. on p. 7).

Grin, N. J. et al. (2017). *The VLT-FLAMES Tarantula Survey. XXV. Surface nitrogen abundances of O-type giants and supergiants*. Astronomy & Astrophysics **600** A82. arXiv: 1609.00197 [astro-ph.SR] (cit. on pp. 27, 60).

Grossman, S. A. and R. E. Taam (1996). *Double-Diffusive Mixing-Length Theory, Semiconvection and Massive Star Evolution*. Monthly Notices of the Royal Astronomical Society **283** 1165. eprint: astro-ph/9608137 (cit. on pp. 10, 42).

Grunhut, J. H. et al. (2017). *The MiMeS survey of Magnetism in Massive Stars: magnetic analysis of the O-type stars*. Monthly Notices of the Royal Astronomical Society **465** 2432. arXiv: 1610.07895 [astro-ph.SR] (cit. on p. 63).

Guerrero, M. A. and Y.-H. Chu (2008a). *An X-Ray Survey of Wolf-Rayet Stars in the Magellanic Clouds. I. The Chandra ACIS Data Set*. Astrophysical Journal Supplement **177** 216. arXiv: 0802.0503 (cit. on p. 40).

– (2008b). *An X-Ray Survey of Wolf-Rayet Stars in the Magellanic Clouds. II. The ROSAT PSPC and HRI Data Sets*. Astrophysical Journal Supplement **177** 238. arXiv: 0802.0493 (cit. on p. 40).

Gurnis, M. (1988). *Large-scale mantle convection and the aggregation and dispersal of supercontinents*. Nature **332** 695 (cit. on p. 9).

Hainich, R., D. Pasemann et al. (2015). *Wolf-Rayet stars in the Small Magellanic Cloud. I. Analysis of the single WN stars*. Astronomy & Astrophysics **581** A21. arXiv: 1507.04000 [astro-ph.SR] (cit. on pp. 14, 22–25, 40, 124).

Hainich, R., T. Shenar et al. (2017). *The metallicity dependence of WR winds*. ArXiv e-prints. arXiv: 1703.02060 [astro-ph.SR] (cit. on pp. 13, 36).

Hamann, W.-R., G. Gräfener and A. Liermann (2006). *The Galactic WN stars. Spectral analyses with line-blanketed model atmospheres versus stellar evolution models with and without rotation*. Astronomy & Astrophysics **457** 1015. eprint: astro-ph/0608078 (cit. on p. 23).

Hamann, W.-R., L. Koesterke and U. Wessolowski (1995). *Spectral analyses of the Galactic Wolf-Rayet stars: hydrogen-helium abundances and improved stellar parameters for the WN class*. Astronomy & Astrophysics **299** 151 (cit. on pp. 25, 43).

Hartwig, T., V. Bromm and A. Loeb (2018). *Detection strategies for the first supernovae with JWST*. Monthly Notices of the Royal Astronomical Society **479** 2202. arXiv: 1711.05742 (cit. on p. 96).

Heger, A., C. L. Fryer et al. (2003). *How Massive Single Stars End Their Life*. Astrophysical Jounal **591** 288. eprint: astro-ph/0212469 (cit. on p. 6).

Heger, A., N. Langer and S. E. Woosley (2000). *Presupernova Evolution of Rotating Massive Stars. I. Numerical Method and Evolution of the Internal Stellar Structure*. Astrophysical Jounal **528** 368. eprint: astro-ph/9904132 (cit. on pp. 12, 42, 46, 66).

Heger, A., S. E. Woosley and H. C. Spruit (2005). *Presupernova Evolution of Differentially Rotating Massive Stars Including Magnetic Fields*. Astrophysical Jounal **626** 350. eprint: astro-ph/0409422 (cit. on p. 54).

Herrero, A., J. Puls and F. Najarro (2002). *Fundamental parameters of Galactic luminous OB stars VI. Temperatures, masses and WLR of Cyg OB2 supergiants*. Astronomy & Astrophysics **396** 949. eprint: astro-ph/0210469 (cit. on p. 77).

Hewish, A. et al. (1968). *Observation of a Rapidly Pulsating Radio Source*. Nature **217** 709 (cit. on p. 6).

Hilditch, R. W., I. D. Howarth and T. J. Harries (2005). *Forty eclipsing binaries in the Small Magellanic Cloud: fundamental parameters and Cloud distance*. Monthly Notices of the Royal Astronomical Society **357** 304. eprint: astro-ph/0411672 (cit. on pp. 14, 70).

Hopkins, P. F. et al. (2014). *Galaxies on FIRE (Feedback In Realistic Environments): stellar feedback explains cosmologically inefficient star formation*. Monthly Notices of the Royal Astronomical Society **445** 581. arXiv: 1311.2073 (cit. on pp. 8, 22, 42, 66).

Hubble, E. (1929). *A Relation between Distance and Radial Velocity among Extra-Galactic Nebulae*. Proceedings of the National Academy of Science **15** 168 (cit. on p. 1).

Hubeny, I. and T. Lanz (1995). *Non-LTE line-blanketed model atmospheres of hot stars. 1: Hybrid complete linearization/accelerated lambda iteration method*. Astrophysical Jounal **439** 875 (cit. on p. 77).

Humphreys, R. M., R. P. Kudritzki and H. G. Groth (1991). *The anomalous A-type supergiants in the Magellanic Clouds - Evidence for post-red supergiant evolution*. Astronomy & Astrophysics **245** 593 (cit. on pp. 58, 59).

Hunter, I., I. Brott et al. (2008). *The VLT FLAMES Survey of Massive Stars: Rotation and Nitrogen Enrichment as the Key to Understanding Massive Star Evolution*. Astrophysical Jounal Letters **676** L29. arXiv: 0711.2267 (cit. on pp. 25, 60).

Hunter, I., P. L. Dufton et al. (2007). *The VLT-FLAMES survey of massive stars: surface chemical compositions of B-type stars in the Magellanic Clouds*. Astronomy & Astrophysics **466** 277. eprint: astro-ph/0609710 (cit. on p. 22).

Hunter, I., D. J. Lennon et al. (2008). *The VLT-FLAMES survey of massive stars: atmospheric parameters and rotational velocity distributions for B-type stars in the Magellanic Clouds*. Astronomy & Astrophysics **479** 541. arXiv: 0711.2264 (cit. on p. 54).

Iglesias, C. A. and F. J. Rogers (1996). *Updated Opal Opacities*. Astrophysical Jounal **464** 943 (cit. on p. 24).

Ivanova, N. et al. (2013). *Common envelope evolution: where we stand and how we can move forward*. Astronomy & Astrophysics Review **21** 59. arXiv: 1209.4302 [astro-ph.HE] (cit. on pp. 17, 38).

Justham, S., P. Podsiadlowski and J. S. Vink (2014). *Luminous Blue Variables and Superluminous Supernovae from Binary Mergers*. Astrophysical Jounal **796** 121. arXiv: 1410.2426 [astro-ph.SR] (cit. on p. 64).

Kalari, V. M. et al. (2018). *How common is LBV S Dor variability at low metallicity?* ArXiv e-prints. arXiv: 1807.01309 [astro-ph.SR] (cit. on pp. 58, 59, 73).

Karakas, A. I. (2010). *Updated stellar yields from asymptotic giant branch models*. Monthly Notices of the Royal Astronomical Society **403** 1413. arXiv: 0912.2142 [astro-ph.SR] (cit. on p. 8).

Kato, S. (1966). *Overstable Convection in a Medium Stratified in Mean Molecular Weight*. Publications of the ASJ **18** 374 (cit. on pp. 10, 63).

Kewley, L. and H. A. Kobulnicky (2007). *The Metallicity History of Disk Galaxies*. Astrophysics and Space Science Proceedings **3** 435 (cit. on pp. 22, 42).

Kippenhahn, R. and A. Weigert (1967). *Entwicklung in engen Doppelsternsystemen I. Massenaustausch vor und nach Beendigung des zentralen Wasserstoff-Brennens*. Zeitschrift fuer Astrophysik **65** 251 (cit. on p. 16).

– (1990). *Stellar Structure and Evolution* 192 (cit. on p. 10).

Koenigsberger, G. et al. (2014). *The HD 5980 Multiple System: Masses and Evolutionary Status*. Astrophysical Journal **148** 62. arXiv: 1408.0556 [astro-ph.SR] (cit. on pp. 22, 24, 28, 38, 39).

Korn, A. J. et al. (2000). *Chemical abundances from Magellanic cloud B stars*. Astronomy & Astrophysics **353** 655 (cit. on pp. 14, 22, 42).

Kruckow, M. U. et al. (2016). *Common-envelope ejection in massive binary stars. Implications for the progenitors of GW150914 and GW151226*. Astronomy & Astrophysics **596** A58. arXiv: 1610.04417 [astro-ph.SR] (cit. on p. 38).

Kudritzki, R. P., A. Pauldrach and J. Puls (1987). *Radiation driven winds of hot luminous stars. II - Wind models for O-stars in the Magellanic Clouds*. Astronomy and Astrophysics **173** 293 (cit. on p. 22).

Lamb, J. B. et al. (2016). *The Runaways and Isolated O-Type Star Spectroscopic Survey of the SMC (RIOTS4)*. Astrophysical Jounal **817** 113. arXiv: 1512.01233 (cit. on pp. 55, 71).

Lamers, H. J. G. L. M. and E. L. Fitzpatrick (1988). *The relationship between the Eddington limit, the observed upper luminosity limit for massive stars, and the luminous blue variables*. Astrophysical Jounal **324** 279 (cit. on p. 37).

Langer, N. (1989). *Standard models of Wolf-Rayet stars*. Astronomy & Astrophysics **210** 93 (cit. on pp. 23, 25).

– (1991). *Evolution of massive stars in the Large Magellanic Cloud - Models with semiconvection*. Astronomy & Astrophysics **252** 669 (cit. on pp. 25, 42, 50).

– (1992). *Helium enrichment in massive early type stars*. Astronomy & Astrophysics **265** L17 (cit. on pp. 22, 53, 66).

– (1998). *Coupled mass and angular momentum loss of massive main sequence stars*. Astronomy & Astrophysics **329** 551 (cit. on p. 22).

– (2012). *Presupernova Evolution of Massive Single and Binary Stars*. Annual Review of Astronomy and Astrophysics **50** 107. arXiv: 1206.5443 [astro-ph.SR] (cit. on pp. 4, 34, 42, 63, 88).

Langer, N., M. F. El Eid and K. J. Fricke (1985). *Evolution of massive stars with semiconvective diffusion*. Astronomy & Astrophysics **145** 179 (cit. on pp. 10, 15, 35, 55).

Langer, N., K. J. Fricke and D. Sugimoto (1983). *Semiconvective diffusion and energy transport*. Astronomy & Astrophysics **126** 207 (cit. on pp. 42, 43, 63).

Langer, N. and A. Maeder (1995). *The problem of the blue-to-red supergiant ratio in galaxies.* Astronomy & Astrophysics **295** 685 (cit. on p. 42).

Langer, N., S. Wellstein and J. Petrovic (2003). "On the evolution of massive close binaries". *A Massive Star Odyssey: From Main Sequence to Supernova*. Ed. by K. van der Hucht, A. Herrero and C. Esteban. Vol. 212. IAU Symposium 275 (cit. on p. 16).

Lattimer, J. M. et al. (1977). *The decompression of cold neutron star matter*. Astrophysical Jounal **213** 225 (cit. on p. 7).

Lau, H. H. B., R. G. Izzard and F. R. N. Schneider (2014). *Numerical tests of rotational mixing in massive stars with the new population synthesis code BONNFIRES*. Astronomy & Astrophysics **570** A125. arXiv: 1409.0229 [astro-ph.SR] (cit. on p. 44).

Lauterborn, D. (1970). *Evolution with mass exchange of case C for a binary system of total mass 7 M sun.* Astronomy & Astrophysics **7** 150 (cit. on p. 16).

Levesque, E. M. et al. (2006). *The Effective Temperatures and Physical Properties of Magellanic Cloud Red Supergiants: The Effects of Metallicity*. Astrophysical Jounal **645** 1102. eprint: astro-ph/0603596 (cit. on pp. 56, 66, 73).

Limongi, M. and A. Chieffi (2018). *Presupernova Evolution and Explosive Nucleosynthesis of Rotating Massive Stars in the Metallicity Range -3 < [Fe/H] < 0*. Astrophysical Journal Supplement **237** 13. arXiv: 1805.09640 [astro-ph.SR] (cit. on pp. 54, 55, 96).

Lubow, S. H. and F. H. Shu (1975). *Gas dynamics of semidetached binaries*. Astrophysical Jounal **198** 383 (cit. on p. 16).

Maeder, A. (1987). *Evidences for a bifurcation in massive star evolution. The ON-blue stragglers*. Astronomy & Astrophysics **178** 159 (cit. on pp. 22, 53, 66).

– (2009). *Physics, Formation and Evolution of Rotating Stars* (cit. on p. 12).

Maeder, A. and J. C. Mermilliod (1981). *The extent of mixing in stellar interiors - Evolutionary models and tests based on the HR diagrams of 34 open clusters*. Astronomy & Astrophysics **93** 136 (cit. on p. 10).

Maeder, A. and G. Meynet (1988). *Tables of evolutionary star models from 0.85 to 120 solar masses with overshooting and mass loss*. Astronomy & Astrophysics Supplement **76** 411 (cit. on pp. 42, 55).

– (1991). *Tables of isochrones computed from stellar models with mass loss and overshooting*. Astronomy & Astrophysics Supplement **89** 451 (cit. on p. 55).

– (1994). *New models of Wolf-Rayet stars and comparison with data in galaxies*. Astronomy & Astrophysics **287** 803 (cit. on p. 22).

– (2000). *Stellar evolution with rotation. VI. The Eddington and Omega -limits, the rotational mass loss for OB and LBV stars*. Astronomy & Astrophysics **361** 159. eprint: astro-ph/0006405 (cit. on p. 42).

– (2012). *Rotating massive stars: From first stars to gamma ray bursts*. Reviews of Modern Physics **84** 25 (cit. on p. 63).

Mamajek, E. E. et al. (2015). *IAU 2015 Resolution B3 on Recommended Nominal Conversion Constants for Selected Solar and Planetary Properties*. ArXiv e-prints. arXiv: 1510.07674 [astro-ph.SR] (cit. on p. 70).

Mandel, I. and S. E. de Mink (2016). *Merging binary black holes formed through chemically homogeneous evolution in short-period stellar binaries*. Monthly Notices of the Royal Astronomical Society. arXiv: 1601.00007 [astro-ph.HE] (cit. on pp. 6, 22).

Marchant, P. et al. (2016). *A new route towards merging massive black holes*. Astronomy & Astrophysics **588** A50. arXiv: 1601.03718 [astro-ph.SR] (cit. on pp. 6, 22, 38).

Marchenko, S. V. et al. (2007). *Spectroscopy of SMC Wolf-Rayet Stars Suggests that Wind Clumping Does Not Depend on Ambient Metallicity*. Astrophysical Jounal Letters **656** L77. eprint: astro-ph/0701516 (cit. on p. 40).

Marino, A. F. et al. (2018). *Different Stellar Rotations in the Two Main Sequences of the Young Globular Cluster NGC 1818: The First Direct Spectroscopic Evidence*. Astrophysical Journal **156** 116. arXiv: 1807.04493 [astro-ph.SR] (cit. on p. 84).

Markova, N., J. Puls and N. Langer (2018). *Spectroscopic and physical parameters of Galactic O-type stars. III. Mass discrepancy and rotational mixing*. Astronomy & Astrophysics **613** A12. arXiv: 1803.03410 [astro-ph.SR] (cit. on p. 54).

Markova, N., J. Puls, T. Repolust et al. (2004). *Bright OB stars in the Galaxy. I. Mass-loss and wind-momentum rates of O-type stars: A pure H\alpha analysis accounting for line-blanketing*. Astronomy & Astrophysics **413** 693 (cit. on p. 77).

Martins, F., E. Depagne et al. (2013). *Evidence of quasi-chemically homogeneous evolution of massive stars up to solar metallicity*. Astronomy & Astrophysics **554** A23. arXiv: 1304.3337 [astro-ph.SR] (cit. on p. 22).

Martins, F., D. J. Hillier et al. (2009). *Properties of WNh stars in the Small Magellanic Cloud: evidence for homogeneous evolution*. Astronomy & Astrophysics **495** 257. arXiv: 0811.3564 (cit. on p. 22).

Martins, F. and A. Palacios (2013). *A comparison of evolutionary tracks for single Galactic massive stars*. Astronomy & Astrophysics **560** A16. arXiv: 1310.7218 [astro-ph.SR] (cit. on p. 54).

Mason, B. D. et al. (2009). *The High Angular Resolution Multiplicity of Massive Stars*. Astrophysical Journal **137** 3358. arXiv: 0811.0492 (cit. on p. 17).

Massey, P. (2002). *A UBVR CCD Survey of the Magellanic Clouds*. Astrophysical Journal Supplement **141** 81. eprint: astro-ph/0110531 (cit. on pp. 19, 71, 81, 85, 87, 89).

Massey, P. and A. S. Duffy (2001). *A Search for Wolf-Rayet Stars in the Small Magellanic Cloud*. Astrophysical Jounal **550** 713. eprint: astro-ph/0010420 (cit. on p. 23).

Massey, P. and K. A. G. Olsen (2003). *The Evolution of Massive Stars. I. Red Supergiants in the Magellanic Clouds*. Astrophysical Journal **126** 2867. eprint: astro-ph/0309272 (cit. on p. 56).

Massey, P., K. A. G. Olsen and J. W. Parker (2003). *The Discovery of a 12th Wolf-Rayet Star in the Small Magellanic Cloud*. Publications of the ASP **115** 1265. eprint: astro-ph/0308237 (cit. on p. 23).

McCray, R. and C. Fransson (2016). *The Remnant of Supernova 1987A*. Annual Review of Astronomy and Astrophysics **54** 19 (cit. on p. 5).

Menon, A. and A. Heger (2017). *The quest for blue supergiants: binary merger models for the evolution of the progenitor of SN 1987A*. Monthly Notices of the Royal Astronomical Society **469** 4649. arXiv: 1703.04918 [astro-ph.SR] (cit. on p. 17).

Merryfield, W. J. (1995). *Hydrodynamics of semiconvection*. Astrophysical Jounal **444** 318 (cit. on pp. 10, 42, 66).

Meynet, G. and A. Maeder (2002). *Stellar evolution with rotation. VIII. Models at Z = 10^{-5} and CNO yields for early galactic evolution*. Astronomy & Astrophysics **390** 561. eprint: astro-ph/0205370 (cit. on p. 12).

Meynet, G., A. Maeder et al. (1994). *Grids of massive stars with high mass loss rates. V. From 12 to 120 M_{sun}_ at Z=0.001, 0.004, 0.008, 0.020 and 0.040*. Astronomy & Astrophysics Supplement **103** 97 (cit. on p. 54).

Milne, E. A. (1928). *The total absorption in the Sun's reversing layer*. The Observatory **51** 88 (cit. on p. 77).

Milone, A. P. et al. (2018). *Multiple stellar populations in Magellanic Cloud clusters - VI. A survey of multiple sequences and Be stars in young clusters*. Monthly Notices of the Royal Astronomical Society **477** 2640. arXiv: 1802.10538 [astro-ph.SR] (cit. on p. 84).

Mokiem, M. R., A. de Koter, C. J. Evans et al. (2006). *The VLT-FLAMES survey of massive stars: mass loss and rotation of early-type stars in the SMC*. Astronomy & Astrophysics **456** 1131. eprint: astro-ph/0606403 (cit. on pp. 22, 30, 53).

Mokiem, M. R., A. de Koter, J. S. Vink et al. (2007). *The empirical metallicity dependence of the mass-loss rate of O- and early B-type stars*. Astronomy & Astrophysics **473** 603. arXiv: 0708.2042 (cit. on pp. 22, 42).

Morgan, D. H., E. Vassiliadis and M. A. Dopita (1991). *A new Wolf-Rayet star in the Small Magellanic Cloud*. Monthly Notices of the Royal Astronomical Society **251** 51P (cit. on p. 23).

Neugent, K. F. et al. (2010). *Yellow Supergiants in the Small Magellanic Cloud: Putting Current Evolutionary Theory to the Test*. Astrophysical Jounal **719** 1784. arXiv: 1006.5742 [astro-ph.SR] (cit. on pp. 37, 88).

Neunteufel, P., S.-C. Yoon and N. Langer (2016). *Models for the evolution of close binaries with He-star and white dwarf components towards Type Ia supernova explosions*. Astronomy & Astrophysics **589** A43. arXiv: 1603.00768 [astro-ph.SR] (cit. on p. 4).

Newman, F. C. (1976). *Temperature Steps in Lake Kivu: A Bottom Heated Saline Lake*. Journal of Physical Oceanography **6** 157 (cit. on p. 11).

Nieuwenhuijzen, H. and C. de Jager (1990). *Parametrization of stellar rates of mass loss as functions of the fundamental stellar parameters M, L, and R*. Astronomy & Astrophysics **231** 134 (cit. on pp. 25, 43).

O'Connor, E. and C. D. Ott (2011). *Black Hole Formation in Failing Core-Collapse Supernovae*. Astrophysical Jounal **730** 70. arXiv: 1010.5550 [astro-ph.HE] (cit. on p. 6).

O'Gorman, E. et al. (2017). *The inhomogeneous submillimeter atmosphere of Betelgeuse*. Astronomy & Astrophysics **602** L10. arXiv: 1706.06021 [astro-ph.SR] (cit. on p. 96).

Ohnaka, K., G. Weigelt and K.-H. Hofmann (2017). *Vigorous atmospheric motion in the red supergiant star Antares*. Nature **548** 310. arXiv: 1708.06372 [astro-ph.SR] (cit. on p. 96).

Paczyński, B. (1965). *Cataclysmic Variables among Binary Stars I. U Geminorum Stars*. Acta Astronomica **15** 89 (cit. on p. 17).

Paxton, B., L. Bildsten et al. (2011). *Modules for Experiments in Stellar Astrophysics (MESA)*. Astrophysical Journal Supplement **192** 3. arXiv: 1009.1622 [astro-ph.SR] (cit. on pp. 14, 24, 43, 69).

Paxton, B., M. Cantiello et al. (2013). *Modules for Experiments in Stellar Astrophysics (MESA): Planets, Oscillations, Rotation, and Massive Stars*. Astrophysical Journal Supplement **208** 4. arXiv: 1301.0319 [astro-ph.SR] (cit. on pp. 14, 24, 43, 54, 69).

Paxton, B., P. Marchant et al. (2015). *Modules for Experiments in Stellar Astrophysics (MESA): Binaries, Pulsations, and Explosions*. Astrophysical Journal Supplement **220** 15. arXiv: 1506.03146 [astro-ph.SR] (cit. on pp. 14, 24, 43, 69).

Paxton, B., J. Schwab et al. (2018). *Modules for Experiments in Stellar Astrophysics (MESA): Convective Boundaries, Element Diffusion, and Massive Star Explosions*. Astrophysical Journal Supplement **234** 34. arXiv: 1710.08424 [astro-ph.SR] (cit. on pp. 14, 43, 69).

Peimbert, M., V. Luridiana and A. Peimbert (2007). *Revised Primordial Helium Abundance Based on New Atomic Data*. Astrophysical Jounal **666** 636. eprint: astro-ph/0701580 (cit. on pp. 15, 24).

Pellegrini, E. W., J. A. Baldwin and G. J. Ferland (2011). *Structure and Feedback in 30 Doradus. II. Structure and Chemical Abundances*. Astrophysical Jounal **738** 34. arXiv: 1101.3778 (cit. on p. 8).

Penny, L. R. and D. R. Gies (2009). *A FUSE Survey of the Rotation Rates of Very Massive Stars in the Small and Large Magellanic Clouds*. Astrophysical Jounal **700** 844. arXiv: 0905.3681 [astro-ph.SR] (cit. on p. 30).

Petermann, I. et al. (2015). *Blue supergiants as descendants of magnetic main sequence stars*. Astronomy & Astrophysics **584** A54. arXiv: 1509.05805 [astro-ph.SR] (cit. on p. 63).

Pian, E. et al. (2017). *Spectroscopic identification of r-process nucleosynthesis in a double neutron-star merger*. Nature **551** 67. arXiv: 1710.05858 [astro-ph.HE] (cit. on pp. 6, 7).

Podsiadlowski, P. and P. C. Joss (1989). *An alternative binary model for SN1987A*. Nature **338** 401 (cit. on pp. 5, 17, 82, 85).

Podsiadlowski, P., P. C. Joss and J. J. L. Hsu (1992). *Presupernova evolution in massive interacting binaries*. Astrophysical Jounal **391** 246 (cit. on pp. 38, 64).

Prantzos, N. et al. (1986). *Nucleosynthesis and evolution of massive stars with mass loss and overshooting*. Astrophysical Jounal **304** 695 (cit. on p. 55).

Renzo, M. et al. (2017). *Systematic survey of the effects of wind mass loss algorithms on the evolution of single massive stars*. Astronomy & Astrophysics **603** A118. arXiv: 1703.09705 [astro-ph.SR] (cit. on p. 13).

Rivinius, T., A. C. Carciofi and C. Martayan (2013). *Classical Be stars. Rapidly rotating B stars with viscous Keplerian decretion disks*. Astronomy & Astrophysics Review **21** 69. arXiv: 1310.3962 [astro-ph.SR] (cit. on p. 84).

Rodriguez, C. L., S. Chatterjee and F. A. Rasio (2016). *Binary black hole mergers from globular clusters: Masses, merger rates, and the impact of stellar evolution*. Physical Review D **93** 084029. arXiv: 1602.02444 [astro-ph.HE] (cit. on p. 6).

Salpeter, E. E. (1955). *The Luminosity Function and Stellar Evolution.* Astrophysical Jounal **121** 161 (cit. on p. 72).

Sana, H. et al. (2012). *Binary Interaction Dominates the Evolution of Massive Stars*. Science **337** 444. arXiv: 1207.6397 [astro-ph.SR] (cit. on pp. 16, 17, 36, 63, 85).

Sanyal, D., L. Grassitelli et al. (2015). *Massive main-sequence stars evolving at the Eddington limit*. Astronomy & Astrophysics **580** A20. arXiv: 1506.02997 [astro-ph.SR] (cit. on pp. 37, 54).

Sanyal, D., N. Langer et al. (2017). *Metallicity dependence of envelope inflation in massive stars*. Astronomy & Astrophysics **597** A71. arXiv: 1611.07280 [astro-ph.SR] (cit. on pp. 28, 37).

Schmid, M., M. Busbridge and A. Wüest (2010). *Double-diffusive convection in Lake Kivu*. Limnology and Oceanography **55** 225 (cit. on pp. 10, 11).

Schneider, F. R. N., R. G. Izzard et al. (2015). *Evolution of Mass Functions of Coeval Stars through Wind Mass Loss and Binary Interactions*. Astrophysical Jounal **805** 20. arXiv: 1504.01735 [astro-ph.SR] (cit. on p. 36).

Schneider, F. R. N., P. Podsiadlowski et al. (2016). *Rejuvenation of stellar mergers and the origin of magnetic fields in massive stars*. Monthly Notices of the Royal Astronomical Society **457** 2355. arXiv: 1601.05084 [astro-ph.SR] (cit. on p. 63).

Schootemeijer, A., Y. Götberg et al. (2018). *Clues about the scarcity of stripped-envelope stars from the evolutionary state of the sdO+Be binary system phi Persei*. Astronomy & Astrophysics **615** A30. arXiv: 1803.02379 [astro-ph.SR] (cit. on p. 17).

Schootemeijer, A. and N. Langer (2018). *Wolf-Rayet stars in the Small Magellanic Cloud as testbed for massive star evolution*. Astronomy & Astrophysics **611** A75. arXiv: 1709.08727 [astro-ph.SR] (cit. on pp. 42–44, 51, 61).

Schulze, S. et al. (2018). *Cosmic evolution and metal aversion in superluminous supernova host galaxies*. Monthly Notices of the Royal Astronomical Society **473** 1258 (cit. on p. 42).

Shapiro, S. L. and A. P. Lightman (1976). *Black holes in X-ray binaries - Marginal existence and rotation reversals of accretion disks*. Astrophysical Jounal **204** 555 (cit. on p. 39).

Shenar, T., R. Hainich et al. (2016). *Wolf-Rayet stars in the Small Magellanic Cloud. II. Analysis of the binaries*. Astronomy & Astrophysics **591** A22. arXiv: 1604.01022 [astro-ph.SR] (cit. on pp. 23–25, 28, 38, 126).

Shenar, T., N. D. Richardson et al. (2017). *The Tarantula Massive Binary Monitoring. II. First SB2 orbital and spectroscopic analysis for the Wolf-Rayet binary R145*. Astronomy & Astrophysics **598** A85. arXiv: 1610.07614 [astro-ph.SR] (cit. on p. 22).

Smartt, S. J. (2009). *Progenitors of Core-Collapse Supernovae*. Annual Review of Astronomy and Astrophysics **47** 63. arXiv: 0908.0700 [astro-ph.SR] (cit. on p. 66).

Smith, N. (2014). *Mass Loss: Its Effect on the Evolution and Fate of High-Mass Stars*. Annual Review of Astronomy and Astrophysics **52** 487. arXiv: 1402.1237 [astro-ph.SR] (cit. on p. 13).

Smith, N. and R. Tombleson (2015). *Luminous blue variables are antisocial: their isolation implies that they are kicked mass gainers in binary evolution*. Monthly Notices of the Royal Astronomical Society **447** 598. arXiv: 1406.7431 [astro-ph.SR] (cit. on p. 37).

Spruit, H. C. (1999). *Differential rotation and magnetic fields in stellar interiors*. Astronomy & Astrophysics **349** 189. eprint: astro-ph/9907138 (cit. on p. 11).

– (2002). *Dynamo action by differential rotation in a stably stratified stellar interior*. Astronomy & Astrophysics **381** 923. eprint: astro-ph/0108207 (cit. on p. 54).

Stephenson, F. R., D. H. Clark and D. F. Crawford (1977). *The supernova of AD 1006*. Monthly Notices of the Royal Astronomical Society **180** 567 (cit. on p. 1).
Stothers, R. B. and C.-W. Chin (1992). *Stellar evolution in blue populous clusters of the Small Magellanic Cloud and the problems of envelope semiconvection and convective core overshooting*. Astrophysical Jounal **390** 136 (cit. on pp. 42, 55).
Suijs, M. P. L. et al. (2008). *White dwarf spins from low-mass stellar evolution models*. Astronomy & Astrophysics **481** L87. arXiv: 0802.3286 (cit. on p. 54).
Sukhbold, T. et al. (2016). *Core-collapse Supernovae from 9 to 120 Solar Masses Based on Neutrino-powered Explosions*. Astrophysical Jounal **821** 38. arXiv: 1510.04643 [astro-ph.HE] (cit. on p. 6).
Sweet, P. A. (1950). *The importance of rotation in stellar evolution*. Monthly Notices of the Royal Astronomical Society **110** 548 (cit. on p. 12).
Talley, L. D. and M. S. McCartney (1982). *Distribution and Circulation of Labrador Sea Water*. Journal of Physical Oceanography **12** 1189 (cit. on p. 9).
Tayler, R. J. (1973). *The adiabatic stability of stars containing magnetic fields-I.Toroidal fields*. Monthly Notices of the Royal Astronomical Society **161** 365 (cit. on p. 11).
Ulmer, A. and E. L. Fitzpatrick (1998). *Revisiting the Modified Eddington Limit for Massive Stars*. Astrophysical Jounal **504** 200. eprint: astro-ph/9708264 (cit. on p. 37).
Venn, K. A. (1999). *A-Type Supergiant Abundances in the Small Magellanic Cloud: Probes of Evolution*. Astrophysical Jounal **518** 405. eprint: astro-ph/9901306 (cit. on pp. 14, 22, 25, 42, 43).
Vink, J. S., A. de Koter and H. J. G. L. M. Lamers (2001). *Mass-loss predictions for O and B stars as a function of metallicity*. Astronomy & Astrophysics **369** 574. eprint: astro-ph/0101509 (cit. on pp. 7, 13, 25, 43).
Vink, J. S. and T. J. Harries (2017). *Wolf-Rayet spin at low metallicity and its implication for black hole formation channels*. Astronomy & Astrophysics **603** A120. arXiv: 1703.09857 [astro-ph.SR] (cit. on p. 28).
von Zeipel, H. (1924). *The radiative equilibrium of a rotating system of gaseous masses*. Monthly Notices of the Royal Astronomical Society **84** 665 (cit. on pp. 12, 46, 84).
Walborn, N. R. et al. (2004). *A CNO Dichotomy among O2 Giant Spectra in the Magellanic Clouds*. Astrophysical Jounal **608** 1028. eprint: astro-ph/0403557 (cit. on p. 22).
Webster, B. L. and P. Murdin (1972). *Cygnus X-1-a Spectroscopic Binary with a Heavy Companion ?* Nature **235** 37 (cit. on p. 6).
Wellstein, S. and N. Langer (1999). *Implications of massive close binaries for black hole formation and supernovae*. Astronomy & Astrophysics **350** 148. eprint: astro-ph/9904256 (cit. on p. 38).
Wellstein, S., N. Langer and H. Braun (2001). *Formation of contact in massive close binaries*. Astronomy & Astrophysics **369** 939. eprint: astro-ph/0102244 (cit. on pp. 16, 38).
Woosley, S. E. (1988). *SN 1987A - After the peak*. Astrophysical Jounal **330** 218 (cit. on p. 5).
Woosley, S. E. and A. Heger (2006). *The Progenitor Stars of Gamma-Ray Bursts*. Astrophysical Jounal **637** 914. eprint: astro-ph/0508175 (cit. on pp. 22, 66).
– (2015). *The Remarkable Deaths of 9-11 Solar Mass Stars*. Astrophysical Jounal **810** 34. arXiv: 1505.06712 [astro-ph.SR] (cit. on p. 4).
Worthey, G. and H.-c. Lee (2011). *An Empirical UBV RI JHK Color-Temperature Calibration for Stars*. Astrophysical Journal Supplement **193** 1. eprint: astro-ph/0604590 (cit. on pp. 69, 76, 83, 85).
Wright, A. E. and M. J. Barlow (1975). *The radio and infrared spectrum of early-type stars undergoing mass loss*. Monthly Notices of the Royal Astronomical Society **170** 41 (cit. on p. 77).
Yang, M. and B. W. Jiang (2012). *The Period-Luminosity Relation of Red Supergiant Stars in the Small Magellanic Cloud*. Astrophysical Jounal **754** 35. arXiv: 1205.1275 [astro-ph.SR] (cit. on p. 37).

Yoon, S.-C. and N. Langer (2005). *Evolution of rapidly rotating metal-poor massive stars towards gamma-ray bursts*. Astronomy & Astrophysics **443** 643. eprint: astro-ph/0508242 (cit. on pp. 22, 25, 53).

Yoon, S.-C., N. Langer and C. Norman (2006). *Single star progenitors of long gamma-ray bursts. I. Model grids and redshift dependent GRB rate*. Astronomy & Astrophysics **460** 199. eprint: astro-ph/0606637 (cit. on pp. 22, 25, 42, 63, 66).

Zaussinger, F. and H. C. Spruit (2013). *Semiconvection: numerical simulations*. Astronomy & Astrophysics **554** A119. arXiv: 1303.4522 [astro-ph.SR] (cit. on pp. 10, 42, 66).

Zinnecker, H. and H. W. Yorke (2007). *Toward Understanding Massive Star Formation*. Annual Review of Astronomy and Astrophysics **45** 481. arXiv: 0707.1279 (cit. on p. 17).

Appendix A: extra information to Chapter 2

Hertzsprung-Russell diagrams with typical inferred hydrogen slopes

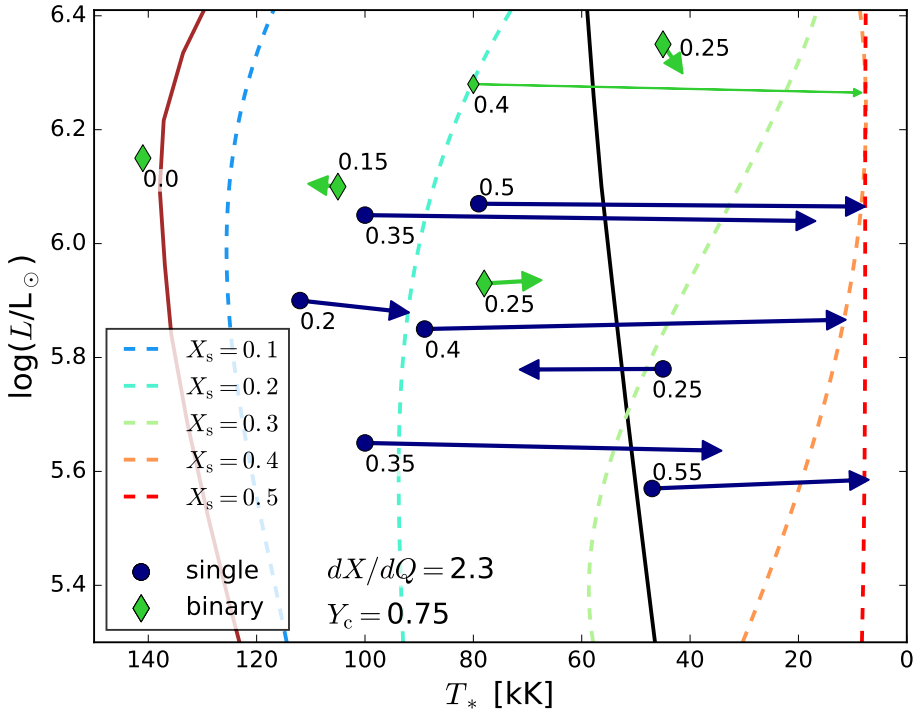

Figure A1: Hertzsprung-Russell diagram of models with helium cores and various hydrogen profiles displayed. The slope of the hydrogen profile has a value dX/dQ = 2.3 (which is the typical value we infer for the SMC WR stars in binaries) for all models. The surface hydrogen mass fraction X_s is indicated by the colors of the dashed lines. Green diamonds indicate observed values for binary SMC WR stars, blue circles indicate apparently singles stars. The arrows point to models with the same log L and X_s as the observed objects. The peculiar SMC AB6 is displayed with a smaller symbol and arrow.

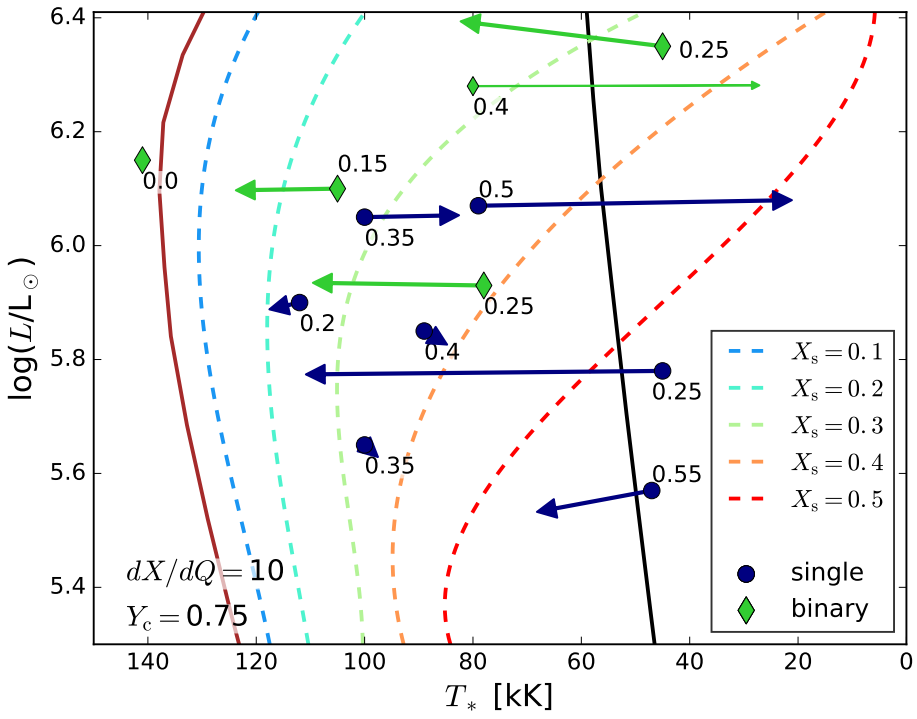

Figure A2: Same as Fig. A1, but instead models with $dX/dQ = 10$ (which is the typical value we infer for the hot apparently single SMC WR stars) are shown.

Best-fitting slopes for all WR stars

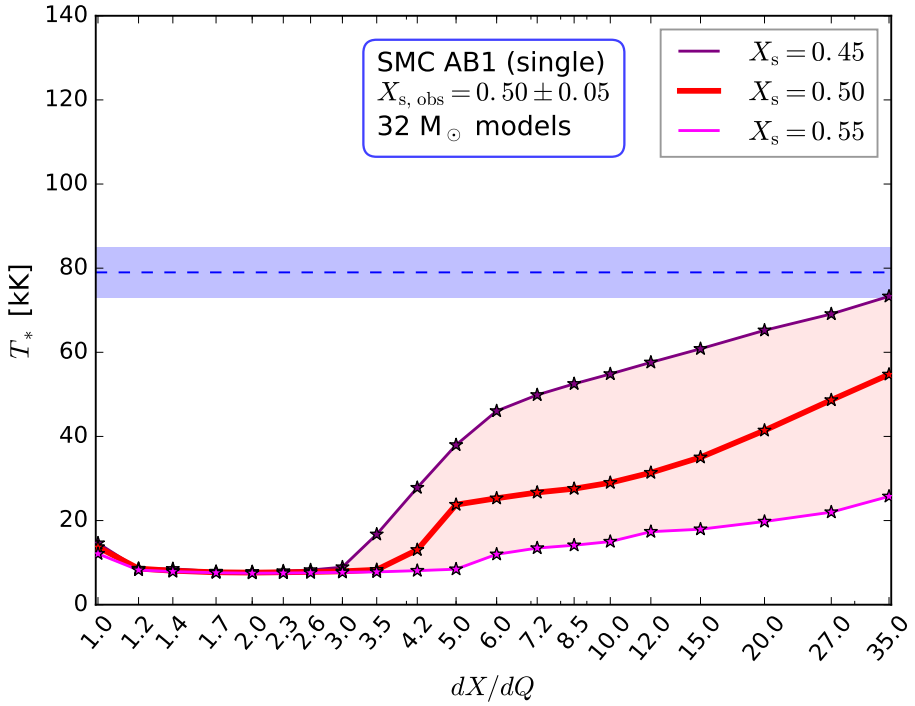

Figure A3: Same as Fig. 2.6, but models are compared to SMC AB1.

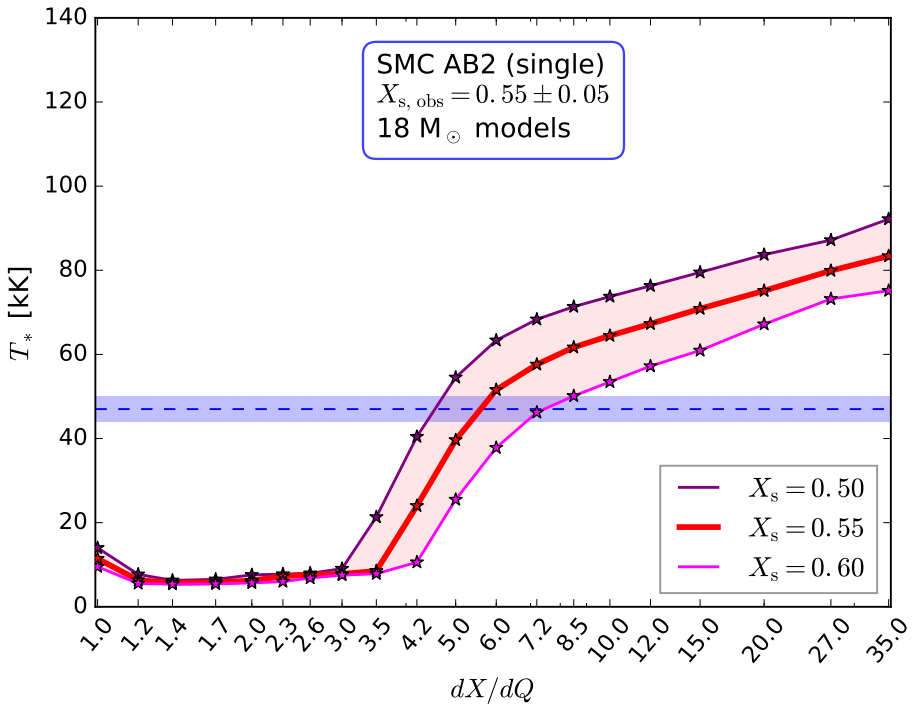

Figure A4: Same as Fig. 2.6, but models are compared to SMC AB2.

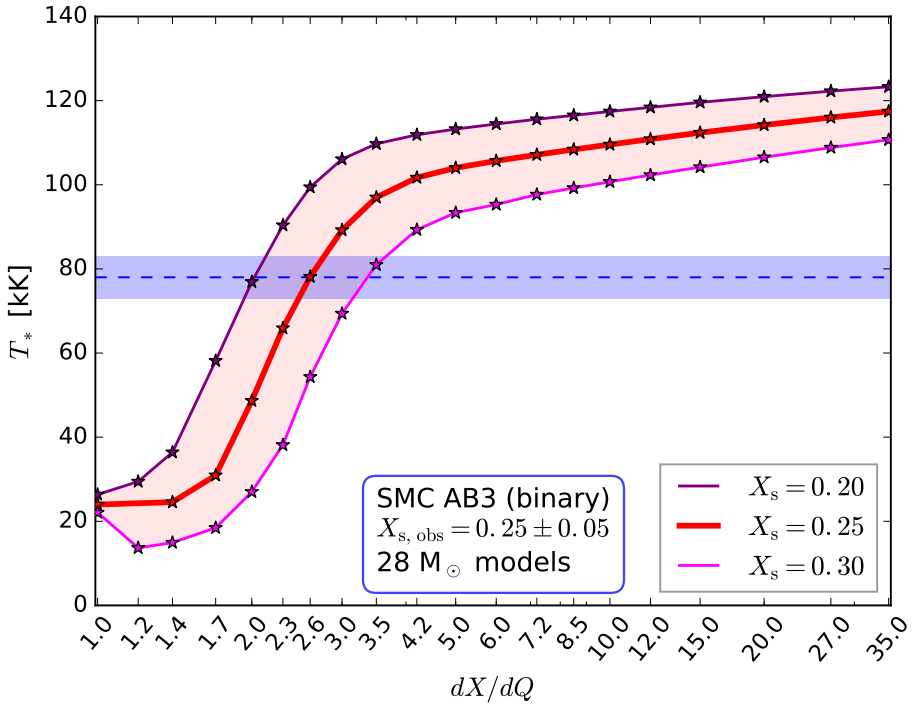

Figure A5: Same as Fig. 2.6, but models are compared to SMC AB3.

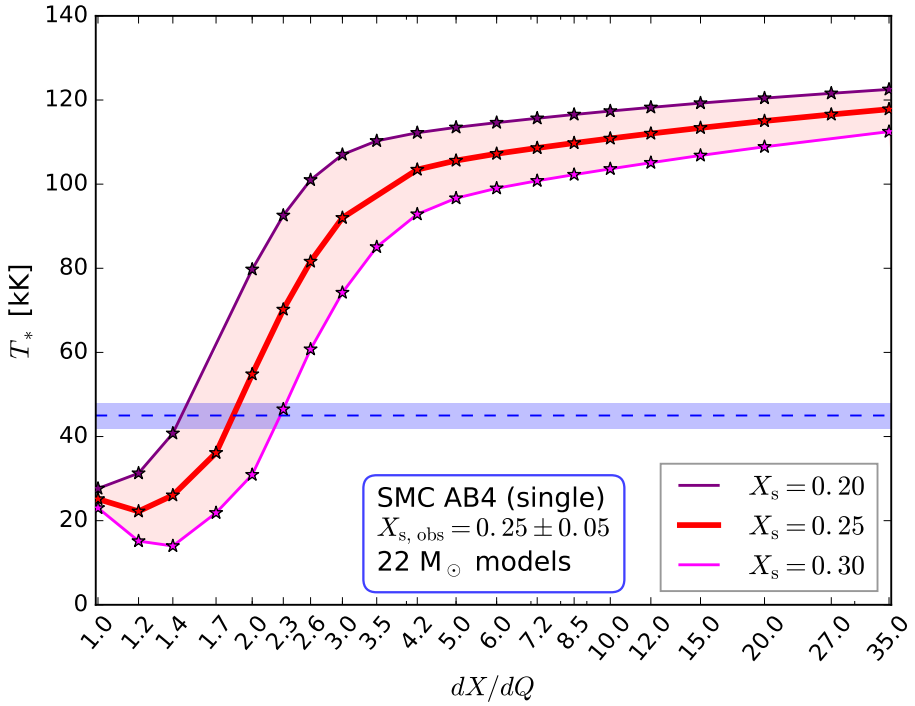

Figure A6: Same as Fig. 2.6, but models are compared to SMC AB4.

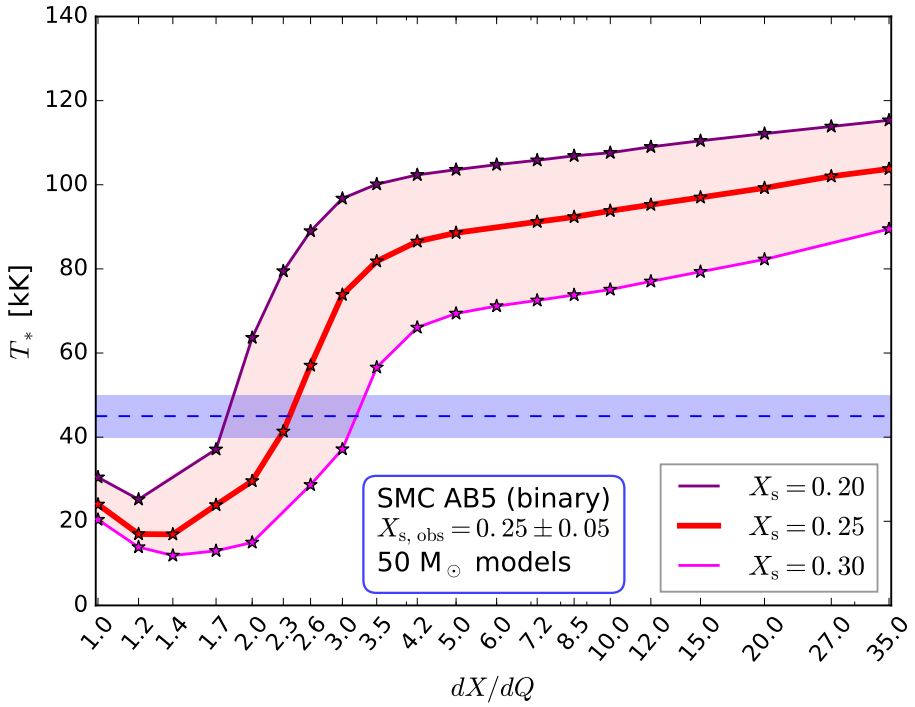

Figure A7: Same as Fig. 2.6, but models are compared to SMC AB5.

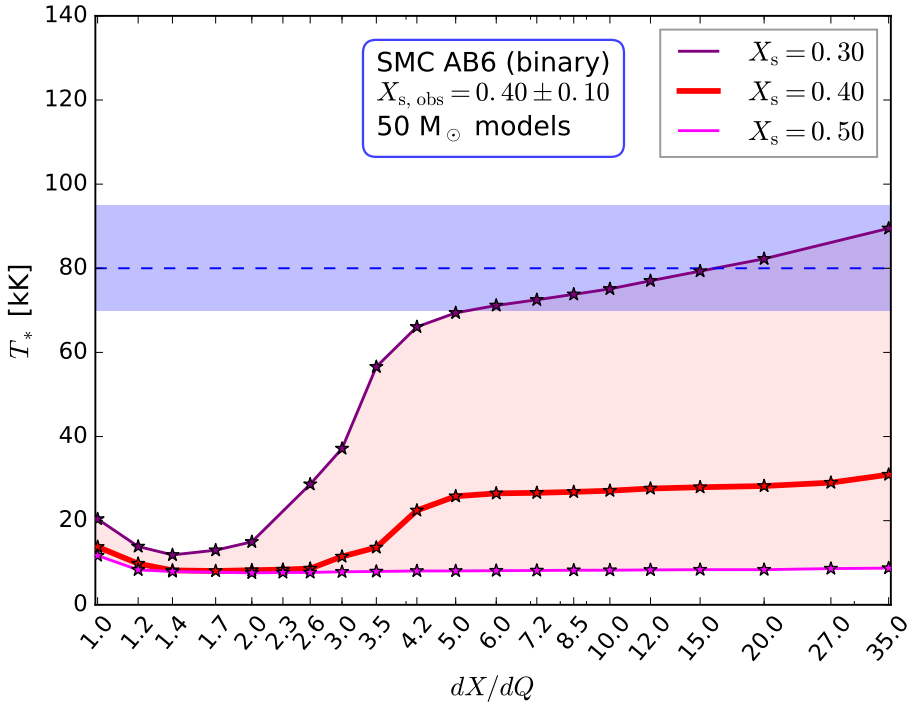

Figure A8: Same as Fig. 2.6, but models are compared to SMC AB6.

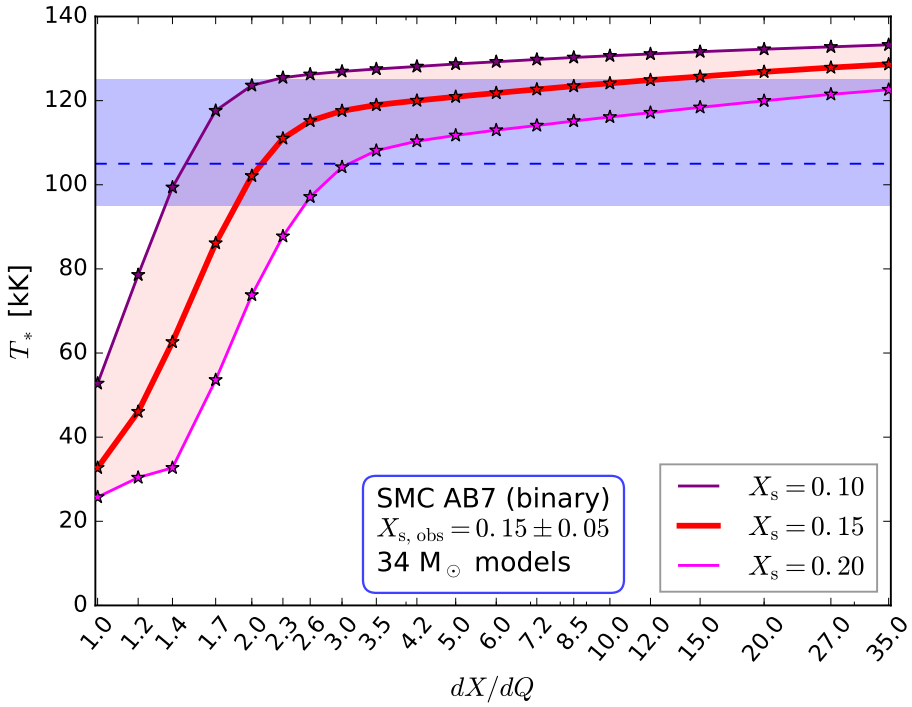

Figure A9: Same as Fig. 2.6, but models are compared to SMC AB7.

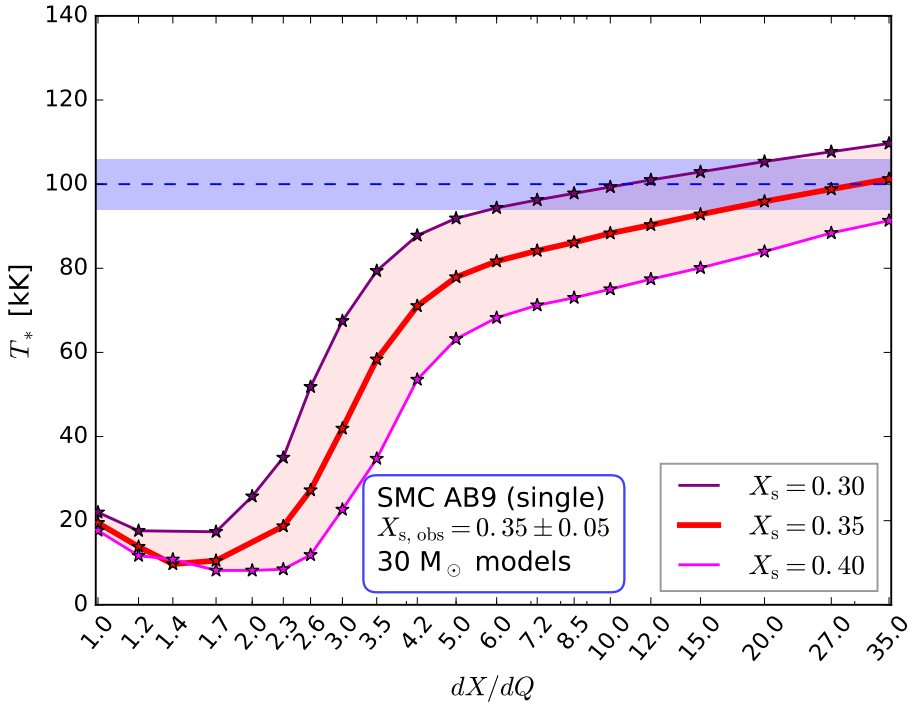

Figure A10: Same as Fig. 2.6, but models are compared to SMC AB9.

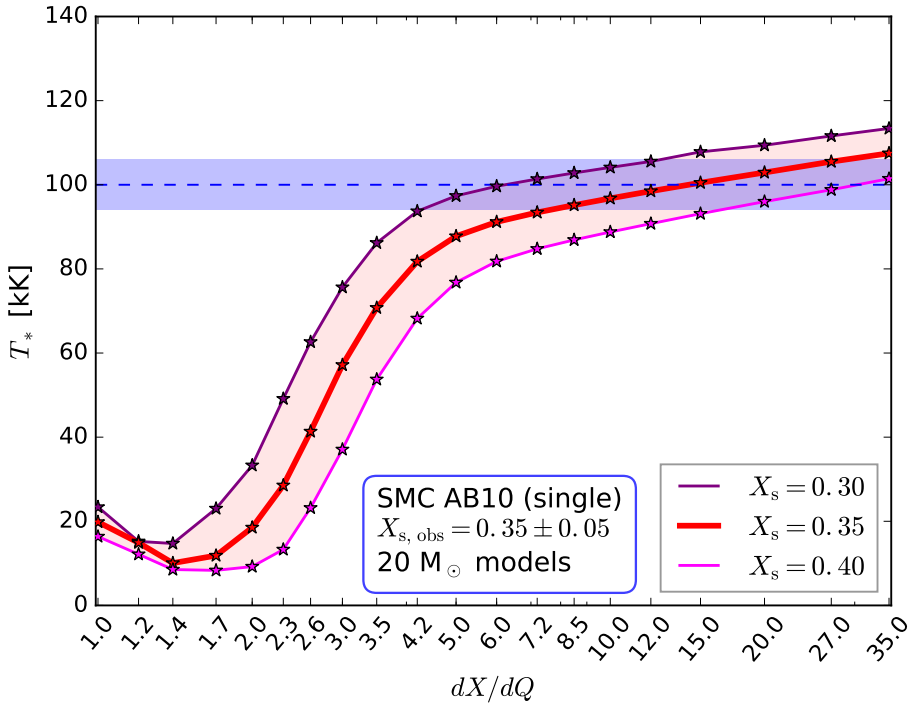

Figure A11: Same as Fig. 2.6, but models are compared to SMC AB10.)

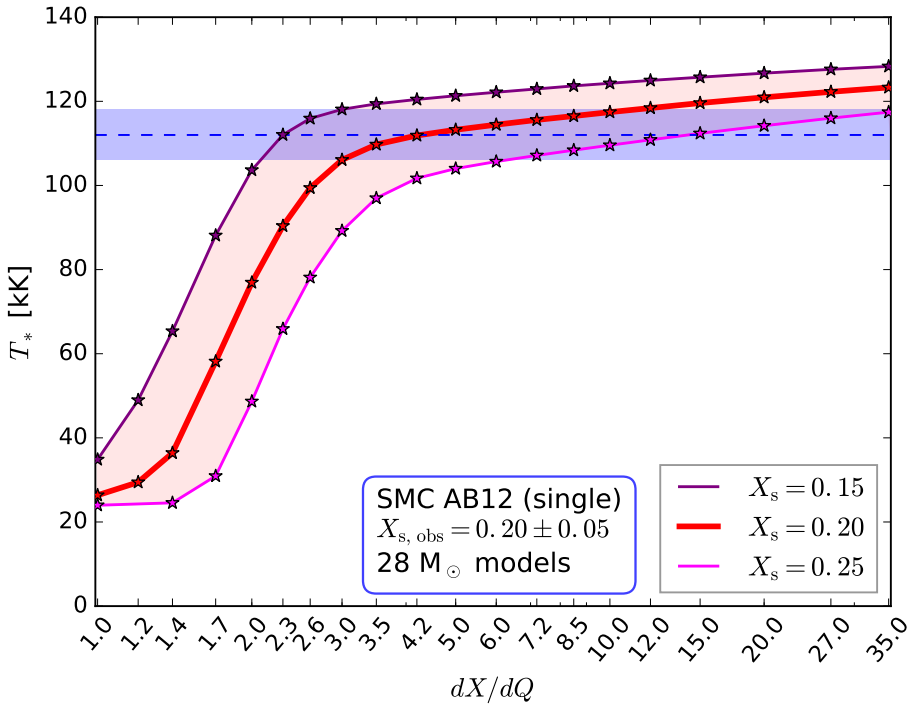

Figure A12: Same as Fig. 2.6, but models are compared to SMC AB12.

Validity of the method

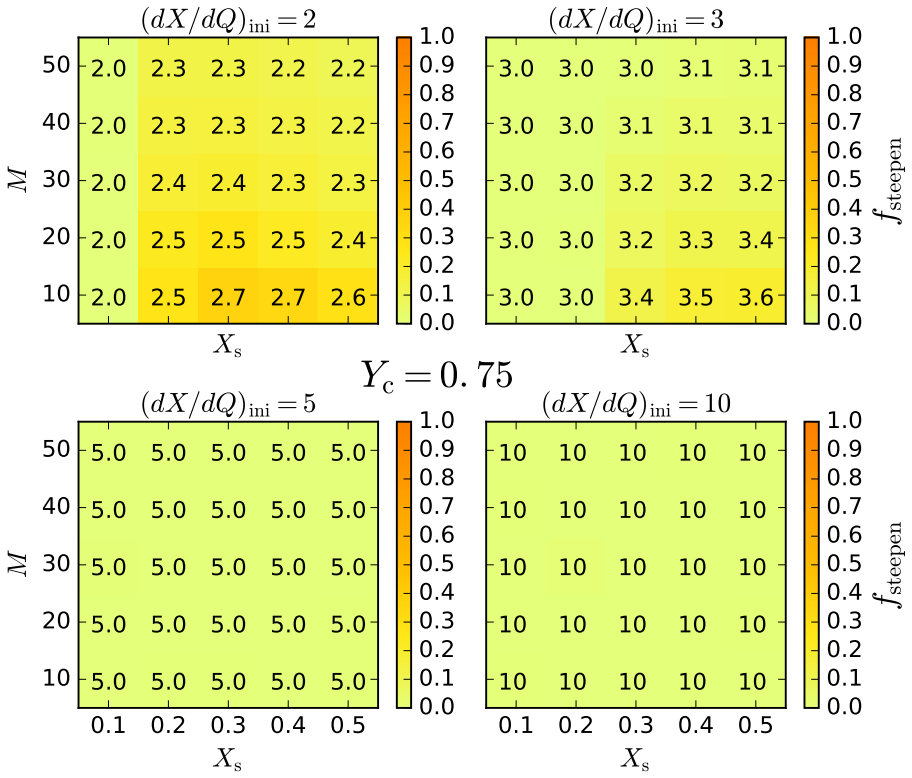

Figure A13: Diagrams showing the change of the hydrogen slope dX/dQ as a result of hydrogen shell burning. Each number indicates the values of dX/dQ at the moment helium burning has proceeded to $Y_{\rm c} = 0.75$ in models with different initial values for dX/dQ, $X_{\rm s}$ and M. Unlike the models discussed in Sect. 2.5, hydrogen shells burning is allowed in these models. The background color indicates by what fraction dX/dQ has increased during helium burning: $f_{\rm steepen}$.

In this appendix, we consider the effect of hydrogen shell burning on the dX/dQ value of the hydrogen profiles in our stripped star models and the timescales on which the hydrogen envelopes we infer would be blown away by wind mass loss. We find that although hydrogen shell burning occurs, it does not dramatically increase the dX/dQ value during helium burning. This is shown in Fig. A13 in the appendix: typically the dX/dQ value increases by less than 25% until $Y_{\rm c} = 0.75$. The largest increase that occurs in the whole parameter space is from $dX/dQ = 2.0$ to $dX/dQ = 4.1$ over the entire core helium burning phase. Models with higher initial $dXdQ$ values are less affected by nuclear burning.

In an extreme case with a strong stellar wind and a low-mass hydrogen envelope (the higher dX/dQ and the lower $X_{\rm s}$, the lower the mass of the hydrogen envelope), it is imaginable that the hydrogen envelope is completely removed during core helium burning. Therefore we consider the lifetimes of the model hydrogen envelopes, $\tau_{\rm H\,env} = M_{\rm H\,env}/\dot{M}_{\rm obs}$, with respect to the model core helium burning lifetimes, $\tau_{\rm He\,core}$. Here, $M_{\rm H\,env}$ follows from the inferred dX/dQ value, the observed hydrogen mass fraction $X_{\rm s}$ and the mass $M_{\rm model}$ that corresponds to the observed luminosity. In a case where $\tau_{\rm H\,env}/\tau_{\rm He\,core} > 1$, there is no moment during helium burning in which the star is hydrogen free. What we find is that the ratio $\tau_{\rm H\,env}/\tau_{\rm He\,core}$ is typically of the order unity (Table 1). That means that for some stars where

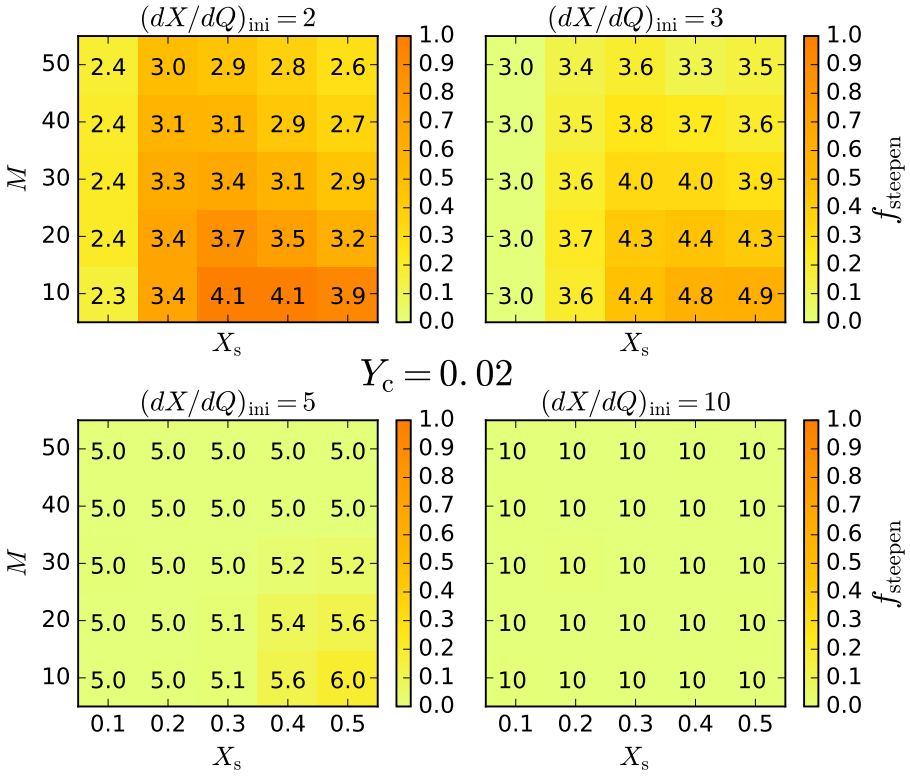

Figure A14: Same as Fig. A13, but now the models are almost at the end of helium burning: $Y_{\rm c} = 0.02$.

the value is below one, the hydrogen-depleted layers would be exposed at a point in time, – given that envelope stripping didn't happen in a late helium burning phase. We note that more efficient convection (a higher value of $\alpha_{\rm MLT}$) would lead to less envelope inflation and somewhat higher values for T_* mainly in the case of luminous and hydrogen-rich stars (i.e., SMC AB1, 6 and 9). A quick test showed that this results in slightly lower dX/dQ values also being compatible with the observed properties, and allows for higher $\tau_{\rm H\,env}$. However, this did not change the conclusion that these objects are incompatible with models where dX/dQ is on the order of 2: their T_* was not significantly affected.

Table 1: Best-fitting dX/dQ values inferred for the single and binary SMC WR stars. Also displayed are the timescale on which the WR star would blow away its hydrogen-containing layers ($\tau_{\mathrm{H\,env}}$) and the ratio of $\tau_{\mathrm{H\,env}}$ to the helium burning timescale. The last column gives the best fitting current masses.

SMC AB	dX/dQ	$\tau_{\mathrm{H\,env}}$ [kyr]	$\frac{\tau_{\mathrm{H\,env}}}{\tau_{\mathrm{He\,burn}}}$	M_{model} [$\mathrm{M}_{\odot}$]
Single:				
1	≥ 35	≤ 175	≤ 0.56	32
2	$5.7^{+1.8}_{-1.2}$	1011^{+282}_{-299}	$2.66^{+0.74}_{-0.65}$	18
4	$1.8^{+0.5}_{-0.3}$	638^{+191}_{-177}	$1.81^{+0.55}_{-0.50}$	22
9	$30^{+?}_{-18.5}$	$158^{+264}_{-?}$	$0.50^{+0.81}_{-?}$	30
10	$13.5^{+?}_{-7.5}$	$233^{+312}_{-?}$	$0.64^{+0.85}_{-?}$	20
11	18^{+17}_{-11}	213^{+354}_{-86}	$0.64^{+1.06}_{-0.26}$	26
12	$4.2^{+10.8}_{-1.9}$	945^{+1023}_{-707}	$2.91^{+3.15}_{-2.18}$	28
Binary:				
3	$2.6^{+0.7}_{-0.5}$	663^{+207}_{-165}	$2.04^{+0.64}_{-1.53}$	28
5	$2.4^{+0.8}_{-0.6}$	207^{+96}_{-61}	$0.75^{+0.34}_{-0.22}$	50
6	≥ 16	≤ 160	≤ 0.58	50
7	$2.1^{+0.9}_{-0.6}$	188^{+168}_{-55}	$0.61^{+0.53}_{-0.18}$	34

Best fits of rotating evolutionary models

Table 2: Models which are able to achieve the best fit for each individual Wolf-Rayet star. For each object we display the initial mass and initial rotation velocity of the best-fitting models and we compare the observed values (Hainich, Pasemann, Todt et al., 2015) of the fit parameters to their model values at the moment the best fit is achieved. Next, we display the observed upper limit on the rotational velocity $v \sin i$ and the model $v_{\rm rot}$ at the moment the best fit is achieved. For models where $v_{\rm rot}$ exceeds the observed upper limit on $v \sin i$ we calculate $P_{\rm inc}$, i.e., the chance that $v \sin i$ does not exceed the upper limit due to a low inclination of the rotational axis. $\chi^2_{\rm min}$ is the lowest χ^2 value achieved with our three fit parameters T_*, $\log L$ and $X_{\rm H}$. In this table, only **single stars** are considered and compared to models that are **core hydrogen burning**.

SMC AB	M_0 [$M_\odot$]	$v_{\rm rot,0}$ [km s^{-1}]	T_* [kK]	$\log L$ [$L_\odot$]	$X_{\rm H}$	$v \sin i$; $v_{\rm rot}$ [km s^{-1}]	$P_{\rm inc}$	$\chi^2_{\rm min}$
1 (obs)			79^{+6}_{-6}	$6.07^{+0.20}_{-0.20}$	$0.50^{+0.05}_{-0.05}$	<100	0.044	11.6
model	100	590	59	6.25	0.48	342		
2 (obs)			47^{+3}_{-3}	$5.57^{+0.10}_{-0.10}$	$0.55^{+0.05}_{-0.05}$	<50	0.014	0.29
model	35	400	47	5.54	0.53	302		
4 (obs)			45^{+3}_{-3}	$5.78^{+0.10}_{-0.10}$	$0.25^{+0.05}_{-0.05}$	<100	0.16	3.07
model	35	420	50	5.81	0.29	183		
9 (obs)			100^{+6}_{-6}	$6.05^{+0.20}_{-0.20}$	$0.35^{+0.05}_{-0.05}$	<200	0.40	45.3
model	70	600	60	6.12	0.32	251		
10 (obs)			100^{+6}_{-6}	$5.65^{+0.20}_{-0.20}$	$0.35^{+0.05}_{-0.05}$	<200	0.36	49.6
model	55	600	60	5.98	0.29	259		
11 (obs)			89^{+6}_{-6}	$5.85^{+0.20}_{-0.20}$	$0.40^{+0.05}_{-0.05}$	<200	0.34	26.1
model	100	600	62	6.31	0.37	267		
12 (obs)			112^{+6}_{-6}	$5.90^{+0.20}_{-0.20}$	$0.20^{+0.05}_{-0.05}$	<200	1	49.9
model	100	600	77	6.31	0.02	13		

Table 3: Lowest obtained χ^2 values for each system. Same as Table 2, but now we compare with **core helium burning** models.

SMC AB	M_0 [$M_\odot$]	$v_{\rm rot,0}$ [km s^{-1}]	T_* [kK]	$\log L$ [$L_\odot$]	$X_{\rm H}$	$v \sin i$; $v_{\rm rot}$ [km s^{-1}]	$P_{\rm inc}$	$\chi^2_{\rm min}$
1 (obs)			79^{+6}_{-6}	$6.07^{+0.20}_{-0.20}$	$0.50^{+0.05}_{-0.05}$	<100	1	8.5
model	55	390	67	6.15	0.40	0.2		
2 (obs)			47^{+3}_{-3}	$5.57^{+0.10}_{-0.10}$	$0.55^{+0.05}_{-0.05}$	<50	1	39.3
model	55	390	39	6.15	0.44	1		
4 (obs)			45^{+3}_{-3}	$5.78^{+0.10}_{-0.10}$	$0.25^{+0.05}_{-0.05}$	<100	1	1.8
model	30	450	45	5.9	0.22	79		
9 (obs)			100^{+6}_{-6}	$6.05^{+0.20}_{-0.20}$	$0.35^{+0.05}_{-0.05}$	<200	1	8.4
model	45	550	100	6.08	0.21	6		
10 (obs)			100^{+6}_{-6}	$5.65^{+0.20}_{-0.20}$	$0.35^{+0.05}_{-0.05}$	<200	1	11.3
model	20	460	99	5.65	0.18	5		
11 (obs)			89^{+6}_{-6}	$5.85^{+0.20}_{-0.20}$	$0.40^{+0.05}_{-0.05}$	<200	1	9.3
model	55	390	75	6.15	0.34	9		
12 (obs)			112^{+6}_{-6}	$5.90^{+0.20}_{-0.20}$	$0.20^{+0.05}_{-0.05}$	<200	1	0.7
model	30	510	111	5.88	0.16	8		

Table 4: Models which are able to achieve the best fit for each individual Wolf-Rayet star. For each object we display the initial mass and initial rotation velocity of the best-fitting models and we compare the observed values (Shenar, Hainich, Todt et al., 2016) of the fit parameters to their model values at the moment the best fit is achieved. The parameter $v_{\rm sync}$ is the rotational velocity that the star would have in a system with (tidally) synchronized orbital and rotation periods. $R_{\rm RL}$ is the current size of the star's Roche lobe, whereas $R_{\rm max}$ is the maximum radius of the models at any point in time before the best fit is achieved. $\chi^2_{\rm min}$ is the lowest χ^2 value achieved with our three fit parameters T_*, $\log L$ and $X_{\rm H}$. Unlike in Table 2, we do not consider the model rotation velocities since these objects do not have observed constraints on the rotation velocity (except SMC AB $5_{\rm A}$ with $v \sin i < 300\,{\rm km\,s^{-1}}$). In this table, only **binary stars** are considered and compared to models that are **core hydrogen burning**.

SMC AB	M_0 [$M_\odot$]	$v_{\rm rot,0}$ [km s^{-1}]	T_* [kK]	$\log L$ [$L_\odot$]	$X_{\rm H}$	$v_{\rm sync}$ [km s^{-1}]	$R_{\rm RL}$ [$R_\odot$]	$R_{\rm max}$ [$R_\odot$]	$\chi^2_{\rm min}$
3 (obs)			78^{+5}_{-5}	$5.93^{+0.05}_{-0.05}$	$0.25^{+0.05}_{-0.05}$	25^{+5}_{-5}	25^{+29}_{-6}		13.3
model	50	600	60	5.96	0.25			9.3	
$5_{\rm A}$ (obs)			45^{+5}_{-5}	$6.35^{+0.10}_{-0.10}$	$0.25^{+0.05}_{-0.05}$	63^{+26}_{-18}	58^{+4}_{-4}		1.0
model	80	540	45	6.29	0.29			24	
6 (obs)			80^{+15}_{-10}	$6.28^{+0.10}_{-0.10}$	$0.40^{+0.10}_{-0.10}$	54^{+24}_{-15}	14^{+3}_{-2}		6.75
model	100	600	63	6.33	0.34			13.1	
7 (obs)			105^{+20}_{-10}	$6.10^{+0.10}_{-0.10}$	$0.15^{+0.05}_{-0.05}$	9^{+3}_{-3}	40^{+8}_{-3}		18.4
model	100	600	77	6.31	0.02			13.1	

Table 5: Same as Table 4, but now we compare with **core helium burning** models.

SMC AB	M_0 [$M_\odot$]	$v_{\rm rot,0}$ [km s^{-1}]	T_* [kK]	$\log L$ [$L_\odot$]	$X_{\rm H}$	$v_{\rm sync}$ [km s^{-1}]	$R_{\rm RL}$ [$R_\odot$]	$R_{\rm max}$ [$R_\odot$]	$\chi^2_{\rm min}$
3 (obs)			78^{+5}_{-5}	$5.93^{+0.05}_{-0.05}$	$0.25^{+0.05}_{-0.05}$	25^{+5}_{-5}	25^{+29}_{-6}		0.5
model	35	480	78	5.96	0.23			27	
$\mathbf{5_A}$ (obs)			45^{+5}_{-5}	$6.35^{+0.10}_{-0.10}$	$0.25^{+0.05}_{-0.05}$	63^{+26}_{-18}	58^{+4}_{-4}		0.04
model	70	520	45	6.33	0.25			103	
6 (obs)			80^{+15}_{-10}	$6.28^{+0.10}_{-0.10}$	$0.40^{+0.10}_{-0.10}$	54^{+24}_{-15}	14^{+3}_{-2}		2.5
model	55	390	75	6.13	0.34			1550	
7 (obs)			105^{+20}_{-10}	$6.10^{+0.10}_{-0.10}$	$0.15^{+0.05}_{-0.05}$	9^{+3}_{-3}	40^{+8}_{-3}		0.03
model	45	530	106	6.10	0.16			33	

Appendix B: extra information to Chapter 3

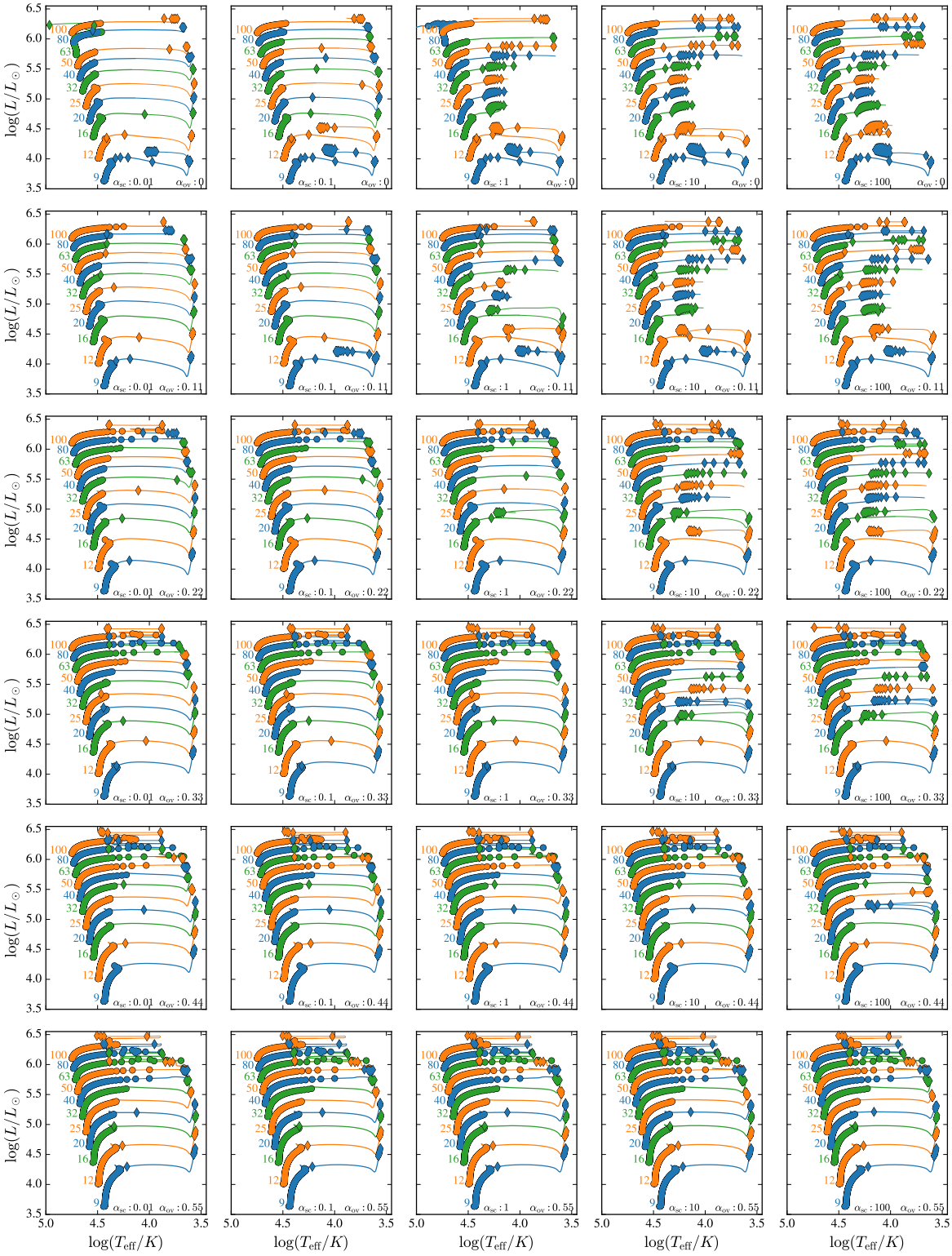

Figure B1: Same as Fig 3.2, but now we show more combinations of α_{sc} and α_{ov} .

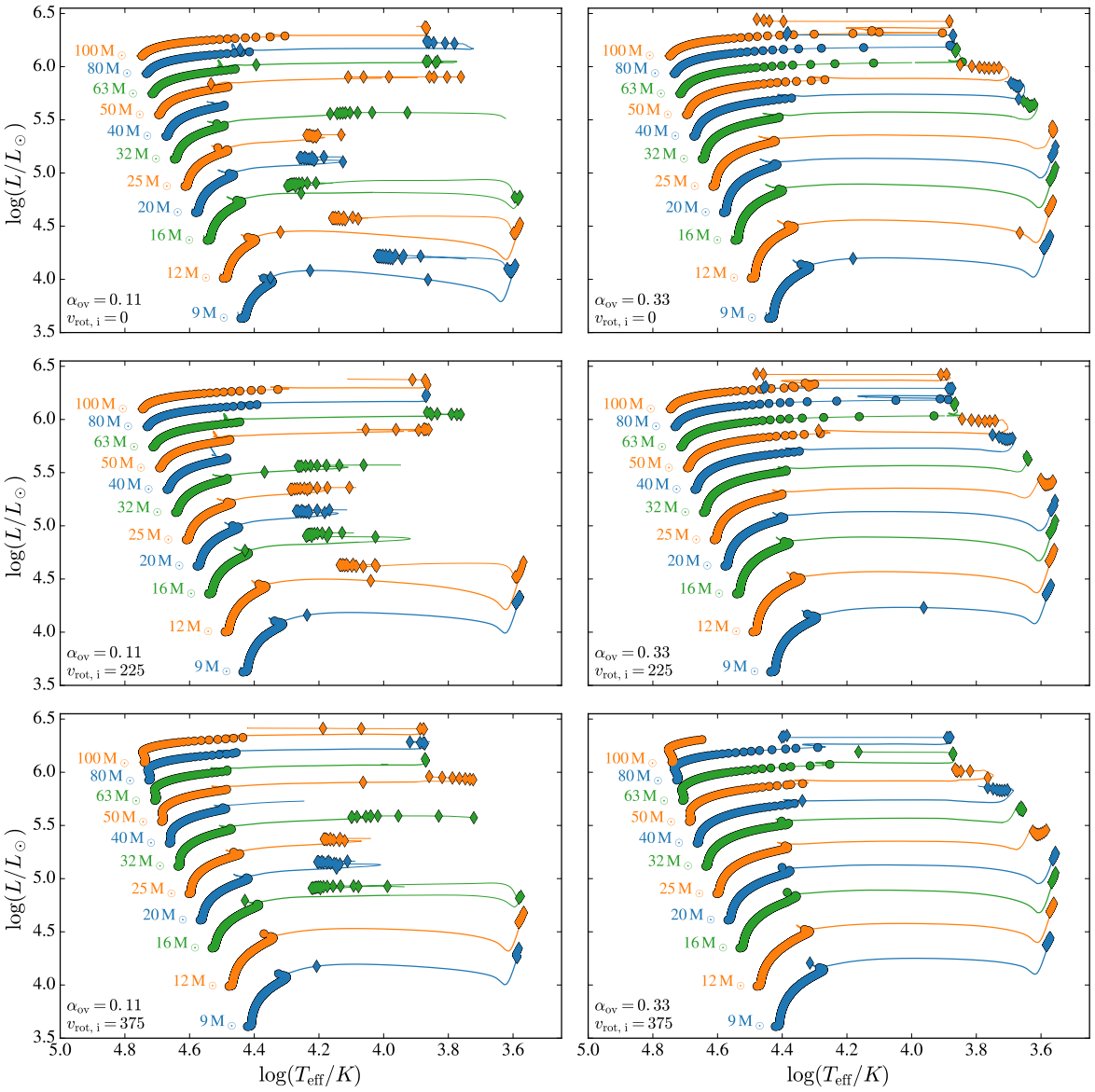

Figure B2: Same as Fig 3.2, but now we vary α_{ov} and the initial rotation velocity (indicated in the bottom left of each panel, in units of $\mathrm{km\,s^{-1}}$). The models were computed with high time resolution and with $\alpha_{sc} = 1$

Acknowledgements

First of all, I would like to thank my PhD supervisor Norbert Langer, who guided me through my work with his universal knowledge of astrophysics. I much appreciate the freedom you have given me during my PhD project, which is a reason why I would come to work with a smile every day.

Of great importance are also the other knowledgeable and kindhearted people in the stellar group. While I am not able to name everyone who deserves to be mentioned, I would like to highlight the following people. Work-wise, I thank a.o. Nathan, David, Götz, Chen, Pablo and Thomas, who worked topics related to mine, for many inspiring discussions. Norberto has my graditute for calculating the colors and magnitudes (presented in Chapter 4) of my evolutionary models with his synthetic spectra and sharing the star catalog we used in that chapter. Next, there is the lunch group that has impressed me immensely with their strong stomachs during our more-often-than-not inappropriate conversation topics (which I can not elaborate on in this context). Götz, Richard, Elvijs, Nathan, Zhengwei, Takashi, Carlo, Pablo, David, Koh, Jonathan and many others – thank you, also for your patience while waiting for me trying to finish my plate. Very importantly, there is the Friday drinks family, which deserves unconditional appreciation for their loyalty and passionate participation. Among these people are Nathan, David, Elvijs, Sandra, Toma, Götz, Joey, Eleni, Eleni, Ana, Benjamin, Sarah and Patrick. I thank my office mates Patrick, David, and Matthias for their very tolerable company, inspiring conversations and innovative ideas for new office themes. I thank the Blazing Suns basketball team and the AIfA Lifting Society. I thank the people who competed wholeheartedly in the AIfA football betting pool during the Euro Cup and World Cup – the 'blank form' competitor stood no chance against most of you.

From the ancient days where I was studying in my first home town Amsterdam, there is a number of people who very much deserve appreciation. I would like to start at the two years I spent during my master studies at the Anton Pannekoek Institute for Astronomy, where I had the pleasure to do my project under supervision of Selma de Mink, who sparked my enthusiasm to keep working in this field. In her 'massive binaries' group I had the valuable company of the at the time starting PhD students Ylva and Manos, who helped me during my master project. I thank Selma and Ylva for writing me poems even after I moved to Bonn. I thank the other master students for the support both related and non-related to the study; highlighting again Nathan, and Sarah. I of course thank Oscar Ramirez-Agudelo.

Going back still further in my student days, I need to thank many of my fellow chemistry students from my bachelor. From the year I started there are my comrades Lukas, Sven, Jurn, Martijn and Tom. From the people who were on board already before me, I mention evenly dear people such as Nikki, Kasper, Rolf[1], Chuchu, Tessel, and Rebecca. None of this would have been possible without the ACD protection department with Rosa, Stijn, Lukas, Jurn, Klaas, Rolf, Sven, Kasper, and Tommy. Finally, I would like to honor the names of a few dinosaurs such as Paddy, Nelis, Pieter, and Ruben.

From the even more distant past, I would like to thank some my school friends which go back up to over 25 years. Despite the distance in space and time, I am glad to be still in touch with you – here I highlight Ynze, Bas, and Daniël, and also Wouter, Twan en Jur. Finally, I would like to thank my parents Han and Annelies for over three decades of unconditional support.

[1] Commemorated as one half of the best sports committee ever

List of Publications

First author papers, refereed

I **Schootemeijer, A.** & Langer, N. — *2018, A&A, 611A, 75S* — Wolf-Rayet stars in the Small Magellanic Cloud as testbed for massive star evolution

II **Schootemeijer, A.**, Götberg, Y., Mink, S. E. de, Gies, D. & Zapartas, E. — *2018, A&A, 615A, 30S* — Clues about the scarcity of stripped-envelope stars from the evolutionary state of the sdO+Be binary system φ Persei

Second-or-later author papers, refereed

i Almeida, L. A., Sana, H., Taylor, W., Barbá, R., Bonanos, A. Z., Crowther, P., Damineli, A., de Koter, A., de Mink, S. E., Evans, C. J., Gieles, M., Grin, N. J., Hénault-Brunet, V., Langer, N., Lennon, D., Lockwood, S., Maíz Apellániz, J., Moffat, A. F. J., Neijssel, C., Norman, C., Ramírez-Agudelo, O. H., Richardson, N. D., **Schootemeijer, A.**, Shenar, T., Soszyński, I., Tramper, F. & Vink, J. S. — *2017, A&A, 598A, 84A* — The Tarantula Massive Binary Monitoring. I. Observational campaign and OB-type spectroscopic binaries

ii Zapartas, E., de Mink, S. E., Izzard, R. G., Yoon, S.-C., Badenes, C., Götberg, Y., de Koter, A., Neijssel, C. J., Renzo, M., **Schootemeijer, A.** & Shrotriya, T. S. — *2017 A&A, 601A, 29Z* — Delay-time distribution of core-collapse supernovae with late events resulting from binary interaction

iii Aguilera-Dena, David R., Langer, Norbert, Moriya, Takashi J. & **Schootemeijer, Abel** — *2018, ApJ, 858, 115A* — Related Progenitor Models for Long-duration Gamma-Ray Bursts and Type Ic Superluminous Supernovae